

UNIVERSITY OF TWENTE

MASTER THESIS

**Constraining the Standard Model effective
field theory Wilson coefficients using Higgs
and diboson data**

Author:
BSc. Bryan KORTMAN

Graduation Committee:
Prof. Dr. Ir. Bob v. EIJK
Dr. Pamela FERRARI
Prof. Dr. Ir. Alexander BRINKMAN
Prof. Dr. Wouter VERKERKE

*A thesis submitted in fulfillment of the requirements
for the degree of Master of Science
in the research chair of*

Energy, Materials and Systems (EMS)

November 14, 2019

“Quiet People have the loudest minds”

Stephen Hawking (1942-2018)

UNIVERSITY OF TWENTE

Abstract

Faculty of Science and Technology

Master of Science

Constraining the Standard Model effective field theory Wilson coefficients using Higgs and diboson data

by BSc. Bryan KORTMAN

A measurement of several free parameters in the Standard Model Effective Field Theory (SMEFT) [1] known as Wilson coefficients is carried out. The measurement is performed using data accumulated between 2015 and 2016 at the ATLAS detector. Proton-proton collisions were produced at Large Hadron Collider in CERN, Geneva, with a total integrated luminosity of 36.1 fb^{-1} and a center-of-mass energy of $\sqrt{s} = 13 \text{ TeV}$. The events are used to study Higgs production in gluon-gluon fusion (ggF) and vector boson fusion (VBF) [2]. The $H \rightarrow W^+W^- \rightarrow e\nu\mu\nu$ decay channel is considered. A dataset from charged vector boson pair production through interactions of quarks and gluons $qq/gg \rightarrow W^+W^- \rightarrow e\nu\mu\nu$ is also incorporated [3]. Constraints on 17 CP-even operators were obtained using Effective Lagrangian Morphing [4]. Only contribution up to order $1/\Lambda^2$ are taken into account. Operators affect the production and decay couplings in both ggF and VBF Higgs production, as well as the $qq/gg \rightarrow W^+W^-$ production. The contribution of these operators are estimated by linking deviations from the Standard Model (SM) in Simplified Template Cross Sections (STXS) [5] to the effects of dimension-6 operators. The SM and interference Monte Carlo (MC) samples are generated at LO with MadGraph5 and Pythia8. The interference samples are obtained by only generating the LO interference between the EFT and SM couplings. The dimensionality of the interpretation is greatly increased using this method. The MC samples are used in the interpolation technique effective Lagrangian morphing. The effective Lagrangian morphing uses the analytical structure of the Lagrangian to interpolate between different phase space regions allowing for theory predictions of kinematic distributions. This results in a continuous description of the kinematic observables as a function of the Wilson coefficients associated to the dimension-6 operators. A reparameterization of the ggF and VBF STXS regions is expressed in terms of the SMEFT Wilson coefficients. Profile Likelihood fits are performed on the reparameterized measurement. The fitting algorithm [6] uses the reparameterized framework of the analyses to obtain constraints on the Wilson coefficients. The analysis incorporates systematic and statistical uncertainties. Finally, the sensitivity of the EFT interpretation is improved by incorporating $qq/gg \rightarrow WW$ data and the corresponding EFT interpretation. The final results show deviations of $\mathcal{O}(1\sigma)$ from the Standard Model prediction.

Acknowledgements

First and foremost I should like to thank my professor and supervisor Bob van Eijk. Without him I would not have been able to dive so deep into this new field and learn so much within the past year. My appreciation also goes out to Wouter Verkerke and Carsten Burgard, who helped a lot with the coding skills needed to understand the tools involved. Next, I should like to thank Pamela Ferrari and Stefano Manzoni for their support from CERN during the weekly meetings. Also many thanks go to Federica Pasquali who helped and guided me considerably during the first few months of getting into all of the necessary skills needed for experimental particle physics. In addition to this I should like to mention Rahul Balasubramanian for tirelessly answering questions concerning several of the aspects touched upon in my research. Furthermore, I want to thank everyone in the ATLAS group and Nikhef for the time spend at the institute and Amsterdam in general. I look forward to continue my work at Nikhef as PhD candidate. At last, I want to thank my family and friends for supporting me during my research.

Contents

Acknowledgements	iii
1 General Introduction	1
2 Theory	4
2.1 The Standard Model of particle physics	4
2.1.1 Fundamental forces	4
2.2 The Higgs particle	6
2.2.1 Higgs production modes	6
2.2.2 Higgs branching fractions	8
2.2.3 Higgs properties	9
2.3 The Lagrangian	10
2.3.1 Relativistic quantum mechanics	11
2.3.2 Interactions in quantum field theory	12
2.3.3 Group theory and gauge symmetries	12
2.4 The architecture of the Standard Model	14
2.4.1 Quantum electrodynamics	14
2.4.2 Yang-Mills theory	16
2.4.3 Electroweak theory	17
2.4.4 Spontaneous symmetry breaking	20
2.4.5 Yukawa terms	23
2.4.6 Quantum chromodynamics	24
2.4.7 Hadrons and mesons	25
2.4.8 Canonical quantization	26
2.4.9 Beyond the Standard Model	26
2.5 Effective field theory	27
2.5.1 Fermi theory	28
2.5.2 Standard Model effective field theory	29
2.5.3 Flavour symmetry assumptions	32
3 Experimental setup	34
3.1 CERN and the Large Hadron Collider	34
3.2 The Large Hadron Collider	34
3.3 The ATLAS detector	36
3.3.1 Inner detector	37
3.3.2 The calorimeter system	38
3.3.3 The muon spectrometer	38
3.3.4 Luminosity and triggers	38
3.3.5 The 2015-2016 dataset	39

4 Monte Carlo Generators and Simulation	40
4.1 Structure of a proton-proton collision	40
4.1.1 Parton distributions	41
4.1.2 Hard scattering process	41
4.1.3 Parton shower	42
4.1.4 Hadronization and decay	42
4.1.5 Jets	43
4.2 SMEFT sample generation	43
5 Monte Carlo Sample Generation	44
5.1 Signal simulation	44
5.2 Truth level objects	46
5.3 Normalising a distribution	46
6 Modelling distributions	47
6.1 Modelling techniques	47
6.2 Matrix element reweighting	48
6.3 Effective Lagrangian morphing	48
6.3.1 Morphing with one BSM coupling parameter in either the production or decay vertex	49
6.3.2 Generalisation to higher-dimensional parameter space	51
6.3.3 Validation	52
7 Simplified Template Cross Sections	55
7.1 The STXS framework	55
7.2 Splitting production modes	57
7.3 Staging	57
7.3.1 Gluon fusion Higgs production	58
Stage 1	58
7.3.2 Vector boson fusion Higgs production	58
Stage 1	59
8 Statistics	61
8.1 Terminology	61
8.2 Data versus theory	61
8.3 The measurements supplied in a RooWorkspace	63
8.4 The Asimov data set	64
8.5 Poisson counting experiments	64
8.6 Parameter estimation	64
9 Measurements	66
9.1 Measurements of gluon-gluon fusion and vector-boson fusion Higgs production	66
9.1.1 Systematic uncertainties	73
9.2 Fiducial and differential W^+W^- cross section measurement	73
9.2.1 The $qq/gg \rightarrow W^+W^- \rightarrow e\nu\mu\nu$ EFT interpretation	75
10 Operator Analysis	76
10.1 Cross section study	76
10.2 Phenomenology	82
10.2.1 Effective operators	82
10.2.2 The $1/\Lambda^4$ contribution	83

10.3 Impact of EFT operators on the STXS analysis	86
10.3.1 Parameterization of the STXS regions	87
11 Individual and simultaneous Wilson Coefficient fitting	91
11.1 $ggF \rightarrow H \rightarrow WW$ analysis	91
11.2 $VBF \rightarrow H \rightarrow WW$ analysis	93
11.3 $qq/gg \rightarrow W^+W^-$ analysis	94
11.4 Combined $ggF + VBF \rightarrow H \rightarrow W^+W^-$ analysis	95
11.5 Combined $ggF + VBF \rightarrow H \rightarrow W^+W^- + qq/gg \rightarrow W^+W^-$ analysis	95
11.6 Individual fit results	96
11.7 Simultaneous fits	98
11.7.1 Individual measurements versus combined measurements	99
11.8 Sanity check	101
12 Results	104
13 Discussion and conclusion	105
Bibliography	107
A Fit results and Nuisance parameter pulls of the STXS signal strength fits	112
B Operator Analysis Cutflow	121
C STXS Truth Decoration Cutflow	124
D Profile Likelihood scans	126
D.1 $ggF \rightarrow H \rightarrow WW$ analysis	126
D.2 $VBF \rightarrow H \rightarrow WW$ analysis	127
D.3 $qq/gg \rightarrow W^+W^-$ analysis	129
D.4 Combined $ggF + VBF \rightarrow H \rightarrow W^+W^-$ analysis	132
D.5 Combined $ggF + VBF \rightarrow H \rightarrow W^+W^- + qq/gg \rightarrow W^+W^-$ analysis	134
E Analytical Lagrangian Morphing validation plots	141
F Narrow Width Approximation	146
G Impact of dimension-8 operators	147

Chapter 1

General Introduction

At the ATLAS experiment located in CERN, Geneva, experimentalists try to emulate the beginning of our universe. The first fraction of second are reproduced by colliding two protons head on. During this process a high energy density is created within a small volume, just like in the early universe. In these collisions, massive subatomic particles may be created due to the collision energy being transformed into new particles. Which particles can be created is described by the Standard Model (SM). The SM is a relativistic quantum field theory that very accurately describes the current experimental observations in particle physics. It also describes how these subatomic particles interact with each other. These interactions are mediated by the weak, strong and electromagnetic forces. This theory is designed to describe what matter is made of. The last missing link in the SM was the Higgs particle. The Higgs boson was observed in 2012 [7] using the pp -collisions at CERN. By studying the latest experimental data it's mass has been determined to be $m_H = 124.97 \pm 0.24 \text{ GeV}$ [8].

Now, a new phase of experimental particle physics is beginning. The measuring of the Higgs properties. These are high precision measurements that, due the stochastic nature of the quantum field theory, require a large amount of data in order to have conclusive results. In this research we will conduct such a high precision measurement with a dataset corresponding to an integrated luminosity of 36.1 fb^{-1} . This set contains proton-proton collisions obtained at the LHC at a centre-of-mass energy of 13 TeV recorded by the ATLAS detector in 2015 and 2016.

With this data we can perform a first study on the Higgs properties. The recently developed Simplified Template Cross Sections [5] provide a framework to transform conventional signal strength (μ) measurements into several fiducial regions, each with its own μ_i . Due to the separation of Higgs event phase space into different regions of interest we obtain more finely grained measurements. This in turn produces more information for theoretical interpretation and coupling measurements.

The goal of this research is to study whether the Higgs couples to the other SM particles like the SM predicts. The Standard Model Effective Field Theory (SMEFT) [1] allows for the presence of new physics at an energy scale Λ . This new physics is incorporated into the SMEFT as effective operators on top of the conventional SM operators. By examining if the new operators are needed to describe the experimental data, the Standard Model Higgs properties can be validated. Should any operator be needed to describe the events we observe, it can be viewed as a violation of the Standard Model. Should any of the effective operator be necessary, it directly points to the Standard Model operators where any new physics might be hiding.

In the first chapters the tools and theories needed for the interpretation will be explained. In chapter 2 the Standard Model will be introduced and explained, along with the relevant terminology. Effective Field theory will also be explained following with the Standard Model Effective Field Theory in the Warsaw Basis. In chapter 3 the experimental setup is described, introducing CERN and the ATLAS experiment. Chapter 4 will go into the Monte Carlo generators, as they form an integral part to the generation of the SMEFT samples that we are using to compare the analyses results too. In chapter 5 the procedure of dealing with all of the events that are generated by the Monte Carlo generator will be explained the settings of the MC sample generations are shown. In Chapter 6 the effective lagrangian morphing tool will be introduced, explained and validated for the purpose of this study. Chapter 7 will touch upon the Simplified Template Cross Section framework. The statistical treatment of determination of the observed best-fit values of the Wilson coefficients will be discussed in chapter 8 as well as the general method of the profile likelihood fits. In chapter 9 the analyses that are used in this study will be introduced and explained in short, covering the necessary information in order to interpret the results of these studies in a EFT. Chapter 10 will then introduce the procedure of selecting the operators that we are sensitive too using these measurements. What and why some assumptions are made. The reparameterization of the signal strengths in terms of the EFT Wilson coefficients will also be explained here. Chapter 11 will present the results of fitting the reparameterized measurements to the observed dataset of 2015-2016 taken with the ATLAS detector at CERN Geneva. Chapter 12 the results of the study will be summarised. At last, chapter 13 will provide a quick discussion of the result and the final conclusion of the study.

In Fig. 1.1 a block scheme is presented highlighting the parts necessary for this work while also providing a structure to the full EFT interpretation. The chapters are ordered in order of appearance in this chain. The work done in this thesis concerns the full HWW STXS EFT interpretation as well as the combination with the SMWW EFT interpretation. Using the respective analyses from the ATLAS collaboration.

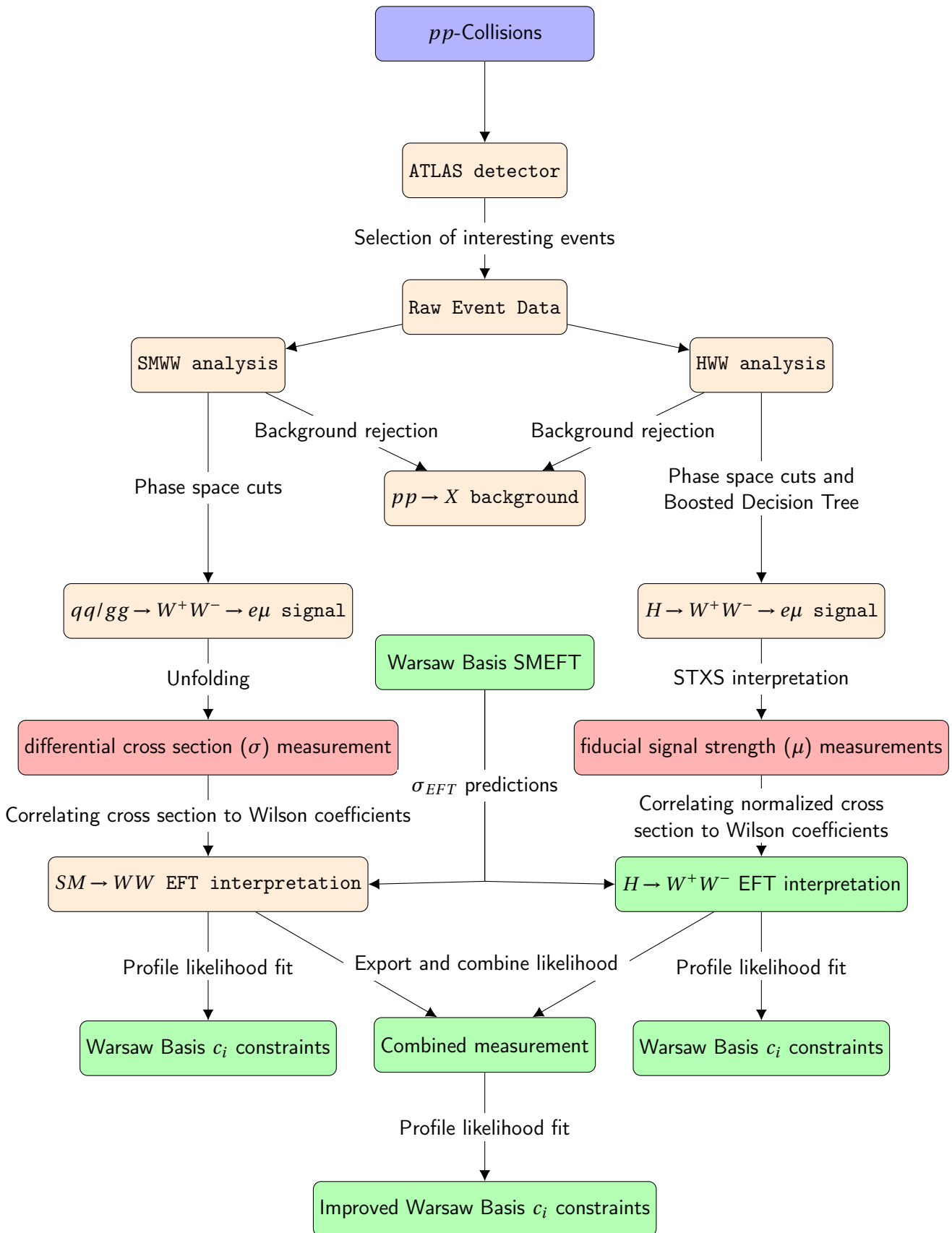


FIGURE 1.1: Overview of the approach taken in the EFT interpretation and the elements that were needed/supplied. In blue, the collisions provided by CERN and the LHC. In red the elements that were supplied for the interpretation. In brown work done by the analyses teams in the ATLAS collaboration. In Green, the work I was involved in and covered in this thesis.

Chapter 2

Theory

Measuring the couplings of the Higgs particle requires a thorough understanding of the Standard Model and the Standard Model effective field theory. This chapter will first sketch a broad picture of the SM and its Higgs interactions in sections 2.1 and 2.2. After this broad introduction to the theory, the other sections of this chapter will build up the Standard Model as we know it and later introduce the SMEFT.

2.1 The Standard Model of particle physics

The Standard Model of particle physics is a relativistic quantum field theory (QFT) and the result of an immense experimental and theoretical effort which started by the discoveries of the first particles and atoms by renowned physicists such as E. Rutherford, J. Thomson, E. Fermi and J. Chadwick. Since its discovery by J. Thomson, the electron is still thought to be a structureless point particle and one of the elementary particles of nature. Other particles that were subsequently discovered were first thought to be elementary and have now been found to have a complex structure.

The fundamental point-like building blocks of the Standard model are the elementary particles. The particle content of the SM is summarised in Fig. 2.1. In this figure we see that the fundamental particle states can be grouped into bosons with integer spin and fermions with spin $\frac{1}{2}$. The fermions are then divided into quarks that carry colour charge, fractional electric charge and weak isospin. The other fractional spin particles are leptons, which are in turn divided into charged leptons and neutrinos that carry no colour charge. The fermions also have their corresponding anti-particle. These anti-particles carry the same mass as the particles of ordinary matter but the opposite quantum mechanical charge.

2.1.1 Fundamental forces

The known fundamental forces in nature are the universal attraction of gravity, the electromagnetic force, the weak nuclear force and the strong nuclear force. Among these, gravity is on a higher energetic scale and governed by Einstein's theory of general relativity, while the other theories are gauge theories. The definition of gauge theories is going to be explained in conjunction with QFT. The gauge force that is produced by the theory is mediated by a spin-1 (vector) boson. The currently known and experimentally verified force mediators are listed in Table 2.1. The photon is the mediator of the electromagnetic force and governs the electromagnetic interactions between fermions. The W^\pm and Z^0 bosons mediate the weak nuclear force. This force is often separated in the charged current that is introduced by the charged vector bosons and the force mediated by the neutral vector bosons called the neutral current. The charged current comes in the negative and

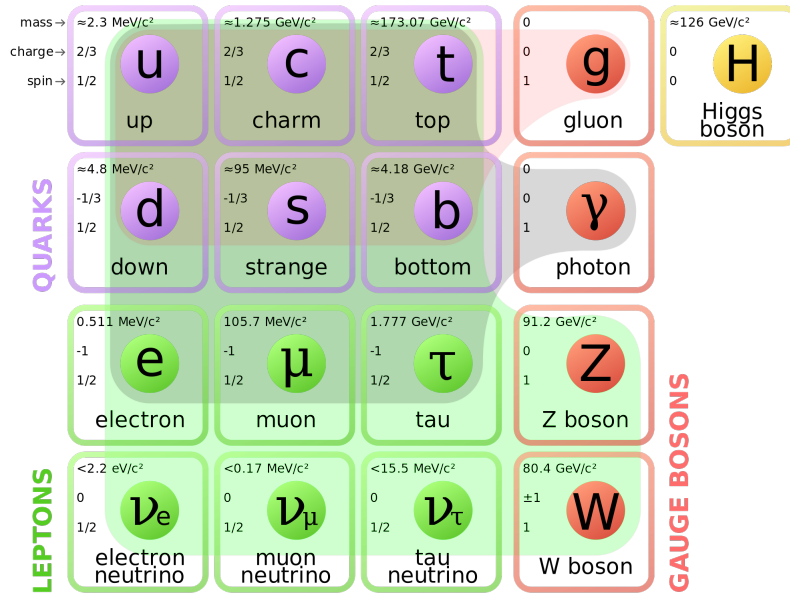


FIGURE 2.1: The particles that enter in the Standard Model [9]. In purple, the 3 observed generations of quark avours which form the Hadrons and Mesons are represented. In green, the 3 generations of charged and neutral leptons are shown. Both, the green and purple sections have corresponding anti-particles. In red, the gauge bosons that cause interactions between the quarks and leptons are pictured. In yellow the Higgs boson is shown, which is responsible for the generation of the masses of the gauge bosons.

positive electromagnetic charge. The gluon has an 8-fold degeneracy due to a degree of freedom known as colour charge. Colour is the charge associated with the strong nuclear force. Particles carrying net colour charges are always confined by other particles due to the strong nuclear force, meaning they can only exist in bound states where the net colour charge is zero. Therefore, no value is listed for the gluon lifetime and since it has the same form of wave equation as the photon its mass and width equal zero.

	Boson	EM Charge	Mass (GeV/c^2)	Width (GeV/c^2)	Lifetime (sec)	Spin	Force
Photon	γ	0	0	0	∞	1	Electromagnetic
Charged Vector Boson	W^\pm	± 1	80.379 ± 0.012	2.085 ± 0.042	3.14×10^{-25}	1	Weak nuclear
Neutral Vector Boson	Z^0	0	91.1876 ± 0.0021	2.4952 ± 0.0023	2.64×10^{-25}	1	Weak nuclear
Gluon	g	0	0			1	Strong nuclear

TABLE 2.1: The fundamental force carriers of the standard model [10].

2.2 The Higgs particle

One of the most sought after particles was the Higgs particle. This particle is discovered in 2012 [7] and part of the main motivations for the construction of the LHC. Still, since the discovery of the Higgs particle many properties of this particle remain unclear. In this part we will introduce the necessary the dynamics of this particle to familiarise the reader with the Higgs measurements.

2.2.1 Higgs production modes

There are many particle interactions in which a Higgs particle can be produced. These can be divided into several production modes. Here, the major production channels used in the ATLAS analyses are introduced.

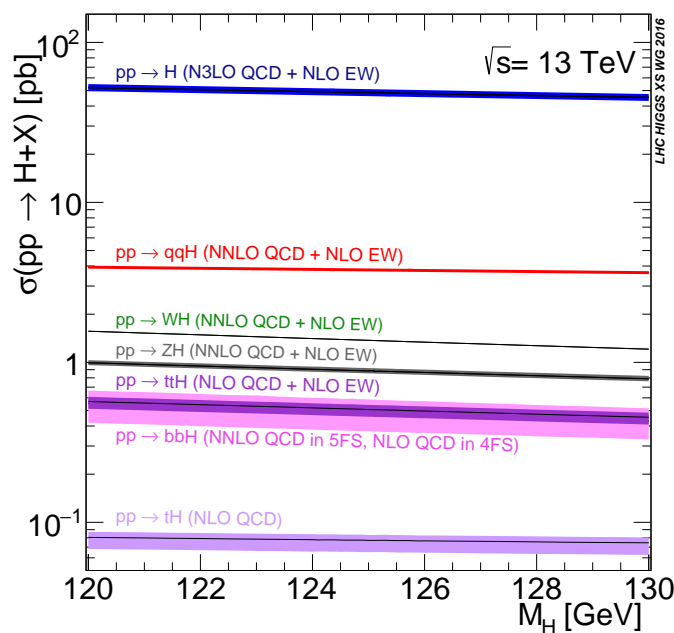


FIGURE 2.2: Cross section as function of the Higgs mass for the most dominant Higgs production modes [11].

The main production mechanisms at the LHC, which originate from proton-proton collision, are gluon fusion (ggF), vector boson fusion (VBF), Higgs production associated with a gauge boson (VH) and Higgs production associated with a pair of top/anti-top quarks (ttH).

An interaction cross section, σ , can be calculated for each of the production modes and can be viewed in the same way as the decay rate. The cross section can be considered as the effective cross sectional area associated with each particle and is a measure of the underlying quantum mechanical probability that the interaction will occur.

The largest contribution to the Higgs production cross section is the gluon gluon fusion process, Fig. 2.3. Two gluons forming a massive particle loop. The VBF process is the second largest contribution, Fig. 2.3. Here a quark and a anti-quark radiate of a vector boson which fuse into a Higgs particle accompanied by two highly energetic jets from the left over quarks. The lowest order Feynman diagram for the Higgs-strahlung, Fig. 2.4,

concerns the production of the Higgs boson accompanied by a single vector boson. It represents the third largest cross section. At last, the associated production with a top quark pair is shown in Fig. 2.5. These directly probe the Higgs to heavy quark couplings but with a significantly lower cross section. Each production mode has a corresponding expected cross section in proton-proton collisions depending on the centre of mass energy, illustrated as function of the mass of the Higgs particle in Fig. 2.2. A lower cross section implies a lower rate of occurrence and thus a lower chance of detecting the process using a certain number of events.

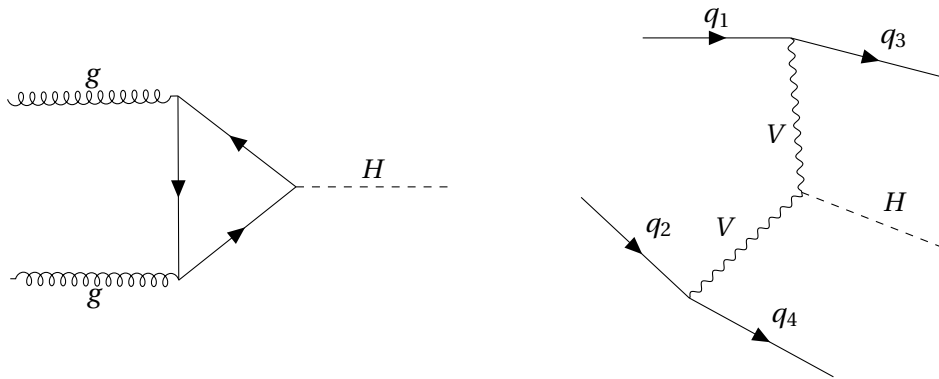


FIGURE 2.3: Lowest order Feynman diagrams of the leading production modes of the Higgs, ggF(left) and VBF(right), the V represents either a W or Z vector boson.

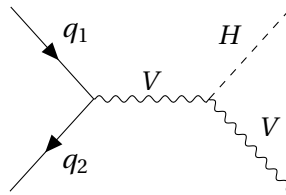


FIGURE 2.4: Lowest order Feynman diagram for $qq \rightarrow HV$, Higgsstrahlung.

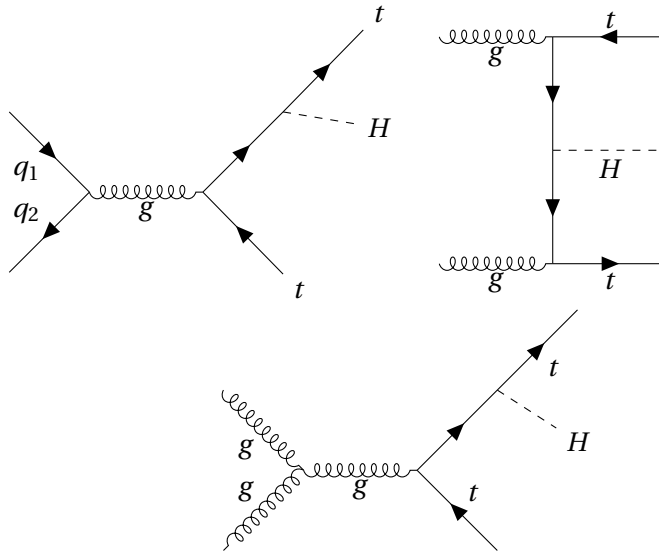


FIGURE 2.5: Lowest order Feynman diagrams dominating in the ttH production mode.

2.2.2 Higgs branching fractions

The Standard model Higgs particle has a predicted life time of $\sim 1.6 \times 10^{-22}$ [12]. Therefore, it decays very quickly into lighter particles before it exits the beam pipe of the LHC. Since the Higgs particle can decay into many particles because of its high mass and its role in the Standard Model. Thus, the understanding of the decay modes of this particle is necessary for studies on the Higgs boson. A branching ratio is defined for a final state A as

$$BR(H \rightarrow A) = \frac{\Gamma(H \rightarrow A)}{\sum_i \Gamma(H \rightarrow X_i)}. \quad (2.1)$$

Γ is the width of the process and is divided by a sum over all possible decay modes. The dominant decay modes from largest to lowest branching ratio are, $H \rightarrow b\bar{b}$, $H \rightarrow WW$, $H \rightarrow gg$, $H \rightarrow \tau\tau$, $H \rightarrow c\bar{c}$, $H \rightarrow ZZ$, $H \rightarrow \gamma\gamma$, $H \rightarrow Z\gamma$ and $H \rightarrow \mu\mu$. The branching ratio is shown as a function of the Higgs mass in Fig. 2.6. The decay mode involving a b -quark pair gives the largest contribution. However, this mode is hard to separate from the QCD background caused by other jets. The relatively high QCD background is one of the drawbacks of a hadron collider. A Higgs boson produced by vector bosons and decaying leptonically gives a cleaner signal relative to the other channels. Decay modes to the second family of particles are even more challenging since their occurrence is even rarer and are also enveloped by a large QCD background. The focus lies on the Higgs decay into two charged vector bosons.

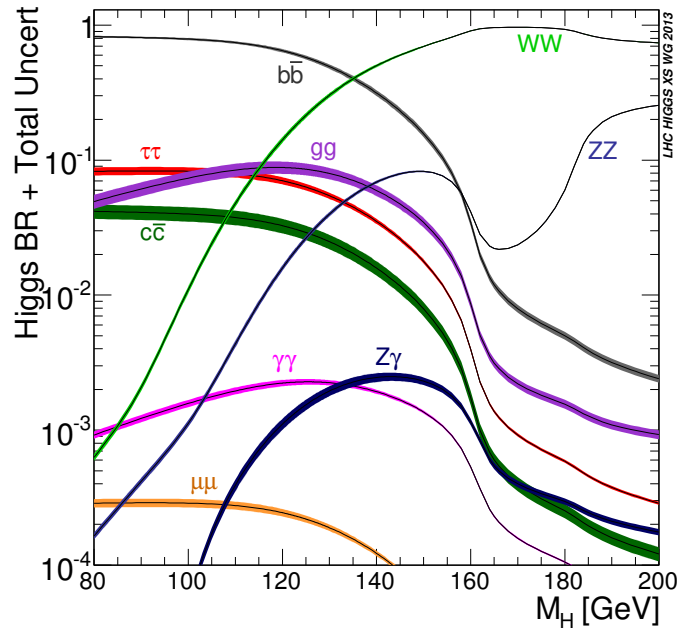


FIGURE 2.6: Branching ratios of the Higgs particle as function of the Higgs mass [13].

2.2.3 Higgs properties

The goal of this thesis is to improve our knowledge about the Higgs properties by measuring if the properties fit the SM predictions. According to the Standard Model the Higgs boson is a CP-even scalar particle with spin-0. Previous studies have excluded the spin-1 hypothesis and spin-2 hypotheses [14]. The Higgs boson mass is measured to be $m_h \approx 125 \text{ GeV}$ and thus implies a Higgs self coupling constant of $\lambda \approx 0.13$. Additionally the Higgs self-coupling has been studied. In these studies the Higgs potential shape has been probed using the self coupling constant $k_\lambda = \lambda_{obs}/\lambda_{SM}$, but only loose constraints on the self coupling have been found [15]. These findings are in accordance with the Standard Model.

The goal of this research is to study whether the Higgs couples to the other SM particles like the SM predicts. Since the Standard Model has been so successful in describing high energy physics, recent measurements are often searching for small deviations from the SM. The effective field theory introduces effective operators that we can interpret as deviations from the Standard Model.

A simple example is the couplings of in VBF production of the Higgs, decaying to two vector bosons. This process can be represented as in Fig. 2.7. In the blob near the HVV vertices, either the Standard Model coupling constant or any other coupling constant corresponding to new physics may be present. Any deviation from the SM couplings will be interpreted in the effective field theory and may lead to clues of new physics hiding in this region.

Is the Higgs boson or it's couplings affected by physics originating from a higher energy scale?

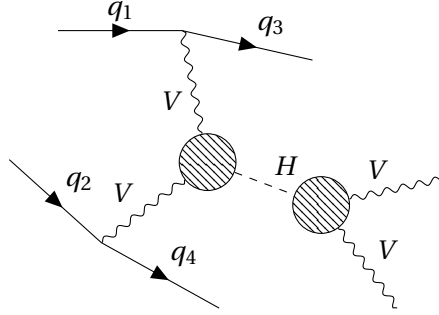


FIGURE 2.7: VBF Higgs production decaying into vector bosons with an EFT operator influencing the HVV vertices, which alters the kinematics of the process.

This is the question which we will try to answer in this study. Next, through a conceptual break the SM will be explained. During my research I spend a great amount of time in understanding this theory and likewise the subtle implications of the effective field theory. With basic knowledge about Lagrangian mechanics and the Standard Model as a quantum field theory, the reader may skip the build up of the Standard Model and continue with the introduction of the SMEFT.

2.3 The Lagrangian

To introduce Lagrangian dynamics a non-field theory setting will be reviewed first. Let the variables $q_n(t)$ describe the configuration of a physical system. A way of describing a system is to define the action on it,

$$S = \int_{t_i}^{t_f} L(q_n, \dot{q}_n) dt. \quad (2.2)$$

Here, t_i and t_f are fixed initial and final times, L is the Lagrangian and q_n are arbitrary variables of the action. The Lagrangian is given in simple systems by

$$L = T - V, \quad (2.3)$$

where T is the total kinetic energy and V is the total potential energy. The usefulness of the action is illustrated by Hamilton's principle, which states that if $q_n(t_i)$ and $q_n(t_f)$ are held fixed as boundary conditions, S is minimised when $q_n(t)$ satisfies the equations of motion. Since S is at an extremum, any small variations of $q_n(t)$ will not lead to change in S . So that $\delta S = 0$ when $q_n(t) \rightarrow q_n(t) + \delta q_n(t)$. Now to compute δS the chain rule is used.

$$\delta L = \sum \left(\delta q_n \frac{\partial L}{\partial q_n} + \delta \dot{q}_n \frac{\partial L}{\partial \dot{q}_n} \right) \quad (2.4)$$

Since,

$$\delta \dot{q}_n = \frac{d}{dt} (\delta q_n) \quad (2.5)$$

Obtaining

$$\delta S = \sum_n \int_{t_i}^{t_f} \left(\delta q_n \frac{\partial L}{\partial q_n} + \frac{d}{dt} (\delta q_n) \frac{\partial L}{\partial \dot{q}_n} \right) dt. \quad (2.6)$$

Now integrating by parts yields,

$$\delta S = \sum_n \int_{t_i}^{t_f} \left(\frac{\partial L}{\partial q_n} - \frac{d}{dt} \left(\frac{\partial L}{\partial \dot{q}_n} \right) \right) dt + \sum_n \delta q_n \frac{\partial L}{\partial \dot{q}_n} \Big|_{t=t_i}^{t=t_f}. \quad (2.7)$$

The last term vanishes because of evaluating the sum while filling in the boundary conditions $\delta q_n(t_i) = \delta q_n(t_f) = 0$. Since we already concluded that δS is supposed to be zero for and $\delta q_n(t)$, we find

$$\frac{\partial L}{\partial q_n} - \frac{d}{dt} \left(\frac{\partial L}{\partial \dot{q}_n} \right) = 0. \quad (2.8)$$

This expression is known as the Euler-Lagrange equation. Everything we need to know about the dynamics of the physical system is encoded in its Lagrangian L . In quantum field theory, it will tell us what the particle masses are and how they interact.

Now the jump is made to relativistic field theory. Consider the system is now a free scalar field $\phi(x^\mu) = \phi(t, \vec{x})$. The action becomes

$$S = \int_{t_i}^{t_f} dt L(\phi, \dot{\phi}) = \int_{t_i}^{t_f} dt \int d^3 \vec{x} \mathcal{L}(\phi, \dot{\phi}). \quad (2.9)$$

Since this expression depends on $\dot{\phi}$, it must also depend on $\vec{\nabla} \phi$ in order to be Lorentz invariant. The action is written as

$$S = \int d^4 x \mathcal{L}(\phi, \partial_\mu \phi). \quad (2.10)$$

The object \mathcal{L} is known as the Lagrangian density. Specifying a particular form of the Lagrangian density defines the theory. To find the classical equations of motion of the field the same steps as before are used to obtain

$$\frac{\partial \mathcal{L}}{\partial \phi} - \partial_\mu \left(\frac{\partial \mathcal{L}}{\partial (\partial_\mu \phi)} \right) = 0. \quad (2.11)$$

This equation forms the basis of the derivation of the two most fundamental fields in the Standard model. The scalar and fermion field.

2.3.1 Relativistic quantum mechanics

To derive the dynamical relations for free scalar fields the Klein-Gordon wave equation is introduced [16]. This equation of motion is found by considering the Lagrangian density choice of

$$\mathcal{L}_{\text{Scalar}} = \frac{1}{2} \partial_\mu \phi \partial^\mu \phi - \frac{1}{2} m^2 \phi^2. \quad (2.12)$$

It follows that

$$\frac{\delta L}{\delta \phi} = -m^2 \phi \quad (2.13)$$

and

$$\frac{\delta \mathcal{L}}{\delta (\partial_\mu \phi)} = \frac{\delta}{\delta (\partial_\mu \phi)} \left(\frac{1}{2} g^{\alpha\beta} \partial_\alpha \phi \partial_\beta \phi \right) = \frac{1}{2} g^{\mu\beta} \partial_\beta \phi + \frac{1}{2} g^{\alpha\mu} \partial_\alpha \phi = \partial^\mu \phi. \quad (2.14)$$

Therefore,

$$\partial_\mu \left(\frac{\delta \mathcal{L}}{\delta (\partial_\mu \phi)} \right) = \partial_\mu \partial^\mu \phi \quad (2.15)$$

The equation of motion is the Klein-Gordon equation. It describes how a free scalar field propagates. Rewritten as

$$(\partial^\mu \partial_\mu + m^2)\psi = 0 \quad (2.16)$$

This equation is a Lorentz-invariant relation between energy and momentum for the quantum mechanical field. However, it admits solutions with negative energy and negative probability densities, which are unphysical. These negative-probability states led Dirac to search for a relation linear in \vec{p} and E , which resulted in the Dirac equation [17].

$$(i\gamma^\mu \partial_\mu - m)\psi = 0 \quad (2.17)$$

In the Dirac equation, γ^μ are the 4×4 Dirac γ -matrices which satisfy the Clifford algebra anti-commutation relation $\{\gamma^\mu, \gamma^\nu\} = \gamma^\mu \gamma^\nu + \gamma^\nu \gamma^\mu = 2g^{\mu\nu} \mathbb{1}$. ψ is a four-component spinor. Using the Dirac equation we can describe the dynamics of free spin- $\frac{1}{2}$ fermions. The probability densities predicted by Dirac's equation are positive, but it still admits solutions with negative energy. In the Feynman-Stückelberg interpretation [17], these $E < 0$ solutions can be interpreted as negative-energy particles moving backwards in time or equivalently as anti-particles moving forwards in time. The predictions by Dirac's equation were confirmed by the discovery of the positron in 1932 [18]. The Dirac Lagrangian density for a single free spinor field can be written as

$$\mathcal{L}_{Dirac} = \bar{\psi} i\gamma^\mu \partial_\mu \psi - m\bar{\psi}\psi, \quad \bar{\psi} = \psi^\dagger \gamma^0 \quad (2.18)$$

2.3.2 Interactions in quantum field theory

The concept of interactions mediated by fields is central to quantum field theory. In order to encode the observed particle interactions in the theory, we require the Lagrangian to have several interaction terms. The principle of gauge symmetry allows additional degrees of freedom corresponding to gauge bosons to be naturally incorporated in the Lagrangian. New degrees of freedom are then added which represent interactions. The interaction term

$$\Delta\mathcal{L} = - \sum_{n \geq 3} \frac{\lambda_n}{n!} \psi^n \quad (2.19)$$

is added to the total Lagrangian. Where ψ^n are the interacting fields, λ the coupling constant and n denoting the number of fields taking part in the interaction.

2.3.3 Group theory and gauge symmetries

Group Theory is the branch of mathematics that underlies the treatment of symmetry [19]. The formal machinery of group theory will not be explained, but the concepts and terminology that belong to particle physics will be pointed out.

Take a rotation group as an example also known as $SO(3)$, meaning special orthogonal. The set of rotations of a system form a group, each rotation being an element of the group. Two successive rotations R_1 followed by R_2 are equivalent to a single rotation, meaning the product $R_1 R_2$ is also part of the group. The set of rotations is closed under multiplication, every rotation has an inverse. There is an identity element $R_1 R_1^{-1} = \mathbb{1}$, no rotation. The product of the rotation matrices is not necessarily commutative, $R_1 R_2 \neq R_2 R_1$.

The rotation group is a continuous group in which each rotation can be labelled by a set of continuously varying parameters (r, θ, ϕ) . The rotation group is a Lie group. Every rotation can be expressed as the product of a succession of infinitesimal rotations. This is a very fundamental property, because we do not want our experimental result to depend on the specific laboratory orientation of the system. The group is a subset of the Lorentz group, denoted as $SO(3,1)$. Where the 1 represents the additional time-like dimension. This group starts with a group of 4×4 matrices performing Lorentz transformations on the 4-dimensional Minkowski space of (t, x, y, z) .

$$g_{\mu\nu} = \begin{pmatrix} -1 & 0 & 0 & 0 \\ 0 & 1 & 0 & 0 \\ 0 & 0 & 1 & 0 \\ 0 & 0 & 0 & 1 \end{pmatrix}, \quad (2.20)$$

When $c \equiv 1$. The transformation leaves the quantity $ds^2 = (t^2 - x^2 - y^2 - z^2) = g_{\mu\nu} dx^\mu dx^\nu$ invariant. In addition to three rotation symmetries the Lorentz group also contains three Lorentz boost symmetries, requiring the physics to be invariant under a change in space-time coordinate frame.

The Lorentz group consists out of coordinate transformations $x^\mu = \Lambda^\mu_\nu x^\nu$ that preserve the line element ds^2 . The Lorentz transformation satisfies $\Lambda^{\mu\rho} \eta^{\rho\sigma} \Lambda^\sigma_\nu = \eta^{\mu\nu}$. This allows the angular momenta (j_1, j_2) of the decomposition to be used to group the fields as scalars $(j_1 = 0, j_2 = 0)$, left and right handed spinors $(\frac{1}{2}, 0), (0, \frac{1}{2})$ and vectors $(1, 1)$ based on their transformation properties. Hence, a scalar field $\phi(x^\mu)$ transforms as $\phi(x^\mu) \rightarrow \phi(\Lambda^{-1} x^\mu)$, a vector field as $A^\mu(x) \rightarrow \Lambda^\mu_\nu A^\nu(\Lambda^{-1} x)$ and a spinor field as $\psi^\alpha(x) \rightarrow S[\Lambda]^\alpha_\beta \phi^\beta(x)$, where $S[\Lambda]$ is a spinor built from 4×4 Dirac γ matrices in the chiral representation. All of these fields can be identified with particle states, which have a definite mass and spin.

Now we make the step towards the Poincaré group, also the fundamental group of a topological space. It is a ten-dimensional non-abelian Lie group. It contains the full symmetry of special relativity. It contains:

- Translation in time and space.
- Rotations in space.
- Lorentz boosts.

An important difference in the study of symmetries in physics is the one between external and internal symmetries. The external symmetries are the symmetries of space-time. Lagrangian's are almost always constructed such that they are invariant under transformations belonging to the Poincaré group. In field theory this gives us the scalar, vector and tensor fields for bosons and fermions. Internal symmetries are symmetries that arise in the Lagrangian because the fields appear in a symmetric way. A complex scalar field with the following Lagrangian,

$$\mathcal{L} = \frac{1}{2} \partial_\mu \phi^* \partial^\mu \phi - \frac{m^2}{2} (\phi^* \phi) - \frac{\lambda}{4!} (\phi^* \phi)^4 \quad (2.21)$$

is invariant under the global phase shift $\phi \rightarrow \exp^{i\alpha} \phi$. In group theory language this symmetry is described by $U(1)$ and are internal in a sense that they do not have anything to do with the Poincaré group, meaning that the generators of an internal group commute with all generators of the Poincaré group.

For any symmetry of the Lagrangian, Noether's theorem finds the associated conserved current that carries a conserved charge. Such that any continuous symmetry of the Lagrangian gives rise to a interaction that transfers the charge. A famous examples of this theorem is the derivation of the four conserved quantities of a relativistic field namely the Energy E and P^i the total momentum of the field configuration.

2.4 The architecture of the Standard Model

The Standard Model is a non-Abelian gauge field theory based on the symmetry groups $SU(3) \otimes SU(2) \otimes U(1)$. The transformation of the group acts on the free fields of this theory. This group has $8 + 3 + 1 = 12$ generators with a complicated commutator algebra. $SU(2) \otimes U(1)$ describes the electroweak (EW) interactions and the electric charge Q . $SU(3)$ is the colour group of the theory and is involved the in strong interactions described in quantum chromodynamics.

2.4.1 Quantum electrodynamics

The Dirac equation describes the dynamics of massive spin- $\frac{1}{2}$ particles. The associated Dirac Lagrangian \mathcal{L}_{Dirac} is denoted as

$$\mathcal{L}_{Dirac} = \bar{\psi} i \gamma^\mu \partial_\mu \psi - m \bar{\psi} \psi, \quad \bar{\psi} = \psi^\dagger \gamma^0. \quad (2.22)$$

Here ψ is the Dirac spinor and γ^μ the Dirac gamma matrices. The Dirac Lagrangian is invariant under the global phase transformation $U(1)_{EM}$. The fields and their derivatives transform as

$$\begin{aligned} \psi &\rightarrow e^{iq\alpha} \psi \\ \partial_\mu \psi &\rightarrow e^{iq\alpha} \partial_\mu \psi. \end{aligned} \quad (2.23)$$

Which corresponds to a global change of phase of the spinor field by an angle α and constant q . Substituting into the Lagrangian gives

$$\mathcal{L}_{Dirac,old} = \mathcal{L}_{Dirac,new}, \quad (2.24)$$

It leaves the Lagrangian invariant under this transformation. We also want our Lagrangian to be invariant under a local phase transformation, replacing α with $\alpha(x)$. The new fields become

$$\begin{aligned} \psi &\rightarrow e^{iq\alpha(x^\mu)} \psi \\ \partial_\mu \psi &\rightarrow e^{iq\alpha(x^\mu)} \partial_\mu \psi + e^{iq\alpha(x^\mu)} i q (\partial_\mu \alpha(x^\mu)) \psi \end{aligned} \quad (2.25)$$

Again, substituting this in the Lagrangian results in

$$\begin{aligned} \mathcal{L}_{Dirac,new} &= e^{-iq\alpha(x)} \bar{\psi} i \gamma^\mu (e^{iq\alpha(x^\mu)} \partial_\mu \psi + e^{iq\alpha(x^\mu)} i q (\partial_\mu \alpha(x^\mu)) \psi) \\ &\quad - e^{iq\alpha(x)} e^{-iq\alpha(x)} m \bar{\psi} \psi \\ &= \mathcal{L}_{Dirac,old} - \bar{\psi} \gamma^\mu q (\partial_\mu \alpha(x^\mu)) \psi \end{aligned} \quad (2.26)$$

Because of the extra term the Lagrangian is not invariant and the symmetry is broken. However, suppose the local $U(1)$ symmetry as a requirement is introduced. The Lagrangian is modified such that it obeys this symmetry. First, replacing the derivative ∂_μ by the so called gauge-covariant derivative results in the new definition

$$\partial_\mu \rightarrow D_\mu \equiv \partial_\mu + iqA_\mu(x). \quad (2.27)$$

This definition introduces a new vector field A_μ , which transforms as

$$A_\mu \rightarrow A_\mu(x) - \frac{1}{q}\alpha(x) \quad (2.28)$$

By inserting the expression for A in the covariant, it appears that it transforms together with the local phase

$$\begin{aligned} D_\mu\psi &\rightarrow e^{iq\alpha(x)}(\partial_\mu\psi + i\partial_\mu\alpha(x)\psi + iqA_\mu\psi - iq\frac{1}{q}\partial_\mu\alpha(x)\psi) \\ &= e^{iq\alpha(x)}D_\mu\psi \end{aligned} \quad (2.29)$$

As a consequence, terms in the derivative that look like $\psi^*D_\mu\psi$ are phase invariant. With this substitution the Dirac Lagrangian and any other real Lagrangians that can be constructed with second order terms satisfy the local phase symmetry.

Now since we require the Lagrangian to be real and since the conserved current is real, the field A^μ must be real as well. We identify the constant q as the charge and the gauge field A^μ as the electromagnetic vector potential. The field A^μ satisfies its own free Lagrangian. The corresponding kinetic term for the electromagnetic vector field is

$$\mathcal{L}_{EM}^{free} = -\frac{1}{4}F_{\mu\nu}F^{\mu\nu}, \quad (2.30)$$

where $F^{\mu\nu}$ is the field strength tensor,

$$F^{\mu\nu} = \partial^\mu A^\nu - \partial^\nu A^\mu = \begin{pmatrix} 0 & -E_x & -E_y & -E_z \\ -E_x & 0 & -B_z & B_y \\ E_y & B_z & 0 & -B_x \\ E_z & -B_y & B_x & 0 \end{pmatrix}. \quad (2.31)$$

The vector field A^μ is associated with the photon and the photons mass term would be proportional to $m_\gamma^2 A_\mu A^\mu$. Taking a local gauge transformation of this term we immediately see that its only invariant if m_γ is equal to zero. Therefore, the requirement of local $U(1)$ invariance automatically implies that the photon is massless.

$$m_\gamma^2 A_\mu A^\mu \rightarrow m_\gamma^2 (A^\mu - \partial^\mu \alpha(x))(A_\mu - \partial_\mu \alpha(x)) \neq m_\gamma^2 A_\mu A^\mu \quad (2.32)$$

Finally, the complete theory quantum electrodynamics can be described by by the QED Lagrangian.

$$\mathcal{L}_{QED} = \bar{\psi}i\gamma^\mu\partial_\mu\psi - m\bar{\psi}\psi - qA_\mu\bar{\psi}\gamma^\mu\psi - \frac{1}{4}F_{\mu\nu}F^{\mu\nu} \quad (2.33)$$

2.4.2 Yang-Mills theory

Chen Ning Yang and Robert Mills extended the concept of gauge theory by implementing a local $SU(2)$ symmetry, hoping they could derive the strong interaction from proton-neutron isospin symmetry. Although, they did not succeed, the $SU(2)$ is still explaining the weak interaction, as demonstrated in the following. The $SU(2)$ symmetry will be explained in a similar manner as earlier for the $U(1)$. Consider the following global $SU(2)$ gauge transformation and bi-spinor doublet,

$$\psi = \begin{pmatrix} \chi_1 \\ \chi_2 \end{pmatrix}, \quad (2.34)$$

$$\psi \rightarrow \psi' = e^{\frac{i}{2} \vec{\alpha} \vec{\tau}}, \quad (2.35)$$

where $\vec{\alpha}$ is real and $\vec{\tau} = (\tau_1, \tau_2, \tau_3)$ are the Pauli spin matrices. Since the matrices have all zero trace the transformations have a determinant of 1. They form the $SU(2)$ group and the matrices $\vec{\tau}$ are the generators of this group. Note, the generators of $SU(2)$ in general do not commute, which makes it a non-Abelian group. Using Noethers theorem we can derive a conserved current. Considering a small $SU(2)$ transformation in doublet space.

$$\psi \rightarrow \psi' = \left(\mathbb{1} + \frac{i}{2} \vec{\alpha} \vec{\tau} \right) \psi \quad (2.36)$$

Consider the massless Dirac Lagrangian and ignore that the particles in the doublets have different mass and charge, this is a problem to deal with later.

$$\delta \mathcal{L} = \partial_\mu \left(\frac{\partial \mathcal{L}}{\partial (\partial_\mu \psi)} \delta \psi \right) + \partial_\mu \left(\frac{\partial \mathcal{L}}{\partial (\partial_\mu \bar{\psi})} \delta \bar{\psi} \right) \quad (2.37)$$

$$\mathcal{L} = \bar{\psi} \begin{pmatrix} i\gamma^\mu \partial_\mu - m & 0 \\ 0 & i\gamma^\mu \partial_\mu - m \end{pmatrix} \psi \quad (2.38)$$

Computing the derivatives of the Lagrangian the left term to gives

$$\delta \mathcal{L} = \partial_\mu \left(-\frac{1}{2} \bar{\psi} \gamma^\mu \vec{\alpha} \vec{\tau} \psi \right) \quad (2.39)$$

Now since $\vec{\alpha}$ is real and just a scaling vector it is dropped to obtain three continuity equations $\partial_\mu J^\mu = 0$ for the three observed currents.

$$J^\mu = \bar{\psi} \gamma^\mu \frac{\vec{\tau}}{2} \psi \quad (2.40)$$

As for the $U(1)$ symmetry, we try to promote the global symmetry to a local one.

$$\psi \rightarrow \psi' = e^{\frac{i}{2} \vec{\tau} \vec{\alpha}(x)} \psi \quad (2.41)$$

Again because the derivative of the field transforms non-trivially. To restore phase invariance, we introduce the 2×2 covariant derivative.

$$D_\mu = \mathbb{1} \partial_\mu + i g B_\mu. \quad (2.42)$$

Here g is a arbitrary coupling constant and B_μ a gauge field. In spinor space the latter is a 2×2 unitary matrix with determinant of 1. It is also customary to parametrize the field in terms of three new real vector fields b_1, b and b_3 , like

$$B_\mu = \frac{1}{2} \vec{\tau} \cdot \vec{b}_\mu = \frac{1}{2} \sum_k \tau^k b_\mu^k = \frac{1}{2} \begin{pmatrix} b_3 & b_1 - ib_2 \\ b_1 + ib_2 & -b_3 \end{pmatrix} \quad (2.43)$$

Now we call the fields b_i the gauge fields of the $SU(2)$ symmetry. Three rather than one field is needed because the $SU(2)$ has three generators. Now these three fields also need a kinetic term in the Lagrangian. Additionally it is noticeable that the generators of the theory do not commute $[\tau_i, \tau_j] = 2\epsilon_{ijk}\tau_k$ there is coupling between the different components of the field. This is known as self coupling and its affect becomes clear if you consider the kinetic term of the $SU(2)$ gauge field. Because again these fields are vector fields try the Lagrangian $\mathcal{L}_b^{free} = -\frac{1}{4} \sum_l F_l^{\mu\nu} F_{\mu\nu,l} = -\frac{1}{4} \vec{F}^{\mu\nu} \cdot \vec{F}_{\mu\nu}$. Mass terms like $m^2 b^\nu b_\nu$ are again excluded because of gauge invariance. The tensor is now given by

$$F_l^{\mu\nu} = \partial^\nu b_l^\mu - \partial^\mu b_l^\nu + g\epsilon_{jkl} b_l^\mu b_k^\nu. \quad (2.44)$$

As a consequence of the last term, the total Lagrangian contains contributions with 2,3, and 4 factors of the b-field. These couplings are referred to as bilinear, trilinear and quadrilinear couplings. Summarising, the total Lagrangian bi-spinor doublet system subject to $SU(2)$ invariance now has become,

$$\mathcal{L}_{SU(2)} = \bar{\psi}(i\gamma^\mu \partial_\mu - m)\psi - g \vec{J}^\mu b_\mu - \frac{1}{4} \vec{F}^{\mu\nu} \cdot \vec{F}_{\mu\nu}. \quad (2.45)$$

Also known as the Yang-Mills Lagrangian.

2.4.3 Electroweak theory

The weak and electromagnetic interactions between leptons and quarks are described by the electroweak theory by Glashow-Weinberg-Salam [20], [21]. To construct this a theory a Lagrangian had to be found with both $U(1)$ and $SU(2)$ invariance.

The fermions are divided into three generations of left-handed and right-handed chiral quarks and leptons and they represent different representations of the gauge group. We define for any Dirac field ψ the left- and right-handed chiral projections,

$$\begin{aligned} \psi_L &\equiv \frac{1}{2}(1 - \gamma^5)\psi \\ \psi_R &\equiv \frac{1}{2}(1 + \gamma^5)\psi. \end{aligned} \quad (2.46)$$

Where $\gamma^5 = i\gamma^0\gamma^1\gamma^2\gamma^3$, for particles with $E \gg m$ these correspond to the negative and positive helicity states, respectively.

It is important not to confuse the concepts of helicity and chirality. Helicity states are defined by the projection of the spin of the particle onto its direction of motion, whereas the chiral states are the eigenstates of the γ^5 -matrix. In Electroweak theory the right-handed fermion fields of each lepton and quark family are grouped into singlets and the left-handed into $SU(2)$ doublets of Dirac spinors, while the neutrinos are assumed to be massless and occur with only their left handed components.

$$\begin{aligned}
L_1 &= \begin{pmatrix} \nu_e \\ e^- \end{pmatrix}_L, & e_{R_1} &= e_R^-, & Q_1 &= \begin{pmatrix} u \\ d \end{pmatrix}_L, & u_{R_1} &= u_R, & d_{R_1} &= d_R \\
L_2 &= \begin{pmatrix} \nu_\mu \\ \mu^- \end{pmatrix}_L, & e_{R_2} &= \mu_R^-, & Q_2 &= \begin{pmatrix} c \\ s \end{pmatrix}_L, & u_{R_2} &= c_R, & d_{R_2} &= s_R \\
L_3 &= \begin{pmatrix} \nu_\tau \\ \tau^- \end{pmatrix}_L, & e_{R_3} &= \tau_R^-, & Q_3 &= \begin{pmatrix} t \\ b \end{pmatrix}_L, & u_{R_3} &= t_R, & d_{R_3} &= b_R
\end{aligned} \tag{2.47}$$

This theory is generated using a combined $SU(2)_L \otimes U(1)_Y$ symmetry. Under this symmetry a left-handed doublet transforms as

$$\Psi \rightarrow \Psi'_L = e^{i\alpha(x)\mathbf{T} + i\beta(x)Y} \Psi_L \tag{2.48}$$

Here $\mathbf{T} = \frac{\boldsymbol{\tau}}{2}$ are the $SU(2)$ generators and Y is the generator for $U(1)$. With this configuration, the right-handed components of the fields in the doublet transform only under hypercharge,

$$\Psi \rightarrow \Psi'_R = e^{i\beta(x)Y} \Psi_R \tag{2.49}$$

Now, the electric charge is connected with the third component of the weak isospin I_3 and hypercharge Y by the sum of the two

$$Q = I_3 + \frac{Y}{2} \tag{2.50}$$

	ν_L	e_L	e_R	u_L	d_L	u_R	d_r
I_3	$+\frac{1}{2}$	$-\frac{1}{2}$	0	$+\frac{1}{2}$	$-\frac{1}{2}$	0	0
Y	-1	-1	-2	$+\frac{1}{3}$	$+\frac{1}{3}$	$+\frac{4}{3}$	$-\frac{2}{3}$
Q	0	-1	-1	$+\frac{2}{3}$	$-\frac{1}{3}$	$+\frac{2}{3}$	$-\frac{1}{3}$

TABLE 2.2: The electric charge Q , the isospin I_3 and the hypercharge Y for the left- and right-handed leptons and quarks.

Now take the generators of the $SU(2)$ symmetry as we have introduced them in the Yang-Mills theory. Notice that the τ_1 and τ_2 matrices mix the components of the doublets, while τ_3 does not because its components are diagonal. Therefore, we define the fields W^\pm as

$$W^\pm \equiv \frac{1}{\sqrt{2}}(b_\mu^1 \mp i b_\mu^2). \tag{2.51}$$

It can be shown that these fields are charge-lowering and charge raising currents.

$$\begin{aligned}
J^{+\mu} &= \frac{1}{2\sqrt{2}} \bar{\nu} \gamma^\mu (1 - \gamma^5) e \\
J^{-\mu} &= \frac{1}{2\sqrt{2}} \bar{e} \gamma^\mu (1 - \gamma^5) \nu
\end{aligned} \tag{2.52}$$

Charge conservation at each Feynman diagram vertex then implies the charge of the gauge boson. We now recognise these currents as the charged current interactions as can be showed the Feynman diagrams in Fig. 2.8.

The third component of the weak isospin gauge field leads to a neutral current interaction, Fig. 2.3, with b_μ^3 the third gauge boson and the conserved current given by.

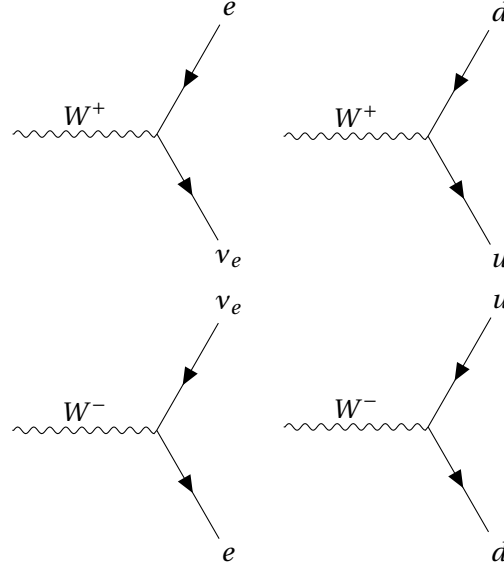


FIGURE 2.8: The Charged current interactions.

$$J_3^\mu = \bar{\Psi}_L \gamma^\mu \frac{\tau_3}{2} \Psi_L \quad (2.53)$$

The conserved current corresponding to the $U(1)_Y$ symmetry is [17]

$$J_Y^\mu = \bar{\Psi} \gamma^\mu Y \Psi. \quad (2.54)$$

The Lagrangian following from the local $SU(2)_L \otimes U(1)_Y$ takes the form of

$$\mathcal{L} = \mathcal{L}_{free} - g \mathbf{J}_T^\mu \cdot \mathbf{b}_\mu - \frac{g'}{2} J_Y^\mu a^\mu. \quad (2.55)$$

Again, a^μ is the gauge field corresponding to $U(1)_Y$ and $\frac{g'}{2}$ is its coupling strength. The transformations corresponding to T_3 and Y lead to neutral current interactions and as a result the gauge boson fields can actually mix. Neither of them couple specifically to the electromagnetic charge. The question arises if these fields can be reparameterized in a way that one becomes a Z^0 and the other a physical field A^μ . Whereby the latter couples to fermion fields via the charge operator only. The physical neutral fields become now linear combinations of the T_3 and Y gauge fields, written as

$$\begin{aligned} A_\mu &= a_\mu \cos(\theta_W) + b_\mu^3 \sin(\theta_W) \\ Z_\mu &= -a_\mu \sin(\theta_W) + b_\mu^3 \cos(\theta_W), \end{aligned} \quad (2.56)$$

where θ_W is called the weak mixing angle. Up till now we have derived the existence of these gauge fields by imposing local gauge invariance under a composite symmetry. This theory has massless spinors that interact with each other and with massless gauge boson. Massless because it is proven that the mass term of the gauge bosons is not invariant under the transformations. We can now formulate the first part of the Standard Model

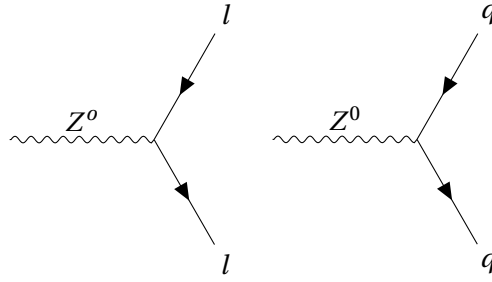


TABLE 2.3: The Neutral current interactions.

Lagrangian with the Lagrangian part of the fermions

$$\begin{aligned}
 \mathcal{L}_F = & -\frac{1}{4}W^{\mu\nu}W_{\mu\nu} - \frac{1}{4}B^{\mu\nu}B_{\mu\nu} \\
 & + \bar{L}_i i D_\mu \gamma^\mu L_i + \bar{e}_{Ri} i D_\mu \gamma^\mu e_{Ri} \\
 & + \bar{Q}_i D_\mu \gamma^\mu Q_i + \bar{u}_{Ri} i D_\mu \gamma^\mu u_{Ri} + \bar{d}_{Ri} i D_\mu \gamma^\mu d_{Ri}
 \end{aligned} \tag{2.57}$$

With the covariant derivative defined as

$$D_\mu = \partial_\mu - i g \frac{\boldsymbol{\tau}}{2} \cdot \mathbf{W}_\mu - i g' \frac{Y}{2} B^\mu. \tag{2.58}$$

This Lagrangian is invariant under local $SU(2)_L \otimes U(1)_Y$ transformation. The mass terms of the vector bosons of the weak interactions are added by breaking the electroweak symmetry spontaneously with the introduction of the Higgs mechanism. The fermionic mass terms will be introduced with the help of gauge-invariant Yukawa interactions of the fermions with the Higgs field.

2.4.4 Spontaneous symmetry breaking

In this section the procedure of spontaneous symmetry breaking [21] of electroweak theory will be introduced. The symmetry is not broken by a term added by hand. It is a particular characteristic of the fields involved in the theory. We are going to add an isospin doublet of two complex scalar fields.

$$\Phi = \begin{pmatrix} \phi^+ \\ \phi^0 \end{pmatrix} = \frac{1}{\sqrt{2}} \begin{pmatrix} \phi_1 + i\phi_2 \\ \phi_3 + i\phi_4 \end{pmatrix} \tag{2.59}$$

The field added is a left-handed doublet like the electron-neutrino doublet. It has a weak isospin $\frac{1}{2}$ and the charges of the upper and lower component are chosen such that the hypercharge $Y = 1$. Also a potential $V(\Phi)$ is chosen

$$V(\Phi) = \mu^2 (\Phi^\dagger \Phi) + \lambda (\Phi^\dagger \Phi)^2, \tag{2.60}$$

with $\mu^2 < 0$. This potential is added to the Lagrangian of the scalar field doublet. The potential is the famous Mexican hat potential seen in Fig. 2.9. A symmetric upward dome with a trough circling around the bottom and symmetric with respect to its centre \hat{z} -axis. The top origin is not a stable point a may spontaneously fall to either side of the dome, to the point of lowest energy. By this action the total system loses its symmetry.

The Lagrangian becomes,

$$\mathcal{L} = (D^\mu \Phi)^\dagger (D_\mu \Phi) - V(\Phi), \tag{2.61}$$

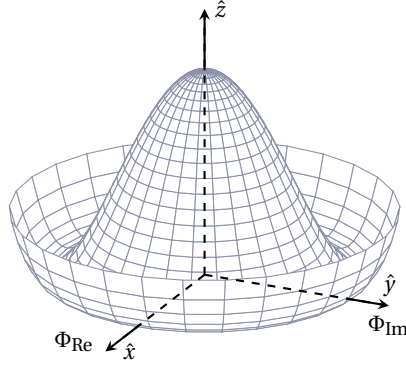


FIGURE 2.9: 3D mexican hat potential.

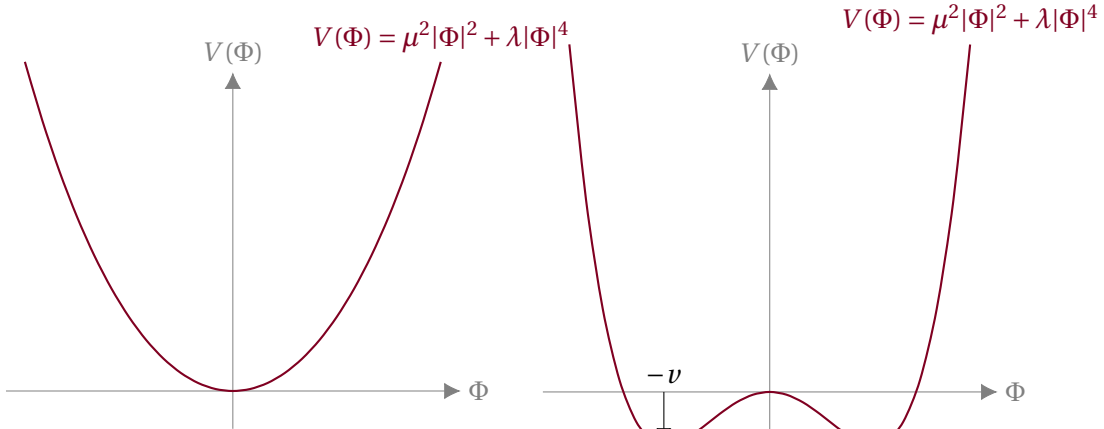
where D_μ is the covariant derivative that was associated to the $SU(2)_L \otimes U(1)_Y$ symmetry.

$$D_\mu = \partial_\mu - ig \frac{\boldsymbol{\tau}}{2} \cdot \mathbf{W}_\mu - ig' \frac{Y}{2} B^\mu \quad (2.62)$$

The potential $V(\Phi)$ can also be written as

$$V(\Phi) = \mu^2 |\Phi|^2 + \lambda |\Phi|^4 \quad (2.63)$$

The shape of the underlying potential depends on the values of μ and λ . A $\lambda > 0$ is required to ensure that the potential is bounded from below and thus guaranteeing the presence of a ground state. In case of a positive μ^2 , the potential has its minimum at $\langle 0|\phi|0\rangle \equiv \phi_0 = 0$.

FIGURE 2.10: The 2D Higgs potential for $\mu^2 > 0$.FIGURE 2.11: The 2D Higgs potential for $\mu^2 < 0$.

As shown in Fig. 2.11, when $\mu^2 < 0$ there is not a singular vacuum located at $(0,0)$. There is now a continuous vacuum in the circle of points that satisfies $\sqrt{Re\Phi^2 + Im\Phi^2} = \sqrt{\frac{-\mu^2}{\lambda}} = v$. Now we have to make a choice for a vacuum. We choose $\phi_1 = \phi_2 = \phi_4 = 0$ and $\phi_3 = v + h$. Where the h represents the actual higgs field. Such that,

$$\text{Vacuum} = \phi_0 = \frac{1}{\sqrt{2}} \begin{pmatrix} 0 \\ v+h \end{pmatrix} \quad (2.64)$$

Invariance implies that $e^{i\alpha(\tau_i, Y)}\phi_0 = \phi_0$. Under infinitesimal rotation this can be written as $(1 + i\alpha(\tau_i, Y))\phi_0 = \phi_0$ so $(\tau_i, Y)\phi_0 = 0$. It can be checked that $\tau_1\phi_0, \tau_2\phi_0, \tau_3\phi_0$ and $Y\phi_0$ are all non-zero and thus broken. Now the masses of the gauge bosons are obtained by substituting the vacuum expectation value in the Lagrangian. The relevant terms arise from the kinetic term for the complex scalar field. For now we will focus on the v term that will produce the masses of the gauge bosons.

$$\begin{aligned} \left| \left(-ig\frac{\boldsymbol{\tau}}{2} \cdot \mathbf{W}_\mu - i\frac{g'}{2}B_\mu \right) \phi \right|^2 &= \frac{1}{8} \left| \begin{pmatrix} gW_\mu^3 + g'B_\mu & g(W_\mu^1 - iW_\mu^2) \\ g(W_\mu^1 + iW_\mu^2) & -gW_\mu^3 + g'B_\mu \end{pmatrix} \begin{pmatrix} 0 \\ v \end{pmatrix} \right|^2 \\ &= \frac{1}{8} v^2 g^2 \left((W_\mu^1)^2 + (W_\mu^2)^2 \right) + \frac{1}{8} v^2 (g'B_\mu - gW_\mu^3)(g'B_\mu - gW_\mu^3) \\ &= \left(\frac{1}{2} v g \right)^2 W_\mu^+ W_\mu^- + \frac{1}{8} \begin{pmatrix} W_\mu^3 & B_\mu \end{pmatrix} \begin{pmatrix} g^2 & -gg' \\ -gg' & g'^2 \end{pmatrix} \begin{pmatrix} W_\mu^3 \\ B_\mu \end{pmatrix} \end{aligned} \quad (2.65)$$

Here we have used the expression $W^\pm = \frac{1}{\sqrt{2}}(W^1 \mp iW^2)$. The expected mass term of a charged gauge boson the appear as $M_W^2 W^+ W^-$, we find the mass to be

$$M_W = \frac{1}{2} v g \quad (2.66)$$

The remaining terms is the off-diagonal of the W_μ^3 and B_μ basis

$$\frac{1}{8} v^2 \left(g^2 (W_\mu^3)^2 - 2gg' W_\mu^3 B_\mu + g'^2 B_\mu^2 \right) = \frac{1}{8} \left(gW_\mu^3 - g'B_\mu \right)^2 + 0 \left(g'W_\mu^3 + gB_\mu \right)^2. \quad (2.67)$$

One of the eigenvalues of the mass weak mixing matrix is zero, and we can include this term with a combination of fields that diagonalize the mass matrix such that 2.67 are identified as the sum of the usual neutral gauge boson masses.

$$\frac{1}{2} M_Z^2 Z_\mu^2 + \frac{1}{2} M_A^2 A_\mu^2 \quad (2.68)$$

Finally the fields become

$$\begin{aligned} A_\mu &= \frac{g'W_\mu^3 + gB_\mu}{\sqrt{g^2 + g'^2}}, \text{ with } M_A = 0 \\ Z_\mu &= \frac{gW_\mu^3 - g'B_\mu}{\sqrt{g^2 + g'^2}}, \text{ with } M_Z = \frac{1}{2} v \sqrt{g^2 + g'^2} \end{aligned} \quad (2.69)$$

Reintroducing the weak mixing angle given earlier as

$$\frac{g'}{g} = \tan \theta_W \quad (2.70)$$

With the spontaneous breaking of the $SU(2)_L \otimes U(1)_Y$ symmetry, the W^\pm and Z bosons acquired masses. The $U(1)_Q$ symmetry remains unbroken and thus its generator, the photon, remains massless. Inserting the mass terms and working out the h part of the Lagrangian will generate the interactions with the Higgs boson. Now we arrive at the Higgs boson Lagrangian.

$$\begin{aligned}
\mathcal{L}_{Higgs} = & \frac{1}{2} \partial_\mu H^\mu \partial^\mu H_\mu - \frac{1}{2} M_H^2 H^2 + M_W^2 W_\mu^+ W^{-\mu} + \frac{1}{2} Z_\mu^2 \\
& + g M_W H W_\mu^+ W^{-\mu} + \frac{g^2}{4} H^2 W_\mu^+ W^{-\mu} \\
& + \frac{g M_Z}{2 c_W} H Z_\mu Z^\mu + \frac{g^2}{4 c_W^2} H^2 Z_\mu Z^\mu \\
& - \frac{g M_H^2}{4 M_W} H^3 - \frac{g^2 M_H^2}{32 M_W^2} H^4
\end{aligned} \tag{2.71}$$

The real field $H(x)$ is used instead of h and describes the physical neutral scalar particle, the Higgs boson, which has a mass of $M_H = \frac{\mu}{\sqrt{2}}$. It has triple and quartic self interactions proportional to M_H^2 . Also Incorporated in the Lagrangian as tri-linear HW^W , HZZ and quadri-linear HHW^W , $HHZZ$ vertices. The Higgs coupling to the gauge bosons is proportional to the gauge boson mass.

2.4.5 Yukawa terms

The fermion masses can be generated with the same self interacting complex scalar field and an isodoublet $\tilde{\Phi} = i\tau_2 \Phi^*$. The additional isodoublet is needed because of the extra symmetry that the quarks are subject to and which we will explore in the next section. The $SU(2)_L \otimes U(1)_Y$ invariant Yukawa Lagrangian for any fermion becomes

$$\mathcal{L}_{Yukawa} = -\lambda_e \bar{L} \tilde{\Phi} e_R - \lambda_d \bar{Q} \tilde{\Phi} d_R - \lambda_u \bar{Q} \tilde{\Phi} u_R + h.c. \tag{2.72}$$

where the $\lambda_{e,d,u}$ are the individual Yukawa coupling constants. The electron obtains

$$\begin{aligned}
\mathcal{L}_{electron} = & -\frac{1}{\sqrt{2}} \lambda_e (\bar{\nu}_e \quad \bar{e}_L) \begin{pmatrix} 0 \\ \nu + H \end{pmatrix} e_R + h.c. \\
= & \frac{1}{\sqrt{2}} \lambda_e (\nu + H) \bar{e}_L e_R + h.c.
\end{aligned} \tag{2.73}$$

Then applying the same mechanism to the quarks we find all of the fermion masses to be:

$$\begin{aligned}
m_f = & \frac{\lambda_f v}{\sqrt{2}}, m_u = \frac{\lambda_u v}{\sqrt{2}}, \\
m_d = & \frac{\lambda_d v}{\sqrt{2}}
\end{aligned} \tag{2.74}$$

2.4.6 Quantum chromodynamics

As final piece of the Standard Model we take a peak into the field of flavour physics, this field is heavily invested into quantum chromodynamics [22]. This theory predicts the interactions between the quarks, gluons and hadrons. It arises from the invariance of the Lagrangian under a local $SU(3)_C$ symmetry, where C stands for colour charge that is N_c -valent, with $N_c = 3$ in the SM. The quarks, or spinor, fields in this group transforms as

$$\psi(x) \rightarrow \psi'(x) = e^{ig_s \alpha^a(x) T^a} \psi(x). \quad (2.75)$$

Here T^a are the generators of the group which are represented by the 3×3 Gell-Mann matrices λ^a as $T^a = \frac{1}{2} \lambda^a$. g_s is the gauge coupling and $\alpha^a(x)$ are the local gauge transformations corresponding to the eight generators. The covariant derivative can be written as

$$\partial_\mu \rightarrow D_\mu = \partial_\mu + ig_s G_\mu^a T^a \quad (2.76)$$

where G_μ^a must transform as

$$G_\mu^a \rightarrow G_\mu^a - \partial_\mu \alpha^a + ig_s G_\mu^a T^a \quad (2.77)$$

Here the last term arises from the non-Abelian nature of QCD because the generators do not commute. They are related through their structure constants $[T^a, T^b] = T^a T^b - T^b T^a = if_{abc} T^c$. The Lagrangian for a free quark field can now be written as

$$\mathcal{L}_{quark} = \Psi(i\gamma^\mu \partial_\mu - m - g_s \gamma^\mu G_\mu^a T^a) \Psi \quad (2.78)$$

The gauge field G_μ^a is associated with the gluons. Notice, $\Psi = (\psi_1 \ \psi_2 \ \psi_3)$ has three components which correspond to the colour states, each of which is a 4-component Dirac spinor. The QCD quark-gluon interaction vertex is then

$$-g_s \bar{\Psi} \gamma^\mu G_\mu^a T^a \Psi \quad (2.79)$$

At last we should add the kinetic gauge invariant term of the gauge bosons.

$$\mathcal{L}_{kinetic} = -\frac{1}{2} Tr[F^{\mu\nu} F_{\mu\nu}] \quad (2.80)$$

Here $F_{\mu\nu} = \partial_\mu G_\nu - \partial_\nu G_\mu = ig_s [G_\mu, G_\nu]$ with $G_\mu = G_\mu^a T^a$ as the QCD gluon field strength tensor. f_{abc} are non-vanishing structure constants and imply that gluons themselves carry colour charge and can interact among themselves, giving rise to a triple-gluon and four-gluon vertex.

The $SU(3)_C$ symmetry of QCD implies the existence of a conserved trivalent colour charge, which is exchanged between quarks and by eight gluons carrying the colour-anticolour in QCD vertices. The dominant contribution to physics processes comes from a direct vertex, however loop corrections to QCD as seen in Fig. 2.12, have to be taken into account because of the running coupling constant of QCD, Fig. 2.13.

The running coupling constant depends on the momentum transfer $Q^2 \equiv -q^2$ following from a feature of the theory called asymptotic freedom. This property is produced by the effect called screening. A charged particle like the electron or gluon is surrounded by virtual particles pairs popping into and out of existence. Because particles with the same charge repel each other, the anti-charge is attracted and is thus screening the net charge of the particle. In QCD vacuum these are virtual $q\bar{q}$ and gluon pairs. Since the gluon cloud

carries colour charge it turns out that the effective charge becomes larger with distance. This results in the QCD coupling becoming smaller at short distances while growing over large distances. This makes it impossible to isolate a single gluon or quark from a hadron. This mechanism is called confinement.



FIGURE 2.12: Left: tri-linear gluon self coupling loop correction. Right: loop correction to quark propagation.

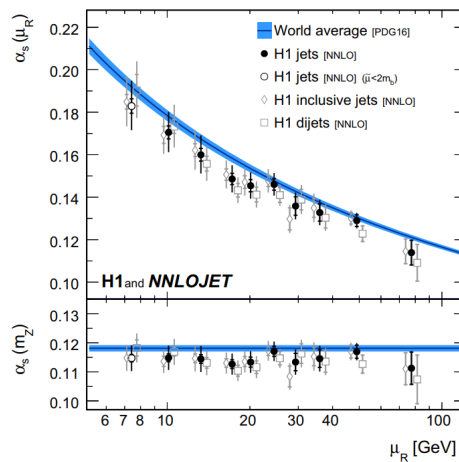


FIGURE 2.13: The running coupling constant. Results for fits to data points comparing several theory predictions to the world average data. $\mu_R = \sqrt{Q^2 + P_T^2}$ being a scale value for the total momentum exchanged and P_T denoting P_T^{jet} in the case of inclusive jet cross sections [23].

2.4.7 Hadrons and mesons

The confinement results in all hadrons being colour singlets. Composed of either two quarks $q\bar{q}$, called mesons. Or composed of three quarks $qqq/\bar{q}\bar{q}\bar{q}$ called baryons. When considering the Yukawa couplings, the individual Yukawa couplings are a little bit more complex than previously discussed. When moving from the previously defined flavour eigenstates to mass eigenstates, the quark mass matrices become diagonalized by different transformations for the left-handed up- and down-quarks. Resulting in the charged-current weak interaction modified by the product of the diagonalizing matrices of the up- and down-type quark mass matrices, so called the CKM matrix [24].

$$V = U_L^u U_L^{d\dagger} = \begin{pmatrix} V_{ud} & V_{us} & V_{ub} \\ V_{cd} & V_{cs} & V_{cb} \\ V_{td} & V_{ts} & V_{tb} \end{pmatrix} \quad (2.81)$$

With U_L^u and $U_L^{d\dagger}$ the unitary matrices obtained by diagonalizing to the mass eigenstates. The neutral-current remains unchanged, meaning no flavour-changing neutral currents at tree level. The V matrix itself is unitary, $VV^\dagger = \mathcal{I}$. This requirement leads to the freedom to choose the global phases of some of the CKM elements, which are in

turn used to explain CP-violation within the Standard Model. QCD together with the CKM matrix explain most interactions between mesons, baryons and quarks.

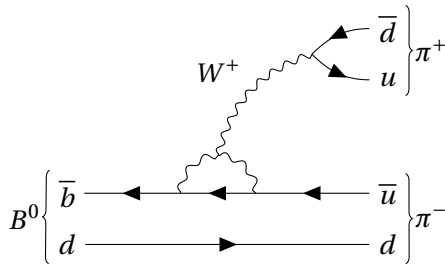


FIGURE 2.14: B^0 meson decaying into two pions

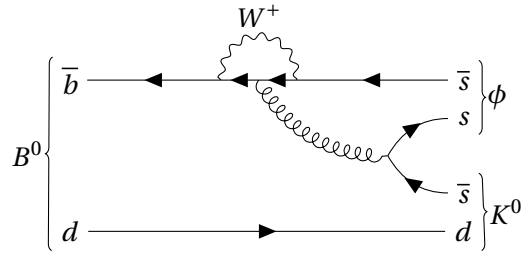


FIGURE 2.15: B^0 meson decaying into a neutral Kaon K^0 and a ϕ -meson

When computing/measuring the entries of the CKM matrix, it reveals an interesting structure

$$|V_{CKM}| \approx \begin{pmatrix} 0.97 & 0.23 & 0.0036 \\ 0.23 & 0.97 & 0.041 \\ 0.0087 & 0.040 & 1 \end{pmatrix} \approx \begin{pmatrix} 1 & \lambda & \lambda^4 \\ \lambda & 1 & \lambda^2 \\ \lambda^3 & \lambda^2 & 1 \end{pmatrix}. \quad (2.82)$$

With $\lambda \approx 0.2$ which is known as the Wolfenstein parametrization [25]. The matrix is almost diagonal and the transition between generations of quarks is heavily suppressed, but can still happen leading to very interesting decay patterns shown in Fig 2.15.

2.4.8 Canonical quantization

Now the most important ingredients in the SM are described. At last we make the relation between fields and particles through canonical quantization. From quantum mechanics it is known in order to describe physics on a sub-atomic scale the particles are quantized. When quantizing the different fields in the SM, several specific types of particles and physically observables roll out. Canonical quantization is performed by promoting the field and the momentum conjugate of the field to operators while imposing canonical commutation relations [26].

Using this approach we are able to reduce our relativistic quantum fields to the good old harmonic oscillator with annihilation and creation operators $\hat{a}_p, \hat{a}_p^\dagger$. This brings the whole relativistic theory of the SM back to low energy quantum mechanics allowing for the observing of the properties of the particles and comparing theoretical predictions to experimental results.

2.4.9 Beyond the Standard Model

The Higgs discovery in 2012 was a milestone of the SM as we know it today. With this discovery at the LHC the last missing particle was added to the SM and with this the theory became mathematically consistent. Meaning it can be extrapolated towards higher energies without internal problems. However, there are still some shortcomings to the SM. Here we will list some of the open problems of the Standard Model

- **Dark matter** The existence of dark matter in the universe provides compelling evidence for physics beyond the Standard Model [16]. Found by an inconsistency in

galaxy rotation curves. This is all explained by the existence of a new stable particle, following the WIMP model [27], that escapes detection and accounts for around 85% of the total matter content in the universe.

- **Hierarchy Problem** The hierarchy problem is the statement that the Higgs mass is unnaturally small. It can be summarised as followed. Difficulties arise from the scalar field. In the Standard Model the Higgs field is the only scalar field. Also under quantum corrections, the scalar mass is not stable. Meaning that we expect physics from higher scales to correct the Higgs mass and push it towards higher values using a similar screening method as in QED and QCD [28]. However, the Higgs boson mass is the same order as the weak scale. This either causes an enormous amount of fine-tuning between the contributions to the Higgs mass from low energy scales and from the ultraviolet (UV) scale to cancel each other out. Or there is a mechanism that protects the Higgs mass from growing.
- **Cosmological Constant** There is a cosmological constant problem or vacuum catastrophe in cosmology. It is caused by the disagreement between the observed values of vacuum energy density and the theoretically predicted zero-point energy predicted by the SM.
- **Grand Unified Theory** The running gauge couplings, when extrapolated to higher energy scales, seem to meet around $10^{16} GeV$ [16]. There are also theories which explain this behaviour in terms of the super-symmetric standard model. We can take advantage of this by introducing models which unify the three gauge couplings and embed the three SM symmetry groups in a bigger symmetry group in a model commonly called the grand unified theory (GUT).

2.5 Effective field theory

The basic idea behind effective field theory (EFT) is the observation that the non-analytic parts of scattering amplitudes are due to intermediate processes where physics particles can exist on shell. In other words, that internal propagators $\frac{1}{p^2 - m^2 + i\epsilon}$ in Feynman diagrams can diverge with $p^2 = m^2$ so that one is sensitive to the $i\epsilon$ [29]. Therefore, when constructing a quantum field theory that correctly accounts for these light particles, all the contribution to the amplitude from virtual heavy particles that cannot be physically created at these energies can be Taylor expanded $\frac{p^2}{M^2}$, where M is the mass of the heavy particle.

The power of this method is that the Taylor expanded amplitude can be computed directly from a quantum field theory which contains only the light particles. The expanded amplitude now contains the local interactions between them that encode the small effects arising from virtual heavy particle exchange. For example, the Standard Model does not contain gauge bosons from the GUT scale, but can be modified such that it accounts for the very small effects such particles could have.

There are two basic applications of effective field theory [29].

- **Top down:** the theory for high energies is known, but do not need all of its complexity to arrive at the desired description of low energy physics. Thus, construct an EFT which incorporates the leading order and light degrees of freedom. Constraining their interaction from the knowledge of the symmetries of the more complete theory.

- Bottom up: explore small effects from higher dimension operators in the low energy regime to gain more knowledge about what might be going on at higher energy scales not accessible at this moment.

2.5.1 Fermi theory

Consider Fermi's theory of weak interactions. Originally it was a bottom-up EFT and designed to account for neutron β decay in the $n \rightarrow p^+ e^- \bar{\nu}_e$ process. The weak interactions refers to processes mediated by the W^\pm or Z^0 bosons, whose masses are about 80 GeV and 91 GeV respectively. The full process is depicted in Fig. 2.16. Where one of the up quarks residing in the proton decays to a down quark by scattering of a W^+ boson.

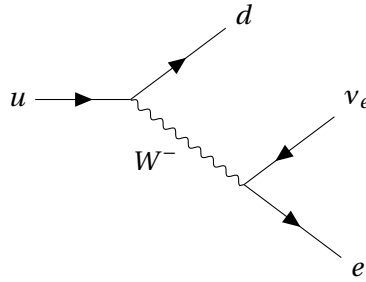


FIGURE 2.16: Flavour changing charged current decaying into leptons

In the SM the matrix element of this process is proportional to the Electroweak-propagator times the electroweak coupling constant squared.

$$|\mathcal{M}| \sim g_2^2 \left| \frac{-i(g^{\mu\nu} - q^\mu q^\nu / M_{Z,W}^2)}{M_{Z,W}^2 - q^2} \right|^2 \quad (2.83)$$

Since the masses of the W^- boson is many times bigger then the quarks or the leptons, it means that the boson is deeply virtual, $m_W^2 \gg q^2$, and the matrix element can be reduced to

$$|\mathcal{M}| \sim G_F \propto -\frac{g}{m_W^2} \quad (2.84)$$

Where G_F is known as the Fermi constant. In this approximation the W -boson propagator has been contracted to a four-point interaction vertex in Fig. 2.17.

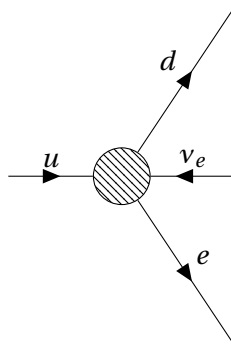


FIGURE 2.17: The effective vertex in the low energy effective field theory.

This amplitude can be reproduced to lowest order in $\frac{q^2}{M_W^2}$ by a low energy EFT with a coupling strength G_F . This interaction is then written in terms of leptons and quarks

only instead of the electroweak definition. The illustration of Fermi theory with respect to the Standard Model gives a good idea of the power of the EFT. One can argue that the Standard Model is also valid up until a certain energy scale when new physics becomes marginal $E \approx \Lambda \sim E_{newphysics}$

2.5.2 Standard Model effective field theory

Recently the SMEFTsim package [30] has been developed implementing a FeynRules package that is open for public use¹. The code supplied defines the SMEFTsim package and covers two different approaches to how the SM Lagrangian parameters are extracted from experimental measurements. Differing in only one parameter, the electroweak coupling constant or the W-boson mass $\{\alpha_{ew}, \hat{m}_Z, \hat{G}_F\}$ and $\{\hat{m}_W, \hat{m}_Z, \hat{G}_F\}$.

Assumed is that physics beyond the Standard Model (SM) resides at scales larger than the electroweak scale ($\Lambda \gg \overline{v_T}$), one can utilise an expansion of this ratio of scales to construct an effective field theory (EFT). Such an EFT captures the low energy limit of the physics beyond the SM so long as no light hidden states are in the particle spectrum and $\overline{v_T}/\Lambda < 1$. The SMEFT is defined using the Warsaw basis [31] and has been studied with increased theoretical sophistication over the recent years.

It may also be used to a wide range of possible extensions of the SM. For example, it can address the strong evidence for dark matter and neutrino masses in addition to the theoretical issue of the hierarchy problem motivating new physics at the scale of TeV . The interest in SMEFT has increased due to the continued operation of the LHC. Utilising the SMEFT is valuable for getting the most out of the run 1 and 2 data sets as well as the data from the high future luminosity LHC.

As discussed, assumed is that the SM constitutes merely an effective theory, which is applicable up to energies not exceeding a certain scale Λ . Therefore, any field theory valid above this energy scale should satisfy the following requirements.

- Its gauge group should contain $SU(3)_C \otimes SU(2)_L \otimes U(1)_Y$ of the Standard Model.
- All the SM degrees of freedom should be incorporated into the theory, either as fundamental or composite field.
- At low energies it should reduce to the SM, provided no undiscovered light particles exist.

The reduction to SM at low energies usually follows from the decoupling of heavy particles with masses of order Λ or larger. This leads to the appearance of higher-dimensional operators in the SM Lagrangian that are suppressed by powers of Λ

$$\mathcal{L}_{EFT} = \mathcal{L}_{SM}^{(4)} + \frac{1}{\Lambda} \sum_k C_k^{(5)} Q_k^{(5)} + \frac{1}{\Lambda^2} \sum_k C_k^{(6)} Q_k^{(6)} + \mathcal{O}\left(\frac{1}{\Lambda^3}\right), \quad (2.85)$$

Here \mathcal{L}_{SM} is the usual renormalizable part of the SM Lagrangian, it contains dimension-two and dimension-four operators only. In the remaining terms, $Q_k^{(n)}$ denote the dimension- n operators, and $C_k^{(n)}$ stand for the corresponding dimensionless coupling constants referred to as Wilson coefficients. We will now give a summary of the SMEFT Lagrangian

¹<http://feynrules.irmp.ucl.ac.be/wiki/SMEFT>

derivation and critical steps during this derivation. The dimension-5 operators, which violate lepton number, will not be taken into account. We will switch to the notation and conventions used in ref. [32].

$$\begin{aligned}
l_{L_1} &= \begin{pmatrix} \nu_e \\ e^- \end{pmatrix}_L, & e_{R_1} &= e_R^-, & q_1^\alpha &= \begin{pmatrix} u \\ d \end{pmatrix}_L, & u_{R_1}^\alpha &= u_R, & d_{R_1}^\alpha &= d_R \\
l_{L_2} &= \begin{pmatrix} \nu_\mu \\ \mu^- \end{pmatrix}_L, & e_{R_2} &= \mu_R^-, & q_2^\alpha &= \begin{pmatrix} c \\ s \end{pmatrix}_L, & u_{R_2}^\alpha &= c_R, & d_{R_2}^\alpha &= s_R \\
l_{L_3} &= \begin{pmatrix} \nu_\tau \\ \tau^- \end{pmatrix}_L, & e_{R_3} &= \tau_R^-, & q_3^\alpha &= \begin{pmatrix} t \\ b \end{pmatrix}_L, & u_{R_3}^\alpha &= t_R, & d_{R_3}^\alpha &= b_R
\end{aligned} \tag{2.86}$$

Here α stands for the colour indices. The chirality indices, (L, R) , will be omitted in the following notation. The Higgs field and its complex conjugate will occur as ϕ and ϕ^\dagger . The well known expression for $\mathcal{L}_{SM}^{(4)}$, before spontaneous symmetry breakdown, becomes

$$\begin{aligned}
\mathcal{L}_{SM}^{(4)} &= -\frac{1}{4}G_{\mu\nu}G^{\mu\nu} - \frac{1}{4}W_{\mu\nu}W^{\mu\nu} - \frac{1}{4}B_{\mu\nu}B^{\mu\nu} + (D_\mu\phi)^\dagger(D^\mu\phi) + m^2\phi^\dagger\phi \\
&\quad - \frac{1}{2}(\phi^\dagger\phi)^2 + i(\bar{l}Dl + \bar{e}De + \bar{q}Dq + \bar{u}Du + \bar{d}Dd) \\
&\quad - (\bar{l}\Gamma_e e\phi + \bar{q}\Gamma_u\phi^\dagger + \bar{q}\Gamma_d d\phi + h.c.)
\end{aligned} \tag{2.87}$$

The Yukawa couplings, $\Gamma_{e,u,d}$, are matrices in the generation space. The covariant derivative acting on a field is defined as

$$(D_\mu q)^{\alpha j} = \left(\delta_{\alpha\beta}\delta_{jk}(\partial_\mu + ig'Y_q B_\mu) + ig\delta_{\alpha\beta}S_{jk}^I W_\mu^I + ig_s\delta_{jk}T_{\alpha\beta}^A G_\mu^A \right) q^{\beta k} \tag{2.88}$$

Here, $T^A = \frac{1}{2}\Lambda^A$ and $S^I = \frac{1}{2}\tau^I$ are the $SU(3)$ and $SU(2)$ generators respectively, while the λ^A and τ^I are the Gell-Mann and Pauli matrices. It is useful to define Hermitian derivative terms that contain $\phi^\dagger \overleftarrow{D}_\mu \phi \equiv (D_\mu\phi)^\dagger\phi$ as follows:

$$\begin{aligned}
\phi^\dagger i \overrightarrow{D}_\mu \phi &\equiv i\phi^\dagger(D_\mu - \overleftarrow{D}_\mu)\phi \\
\phi^\dagger i \overleftarrow{D}_\mu^I \phi &\equiv i\phi^\dagger(\tau^I D_\mu - \overleftarrow{D}_\mu \tau^I)\phi
\end{aligned} \tag{2.89}$$

The gauge field strength tensors and their covariant derivatives have a very similar structure as derived before

$$\begin{aligned}
G_{\mu\nu}^A &= \partial_\mu G_\nu^A - \partial_\nu G_\mu^A - g_s f^{ABC} G_\mu^B G_\nu^C \\
W_{\mu\nu}^I &= \partial_\mu W_\nu^I - \partial_\nu W_\mu^I - g\epsilon^{IJK} W_\mu^J W_\nu^K \\
B_{\mu\nu} &= \partial_\mu B_\nu - \partial_\nu B_\mu
\end{aligned} \tag{2.90}$$

$$\begin{aligned}
(D_\rho G_{\mu\nu})^A &= \partial_\rho G_{\mu\nu}^A - g_s f^{ABC} G_\rho^B G_{\mu\nu}^C \\
(D_\rho W_{\mu\nu})^I &= \partial_\rho W_{\mu\nu}^I - g\epsilon^{IJK} W_\rho^J W_{\mu\nu}^K \\
D_\rho B_{\mu\nu} &= \partial_\rho B_{\mu\nu}
\end{aligned} \tag{2.91}$$

Now we will set in the process of making an EFT of this Lagrangian. Remember that the new operators $Q_i^{(d)}$ are suppressed by $d - 4$ powers of the cutoff scale Λ and $C_i^{(d)}$ are the Wilson coefficients. The factors of $\frac{1}{\Lambda}$ are absorbed into the Wilson coefficients. Utilising the Warsaw basis is also theoretically favoured as it is the only basis that has been completely normalised [33]. We switch from the ϕ Higgs doublet notation to

$$\phi \rightarrow H = \frac{1}{2} \begin{pmatrix} 0 \\ (1 + c_{H,kin})h + \bar{v}_T \end{pmatrix}, \quad (2.92)$$

where,

$$\begin{aligned} c_{H,kin} &\equiv (C_{H\Box} - \frac{1}{4}C_{HD})\bar{v}^2, \\ \bar{v}_T &\equiv (1 + \frac{3C_H\bar{v}^2}{8\lambda})\bar{v}. \end{aligned} \quad (2.93)$$

This results in a formalised h field when the Lagrangian is written in mass eigenstate fields. The distinction between \bar{v}_T and \bar{v} is at dimension eight when \bar{v} multiplies with a Wilson coefficient. Because the Higgs field is changed so do the gauge fields and the coupling strength. The gauge fields are redefined as

$$\begin{aligned} G_\mu^A &= \mathcal{G}_\mu^A (1 + C_{HG}\bar{v}_T^2), \\ W_\mu^I &= \mathcal{W}_\mu^I (1 + C_{HW}\bar{v}_T^2), \\ B_\mu &= \mathcal{B}_\mu (1 + C_{HB}\bar{v}_T^2). \end{aligned} \quad (2.94)$$

Here the $\mathcal{G}, \mathcal{W}, \mathcal{B}$ fields are the canonically normalised fields. The modified coupling constants are also redefined as

$$\begin{aligned} \bar{g}_3 &= g_3 (1 + C_{HG}\bar{v}_T^2), \\ \bar{g}_2 &= g_2 (1 + C_{HW}\bar{v}_T^2), \\ \bar{g}_1 &= g_2 (1 + C_{HB}\bar{v}_T^2). \end{aligned} \quad (2.95)$$

Now, the mass eigenstate basis for W_μ^3, B_μ in the SMEFT is given by

$$\begin{pmatrix} \mathcal{W}_\mu^3 \\ \mathcal{B}_\mu \end{pmatrix} = \begin{pmatrix} 1 & -\frac{1}{2}v_T^2 C_{HWB} \\ -\frac{1}{2}v_T^2 C_{HWB} & 1 \end{pmatrix} \begin{pmatrix} \cos\bar{\theta} & \sin\bar{\theta} \\ -\sin\bar{\theta} & \cos\bar{\theta} \end{pmatrix} \begin{pmatrix} \mathcal{Z}_\mu \\ \mathcal{A}_\mu \end{pmatrix} \quad (2.96)$$

with $\cos\bar{\theta} = \frac{\bar{g}_2}{\sqrt{\bar{g}_2^2 + \bar{g}_1^2}}$ and $\sin\bar{\theta} = \frac{\bar{g}_1}{\sqrt{\bar{g}_2^2 + \bar{g}_1^2}}$. This way also the reparameterization of the mass fields is modified by Wilson coefficients. The SMEFT theory uses unitary gauge and several simplifications. Resulting in a LO SMEFT model.

In order to define the numerical values of the SM Lagrangian several free parameters need to be used. To determine the numerical value of the SM Lagrangian we use the electroweak inputs. The Lagrangian parameters in the SMEFT differ from the SM Lagrangian due to $\mathcal{L}^{(6)}$ local operator correction. Meaning a generic parameter κ receives a shift from its SM value due to $\mathcal{L}^{(6)}$ operators by $\delta\kappa = \bar{\kappa} - \hat{\kappa}$ and in the SM limit, when $C_i \rightarrow 0$ one has $\delta\kappa \rightarrow 0$. The input electroweak parameters are α_{EW}, m_Z and G_F , the method extraction of

Input parameters	Value
$\alpha_{Ew}(m_Z)$	$1/(127.950 \pm 0.017)$
m_W	$80.365 \pm 0.016 \text{ GeV}$
m_Z	$91.1876 \pm 0.0021 \text{ GeV}$
G_F	$1.1663787(6) \times 10^{-5} \text{ GeV}^{-2}$
m_h	$125.09 \pm 0.21 \pm 0.11 \text{ GeV}$
α_S	0.1181 ± 0.0011
m_e	$0.5109989461(31) \times 10^{-3} \text{ GeV}$
m_μ	$105.6583745(24) \times 10^{-3} \text{ GeV}$
m_τ	$1.77686 \pm 0.00012 \text{ GeV}$
m_u	$2.2^{+0.6}_{-0.4} \times 10^{-3} \text{ GeV}$
m_c	$1.28 \pm 0.03 \text{ GeV}$
m_t	$173.21 \pm 0.51 \pm 0.71 \text{ GeV}$
m_d	$4.7^{+0.5}_{-0.4} \times 10^{-3} \text{ GeV}$
m_s	$0.096^{+0.008}_{-0.004} \text{ GeV}$
m_b	$4.18^{+0.04}_{-0.03} \text{ GeV}$

TABLE 2.4: The set of parameters used as inputs for the SMEFT [10].

these parameters can be found in ref. [30]. The numerical values used to define the mass and coupling input parameters in the model are given in Table 2.4.

2.5.3 Flavour symmetry assumptions

The $U(3)^5$ limit is the assumption that will be used and deals with the limit of unbroken global flavour symmetry in the SM Lagrangian. By requiring this symmetry the number of free parameters in the model decreases significantly. From 1350 CP-even and 1149 CP-odd parameters to around 52 CP-even and around 17 CP-odd. Therefore, the CKM matrix is not changed with respect to the SM and is also not depended of any Wilson coefficients. Also note that the Pontecorvo Maki Nakagawa Sakata (PMNS) matrix is also not implemented in the SMEFT as neutrino masses are neglected. The remaining dimension-6 when taking the $U(3)^5$ are summarised in Fig. 2.5.

Most $\mathcal{L}^{(6)}$ operators each have only 1 corresponding Wilson coefficient. Each of these parameters have their exact analogous copy in the SMEFTsim model. The Wilson coefficients in the model files are free input parameters. Real Wilson coefficients are defined as external parameters and values can be assigned directly by the user. Complex Wilson coefficients are technically defined as internal parameters in the form of $cXX = cXX_{Abs} e^{I \cdot cXX_{ph}}$ with two independent external parameters: the absolute value cXX_{Abs} and the complex phase cXX_{ph} can be assigned by the user.

The $U(3)^5$ -SMEFT with non SM phases has, excluding the SM input parameters and the cutoff scale of the EFT, a total of 81 free external parameters. 17 determine the complex phase of its corresponding Wilson coefficient. Remaining are 64 real Wilson coefficients which includes 5 pairs that belong to the same $\mathcal{L}^{(6)}$ operator. Resulting in a total of 59 free operators in the Standard Model Effective Field theory with a total to 64 Wilson coefficients. The model is now able to perform numerical studies at LO (tree-level) interference of the SMEFT with the SM, while neglecting NLO (next-to-leading-order) corrections. In order to still be able to simulate the processes $h \rightarrow gg$, $h \rightarrow \gamma\gamma$, $h \rightarrow \gamma Z$, since they occur at one loop in the SM. An explicit SM Lagrangian term is defined in order to obtain a non-zero interference for these processes.

1 : χ^3		2 : H^6		3 : $H^4 D^2$		5 : $\psi^2 H^3 + \text{h.c.}$	
Q_G	$f^{ABC} G_\mu^{A\nu} G_\nu^{B\rho} G_\rho^{C\mu}$	Q_H	$(H^\dagger H)^3$	$Q_{H\Box}$	$(H^\dagger H)\Box(H^\dagger H)$	Q_{eH}	$(H^\dagger H)(\bar{l}_p e_r H)$
$Q_{\tilde{G}}$	$f^{ABC} \tilde{G}_\mu^{A\nu} G_\nu^{B\rho} G_\rho^{C\mu}$			Q_{HD}	$(H^\dagger D^\mu H)^\dagger (H^\dagger D_\mu H)$	Q_{uH}	$(H^\dagger H)(\bar{q}_p u_r \tilde{H})$
Q_W	$\epsilon^{IJK} W_\mu^{I\nu} W_\nu^{J\rho} W_\rho^{K\mu}$					Q_{dH}	$(H^\dagger H)(\bar{q}_p d_r H)$
$Q_{\tilde{W}}$	$\epsilon^{IJK} \tilde{W}_\mu^{I\nu} W_\nu^{J\rho} W_\rho^{K\mu}$						
4 : $X^2 H^2$		6 : $\psi^2 XH + \text{h.c.}$		7 : $\psi^2 H^2 D$			
Q_{HG}	$H^\dagger H G_{\mu\nu}^A G^{A\mu\nu}$	Q_{eW}	$(\bar{l}_p \sigma^{\mu\nu} e_r) \tau^I H W_{\mu\nu}^I$	$Q_{Hl}^{(1)}$	$(H^\dagger i \overleftrightarrow{D}_\mu H)(\bar{l}_p \gamma^\mu l_r)$		
$Q_{H\tilde{G}}$	$H^\dagger H \tilde{G}_{\mu\nu}^A G^{A\mu\nu}$	Q_{eB}	$(\bar{l}_p \sigma^{\mu\nu} e_r) H B_{\mu\nu}$	$Q_{Hl}^{(3)}$	$(H^\dagger i \overleftrightarrow{D}_\mu^I H)(\bar{l}_p \tau^I \gamma^\mu l_r)$		
Q_{HW}	$H^\dagger H W_{\mu\nu}^I W^{I\mu\nu}$	Q_{uG}	$(\bar{q}_p \sigma^{\mu\nu} T^A u_r) \tilde{H} G_{\mu\nu}^A$	Q_{He}	$(H^\dagger i \overleftrightarrow{D}_\mu H)(\bar{e}_p \gamma^\mu e_r)$		
$Q_{H\tilde{W}}$	$H^\dagger H \tilde{W}_{\mu\nu}^I W^{I\mu\nu}$	Q_{uW}	$(\bar{q}_p \sigma^{\mu\nu} u_r) \tau^I \tilde{H} W_{\mu\nu}^I$	$Q_{Hq}^{(1)}$	$(H^\dagger i \overleftrightarrow{D}_\mu H)(\bar{q}_p \gamma^\mu q_r)$		
Q_{HB}	$H^\dagger H B_{\mu\nu} B^{\mu\nu}$	Q_{uB}	$(\bar{q}_p \sigma^{\mu\nu} u_r) \tilde{H} B_{\mu\nu}$	$Q_{Hq}^{(3)}$	$(H^\dagger i \overleftrightarrow{D}_\mu^I H)(\bar{q}_p \tau^I \gamma^\mu q_r)$		
$Q_{H\tilde{B}}$	$H^\dagger H \tilde{B}_{\mu\nu} B^{\mu\nu}$	Q_{dG}	$(\bar{q}_p \sigma^{\mu\nu} T^A d_r) H G_{\mu\nu}^A$	Q_{Hu}	$(H^\dagger i \overleftrightarrow{D}_\mu H)(\bar{u}_p \gamma^\mu u_r)$		
Q_{HWB}	$H^\dagger \tau^I H W_{\mu\nu}^I B^{\mu\nu}$	Q_{dW}	$(\bar{q}_p \sigma^{\mu\nu} d_r) \tau^I H W_{\mu\nu}^I$	Q_{Hd}	$(H^\dagger i \overleftrightarrow{D}_\mu H)(\bar{d}_p \gamma^\mu d_r)$		
$Q_{H\tilde{W}B}$	$H^\dagger \tau^I H \tilde{W}_{\mu\nu}^I B^{\mu\nu}$	Q_{dB}	$(\bar{q}_p \sigma^{\mu\nu} d_r) H B_{\mu\nu}$	$Q_{Hud} + \text{h.c.}$	$i(\tilde{H}^\dagger D_\mu H)(\bar{u}_p \gamma^\mu d_r)$		
8 : $(\bar{L}L)(\bar{L}L)$		8 : $(\bar{R}R)(\bar{R}R)$		8 : $(\bar{L}L)(\bar{R}R)$			
Q_{ll}	$(\bar{l}_p \gamma_\mu l_r)(\bar{l}_s \gamma^\mu l_t)$	Q_{ee}	$(\bar{e}_p \gamma_\mu e_r)(\bar{e}_s \gamma^\mu e_t)$	Q_{le}	$(\bar{l}_p \gamma_\mu l_r)(\bar{e}_s \gamma^\mu e_t)$		
$Q_{qq}^{(1)}$	$(\bar{q}_p \gamma_\mu q_r)(\bar{q}_s \gamma^\mu q_t)$	Q_{uu}	$(\bar{u}_p \gamma_\mu u_r)(\bar{u}_s \gamma^\mu u_t)$	Q_{lu}	$(\bar{l}_p \gamma_\mu l_r)(\bar{u}_s \gamma^\mu u_t)$		
$Q_{qq}^{(3)}$	$(\bar{q}_p \gamma_\mu \tau^I q_r)(\bar{q}_s \gamma^\mu \tau^I q_t)$	Q_{dd}	$(\bar{d}_p \gamma_\mu d_r)(\bar{d}_s \gamma^\mu d_t)$	Q_{ld}	$(\bar{l}_p \gamma_\mu l_r)(\bar{d}_s \gamma^\mu d_t)$		
$Q_{lq}^{(1)}$	$(\bar{l}_p \gamma_\mu l_r)(\bar{q}_s \gamma^\mu q_t)$	Q_{eu}	$(\bar{e}_p \gamma_\mu e_r)(\bar{u}_s \gamma^\mu u_t)$	Q_{qe}	$(\bar{q}_p \gamma_\mu q_r)(\bar{e}_s \gamma^\mu e_t)$		
$Q_{lq}^{(3)}$	$(\bar{l}_p \gamma_\mu \tau^I l_r)(\bar{q}_s \gamma^\mu \tau^I q_t)$	Q_{ed}	$(\bar{e}_p \gamma_\mu e_r)(\bar{d}_s \gamma^\mu d_t)$	$Q_{qu}^{(1)}$	$(\bar{q}_p \gamma_\mu q_r)(\bar{u}_s \gamma^\mu u_t)$		
		$Q_{ud}^{(1)}$	$(\bar{u}_p \gamma_\mu u_r)(\bar{d}_s \gamma^\mu d_t)$	$Q_{qu}^{(8)}$	$(\bar{q}_p \gamma_\mu T^A q_r)(\bar{u}_s \gamma^\mu T^A u_t)$		
		$Q_{ud}^{(8)}$	$(\bar{u}_p \gamma_\mu T^A u_r)(\bar{d}_s \gamma^\mu T^A d_t)$	$Q_{qd}^{(1)}$	$(\bar{q}_p \gamma_\mu q_r)(\bar{d}_s \gamma^\mu d_t)$		
				$Q_{qd}^{(8)}$	$(\bar{q}_p \gamma_\mu T^A q_r)(\bar{d}_s \gamma^\mu T^A d_t)$		
8 : $(\bar{L}R)(\bar{R}L) + \text{h.c.}$		8 : $(\bar{L}R)(\bar{L}R) + \text{h.c.}$					
$Q_{ltdq}^{(1)}$	$(\bar{l}_p^j e_r)(\bar{d}_s q_{tj})$	$Q_{quqd}^{(1)}$	$(\bar{q}_p^j u_r) \epsilon_{jk} (\bar{q}_s^k d_t)$				
		$Q_{quqd}^{(8)}$	$(\bar{q}_p^j T^A u_r) \epsilon_{jk} (\bar{q}_s^k T^A d_t)$				
		$Q_{lequ}^{(1)}$	$(\bar{l}_p^j e_r) \epsilon_{jk} (\bar{q}_s^k u_t)$	$H^\dagger i \overleftrightarrow{D}_\mu H \equiv H^\dagger i D_\mu H - (i D_\mu H^\dagger) H$			
		$Q_{lequ}^{(3)}$	$(\bar{l}_p^j \sigma_{\mu\nu} e_r) \epsilon_{jk} (\bar{q}_s^k \sigma^{\mu\nu} u_t)$	$H^\dagger i \overleftrightarrow{D}_\mu^I H \equiv H^\dagger i \tau^I D_\mu H - (i D_\mu \tau^I H^\dagger) H$			

TABLE 2.5: The $\mathcal{L}^{(6)}$ operators built from the Standard Model fields which conserve baryon number. The operators are divided into eight Classes: χ^3 , H^6 , etc. Operators with $+h.c.$ in the table heading also have Hermitian conjugates, as does the $\psi^2 H^2 D$ operator Q_{Hud} . The subscripts p, r, s, t are flavour indices which are suppressed on the left had sides of the sub-tables [30].

Chapter 3

Experimental setup

In this chapter the Large Hadron Collider (LHC) and the ATLAS experiment will be introduced. First some background information is given and the LHC is described in section 3.1 and 3.2. In section 3.3 the most important parts of the ATLAS detector are explained.

3.1 CERN and the Large Hadron Collider

The origins of the European Organisation for Nuclear Research or commonly referred to as CERN, which is the French acronym of CONSEIL EUROPÉEN POUR LA RECHERCHE NUCLÉAIRE, date back to the end of the Second World War. Following a handful of scientists from several countries created a Central European atomic physics laboratory. Such a laboratory would not only unite the European scientists but also allow them to share the increasing costs of nuclear physics facilities. The institute was established in 1954 based in Geneva and currently has 23 member states. Today CERN's main function is to provide the particle accelerators and other infrastructure needed for high-energy physics research.

3.2 The Large Hadron Collider

CERN is currently housing the largest accelerator ever built called the Large Hadron Collider (LHC). This is a circular collider with a circumference of 27 *km*, currently capable of producing 7 *TeV* proton beams travelling in opposite directions in tubes of ultrahigh vacuum [34]. These are guided by strong magnetic fields produced by superconducting electromagnets all kept at sub-zero temperatures to maintain their superconducting properties. In total 1232 dipole magnets of 15 m in length bend the beams to be circular and 392 quadrupole magnets confine them to a smaller space to ensure a high collision rate when the two beams cross paths inside the 4 major experiments located across the ring of the LHC. These four experiments are the ATLAS, CMS, ALICE and LHCb. This thesis was made under the flag of the ATLAS experiment.

- **ATLAS** (A Toroidal LHC Apparatus) - experiment is a general-purpose particle detector and currently the largest ever built. It is designed to exploit all the debris coming from the proton collisions and discover all the physics happening by carefully analysing its debris.
- **CMS** (Compact Muon Solenoid) - Also a general-purpose detector at the LHC and has very broad physics interests. Although it has the same scientific goals as the ATLAS experiment, it uses different technical solutions and magnet system design.
- **ALICE** (A Large Ion Collider Experiment) - is a heavy-ion detector and designed to study the physics of strongly interacting matter, more specifically where a phase of matter called quark-gluon plasma forms.

- **LHCb** (Large Hadron Collider beauty experiment) - A detector designed specifically for beauty/bottom and anti-beauty/bottom Hadrons, known as B mesons. Which are quite hard to detect because they are formed close to the line of the beam pipe.

But there are also many other experiments located at CERN which do not use the LHC, but other particle accelerator facilities, Fig. 3.1 For example, the Super Proton Synchrotron (SPS), Proton Synchrotron (PS) or Antiproton Decelerator. Furthermore, CERN is looking into what is going to follow up the LHC. Currently two projects are competing, the Future Circular Collider (FCC), which is a higher performance circular collider aiming to reach collision energies of 100 TeV and the Compact Linear Collider (CLIC) looking to collide electrons and positrons in the same energy range as the LHC instead of hadron collisions.

CERN's Accelerator Complex

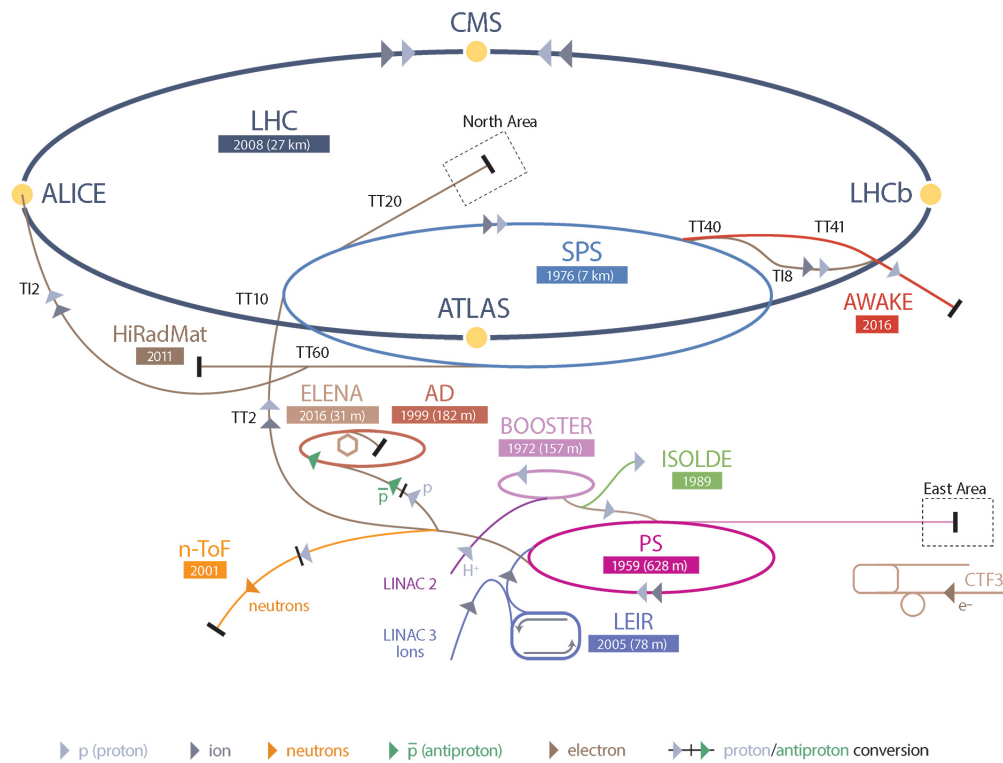


FIGURE 3.1: Accelerator complex of CERN (2016) [35]

Most of the recent breakthroughs in particle physics have come from experiments at high-energy particle accelerators. In order to produce massive particles high energies are required. More precisely, the energy available in the centre-of-mass has to be greater than the sum of the masses of the particles that you want to produce. The centre of mass energy \sqrt{s} for a circular collider such as the LHC is given by $\sqrt{s} = 2E$, where E is the energy of a single beam. Only charged stable particles can be accelerated to high energies, therefore the possible types of accelerators are e^+e^- colliders, hadron colliders pp or $\bar{p}\bar{p}$ and electron-proton colliders, e^-p or e^+p . The LHC's next important feature is the instantaneous luminosity L , which determines the event rates. For a given process, the number of interactions is the product of the luminosity integrated over the lifetime of the operation of the machine and the cross section for the process,

$$N = \sigma \int L(t) dt. \quad (3.1)$$

The particles in the LHC are grouped into bunches that are brought into collision at the middle of the detectors. At the LHC the bunches are separated by 25 ns . Assuming that the beams have a Gaussian profile of proton density and collide head-on, the instantaneous luminosity [36] is given by

$$L = f \frac{n_1 n_2}{4\pi\sigma_x\sigma_y}. \quad (3.2)$$

Here n_1 and n_2 are the numbers of particles in the colliding bunches, f is the frequency with which the bunches collide, which is 40 Hz for the LHC. Further, σ_x and σ_y denote the root-mean-square horizontal and vertical beam sizes respectively.

3.3 The ATLAS detector

The ATLAS detector [37], Fig. 3.5, is the largest volume detector ever constructed. It has the dimensions of a cylinder, which is 44 m long and 25 m in diameter and sits in a cavern approximately 100 m underground. The detector is a layered instrument designed to, layer-by-layer, detect all the particles that pass through, with the exception of neutrinos. The detector is centred on the interaction point and is designed with a forward-backward symmetry. In order to detect all particles that come out of the interaction point upon collision it has a good spatial coverage thanks to a system of sub-detectors. The list of sub-parts starts with the inner detector, is then followed by the electromagnetic calorimeter, then comes the hadronic calorimeter and finally the muon spectrometer. The inner detector contains a longitudinal field of $2T$ generated by a solenoid magnet. The outer part of the detector is filled with a toroidal field of $4T$, which is generated by 8 separate coils that form the Barrel Toriod magnet. The End-cap Toriods cover the sides with magnetic fields of also $4T$. All seen in the Fig. 3.2, 3.3, 3.4. These fields are used to bend the tracks of the outgoing particles for momentum measurements.



FIGURE 3.2: ATLAS Central Solenoid magnet [38]

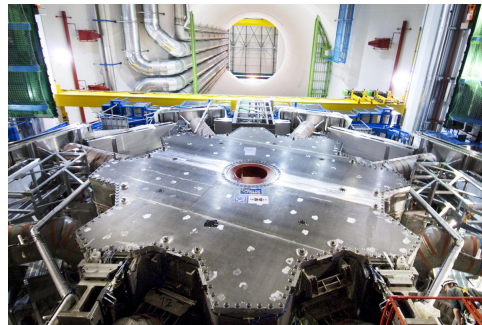


FIGURE 3.3: One of the ATLAS End-cap Toriods [38]

When referring to locations of particles in the detector, a cylindrical coordinate system is used. The beam axis is defined as the z -direction. The polar angle, $\theta \in [0, \pi]$, is the angle from the beam axis. The azimuthal angle, $\phi \in [-\pi, \pi]$, is the angle around the beam axis. The pseudo-rapidity is often used to describe the direction of a massless particle and is defined as

$$\eta = -\ln \tan\left(\frac{\theta}{2}\right). \quad (3.3)$$



FIGURE 3.4: The ATLAS Barrel Toroid magnet [38]

While for massive particles the rapidity is used and is defined as

$$y = \frac{1}{2} \ln \left[\frac{E + p_z}{E - p_z} \right]. \quad (3.4)$$

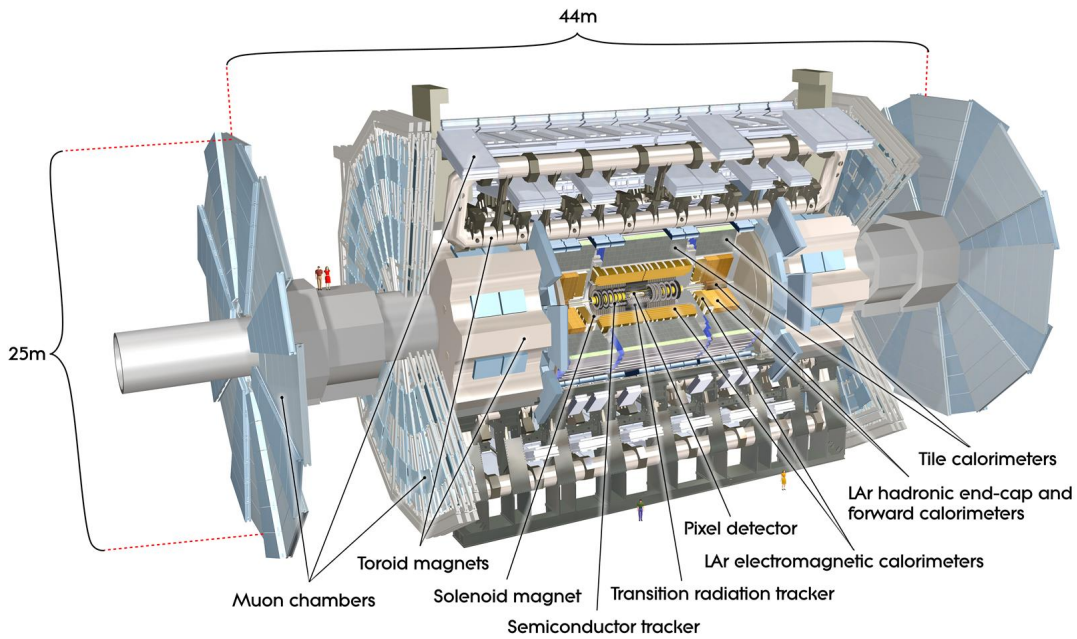


FIGURE 3.5: Schematic drawing of the ATLAS detector indicating the most important modules of the construction [38].

3.3.1 Inner detector

The inner detector (ID) is the inner most part of the detector, and the closest to the actual collisions. It is designed such that it has minimal radiation length, which is a characteristic of a material, related to the energy loss of high energy particles electromagnetically interacting with it. It is positioned such that it can measure the curvature of the trajectory of the charged particles. Also the ID is made up out of several layers of detection hardware. The layer closest to the beam is the silicon based Pixel detector, which is made 1744 pixel modules that are fixed in three layers around the beam line and interaction point. The innermost layer is the insertable b-layer, which takes care of the position of the interaction vertex. This layer replaced the initial b-layer before the start of Run 2 because of

degradation due to heavy radiation effects. Surrounding this there are multiple layers of Semiconductor tracker, which is a strip detector consisting of silicon sensors. At last, the outer part of the ID is the Transition Radiation Tracker. This is a straw tube detector which is filled with a gas mixture of 70% Xenon, 27% CO_2 and 3% O_2 . This gas mixture interacts with the charged particles and the pulses produced are picked up by thin metal wire in the tube. Allowing for positioning of the particles or the distinction between charged pions and electrons because of the difference in charge deposition.

3.3.2 The calorimeter system

This system contains two different types. The Electromagnetic Calorimeter (ECAL) and the Hadronic Calorimeter (HCAL) each designed to deal either with hadronic or electromagnetic active particles. The ATLAS calorimeter cover a range up to $|\eta| < 4.9$ and are build from alternating layers of active and passive materials. The passive material interacts heavily with the incoming particles and triggers the showering process, while the active layers detect the produced particles and measure their energy. This measurement is important for calculating the total energy in the interaction, and this part is thus build to maximise radiation length. The absorbing material of the ECAL is lead and the active material is liquid argon. The ECAL covers up to $|\eta| < 1.475$, while the endcap region covers $1.375 < |\eta| < 3.2$. The HCAL is particularly designed to stop particles interacting strongly producing hadronic jets and measuring their energy. The passive absorbing material is steel and the active material is made up out of scintillators that are organised in a accordion fashion. In the end-caps the absorbing material is copper and the active material is liquid Argon.

3.3.3 The muon spectrometer

Since the Muons have a very low interaction cross section with the other detectors systems, almost all of them pass through undetected. They do not emit the bremsstrahlung as the electrons do and therefore can be assumed to carry the amount of energy they had at the start of their creation. Therefore, the Muon system is placed on the outermost part of the ATLAS detector. Its most important task is to measure the momentum of the passing muons as precisely as possible up to a pseudorapidity of $|\eta| < 2.7$. The system consists of three cylindrical layers around the beam axis. The muon chambers are placed around and within the superconducting coils of the toroid magnets which generate its magnetic field. The tracks are measured with drift tubes, that are made of a anode and cathode filled with gas to be ionised by the incoming muon. Due to the electric fields between the anode and cathode. The electron drift can be determined, and thus the arrival of the muon at that time and place. In the innermost endcap layer with $|\eta| > 2.0$, so called Cathode Strip Chambers are used, which have a higher rate capability and time resolution. To guarantee the its design resolution the Monitored Drift Tubes, that provide the best precision with a spacial resolution of $80 \mu m$ and are placed per chamber, are aligned using optics and are monitoring the positions and deformations of the chambers.

3.3.4 Luminosity and triggers

In the forward region of the ATLAS detector three small detectors systems are installed to measure the luminosity delivered to ATLAS. They extract the bunch luminosity by measuring the inelastic pp collision cross section. This cross section is proportional to the instantaneous luminosity by taking into account the number of bunches, the frequency of the bunches, the visible average number of inelastic interactions and the total inelastic cross section multiplied with the efficiency of the detector. These detectors where first

calibrated using other data where the instantaneous luminosity was already known. Since there are many events in the ATLAS detector, every 25 ns two bunches are collided, the event rate is 40 MHz. With a events size of about 1 Megabyte it is impossible to read out and store every event delivered by the LHC. However, the most interesting events have a very low occurrence rate because of their low cross section. Therefore, the triggers [39] are designed to select the most interesting events and bring down the event rate to about 400 Hz. This process is divided into three levels. The first level is a pure hardware trigger, that is implemented in the detector. It searches for high- p_T muons, electrons, photons, jets, taus and large missing transverse momenta using the trigger chambers in the muon system and the calorimeter system. The lever 2 trigger is a software based trigger that uses fine-granularity data of the complete detector which are only processed in several regions of interest. When the event has surpassed the level 2 trigger it is completely reconstructed. Then the level 3 triggers consist of the event filters, the event filtering is done during the analysis procedure and includes more complex criteria for event patterns.

3.3.5 The 2015-2016 dataset

The data used in this thesis corresponds to an integrated luminosity of about $36.1 fb^{-1}$ with an uncertainty of 2.1%. The uncertainty is determined using the luminosity detectors. This data set represents the full data of the pp collisions collected in 2015 and 2016 at a $\sqrt{s} = 13 TeV$ with a bunch spacing of 25 ns.

Chapter 4

Monte Carlo Generators and Simulation

Monte Carlo (MC) event generators are widely used, especially by experimentalists and theorists in particle physics. They are predominantly used to make predictions for collider experiments and compare them to data. This chapter explains the techniques used in a MC generation. In addition, what settings and assumptions are necessary to produce a valid MC sample.

4.1 Structure of a proton-proton collision

Four main steps are used to make up the full structure of simulating a proton-proton collision at for example the Large Hadron Collider. The time and energy scales of the steps are significantly separated, such that events are able to be separated into these parts. This process is called factorization. The steps are

- Hard interaction process and underlying event
- Parton shower
- Hadronization
- Particle decays

When studying proton-proton collisions most of the collisions are "soft". Which means there is a low amount of momentum transfer, this happens when the constituents of the proton only scratch each other or miss each other completely. All these events are filtered out of the data and only the so called "hard" processes remain. These events have high momentum transfer and are the most interesting, since here highly energetic particles are ejected and can possibly form exotic forms of matter. This is why the simulation is started at the heart of the collisions. The Parton Distribution Functions (PDFs) describe partons coming into the process and perturbation theory gives a probabilistic distribution of the outgoing partons. After the hard process we are left with the incoming and outgoing partons of the event. The parton shower phase of the event generators starts from the hard process and works downwards to lower momentum scales to a point where perturbation theory breaks down. The partons involved in the process are coloured particles, quarks and gluons. From QED it is known that moving electric charges radiate photons, this is called Bremsstrahlung. In that same way, scattered colour charges radiate gluons, which happens for partons going in and going out of the collision. Only as we discussed in chapter 1, in QCD due to the non-Abelian structure $SU(3)$, gluons themselves are coloured and can thus trigger even more radiation when already radiated of a parton. Leading to

a extended shower and the phase space fills up with mostly soft gluons. When the event has been showered it is necessary to switch to hadronization models, these take account of the confinement of a system of parton into colourless hadrons, which we can observe with the detector. Take into account that the initial hadrons that started the collision have a coloured parton taken out and are thus left in a coloured state. It very likely that during the hard collision also several secondary soft collisions between the protons remnants have taken place, these will also have to be simulated since they will hadronize as well and will overlies or contaminate the already produced hard process. The last processes of event generation is the decay into stable particles. The hadrons that are produced in the hadronization are not always stable. To be precise most of the hadrons are heavy resonances of lighter mesons or baryons. These resonances will then decay into more and more stable secondary particles in a tree like fashion.

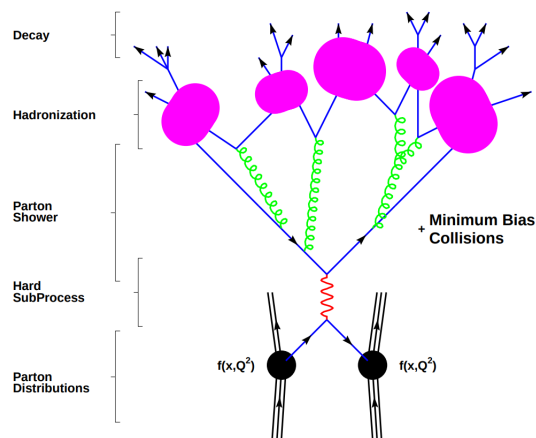


FIGURE 4.1: Schematic overview of the different stages of a Monte Carlo event [40]

4.1.1 Parton distributions

The calculation of the cross section of a particular process relies upon the knowledge of the distribution of momentum fraction x of the partons. Which are the quarks and gluons inside the hadrons being collided. The parton density functions (PDF's) are determined by global fits to data from deep inelastic scattering experiments, Drell-Yan and jet production inside colliders. Every proton contains three valence quarks, which are in turn surrounded by a sea of quark-antiquark pairs produced by virtual gluons. When the total energy of the proton increases, the partons move independently and freely inside the proton. This causes each of the partons to carry a certain amount of the total energy of the proton $p_i = x p_{tot}$. In order to quantify this, a probability, the PDF, is defined $f(x, Q^2)$ which is the probability that a certain parton carries a momentum fraction x_i of the total momentum on a certain energy scale Q^2 . The DGLAP [41] equation provides an analytical formula for these densities and together with fits, many different PDF sets for the proton are produced, up to NNLO accuracy. In Fig. 4.2 the PDFs for quarks and gluons in the proton are shown. One can see that in the higher x regions the sea quarks do most of the momentum carrying, while in the lower energy scales the gluons are more dominant.

4.1.2 Hard scattering process

The events that we are interested in almost always involve high momentum transfer between the partons. Thus simulation of these partons interacting with each other at large

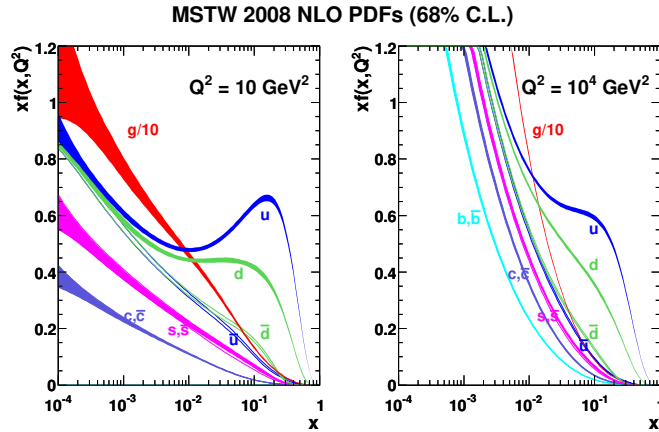


FIGURE 4.2: The PDFs supplied by Martin-Stirling-Thorne-Wattt(MSTW), determined up to NNLO(showing NLO) by global analysis of hard-scattering data [42].

invariant momentum transfer is the hart of the Monte Carlo generator. QCD offers a good theoretical description of interaction partons producing jets and heavy particles. These reactions are then calculated using perturbation theory [43]. Cross sections for a scattering process at hadron colliders can be broken down to [44]

$$\sigma_{ab \rightarrow n} = \sum_{a,b} \int_0^1 dx_a dx_b \int d\Phi_n f_a^{h_1}(x_a, Q^2) f_b^{h_2}(x_b, Q'^2) \times \frac{1}{2s} |\mathcal{M}_{ab \rightarrow n}|^2(\Phi_n, Q^2, Q'^2). \quad (4.1)$$

Here, $f_a^h(x, Q^2)$ are again the PDFs from the partons involved. The fully differential parton level cross section is given by the square of the Matrix Element \mathcal{M} and the parton flux $\frac{1}{2s} = \frac{1}{2sx_a x_b}$ and where s is the centre of mass energy squared. The matrix element is the sum of all the Feynman diagrams involved in the process. In which the Feynman diagrams constitute the actual physics processes as derived from the Standard Model and Quantum Chromodynamics. This is integrated over the total differential phase space of all of the final state particles. Some leading order matrix element generators are AlpGen [45], Sherpa [46] or Madgraph/MadEvent [47].

4.1.3 Parton shower

The parton shower approximates the effect of higher order interactions, it reproduces a series of emissions in the incoming and outgoing particles. Referred to as initial state radiation (ISR) and final state radiation (FSR). The parton shower generator we will be using in the theses is Pythia8 [48].

4.1.4 Hadronization and decay

The process of hadronization starts when the particles invariant mass Q^2 reaches the scales of QCD. Then the quarks and gluons from into colourless states. After which the Hadrons will decay into stable particles. The hadronization process regulates the transformation from partons into a cone of hadrons called jets. The final jets are then evaluated by reconstruction algorithms with the aim of obtaining the properties of the original partons of the jets. Soft and collinear emissions can still take place during the parton shower and the hadronization process.

4.1.5 Jets

The Hadronization process makes it so that whenever quarks or gluons are produced we cannot observe them directly, since colour confinement forbids the existence of isolated colour states. This is why the events with gluons and quarks in the final state can be observed experimentally as cluttered hadrons in a jet of particles. This feature of quantum chromodynamics makes it possible to make measurements on macroscopic scales and connect them to the partons momenta and quantum numbers. In order to identify clusters of particles as jets a cluster algorithm is applied. This is done in the ATLAS detector for analysis of the event topology, but can also be applied to truth events simulated by a MC generator. The most common jet reconstruction algorithm used is the anti-kt algorithm [49]. Here the distance between the particle clusters is used to determine the properties of the jets. Then a radius parameter R is applied to give the cone radius of a single jet. In the case of the analyses used the radius parameter equals 0.4.

4.2 SMEFT sample generation

The introduction of SMEFT in the Monte Carlo generator involves altering the hard and underlying interaction of the event generation process. Additional diagrams corresponding to the new physics are generated when asking for a specific interaction. In Madgraph5 [50], all of the parameters that enter in the calculation are given in the parameter card. This card contains the masses of the particles, the physical constants used, the widths that have to be generated and which are assumed to be Standard Model like. The model also contains a vertices file, which holds all of the vertices that enter in the physics model as a function of the parameters in the parameter card. When generating a process in the SMEFT model it is always necessary to specify the order $NP = 1$ to make sure that all and only the diagrams giving linear $\mathcal{L}^{(6)}$ are included. In the run card any options to the generation may be specified, such as the flavour scheme used or requirements on any of the particles that should be produced.

In order to extract the tree level interference contribution between $\mathcal{L}^{(6)}$ and SM the order $NP^2 == 1$ needs to be specified, this corresponds to the $1/\Lambda^2$ contribution to the total cross section. The $1/\Lambda^4$ order contribution can be calculated using $NP^2 == 2$ and corresponds to the squared BSM contribution of the new physics model. Λ is chosen to be 1 TeV and assumes that the energy scale of new physics lies beyond Λ . Which is sufficiently far away from the Higgs and top energy scales. In general, due to the fact that SM Lagrangian parameters can multiply the Wilson coefficients in the Lagrangian a given interaction vertex can have multiple interaction orders. The relevant widths are calculated using MadWidth during the generation process. This is because the value of the particle width is used to compute some of the cross sections in a narrow-width approximation. The values of the width are often inconsistent with a LO SMEFT prediction and has a particular big effect on the Higgs case. The default value to its width is obtained with the inclusion of radiative corrections, and is significantly smaller than the tree level value, mainly due to a large negative loop contribution from the $H \rightarrow b\bar{b}$ partial width. When generating events with this model it is important to simulate the full process and not exclude particles from the interaction as the model uses the interference of some interaction to make a fully gauge invariant process. When generating a 5-flavour scheme is used to include the bottom quark, if required, and no cuts are applied to the generation.

Chapter 5

Monte Carlo Sample Generation

This chapter explains how we generate the MC samples that are compared to the signals in the analyses. Also which settings were used in the process. Section 5.1 will cover the MC production and setting. 5.2 introduces how the HepMC [51] data of the MC samples is processed. Section 5.3 quickly explains the basics on how to compare MC samples with observed signals.

5.1 Signal simulation

All of the MC samples were generated using MadGraph5 v2.6.2 and the imported the SMEFTsim $U(3)^5$ model [30]. The samples were made with a PDF that uses the DGLAP equations formulated at LO precision, since the SMEFT model is also leading order. The name of the data set is NNPDF23_lo_as_0130_qed and validation plots can be found at Ref. [52].

First we generate the gluon-gluon fusion Higgs production along with b-quark pair associated Higgs production (bbH). To do this we restrict any quark from entering the process in the initial state and let jets be defined as an outgoing gluon or quark excluding only the top quark. Leaving only the gluons left in the protons to participate in the production of a single on shell non-boosted Higgs. In order to also include higher order Feynman diagrams jet matching is applied conform the ATLAS recommendations using Pythia8. This ensures the use of the LO approach to produce higher order diagrams without double counting diagrams. We restrict the number of QED vertices that appear in the processes to one. The obtained SM cross section for ggF Higgs production including bbH is

$$\sigma_{ggF} = 45.02 \pm 0.23 pb, \quad (5.1)$$

generated at leading order. When comparing this to the more precise calculations of the LHC cross section working group [11] we find a small deviation of about 6%. Which is also within the limits of the NNLO predictions. During the generation the width of the Higgs is set to auto which makes it a function of the EFT parameters. The CKKW merging is activated using $kt_{durham} = 30$ and a $dparameter = 0.4$. The maximum jet flavour is set to include the bottom quark and no cuts on decay products are applied. The samples in the final reparameterization are generated ignoring the masses of the light quarks, only taking into account the mass of the bottom and top quark.

The obtained SM cross section for the VBF only Higgs production is

$$\sigma_{VBF} = 3.343 \pm 0.0043 pb, \quad (5.2)$$

In the sample generation we explicitly differ between the production, decay and full process. When mentioning production only samples we have generated the sample using the Higgs particle as a final state. Which is later processed with a parton shower using Pythia8. We do this by providing the generation syntax to MadGraph5, we can influence the generation by excluding or including several particles. This can be done by forcing particles to be on/off shell or to prevent particles entering in the hard scattering event. The generation syntax of the production only samples is summarised in Tab. 5.1. The generation syntax of the full process samples is summarised in Tab. 5.2.

ggF	generate p p > h QED = 1 add process p p > h jb QED = 1 add process p p > h jb jb QED = 1
VBF	generate p p > h j j \$\$ w+ w- z QCD = 0

TABLE 5.1: Production only generation syntax

ggF	generate p p > h > e+ mu- ve vm QED = 1 add process p p > h > e- mu+ ve vm QED = 1 add process p p > h > e- mu+ ve vm jb QED = 1 add process p p > h > e+ mu- ve vm jb QED = 1 add process p p > h > e- mu+ ve vm jb jb QED = 1 add process p p > h > e+ mu- ve vm jb jb QED = 1
VBF	generate p p > h > e- mu+ ve vm j j \$\$ w+ w- z QCD = 0 generate p p > h > e+ mu- ve vm j j \$\$ w+ w- z QCD = 0

TABLE 5.2: full process generation syntax

The generation of the widths can be directly assessed by using the syntax in Tab. 5.3 and using the massive SMEFT model.

Decay signature	Madgraph5 simulation syntax
$H \rightarrow e^- \mu^+ \bar{\nu}_e \nu_\mu$	generate h > e- mu+ ve vm
$H \rightarrow e^+ \mu^- \bar{\nu}_\mu \nu_e$	add process h > e+ mu- vm ve

TABLE 5.3: Decay chain syntax of Madgraph5

In the tables above the proton is defined as containing the up, down, charm, strange and bottom quarks as well as gluons. The jets (j) are defined to contain the same particles as the proton excluding the bottom quark. jb allows for b quarks in the final state. The contribution from the possible top quarks in the initial and final state is not significant. The QED and QCD operations allow us to specify the amount of couplings that are allowed to enter in the events.

The raw data obtained are millions of events that needs to be transformed into HepMC data format [51] in order to be read by the Rivet [53] based classification tool. This tool assigns the events to the corresponding STXS region based on the truth level objects in the next section.

5.2 Truth level objects

The samples that are generated are analysed at truth level using the official ATLAS STXS TRUTH decoration [54], [55]. In order to separate the events topology into separate organised chunks we apply a derivation on the raw event data. Because the generated samples of the ATLAS MC software produce a format called EVNT, which contains a wrapped truth record in HepMC format. These formats cannot easily be read by ROOT. Software from ATLAS is used to convert EVNT into a xAOD format which can be read with ROOT. Our samples will be cast into a TRUTH1 format. This is the main truth analysis format and contains a extra containers for specific states, while keeping the main truth record. Which is the mother-daughter information. The jet finding algorithm used is anti- k_t with $R = 0.4$ and a minimum p_T of 20 GeV . Also no W or Z bosons are taking the the jets so no muons or neutrinos are present. The isolated electrons, muons and photons are selected by demanding a status 1, other words a final-state particle. For photons a $p_T > 20 \text{ GeV}$ is demanded. The dressed lepton 4 vectors are used with an isolation cone of $R = 0.1$, while for taus the default dressing uses $R = 0.2$. The other particles are simply found using the HepMC truth information to find the mother-daughter relations and assigning them to the right container. For the samples involved in the reparameterization of the STXS stage 1 scheme only the HepMC truth information is used and the p_T^{jet} is required to be bigger then 30 GeV .

5.3 Normalising a distribution

When a Monte Carlo (MC) sample is generated the size of the sample is determined by requesting the generation of a certain number of events. The cross section of the sample is a fixed quantity dependent on the process generated. Since number of events, sample size, and luminosity are related according to $\sigma = \frac{N_{events}}{L}$, the luminosity of a MC sample varies according to the number of events generated and the cross section of the process. The amount of data collected in an experiment is expressed in terms of luminosity since this quantity can be determined from knowing properties of the colliding beams. In order to perform a simulation of the data at given luminosity, it is necessary to weigh the MC sample to correspond to this luminosity. This allows, for example, to predict the number of top events that will be produced in an amount of data corresponding to that luminosity. The weighting of the MC can be expressed as $N = W_0$, where N is the number of weighted events, N_0 is the number of events in the original sample, and W is the weight. The weight must be a ratio of the desired luminosity to the original luminosity of the sample, $W = L/L_0$. Expressing the original luminosity in terms of cross section and number of events, $W = \frac{\sigma L}{N_0}$. All histograms are weighted by multiplying the quantity used to fill the histogram (N , p_T , η , etc) by the event weight. This is equivalent to scaling the histogram with one single value/weight when only one particular process is filled within a histogram.

Chapter 6

Modelling distributions

In this chapter some modelling techniques and effective Lagrangian morphing are introduced. In section 6.1 some background information is supplied. Section 6.2 covers matrix element reweighing which was almost used in this EFT-interpretation. Section 6.3 introduces effective Lagrangian morphing. This tool is covered in detail since some time was spend updating the package for the current application.

6.1 Modelling techniques

Modelling techniques come in different shapes and forms. The goal is to describe any type of deviations of the underlying theory, be it an effective field theory or otherwise, with the free parameters of that theory. This often has non-trivial and has consequences on the final predictions of that theory. The usual procedure involves a multi-step, resource intensive process.

- The usual Monte Carlo simulation techniques

The generation of

- the Matrix Elements involved in the hard scatter
- the parton-level cross section
- the parton shower and hadronization

The simulation of

- the additional interaction from the same or different bunch crossings
- interactions of the particles with the detector material
- the data acquisition by the detector
- the reconstruction of physical objects used for the analysis

- The samples needed for interpolating

- redoing the steps above for each phase space point needed to fully describe the range of the theory
- interpolating between the different input samples
- creating a likelihood model linking the prediction to the observed values

When taking into account the computational cost it is worthwhile to note that the simulation stage consumes less computing time than the generation stage. Samples, events or particles that have not been processed by the simulation and reconstruction are referred to as "truth", whereas the final physics objects that can be directly compared to

measured data events are referred to as "reconstructed". Most of the computing time in analyses is spent on background estimates. The creation of the dedicated signal samples for such searches is often much less costly. Only when requiring a near continuous description of the phase space spanned by the theory the computing time increases heavily. In that case, the method of likelihood fitting would in principle call for the creation of a dedicated Monte Carlo sample, fully generated and simulated for every parameter point. Taking into account that a likelihood fit of a complicated combined model can easily call for thousands of evaluations, this is unfeasible.

6.2 Matrix element reweighting

A common practice to obtain a large quantity of sampling points in the BSM parameter space is the technique of matrix element reweighting [56]. It is common practice to produce Monte Carlo events with some event weight. These event weights are technical artefacts allowing the Monte Carlo generators to more easily and efficiently sample the phase space by assigning individual points a larger weight than others. While generators like MadGraph5@NLO produce samples with uniform weight at leading order, others can produce large or negative weights. The idea of Matrix Element Reweighting takes this concept one step further. It assumes the weight of each event is proportional to the Matrix Element modulus squared, evaluated at the corresponding phase space point. If one were to change the parameters of the underlying theory, the Matrix element and thus the weight would change accordingly. Because the weight are multiplicative and do not alter any of the observable quantities of the event, they can be applied at any processing stage. Thus, one can reweight an event from the theory parameters it was originally generated for to a different set of theory parameters, using

$$w_o = w_i * \frac{||\mathcal{M}_o^2||}{||\mathcal{M}_i^2||} \quad (6.1)$$

here w_i and w_o stand for the input and output weights of the event, and \mathcal{M}_o and \mathcal{M}_i for the Matrix Elements accordingly. This technique can be applied on readily simulated and reconstructed samples. Thus it provides a efficient way of obtaining simulated signal samples. However, there are some drawbacks to this approach. If the target parameter set is very different from the initial one, the weights of the individual events can become very large. The resulting samples are then effectively dominated by a few high weight samples from the tails of the kinematic distributions, thus reducing the statistical power. Also, all the samples obtained from reweighting the same source sample are statistically dependent. Taking this interdependence into account will in general increase the uncertainty on the prediction.

6.3 Effective Lagrangian morphing

Most analyses find agreement between the Standard Model predictions including the Higgs sector. However, if a significant deviation in signal strength is found in any channel, there must be a methodology on how to construct a quantum field theory that describes the observed data better than the Standard Model. The type of excess or deficit or the change in shape that was observed needs to be analysed carefully to understand its theoretical implications. Using Effective Lagrangian Morphing developed by the ATLAS collaboration, in [4], we provide an EFT interpretation of possible deviations in the Higgs and non-Higgs sector.

When employing this technique for a tree level calculation of a $2 \rightarrow 2$ s-channel process like the production and decay of a Higgs boson at the LHC at leading order, the cross section prediction can be expressed as

$$\sigma(\vec{g}) = \vec{P}(\vec{g}) * A * \sigma(\vec{g}) \quad (6.2)$$

Here $\vec{P}(\vec{g})$ is a vector of fourth-order polynomials in the couplings g , $\sigma(\vec{g})$ is a vector of precomputed cross sections at the input parameter points, and A is the inverted morphing matrix. Additional coupling parameters in the Higgs sector change the predicted cross section as well as the shape of the differential distributions. Effective Lagrangian morphing provides a continuous description of arbitrary physical signal observables such as cross sections or differential distributions in a multidimensional space of coupling parameters. Using this technique, ATLAS aims to have signal models which depend on a large number of coupling parameters. The morphing based signal is a linear combination of a minimal set of orthogonal base samples spanning the full coupling parameter space. The weight of each sample (template) is based on the beyond the Standard Model (BSM) theory in question.

6.3.1 Morphing with one BSM coupling parameter in either the production or decay vertex

As the simplest case, a morphing function is determined with only one BSM (non-SM) Higgs coupling, namely g_{BSM} , contributing to either the production or decay in addition to the SM Higgs boson coupling g_{SM} . The matrix element of such a scenario for given values of g_{SM} and g_{BSM} can be written as the sum of the pure SM and the pure BSM contribution to the matrix element times some scaling coefficient c_i .

$$M(g_{SM}, g_{BSM}) = g_{SM}O_{SM} + c_i g_{BSM}O_{BSM} \quad (6.3)$$

This then translates into the description of a physical observable T from the above process,

$$|M(g_{SM}, g_{BSM})|^2 = g_{SM}^2 |O_{SM}|^2 + c_i^2 g_{BSM}^2 |O_{BSM}|^2 + 2c_i g_{SM} g_{BSM} \Re(O_{SM}O_{BSM}) \quad (6.4)$$

$$T(g_{SM}, g_{BSM}) \propto |M(g_{SM}, g_{BSM})|^2 \quad (6.5)$$

The physical observable T can be used to morph to an arbitrary parameter point. The number of input distributions required to morph to a parameter point $g_{target} = (g_{SM}, g_{BSM})$ is equal to the number of unique terms in the matrix element squared, which in this case is three. It is sufficient to generate a pure SM distribution $T_{SM}(1, 0)$, a pure BSM distribution $T_{BSM}(0, 1)$ and a mixed distribution $T_{mixed}(1, 1)$.

$$\begin{aligned} T_{SM}(1, 0) &= |O_{SM}|^2 \\ T_{BSM}(0, 1) &= c_i^2 |O_{BSM}|^2 \\ T_{mixed}(1, 1) &= g_{SM}^2 |O_{SM}|^2 + c_i^2 g_{BSM}^2 |O_{BSM}|^2 + 2c_i g_{SM} g_{BSM} \Re(O_{SM}O_{BSM}) \end{aligned} \quad (6.6)$$

Applying these three equations to the equation computing the matrix element squared results in the morphing function for a distribution at an arbitrary parameter point.

$$\begin{aligned} T_{out}(g_{SM}, g_{BSM}) &= (g_{SM}^2 - c_i g_{SM} g_{BSM}) T_{SM}(1, 0) + (c_i^2 g_{BSM}^2 - c_i g_{SM} g_{BSM}) T_{BSM}(0, 1) \\ &\quad + c_i g_{SM} g_{BSM} T_{mixed}(1, 1) \end{aligned} \quad (6.7)$$

The output distribution can be created by only three input distributions multiplied by the appropriate weight factor w_i . Since fixed parameters for the input distributions were used, the weights only depend on the desired parameters for the output distribution. To be able to minimise statistical uncertainty in the parameter space, it is favourable to be flexible in choosing the parameters for the input distributions. In order to develop a generalisation for a morphing function with arbitrary input parameters \vec{g}_i , the proportionality to the matrix element squared of the three input distributions can be written in the following way

$$T_{in}(g_{SM,i}, g_{BSM,i}) = g_{SM,i}^2 |O_{SM}|^2 + c_i^2 g_{BSM,i}^2 |O_{BSM}|^2 + 2c_i g_{SM,i} g_{BSM,i} \Re(O_{SM} O_{BSM}) \quad (6.8)$$

with $i = 1, 2, 3$. Now, the following Ansatz can be made for the morphing function. We introduce the unknown variables a_{ij} and demand that the morphing function should regain the input distribution for any of the input parameters $T_{out} = T_{in}$ for $\vec{g}_{target} = \vec{g}_i$.

$$\begin{aligned} T_{out}(g_{SM}, g_{BSM}) &= (a_{11} g_{SM}^2 + a_{12} g_{BSM}^2 + a_{13} g_{SM} g_{BSM}) T_{in}(g_{SM,1}, g_{BSM,1}) \\ &+ (a_{21} g_{SM}^2 + a_{22} g_{BSM}^2 + a_{23} g_{SM} g_{BSM}) T_{in}(g_{SM,2}, g_{BSM,2}) \\ &+ (a_{31} g_{SM}^2 + a_{32} g_{BSM}^2 + a_{33} g_{SM} g_{BSM}) T_{in}(g_{SM,3}, g_{BSM,3}) \end{aligned} \quad (6.9)$$

This in turn results in exactly the right number of constraints needed to recover the unknown variables a_{ij}

$$\begin{aligned} 1 &= a_{11} g_{SM}^2 + a_{12} g_{BSM}^2 + a_{13} g_{SM} g_{BSM} \\ 0 &= a_{21} g_{SM}^2 + a_{22} g_{BSM}^2 + a_{23} g_{SM} g_{BSM} \\ &\dots \end{aligned} \quad (6.10)$$

All constraints can be written in a compact matrix form

$$A * G = \mathbb{1} \quad (6.11)$$

$$\begin{bmatrix} a_{11} & a_{12} & a_{13} \\ a_{21} & a_{22} & a_{23} \\ a_{31} & a_{32} & a_{33} \end{bmatrix} * \begin{bmatrix} g_{SM,1}^2 & g_{SM,2}^2 & g_{SM,3}^2 \\ g_{BSM,1}^2 & g_{BSM,2}^2 & g_{BSM,3}^2 \\ g_{SM,1}, g_{BSM,1} & g_{SM,2}, g_{BSM,2} & g_{SM,3}, g_{BSM,3} \end{bmatrix} = \mathbb{1} \quad (6.12)$$

The unique solution $A = G^{-1}$ requires the input parameters to fulfil the condition $\det(G) \neq 0$.

It is useful to extend this formalism to an example with a BSM coupling entering both in production and decay. In, for example, the VBF Higgs boson production with a decay to two vector bosons, the same coupling appears in the production and decay vertex. Having this BSM parameter enter several adjustments to the morphing have to be made. Again the matrix element squared can be factorised in the following way, assuming that the Narrow Width Approximation (NWA) holds. The NWA should not be used everywhere, for an explanation see Appendix. [G](#).

$$M(g_{SM}, g_{BSM}) = (g_{SM} O_{SM,p} + c_i g_{BSM} O_{BSM,p})(g_{SM} O_{SM,d} + c_i g_{BSM} O_{BSM,d}) \quad (6.13)$$

$$\begin{aligned}
|M(g_{SM}, g_{BSM})|^2 &= (g_{SM}O_{SM,p} + c_i g_{BSM}O_{BSM,p})^2 (g_{SM}O_{SM,d} + c_i g_{BSM}O_{BSM,d})^2 \\
&= g_{SM}^4 O_{SM,p}^2 O_{SM,d}^2 + c_i^4 g_{BSM}^4 O_{BSM,p}^2 O_{BSM,d}^2 \\
&\quad + c_i g_{SM}^3 g_{BSM} (O_{SM,p}^2 \Re(O_{SM,d}^* O_{BSM,d}) + \Re(O_{SM,p}^* O_{BSM,p}) O_{SM,d}^2) \\
&\quad + c_i^2 g_{SM}^2 g_{BSM}^2 (O_{SM,p}^2 O_{BSM,d}^2 + O_{BSM,p}^2 O_{SM,d}^2) \\
&\quad + c_i^3 g_{SM} g_{BSM}^3 (O_{BSM,p}^2 \Re(O_{SM,d}^* O_{BSM,d}) + \Re(O_{SM,p}^* O_{BSM,p}) O_{BSM,d}^2)
\end{aligned} \tag{6.14}$$

The matrix element now is a 4th order polynomial in the coupling parameters g . Each unique term in coupling parameters requires an input distribution for the morphing, which results in 5 different samples for this scenario. The morphing function for arbitrary values of g_{SM} and g_{BSM} for the input distributions is obtained again by inverting the morphing matrix. Again the input distributions are proportional to the matrix element squared.

$$T_{in}(g_{SM,i} g_{BSM,i}) \propto |M(g_{SM}, g_{BSM})|^2, i = 1, \dots, 5 \tag{6.15}$$

The same Ansatz is used for this morphing function. The input functions should equal the output if the parameters are equal. Requiring that the output distribution reproduces the input distributions at their respective parameters, constraints can be set to calculate the unknown variables a_{ij} . In matrix form, the constraints can be written as in the example above.

6.3.2 Generalisation to higher-dimensional parameter space

The case of a morphing function with an arbitrary number of BSM coupling parameters in two vertices requires generalisation. This consists of first constructing a general matrix element squared.

$$|M(\vec{g})|^2 = \left(\sum_{x \in p,b} g_x O(g_x) \right)^2 * \left(\sum_{x \in d,b} g_x O(g_x) \right)^2 \tag{6.16}$$

Then expand the matrix element squared to a 4th degree polynomial in the coupling parameters

$$|M(\vec{g})|^2 = \sum_{i=1}^N X_i * P_i(\vec{g}) \tag{6.17}$$

Here X_i is a prefactor. It will be represented by an input distribution. In the polynomial $P_i(\vec{g}) = g_a g_b g_c g_d$ of the coupling parameters \vec{g} , the same coupling can occur multiple times (namely g_{SM}^4 or $g_{BSM,1}^2 g_{BSM,2} g_{BSM,3}$). The number of different expressions in the polynomial N is equal to the number of samples needed for the morphing.

Generate the input distributions at arbitrary fixed parameter points \vec{g}_i

$$T_{in,i} \propto |M(\vec{g}_i)|^2 \tag{6.18}$$

Construct the morphing function with the usual Ansatz

$$\begin{aligned}
T_{out}(\vec{g}) &= \sum_{i=1}^N * \left(\sum_{j=1}^N A_{ij} P_j(\vec{g}) \right) T_{in,i} \\
&= \vec{P}(\vec{g}) * A \vec{T}
\end{aligned} \tag{6.19}$$

Now exploiting the fact that the output distribution should be equal to the input distribution at the respective input parameters

$$T_{out}(\vec{g}_i) = T_{in,i} \text{ for } i = 1, \dots, N \tag{6.20}$$

And in matrix notation as

$$A * (P_j(\vec{g}_i))_{ij} = \mathbb{1} \tag{6.21}$$

The unique solution $A = P_j(\vec{g}_i)_{ij}^{-1}$ requires the input parameters to fulfil the condition $\det(G) \neq 0$.

Notice, the number of base samples increases if there are additional coupling parameters to be considered in the production or decay vertex. For example, in the case of combination of measurements in several production and decay modes. The general morphing principle remains the same and the method can be generalised to a higher-dimensional coupling parameter space. The number N of input template samples depends on how many of the n studied coupling parameters enter in the production or decay vertex. This both depends on how much the production and decay operator sets are disjoint. A general expression for the number of samples required as function of n_p couplings appearing only in production, n_d couplings appearing only in decay and n_s couplings shared in production and decay is

$$\begin{aligned}
N &= \frac{n_p(n_p+1)}{2} * \frac{n_d(n_d+1)}{2} + \binom{4+n_s-1}{4} \\
&+ \left(n_p * n_s + \frac{n_s(n_s+1)}{2} \right) * \frac{n_d(n_d+1)}{2} \\
&+ \left(n_d * n_s + \frac{n_s(n_s+1)}{2} \right) * \frac{n_p(n_p+1)}{2} \\
&+ \frac{n_s(n_s+1)}{2} * n_p * n_d + (n_p + n_d) \binom{3+n_s-1}{3}
\end{aligned} \tag{6.22}$$

6.3.3 Validation

In order to check if the analytical Lagrangian morphing in combination with separate LO tree interference samples works, several have been produced for this validation. The samples are produced with showering and hadronization through Pythia8 and matrix element calculation with Madgraph5, not including detector effects. Samples from LO gluon fusion Higgs production decaying into a muon and an electron have through the decay of the Higgs boson into two charged vector bosons, see Fig. 6.1. The SMEFT model has been used for a BSM framework and the PDF used is LO NNPDF23 set. Several distributions sensitive the BSM couplings are used for the validation which are also used in the STXS interpretation. This validation also serves as a way of showing how the other signal samples are produced in this research. The samples used in the validation are shown in Tab. 6.1.

Morphing Input samples	σ_{SM} contribution (pb)	$\sigma_{\frac{1}{\Lambda^2}}$ contribution (pb)	$\sigma_{\frac{1}{\Lambda^4}}$ contribution (pb)	$c_i = 0.1$
Morphing sample 1	0.08762	-	-	-
Morphing sample 2	-	0.001065	-	c_{Hbox}
Morphing sample 3	-	-	3.224×10^{-6}	c_{Hbox}
Morphing sample 4	-	0.316	-	c_{HG}
Morphing sample 5	-	-	0.2846	c_{HG}
Morphing sample 6	-	-7.97×10^{-4}	-	c_{HW}
Morphing sample 7	-	-	2.939×10^{-6}	c_{HW}
Validation samples	σ_{tot}	c_i	nominal value	
validation sample 1	0.089	c_{Hbox}	0.1	
validation sample 2	0.68	c_{HG}	0.1	
validation sample 3	0.087	c_{HW}	0.1	
validation sample 4	0.09903	c_{Hbox}	1.0	
validation sample 5	8.786	c_{HG}	0.5	
validation sample 6	0.087	c_{HW}	1.0	
validation sample 5	0.09118	c_{HG}	0.01	
validation sample 6	0.07314	c_{HW}	2.0	

TABLE 6.1: Overview of the samples used in the morphing validation study.

A quick and way to check the validity of the interference samples is the addition of the cross sections. The cross section of the interference samples plus the Standard model sample should equal the cross section of the validation sample with equal Wilson coefficient value. When looking at the coefficient value of 0.1 the cross section indeed add up to each other. Conforming the use and implication of the narrow width approximation. This shows that the rate can indeed be used to interpolate between Wilson coefficients. To confirm this for shape effects we need to look at the distributions of the observables. The distribution used are the total transverse mass m_T , the electron transverse momentum p_T , the difference of the pseudo rapidity between the leptons Δ_{ll} , the invariant mass of the leptons m_{ll} and the Higgs transverse momentum p_T^H . The BSM coupling c_{HG} is used, which is affecting the Higgs production, and the couplings c_{HW} and c_{Hbox} are used, which affect the Higgs decay.

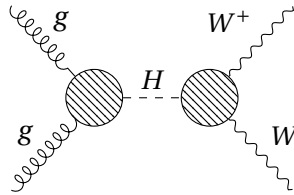


FIGURE 6.1: Gluon fusion Higgs production, EFT operator c_{HG} influencing the right production vertex and c_{HW}, c_{Hbox} influencing the right decay vertex.

All generated samples consist of 50.000 Monte Carlo events each. The statistical uncertainty arising from the morphing function on the number of events is also displayed in the plots. All of the input distributions are scaled to their respective number of events and cross section, as well as the validation samples. The validation of the morphing using interference samples is confirmed and seen in the distributions of Fig. 6.2, requiring that they agree with each other within the statistical uncertainty of the morphing. Additional plots can be found in Appendix E.

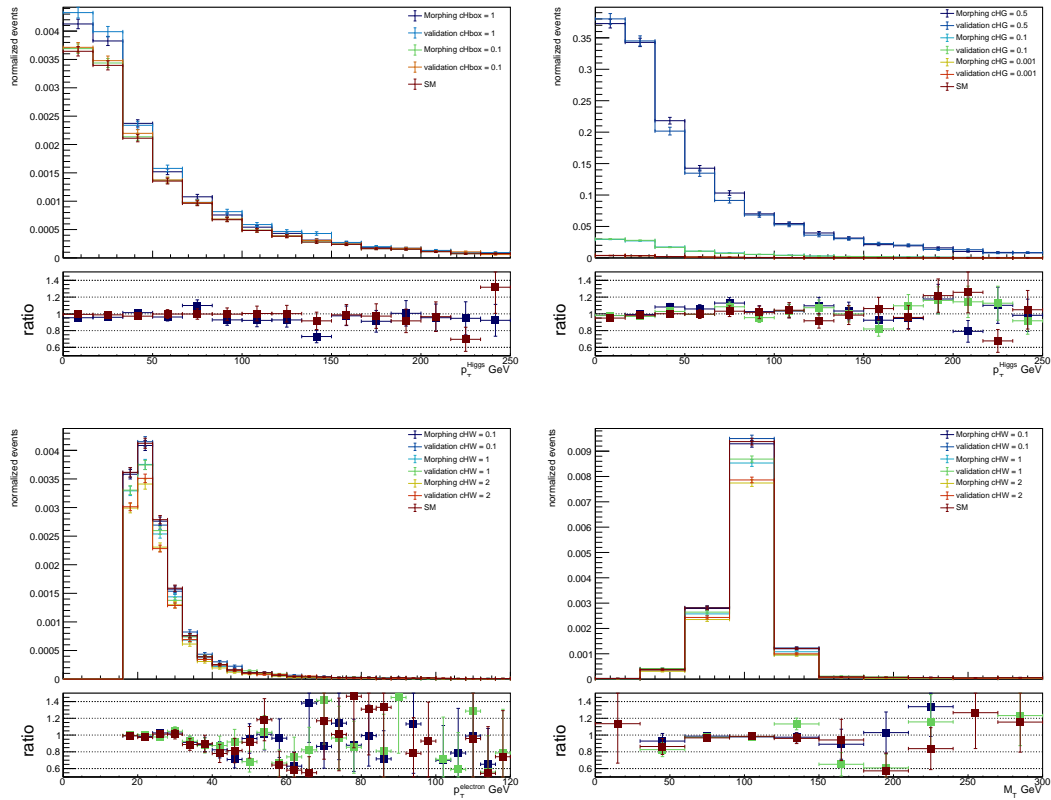


FIGURE 6.2: Several morphed and validation distributions plotted together to show the validity of the morphing approach. Top-left: c_{Hbox} influenced distribution of p_T^H . Top-right c_{HG} influenced distribution of p_T^H . Bottom-left c_{HW} influenced distribution of p_T^e . Bottom-right c_{HW} influenced distribution of M_T .

Chapter 7

Simplified Template Cross Sections

In Chapter 7 the STXS framework is introduced and plays a central role in this study. Section 7.1 will provide the ideas behind the framework and the basics of how its implemented into the measurement. Section 7.2 and 7.3 will cover the cuts made during the STXS interpretation of our measurements.

7.1 The STXS framework

Simplified template cross sections [5] are developed to provide a way to evolve the signal strength measurements. The STXS procedure allows to, in streamlined methodology, reduce the theory dependencies of any measurement. This includes the dependence on the underlying physics model, which may be SM or BSM models. In addition, they provide more finely-grained measurements in all decay channels to allow for an EFT interpretation.

Additional goals of the simplified template cross section framework is to maximise the sensitivity of the measurements while at the same time to minimise their theory dependence. This results in

- combination of all decay channels
- measurement of cross sections instead of signal strengths, in exclusive regions of phase space
- cross sections are measured for specific production modes
- measurements are performed in simplified volumes
- allow the use of advanced analysis techniques such as event categorisation, multivariate techniques, etc.

The measured exclusive regions of phase space, which can be called bins for simplicity, are specific to the different production modes. Their definitions are motivated by

- minimising the dependence on theoretical dependencies
- maximising experimental sensitivity
- isolation of possible BSM effects
- minimising the number of bins without loss of experimental sensitivity

In the Fig. 7.1 a schematic overview of the STXS framework is shown. The experimental analyses shown on the left are all unique in the way they select their event candidates and also how they extract signal strength from the data. Making use of each specific channel topology to distinguish them from the background. Typically, a subset of the experimental event categories is defined to increase their expected signal-to-background ratio. The long term idea behind STXS is to combine analyses into a global fit that combines all decay channels and represent the main results of the experimental measurements.

In this study we will focus on the EFT coefficients interpretation. For this purpose, the experimental results should quote the full covariance among the different bins in order to disentangle correlations between operators.

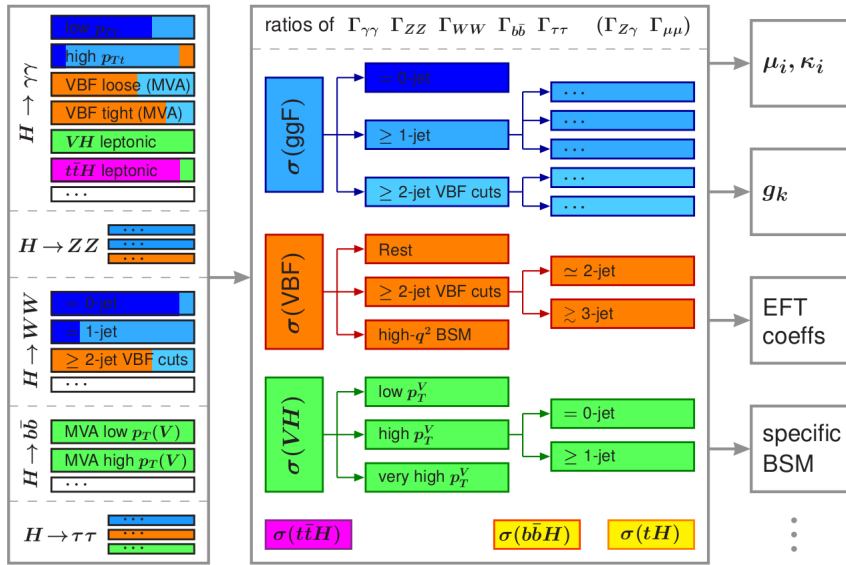


FIGURE 7.1: Schematic overview of the simplified template cross section framework

A requirement of the measurements is to extrapolate from a certain region in phase space to the full region. To maximise experimental sensitivity, the analysis should continue to use event categories optimised for sensitivity, while the truth bins should take into consideration the experimental requirements for the event selection. Another design goal is to isolate regions of phase space, typically at large kinematic scales, where BSM effects could potentially be large and visible above the SM background.

The implementation of the STXS truth binning in the analysis is realised by expressing the number of signal events in a particular reconstruction category r . The number of reconstructed signal events can be expressed as the sum of each STXS truth bin t .

$$n_r = \sum_t \epsilon_{tr}^{SM} L \cdot Br^{SM} \cdot \sigma_t^{SM} \cdot \mu_t \quad (7.1)$$

In this expression ϵ_{tr}^{SM} is the efficiency of the STXS truth bin as predicted by the SM. defined as

$$\epsilon_{tr}^{SM} = \frac{n_{tr}^{SM}}{n_t^{SM}} \quad (7.2)$$

Where n_{tr}^{SM} is the number of reconstructed events entering the STXS bin t and n_t^{SM} the number of truth events entering the STXS bin t . L is the luminosity, Br^{SM} is the SM predicted branching ratio and σ_t^{SM} the cross section in bin t . μ_t is the signal strength of the STXS bin t . By taking account of the efficiencies for the STXS bin and correcting for them the signal strength μ_t . μ_t is extrapolated for the entire fiducial region t and quote a inclusive signal strength. By using these efficiencies the STXS implementation is assumed to not be affected by any acceptance effects induced by cuts used in any particular analysis.

7.2 Splitting production modes

There is distinction between $q\bar{q} \rightarrow VH$ and VBF processes, and similarly between $gg \rightarrow VH$ and gluon-gluon fusion production. In the STXS framework, the VH production mode is explicitly defined as Higgs production in association with a leptonically decaying V boson. The $q\bar{q} \rightarrow VH$ process with a hadronically decaying V boson is considered to be part of the VBF production, which is defined as electroweak qqH production. Additionally, the $gg \rightarrow ZH$ process with hadronically decaying Z boson is included in what is called gluon-fusion production. However, in our analysis the VH is not taken into account as they are separately split into STXS bins and included as backgrounds.

7.3 Staging

In practice, it will be impossible to define a set of bins that satisfies all of the above requirements for every analysis. Some analyses will only be able to constrain a subset of all bins or only constrain the sum of a set of bins. When the amount of data increases. So does the possible amount of STXS bins that can be constrained. For this reason, several stages with an increasing number of bins are defined.

Stage 0 is summarised in Fig. 7.2. In this stage, each main production mode has a single inclusive bin, with the associated Higgs production separated into $q\bar{q} \rightarrow WH$, $q\bar{q} \rightarrow ZH$ and $gg \rightarrow ZH$ channels. VBF production is defined as electroweak qqH production.

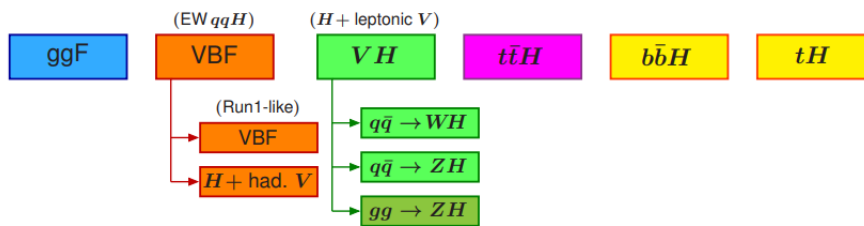


FIGURE 7.2: Stage 0 bins.

Stage 1 is used during the measurement in this research and by the HWW measurement which will be introduced in chapter 9. It defines a binning that is targeted to be used by all analyses in the future. In the diagrams below, the possibilities for merging bins are indicated by a plus sign. At the point of writing this thesis, only the ggF and VBF STXS binning of the measurements have been done. These are the ones that we will consider. I will gradually go over the different cuts and assumptions made during the binning of both production modes.

7.3.1 Gluon fusion Higgs production

At this point, the STXS implementation does not cover the bbH and tH processes.. Right now the bbH contribution is merged with the ggF process and is subject to the same binning. Practically bbH is assumed to be 1% of the ggF contribution.

In stage 0 all the gluon fusion events are contained into a single bin within $|Y_H| < 2.5$. When the measurements start to have an acceptance beyond 2.5, an additional bin for $|Y_H| > 2.5$ can be included.

Stage 1

- Split into jet bins: $N_j = 0, N_j = 1, N_j \geq 2, N_j \geq 2$ with VBF topology cuts. These cuts are defined the same way as the corresponding bin in VBF production. For the $N_j \geq 2$ with VBF topology cuts, $p_T^H < 200\text{GeV}$ is required, which gives priority to the $p_T^H > 200\text{GeV}$ bin for $N_j \geq 2$. The jet bins are motivated by the use of jet bins in the experimental analysis.
- The $N_j \geq 2$ with VBF topology bin is split further into an exclusive 2-jet-like and inclusive 3-jet-like bin. The split is implemented by a cut on $p_T^{Hjj} = \left| \vec{p}_T^H + \vec{p}_T^j + \vec{p}_T^j \right|$ at 25 GeV .
- The $N_j = 1$ and $N_j \geq 2$ bins are further split into p_T^H bins.
 - $0\text{GeV} < p_T^H < 60\text{GeV}$: The vector boson channels have most sensitivity in the low p_T^H region. The upper cut is chosen as low as possible to give a more even split of events but at the same time high enough that no resummation effects are expected.
 - $60\text{GeV} < p_T^H < 120\text{GeV}$: This is the resulting intermediate bin between the low and high p_T^H region. The lower cut here is high enough that it can be treated as a hard $H + j$ system in the theoretical description
 - $120\text{GeV} < p_T^H < 200\text{GeV}$: The boosted selection in $H \rightarrow \tau\tau$ contributes to the high p_T^H region. Defining a separate bin avoids large extrapolations for the $H \rightarrow \tau\tau$ contribution. For $N_j = 2$, this bin likely provides a substantial part of the gluon-fusion contribution in the hadronic VH selection.
 - $p_T^H > 200\text{GeV}$: Beyond the top-quark mass, the top-quark loop gets resolved and its mass effects become relevant. Splitting off the high- p_T^H region ensures the usability of the heavy-top expansion for the lower- p_T^H bins. At the same time, the high p_T^H bin in principle offers the possibility to distinguish a point like ggH vertex induced by heavier BSM particles in the loop from the resolved top-quark loop.

At the intermediate stages, all of the lower three p_T^H bins, or any two adjacent bins can be merged. Also $N_j = 1$ and $N_j \geq 2$ bins can be merged by individual analyses as needed, and potentially also when the combination is performed at an intermediate stage. The ggF cuts in stage 1 are depicted in Fig. 7.3.

7.3.2 Vector boson fusion Higgs production

Stage 0 has an inclusive vector boson fusion cross section within $|Y_H| < 2.5$. Should measurements start to have acceptance beyond 2.5, an additional bin for $|Y_H| > 2.5$ can be included.

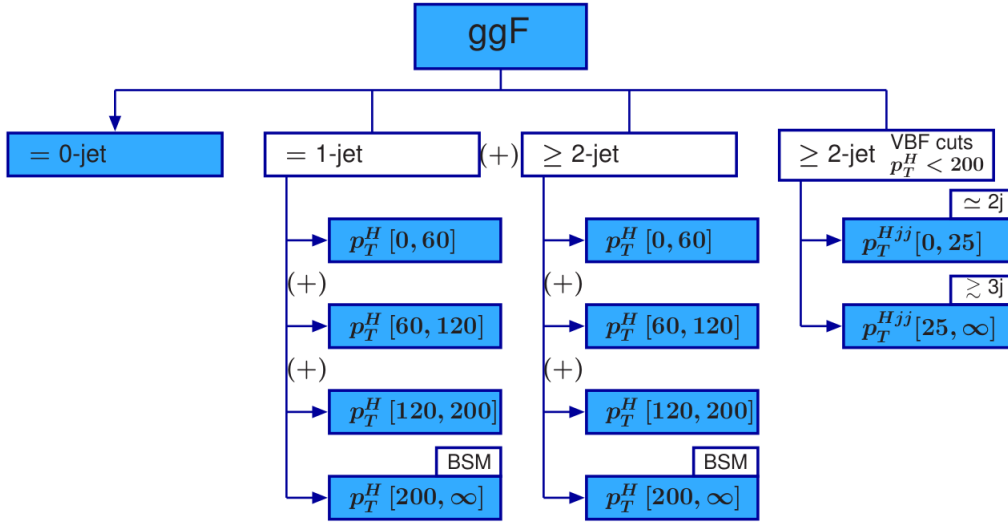


FIGURE 7.3: Stage 1 binning for gluon fusion production [5].

Stage 1

Stage 1 refines the binning for $|Y_H| < 2.5$.

- VBF events are split by p_T^{j1} , the transverse momentum of the highest p_T jet. the lower p_T^{j1} region is expected to be dominated by SM-like events, while the high- p_T^{j1} region is sensitive to potential BSM contributions, including events with typical VBF topology. The suggested cut is at 200 GeV , to keep the fraction of SM events in the BSM small.
- The $p_T^{j1} < 200 \text{ GeV}$ bin is split further
 - Typical VBF topology: the adopted VBF topology cuts are $m_{jj} > 400 \text{ GeV}$, $\Delta\eta_{jj} > 2.8$. Which is a compromise among the various VBF selection cuts employed by different channels.
 - * The bin with typical VBF topology is split into an exclusive 2-jet-like and inclusive 3-jet-like bin using a cut on p_T^{Hjj} at 25 GeV , where the cut value is a compromise between providing a good separation of gluon fusion and VBF and the selections used in the measurements. p_T^{Hjj} as quantity to define this split is chosen as a compromise between the different kinematic variables used by the different channels to enrich VBF production
 - Typical $V(\rightarrow jj)H$ topology: events with at least two jets and $60 \text{ GeV} < m_{jj} < 120 \text{ GeV}$.
 - Rest: all remaining events, including events with zero or one jet. The "rest" bin can be sensitive to certain BSM contributions that do not follow the typical SM VBF signature with two forward jets

The VBF cuts in stage 1 are depicted in Fig. 7.4.

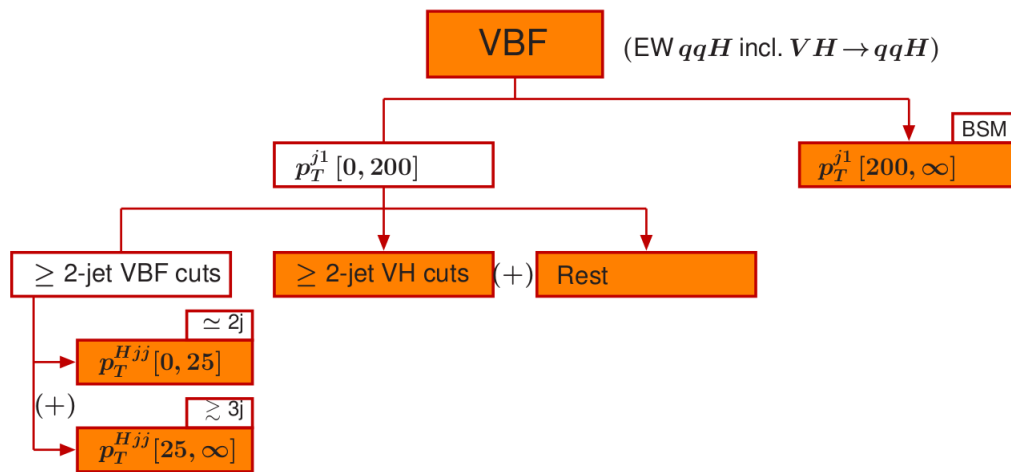


FIGURE 7.4: Stage 1 binning for Vector Boson fusion production [5].

Chapter 8

Statistics

In this chapter we will touch upon the statistical methods, tools and theory that are used in this research. Since high energy physics relies on a SM hypothesis we have to statistically convince ourselves and the public that new physics is observed and not just a statistical anomaly. The complexity of the detector and the theoretical models suffer from large systematic errors that have to be taken care of in a correct way. Section 8.1 will introduce some essential terminology. Sections 8.2-8.5 will introduce the tools used in the interpretation.

8.1 Terminology

First, we introduce some essential terminology. The expected signal and background are determined by the corresponding cross section σ , the luminosity L given by the accelerator and the detector response/efficiency ϵ . The signal is given by $s = L \cdot \sigma \cdot \epsilon$ [57]. when assuming a counting experiment and n is the number of observed events then we can define

$$n = \mu \cdot s + b, \quad (8.1)$$

where b is the expected background and μ is a signal strength given by $\mu = \frac{N_{\text{Observed}}}{N_{\text{Expected}}}$. There are two hypotheses. One with a strength $\mu = 1$ on top of the background and one where the signal $\mu \neq 1$. When we are measuring the signal that we are expecting we observe a signal strength of 1. Any deviation from this can be seen as a deviation from the expected hypothesis.

8.2 Data versus theory

The data collected at the LHC is analysed and used to test several different theories. The theory provides an expected distribution for different physical observables. These distributions are compared to data and the probability, $P(O)$, conditional probability of finding the measured data given the theory observable that can be measured. The measured probability is called the likelihood,

$$L(H_0) = \text{Prob}(\text{data}|H_0). \quad (8.2)$$

Where H_0 is the hypothesis. There are many ways to test a theory. One of the most common ways is the Profile Likelihood approach. During this work we will use the Profile Likelihood method. By using an interpolation algorithm that morphs the shape of the distribution from $H(-1\sigma)$ to $H(\text{nominal})$ to $H(+1\sigma)$ controlled by additional so called nuisance parameters θ . In this method the likelihood ratio is used as a test statistic as a

function of the parameters of interest such as the signal strength. The nuisance parameters are denoted by θ . The Likelihood is a function of the parameter of interest, in our case μ , and the nuisance parameters. The procedure for statistical computations used the profile likelihood ratio test statistic \tilde{q}_μ .

First the profile likelihood ratio [58] is defined as

$$\begin{aligned}\tilde{\lambda}(\mu) &= \frac{L(\mu, \hat{\hat{\theta}}(\mu))}{L(\hat{\mu}, \hat{\theta})}, \mu \geq 0 \\ &= \frac{L(\mu, \hat{\hat{\theta}}(\mu))}{L(0, \hat{\theta}(0))}, \mu < 0\end{aligned}\quad (8.3)$$

A hat stands for the MLE (Maximum Likelihood Estimator) while a double hat is the constrained MLE. Hence the MLE of θ , while fixing μ . When testing a Hypothesis H_μ the Profile Likelihood test statistic in the presence of nuisance parameters becomes,

$$\begin{aligned}q_\mu &= -2 \ln \frac{L(\mu, \hat{\hat{\theta}}(\mu))}{L(0, \hat{\theta}(0))}, \hat{\mu} < 0 \\ &= -2 \ln \frac{L(\mu, \hat{\hat{\theta}}(\mu))}{L(\hat{\mu}, \hat{\theta})}, 0 \leq \hat{\mu} \leq \mu \\ &= 0, \hat{\mu} > \mu\end{aligned}\quad (8.4)$$

When the test statistic is minimised this is taken as the most probable solution to the fit. The method RooFit uses is the modified frequentist method CLs and computes the 68% *C.L.* intervals on the parameter of interest. In the case of the signal strength measurements, the signal strength is two sided with the constraint $0 \leq \hat{\mu} \leq \mu$. The compatibility of the hypothesis is expressed in the p-value, the probability to observe the signal as the observed data suggests. This is calculated as

$$p = \int_{q_\mu}^{\infty} f(q_\mu) dq_\mu. \quad (8.5)$$

This p-value can then be translated into a significance, Z , of the signal. This is defined as the number of standard deviations corresponding to the p-value. If the distribution of q_μ is independent of μ which is asymptotically the case, an interval of the parameter of interest is constructed for which q_μ is exactly equal to the value of the stated confidence level. The MINUIT [6] package and the MINOS procedure is designed to find the intervals according to this concept.

The experimental uncertainties in this analysis are estimated by varying the value of the object with $\pm\sigma$ variations and define the variations of the parameter of interest as systematic uncertainty. The theoretical uncertainties are treated the same way. The pull of such a nuisance parameter θ , with an expectation θ_0 is defined as,

$$pull(\theta) = \frac{\hat{\theta} - \theta_0}{\sigma_\theta}. \quad (8.6)$$

This pull is important since it quantifies how much from its expected value the fit had to pull the parameter while finding the MLE. In a perfect world the pull average is zero with a standard deviation close to 1, if this is not the case, further investigation is required. A

sigma of 1 is where the input uncertainty is assumed. A sigma of bigger than 1 should not exist indicates underlying problems such as failed fits. Parameters which have a 1 sigma value of less than 1 represent profile parameter for which the fit to data has sufficient sensitivity to the systematic uncertainty that it can constrain the allowed variations of the corresponding nuisance parameter.

8.3 The measurements supplied in a RooWorkspace

The fits performed in this thesis were all made using the RooFit library. This library provides a toolkit for modeling the expected distribution of events in physics analysis. These distributions are called probability density functions. The PDFs are then fitted to data sets to obtain the MLE. The workspaces are provided in the RooWorkspace format and contain the full statistical procedure of the measurements. This format contained

- The PDF, which is often a composite of multiple PDFs. The single PDFs are applied to their respective signal region or control region and then combined to form one singular likelihood function
- The nuisance parameters, the parameters that are used to estimate the systematic uncertainties on the measurement. These parameters contain the estimated value as well as the shape and form based on the data to be fitted
- The Global Observables, these values are associated with auxiliary measurements. This value is held constant at some particular value since it is observed elsewhere.
- The data set, this object contains the distributions our PDF will fit to. These are often the signal regions and the control regions after all the event cuts and selections have been applied.
- The parameters of interest, these are parameters that are to be evaluated based on the data and all of the systematic uncertainties.

The Global observable are often used to reduce the effect of systematic uncertainties. The likelihood in the HWW analysis is defined as

$$\mathcal{L}(\mu, \mu_b) = P(N|\mu s + \mu_b b_{SR}^{exp}) \times P(M|\mu_b b_{CR}^{exp}) \quad (8.7)$$

where b_{SR}^{exp} and b_{CR}^{exp} are expected background yields in the signal and control region, μ is the signal strength parameter and μ_b is the background strength parameter. The nuisance parameters are added by multiplying the likelihood function with

$$\prod_{i=1}^{N_\theta} N(\tilde{\theta}, \theta). \quad (8.8)$$

Where θ is the nuisance parameter. Consider a constraint $N(\tilde{\theta}, \theta)$ representing a global observable $N(\tilde{\theta}, \theta)$ related to the nuisance parameter θ . Two cases are used in the analyses, a Gaussian constraint

$$G(\tilde{\theta}|\theta, 1) = \frac{1}{\sqrt{2\pi}} e^{-\frac{(\tilde{\theta}-\theta)^2}{2}} \quad (8.9)$$

or a Poissonian constraint

$$P(\tilde{\theta}|\theta, \lambda) = \frac{(\theta\lambda)^{\tilde{\theta}} e^{-\theta\lambda}}{\tilde{\theta}!} \quad (8.10)$$

Here λ is taken as the nominal value of $\tilde{\theta}$. This likelihood function is then expanded by taking the product over all of the signal regions. Now the signal and background are functions of the nuisance parameters. Then the likelihood is maximised using the test statistic above.

8.4 The Asimov data set

It is useful to quantify the sensitivity of an experiment by reporting the expected significance one would obtain with a given measurement under the assumption of different hypothesis. For example, in the SM there is only one Higgs boson with well defined couplings. Hence, one knows what to search for. If going beyond the standard model you face a multidimensional parameter space where the Higgs boson couplings and its production cross section varies as a function of these parameters. The Asimov dataset delivers a median sensitivity. This dataset is constructed such that when one uses it to evaluate the estimators of all parameters, you obtain the true parameter values [59]. This median can be used to estimate your actual sensitivity on unbiased real data.

8.5 Poisson counting experiments

When fitting a binned data set each bin is a mini Poisson counting experiment where the observable x corresponds to the observed count n in a given selection of collision events. The likelihood for this analysis is given by the Poisson distribution,

$$L(\text{count}|H_0) = \text{Poisson}(n|\nu). \quad (8.11)$$

Here ν is the expected count. Since at the LHC we measure distributions of the collision events because of their stochastic nature we would like to model these observables with a continuous analytical formula. However, these formulas to this day are not known. Therefore, the distributions are modelled using Monte Carlo simulations and then expressed in histograms. Since a histogram is again a counting experiment the probability for binned data sets in a continuous observable can be expressed as a product of Poisson distributions, one Poisson distribution for each bin.

$$L(x|H) = \prod_{i=1}^n \text{Poisson}(n_i|\nu_i) \quad (8.12)$$

All of the uncertainties can be incorporated into a physics measurement. The full likelihood becomes

$$L(O|H, \theta) = L_{\text{physics}}(O|\nu_b(\theta) + \mu\nu_s(\theta))L_{\text{glob.obs.}}(O|1, \theta) \quad (8.13)$$

8.6 Parameter estimation

When maximising the likelihood function one finds the value of the parameters of interest as well as the nuisance parameters for which the data is most probable. RooFit uses the MINUIT package [6], which is used by most of the LHC analyses. The MINOS algorithm is designed to measure intervals in using the likelihood approach. The profiled ratio is used as a test statistic as described above. The HESSE algorithm used by MINUIT measures the Hessian matrix using steps in the likelihood function to obtain the variance-covariance matrix defined as

$$H_{ij}(\hat{\alpha}) = \left. \frac{\partial^2 \ln L(\alpha)}{\partial \alpha_i \partial \alpha_j} \right|_{\hat{\alpha}} \quad (8.14)$$

The intervals obtained by Minos allow us to say something about the confidence level of the found values for our parameters of interest. The Hessian correlation matrix allows us to see the influence our parameters have on the fit and on each other. When a parameter shows high correlations with another parameter of interest. The parameters cause similar effects in the fitted distributions and can thus not be told apart to a certain extent. A reparameterization may be then used to get better sensitivity for a linear combination of the parameters of interest.

Chapter 9

Measurements

This chapter introduces the measurements that will be used for the EFT interpretation. It also describes in short what signal they are selecting and what techniques are used. Then the result of the analyses is presented. Section 9.1 covers the $H \rightarrow W^+ W^- \rightarrow e\nu\mu\nu$ measurement. Section 9.2 the $qq/gg \rightarrow W^+ W^- \rightarrow e\nu\mu\nu$ measurement.

9.1 Measurements of gluon-gluon fusion and vector-boson fusion Higgs production

The first measurement that implemented in our EFT interpretation is the measurement of the $H \rightarrow WW^* \rightarrow e\nu\mu\nu$ channel with the ATLAS detector [3]. This measurement is taken using 36.1 fb^{-1} of proton proton collisions at a centre-of-mass energy of 13 TeV . The ggF production modes allows for the direct probing of the Higgs boson to a virtual quark loop, while the VBF production probes the couplings of the Higgs with the W and Z bosons.

The signal topology is characterised by two isolated, charged opposite sign leptons. Since the W-bosons can decay fully hadronically, $qqqq$, semi hadronically $qq\ell\nu$, and fully leptonic $\ell\nu\ell\nu$ we only use part of the signal. The full leptonic decay is the least prone to the QCD background. Also when selecting different flavour leptons we suppress the Drell-Yann background. The presence of a missing transverse energy is required due to the two neutrinos in the final state. In the analysis, the kinematic properties of the di-lepton are characterised. Since the SM Higgs is a spin zero particle and the W bosons have helicity states 1, 0 and -1. Three different combinations of spin projections of the W bosons are allowed. Due to the structure of the weak interaction, neutrinos have negative helicity and anti-neutrinos have positive helicity. Thus the charged leptons are preferably emitted in the same direction while the neutrinos travel in opposite directions with respect to the leptons, resulting in a large missing E_T . Because the leptons are emitted in the same direction, the angle $\Delta\phi_{ll}$ is also quite small. Resulting in a small combined invariant mass, which is defined as

$$m_{l_1, l_2} \approx \sqrt{E_{l_1} E_{l_2} (1 - \cos \Delta\Phi_{l_1, l_2})}. \quad (9.1)$$

The total transverse mass m_T of the Higgs boson can be approximated by

$$m_T = \sqrt{(E_{ll} + E_T^{miss})^2 - |p_{T, ll} + E_T^{miss}|^2} \quad (9.2)$$

With $E_{ll} = \sqrt{|p_{T, ll}|^2 + m_{ll}^2}$ and $p_{T, ll}$ the combined dilepton transverse momentum four vector. The ggF Higgs production is almost never associated with more than 1 high energetic jet. While the VBF production mode is always accompanied by two scattering

quarks, which in turn produce two highly energetic forward jets. They present a high invariant mass m_{jj} and a large rapidity gap.

After the events are triggered by the single-lepton and dilepton $e\mu$ trigger, several selection cuts are applied. Electron candidates are reconstructed from the calorimeter data and are required to satisfy $|\eta| < 2.47$ and must also satisfy $1.37 > |\eta| > 1.52$ because of the transition region between the endcap and the barrel calorimeters. Muon candidates are reconstructed in the muon spectrometer and are required to satisfy $|\eta| < 2.5$. The final lepton-selection criteria require that the two are different flavour with opposite charge, while the leading lepton has a $p_t > 22 \text{ GeV}$ and the sub-leading a $p_T > 15 \text{ GeV}$. The jets are reconstructed using the anti- k_t algorithm [49] with a cone radius parameter of $R = 0.4$. Jets are required to have a $p_T > 20 \text{ GeV}$ and $|\eta| < 4.5$. Jets with $p_T > 20 \text{ GeV}$ and $|\eta| < 2.5$ containing b -hadrons, also called b -jets, are identified using a multivariate technique and are vetoed out if labelled. The events are categorised in three categories based on the number of jets exceeding a p_T of 30 GeV . Events with zero jets and with exactly one jet target the ggF production mode and events with at least two jets target the VBF production mode. These cuts are summarised in Tab. 9.1.

Selection requirement	Selection value		
	$N_{jet} = 0 \text{ ggF}$	$N_{jet} = 1 \text{ ggF}$	$N_{jet} \geq 2 \text{ VBF}$
Two isolated, different flavour leptons	Yes		
$p_T^{lead}, p_T^{sublead}$	$> 22 \text{ GeV}, > 15 \text{ GeV}$		
m_{ll}	$> 10 \text{ GeV}$		
p_T^{miss}	$> 20 \text{ GeV}$		
$N_{b-jet}(p_T > 20 \text{ GeV})$	0		
$\Delta\phi(ll, E_T^{miss})$	$> \pi/2$		
$\max(m_T^l)$		$> 50 \text{ GeV}$	
p_T^{ll}	30 GeV		
$m_{\tau\tau} < m_Z - 25 \text{ GeV}$			yes
m_{ll}	$< 55 \text{ GeV}$		
$\Delta\phi_{ll}$	< 1.8		
central jet veto			Yes
outside lepton veto			Yes

TABLE 9.1: The event selection criteria in the HWW analysis. The discriminant variable of the ggF process is m_T . The VBF process is run through a Boosted Decision Tree.

The signal of this measurement is defined as the ggF Higgs production and the VBF Higgs production both decaying via $H \rightarrow W^- W^+ \rightarrow l\nu l\nu$, where $l = e$ or μ . This always includes a small contribution from $W \rightarrow \tau\nu \rightarrow l\nu\nu\nu$ decays, but is neglected. The $t\bar{t}H$ and $b\bar{b}H$ associated production is also neglected. The other backgrounds are listed in Tab. 9.2, together with the signals.

Signal	$\sigma \cdot Br(pb)$
ggF $H \rightarrow W^+ W^-$	10.4
VBF $H \rightarrow W^+ W^-$	0.808
Background	$\sigma \cdot Br(pb)$
$WH H \rightarrow W^+ W^-$	0.293
$ZH H \rightarrow W^+ W^-$	0.189
$Z/\gamma^* \rightarrow ll$	8.907×10^3
$(W \rightarrow l\nu)\gamma$	452
$(Z \rightarrow ll)\gamma$	175
$t\bar{t}$ di-leptonic (e, μ, τ)	87.6
Wt leptonic	7.55
$q\bar{q}/gg \rightarrow WW \rightarrow l\nu l\nu$	49.74
$ZZ \rightarrow 2l2\nu$	6.53
$gg \rightarrow 2l2\nu$	0.87
$q\bar{q}/g \rightarrow l\nu ll$	11.9
$q\bar{q}/g, gg \rightarrow llll$	11.5
EW $WW + 2$ jets ($l\nu l\nu$)	0.012
EW $WZ + 2$ jets ($l\nu l\nu$)	0.038
EW $ZZ + 2$ jets ($l\nu l\nu$)	0.116
EW $q\bar{q} \rightarrow (Z \rightarrow \tau\tau)q\bar{q}$	2.54

TABLE 9.2: Signal and background processes and corresponding cross sections [3].

The ggF and VBF total cross sections are obtained by simultaneously fitting of the data samples in all signal and control regions by applying a profile likelihood method. The CR are used to determine the normalisation of the corresponding backgrounds and to check if the background is fully understood. All of the systematic uncertainties enter in the fit as nuisance parameters of the likelihood function.

Using a SM Higgs with a $m_H = 125$ GeV in the expected a cross section was $43.92^{+7.4\%+7.1\%}_{-7.9\%-6.0\%} (PDF + \alpha_s) pb$ for ggF, and $3.748^{+0.7\%+3.2\%}_{-0.7\%-3.2\%} (PDF + \alpha_s) pb$ accompanied with a SM branching ratio of $2.14^{+4.3\%}_{-4.2\%} \times 10^{-1}$. The cross-sections times branching ratio are simultaneously found to be

$$\begin{aligned}\sigma_{ggF} \cdot B_{H \rightarrow WW^*} &= 11.4^{2.2}_{-2.1} pb, \\ \sigma_{VBF} \cdot B_{H \rightarrow WW^*} &= 0.50^{0.29}_{-0.28} pb.\end{aligned}\tag{9.3}$$

The measured signal strength for both of the channels is then obtained by dividing the measured signal yield with the predicted signal yield and are also simultaneously found to be,

$$\begin{aligned}\mu_{ggF} &= 1.10^{+0.21}_{-0.20} pb, \\ \mu_{VBF} &= 0.62^{+0.36}_{-0.35} pb.\end{aligned}\tag{9.4}$$

In Figure 9.1 The combined m_T distribution for $N_{jet} \leq 1$ is shown. The signal that was observed is in agreement with the expected SM signal.

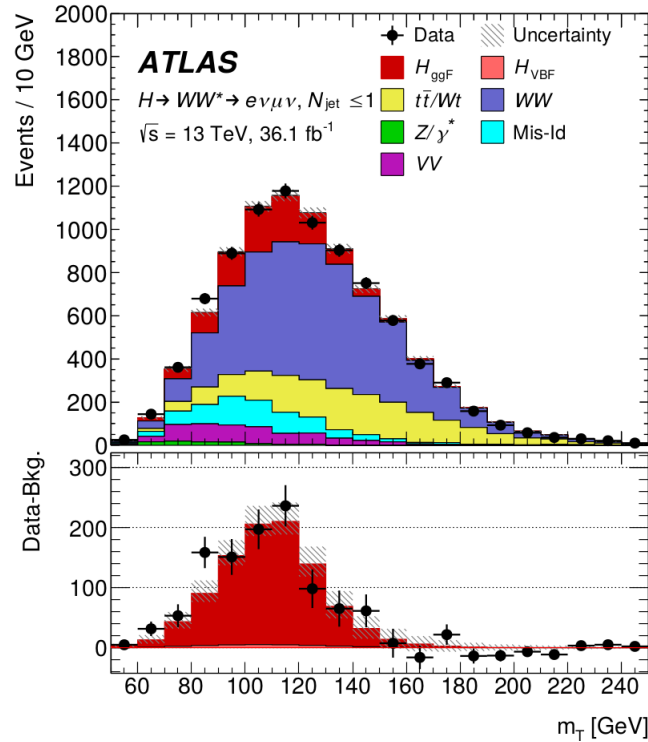


FIGURE 9.1: The post-fit transverse mass distribution for $N_{jet} \leq 1$. The top panel showing all of the channels included into the analysis, while the bottom panel is showing the difference between data and the estimated background compared to a SM Higgs boson distribution. The hatched bands are showing the total uncertainty on the signal and the backgrounds

This analysis is now slightly altered to allow combining with the other Higgs measurements. The STXS framework is applied binning the signal regions of ggF and VBF into the STXS definitions, illustrated in Fig. 7.3 and Fig. 7.4 respectively. The backgrounds are also binned in the same STXS regions. By doing this the total signal events that are observed by the analysis, which are approximately 1000, get separated based on the reconstructed transverse momentum and jet topology into different fiducial signal regions. Based on the cuts introduced in chapter 8. Thereby allowing for the combination with other channels. Each of the STXS bins is assigned a signal strength parameter which is again the ratio of the observed signals in that bin divided by the expected signal in that bin. Now the total inclusive cross section of the ggF and VBF production processes are the sum of all of the associated STXS bins. Therefore, the sensitivity per fiducial region, which is well illustrated by the signal strength, is less than the sensitivity to the total inclusive cross section. However, because the fiducial regions are separated in terms of total Higgs p_T . Any deviations of the SM can be studied per fiducial region, by fitting and finding a signal strength for each of them.

During this research I was handed the ggF and VBF STXS workspace. Both the ggF and the VBF workspaces contained all of the data, MC Backgrounds and systematic uncertainties, used by the analysis, binned in the newly defined STXS regions. These measurements are then combined by correlating the parameters that enter in both measurements. A profile likelihood fit is performed to all of the STXS regions signal strength. Both to an Asimov dataset provided by the analysis as the observed data set. We observe the following signal strengths in each of the bins including the the statistical and systematic uncertainty. We

notice that in particular for the ggF measurements, the sensitivity lies in the lower p_T region. This is because the Higgs is not boosted in this production mode. The results from the separate channel analyses can be found in Appendix A. The results from the combined HWW (ggF+VBF) STXS measurement are shown in Fig. 9.2 and Tab. 9.3. The correlations between the fitted STXS bin are shown in Fig. 9.3.

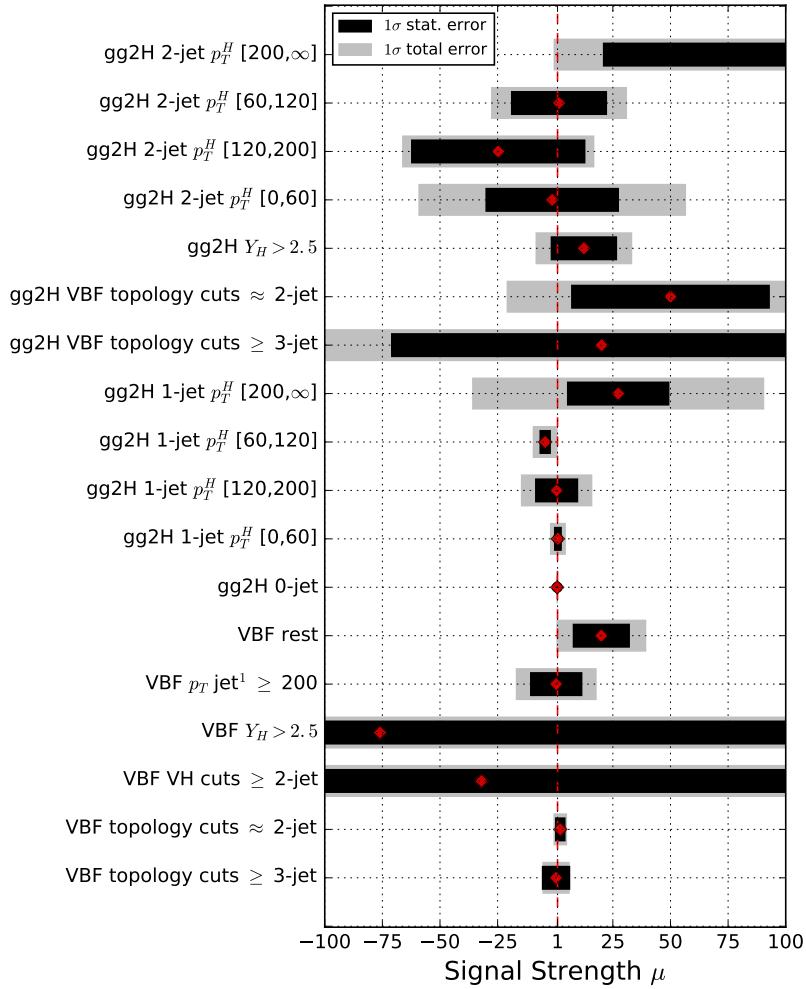


FIGURE 9.2: Signal strength results of the combined HWW STXS measurement showing the 68% $C.L.$ errors.

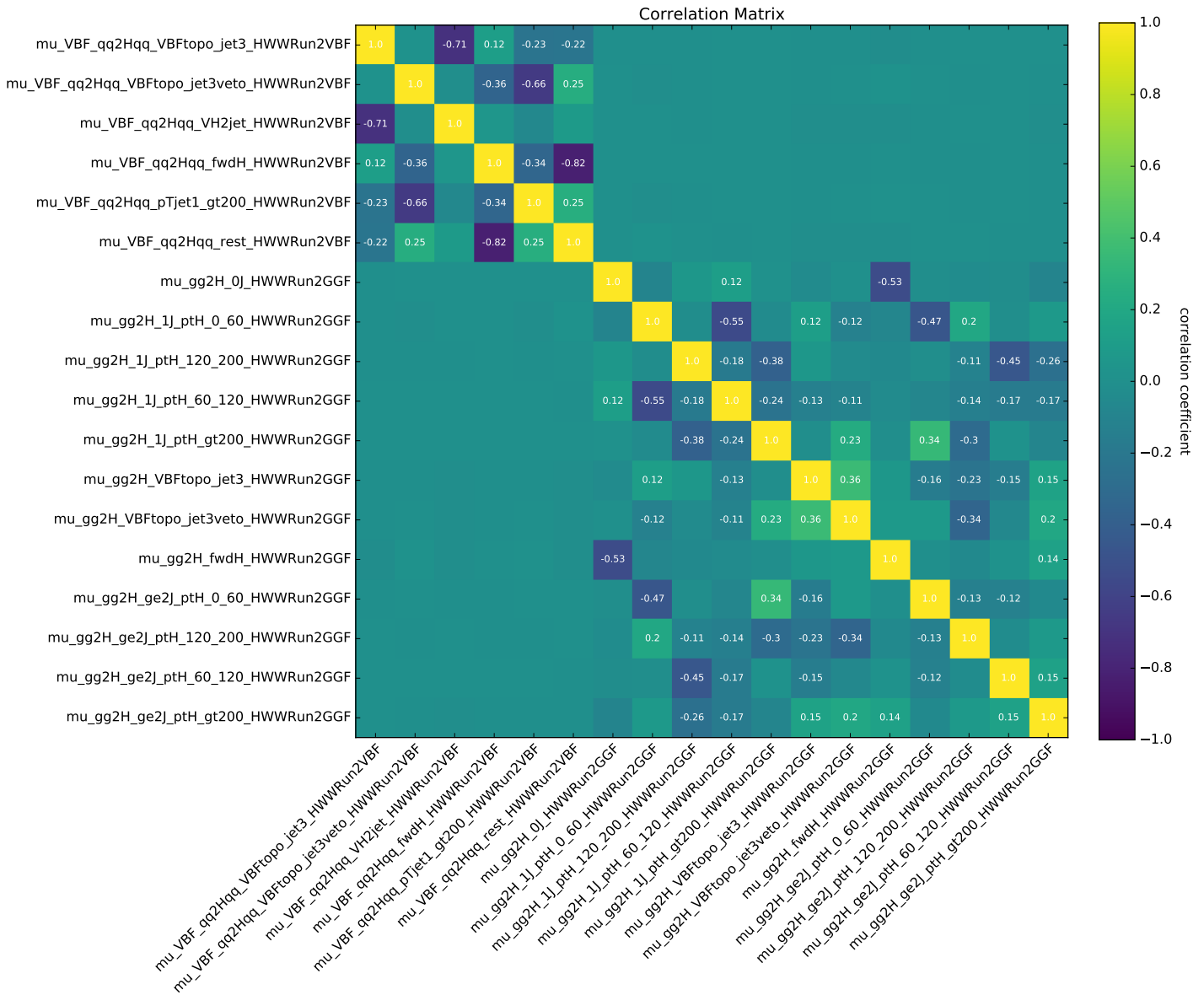


FIGURE 9.3: Correlations between the fitted STXS signal strengths of the combined ggF and VBF measurements

STXS region	signal strength(μ) 68% <i>C.L.</i>
VBF topology \geq 3-jet	$0.35^{+5.9}_{-5.9}$
VBF topology \approx 2-jet	$2.19^{+2.9}_{-2.9}$
VBF VH cuts \geq 2-jet	-32.2^{+901}_{-901}
VBF $Y_H > 2.5$	-76.2^{+446}_{-446}
VBF p_T jet-1 > 200	0.42^{+17}_{-17}
VBF p_T jet-1 > 200	19.1^{+18}_{-19}
gg2H 0-jet	$0.84^{+0.3}_{-0.3}$
gg2H 1-jet p_T^H [0,60]	$1.15^{+3.4}_{-3.4}$
gg2H 1-jet p_T^H [60,120]	$-4.36^{+5.4}_{-5.4}$
gg2H 1-jet p_T^H [120,200]	0.60^{+16}_{-15}
gg2H 1-jet p_T^H [200, ∞]	27.3^{+63}_{-63}
gg2H VBF topology \geq 3-jet	20.1^{+140}_{-138}
gg2H VBF topology \approx 2-jet	50.0^{+71}_{-71}
gg2H $Y_H > 2.5$	12.4^{+20}_{-20}
gg2H 2-jet p_T^H [0,60]	-1.31^{+58}_{-58}
gg2H 2-jet p_T^H [60,120]	-1.64^{+29}_{-29}
gg2H 2-jet p_T^H [120,200]	-24.7^{+41}_{-41}
gg2H 2-jet p_T^H [200, ∞]	-107.7^{+110}_{-108}

TABLE 9.3: Observed signal strengths in HWW(ggF+VBF) STXS fiducial regions

9.1.1 Systematic uncertainties

The analysis is affected by different systematic uncertainties. Since one can not measure precisely the energy of a particle, the uncertainty on this has to be estimated. Often the systematic uncertainties on energy, momentum, scale or resolution are calculated by shifting the value by a scale factor before selecting the events. Doing this for a nominal scaling value and values with a standard deviation of ± 1 , results in the smearing of the observable. Then the uncertainty on the observable is evaluated by comparing the event yield with scaled event yield, thus applying weights to each event. The standard set of experimental uncertainties used in this analysis is given in Ref. [2]. To give some examples these are the Trigger efficiency uncertainty, Electron reconstruction and identification, Muon reconstruction and identification to the uncertainty on the total integrated luminosity. In order to combine the two measurements into the combined HWW measurement we need to correlate all of the common parameters and observables used by the two measurements. The post-fit systematic uncertainties are given in the Appendix for each of the STXS fits. The pulls from the nuisance parameters be found in Appendix A.

9.2 Fiducial and differential W^+W^- cross section measurement

The next measurement added is the electroweak boson pair production measurement [3]. At the LHC, di-boson measurements are used to probe the electroweak sector of the Standard Model at the TeV scale and provide new measurements on the produced cross sections. While the Vector Bosons decay channels could also indicate the existence of new particles and probe beyond the Standard Model physics. The processes involved are sensible to triple gauge couplings (TGC) and also present a background to the Higgs boson searches using the same final state. Additionally, WW measurements can be used to probe quartic gauge couplings. The SM describes three main diboson production processes at leading order. the s-channel, t-channel and box-diagrams, Fig. 9.4. The di-quark initial state is specific to hadron colliders and is the dominant production mechanism of WW boson pairs at the LHC. Higgs gluon-gluon fusion contributes a small amount to the cross section, but is considered as a background.

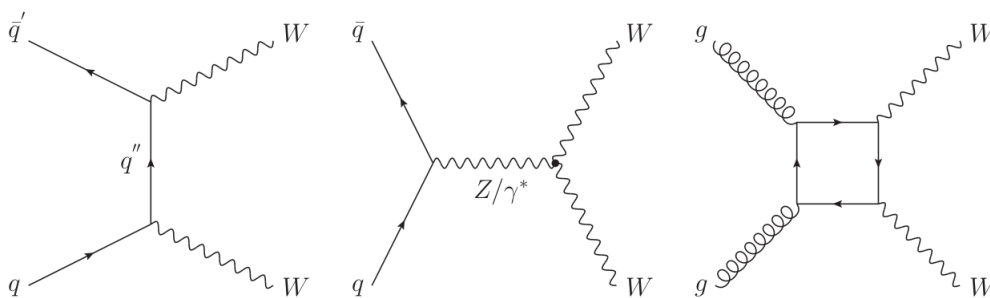


FIGURE 9.4: Feynman diagrams for SM WW production at tree level. From left to right $q\bar{q}$ initial state t-channel, $g\bar{g}$ initial state s-channel and $g\bar{g}$ initial state resonant production. The s-channel production contains WWZ and WW γ triple-gauge-coupling vertices [3].

The fiducial phase space is defined to be orthogonal to the $H \rightarrow WW$ measurements using a requirement on the dilepton invariant mass of $m_{ll} > 55 \text{ GeV}$. This measurement is taken using the same dataset as the $H \rightarrow WW$. However, due to the invariant mass requirement no events are shared between the measurements making them perfect for combination. In the $WW \rightarrow e\mu + \mu e$ channels studied. The electrons are required to

have a $E_T > 27 \text{ GeV}$ and a pseudorapidity of $|\eta| < 2.47$, excluding the transition region between the endcaps. The muon candidates are required to have $p_T > 27 \text{ GeV}$ and $|\eta| < 2.5$. The jet candidates are reconstructed using the anti- k_t jet clustering algorithm with a radius parameter of 0.4. Missing transverse momentum is required to be bigger than 20 GeV , further the combined transverse momentum of the electron and muon is required to be bigger than 30 GeV in order to suppress the Drell-Yan background. The last cut of $m_{e\mu} > 55 \text{ GeV}$ reduces the $H \rightarrow WW$ contribution to a level below 1% of the expected signal.

Selection requirement	Selection Value
p_T^l	$> 27 \text{ GeV}$
η^l	$ \eta^e < 2.47$ (excluding $1.37 < \eta^e < 1.52$), $ \eta^\mu < 2.5$
Number of additional leptons ($p_T > 10 \text{ GeV}$)	0
Number of jets ($p_T > 35 \text{ GeV}, \eta < 2.5$)	0
Number of b-tagged jets ($p_T > 20 \text{ GeV}, \eta < 2.5$)	0
E_T^{miss}	$> 20 \text{ GeV}$
$p_T^{e\mu}$	$> 30 \text{ GeV}$
$m_{e\mu}$	$> 55 \text{ GeV}$

TABLE 9.4: Summary of the lepton and jet event selection criteria for the WW candidate events [3]

The measured fiducial cross-section for the $WW \rightarrow e\mu$ production at $\sqrt{s} = 13 \text{ TeV}$ is $\sigma_{fid} = 379.1 \pm 5.0(\text{stat}) \pm 25.4(\text{syst}) \pm 8.0(\text{lumi}) \text{ fb}$. One of the measured fiducial cross section as a function of $p_T^{lead,l}$ is shown in Fig. 9.5. The fiducial cross section is calculated taking into account the integrated luminosity and the detector inefficiencies, resolution effects and contributions from τ -lepton decays. Unfolding of the distribution is done using an iterative Bayesian unfolding method. The procedure corrects for migrations between bins in the distributions during the reconstruction of the events and applies the fiducial reconstruction efficiencies as well. Finally, results are compared with several theoretical predictions and normalised to the NNLO theoretical prediction for the total cross section.

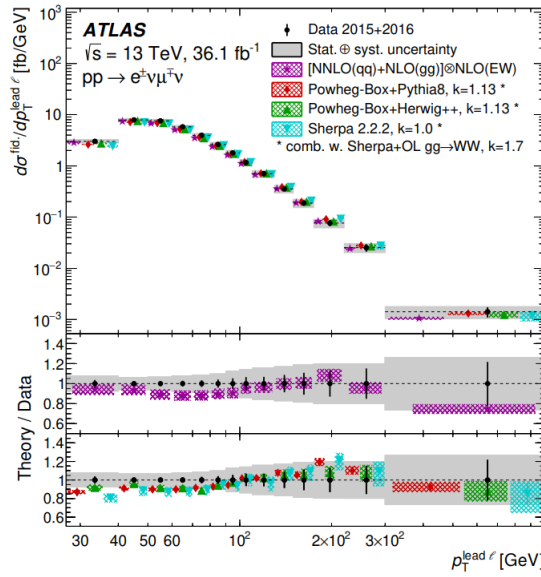


FIGURE 9.5: Measured fiducial cross-section of $WW \rightarrow e\mu$ production for the leading lepton transverse momentum $p_T^{lead,l}$. The cross section values are shown as points with error bars giving the statistical uncertainty and solid bands the total uncertainty. The results are compared with the theory for validation of the measurement [3].

9.2.1 The $qq/gg \rightarrow W^+W^- \rightarrow e\nu\mu\nu$ EFT interpretation

The distribution in Fig. 9.5 is used in an EFT interpretation recently developed. The EFT interpretation of this study will be combined with our interpretation in order to increase our overall sensitivity. The sensitivity is expected to increase most for W^+W^- EFT effects as well as the light fermion operators. In this study we will not go into this measurement too much, but we will use it as a statistical tool to improve the $H \rightarrow WW$ EFT interpretation.

The EFT interpretation of this measurement is supplied to this study in the RooFit workspace format. Taking into account the systematic uncertainties of the MCProd of the EFT samples. The systematic uncertainties of the measurement are all folded into the distribution itself due to the unfolding. The nuisance parameters that are affecting the EFT interpretation are the normalisation of the distribution (referred to as `ww_norm`), the uncertainty on the PDF used to generate the EFT samples (`ww_pdf`), the QCD scale uncertainty (`ww_scale`) and the electroweak constant uncertainty (`ww_ewk`). Which are all associated with the generation of the new samples for the EFT interpretation. The EFT interpretation is conducted up until order $\frac{1}{\Lambda^2}$. Using this measurement we hope to increase our sensitivity to the operators affecting the light fermions and electroweak sector.

Chapter 10

Operator Analysis

This chapter will cover the selection of EFT operators, along with the assumptions made. This will be discussed in section 10.1. Further the effect of several of the operators is explained in section 6.2. At last the simulation of the samples and the reparameterization is performed in 6.3.

10.1 Cross section study

In order to select the operators that we are most interested in, a small selection is made of all the dimension-6 operators that enter in the signals selected by the measurements. Included is the $H \rightarrow W^+W^- \rightarrow e\nu\mu\nu$ decay channel. The production processes for this channel is the gluon-gluon fusion process accompanied with or without jets and the electroweak produced Higgs boson through the VBF production mode. The VBF production is always accompanied by two or more jets. At last the electroweak production of two oppositely charged vector bosons is added.

Incorporating these three processes means that interpretation is only sensitive to the operators have a non-negligible contribution to the cross section of these processes or significantly alter the shape of the p_T^H distribution.

For the operator analysis, we now only focus on the linear order in operator coefficients. Only taking into account one new physics coupling per process, as per the recommendations of the SMEFT authors [30]. We assume a $U(3)^5$ symmetry for fermion operators, bringing down the number of effective dimension-6 operators from 2500 to 70. Because the STXS interpretation treats the Higgs boson as the final state we consider only the operators occurring before the decay of the Higgs boson, hence only the operators that enter into the production. The operators that enter into the decay of the Higgs boson can later be probed in terms of the branching ratios.

All of the operators that enter in the channels are now simulated using Madgraph5 and the massive SMEFT model according to the settings described in Chapter 4. The SM interference contribution of each operator is shown per channel. Also the full dimension-6 contribution is calculated, which is per definition a positive contribution because of the structure of the theory. The contributions are normalised with respect to the SM cross section of the respective process.

The ggF process contributes most from the operators that alter the Higgs field and the top loop initiated by two gluons. This translates into sensitivity on the operators $c_{HG}, c_{HDD}, c_{Hbox}$ and c_{HW} along with their CP-odd counter parts and some light fermion

operators. Shown in Fig. 10.1 for the production cross section and Fig. 10.2 for the process including $H \rightarrow W^+ W^- \rightarrow e\nu\mu\nu$ decay.

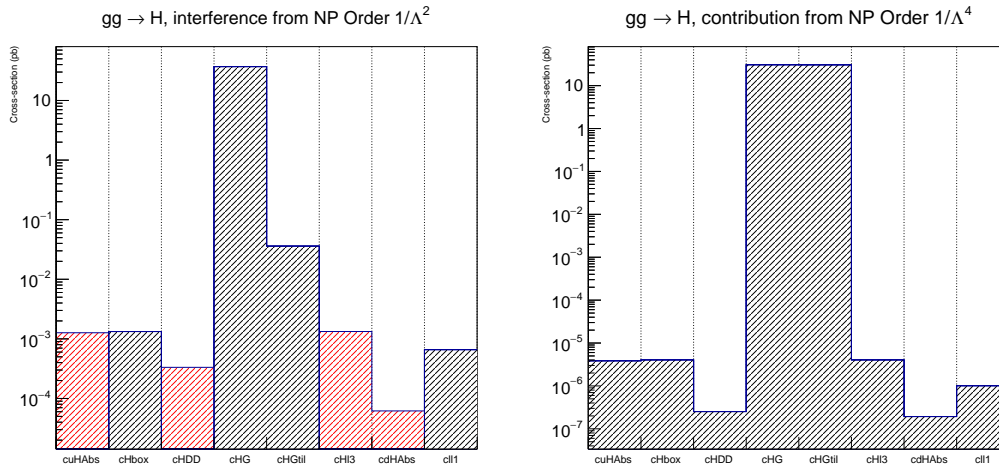


FIGURE 10.1: The interference with the standard model shown per operator for the ggF single Higgs production mode

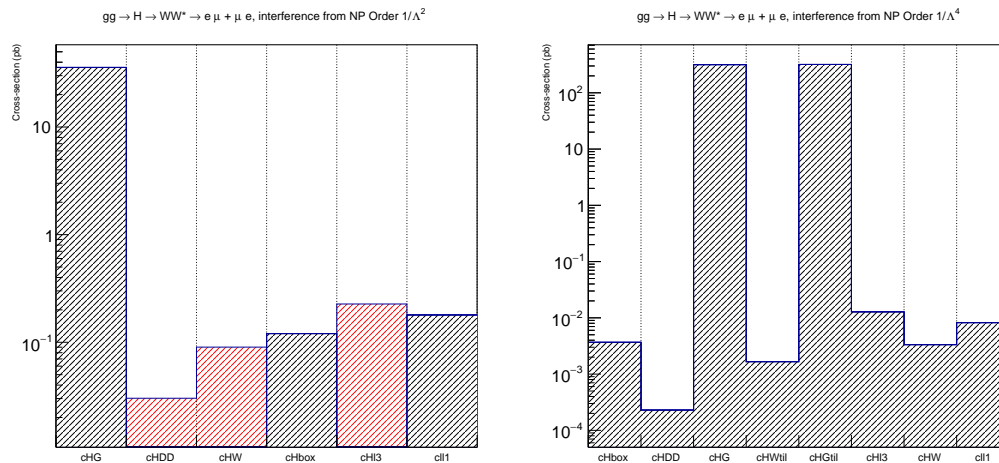


FIGURE 10.2: The interference with the standard model shown per operator for the ggF single higgs production mode, subsequently decaying into vector bosons

The VBF samples were produced including a small VH contribution for the purpose of the operator analysis alone. This process involves more operators than the ggF production because of its more complicated structure. The same operators enter as in the ggF process excluding c_{HG} because of the absence of QCD couplings accompanied with a lot of light fermion operators. Shown in Fig. 10.3 for the production cross section and Fig. 10.4 for the process including $H \rightarrow W^+ W^- \rightarrow e\nu\mu\nu$ decay.

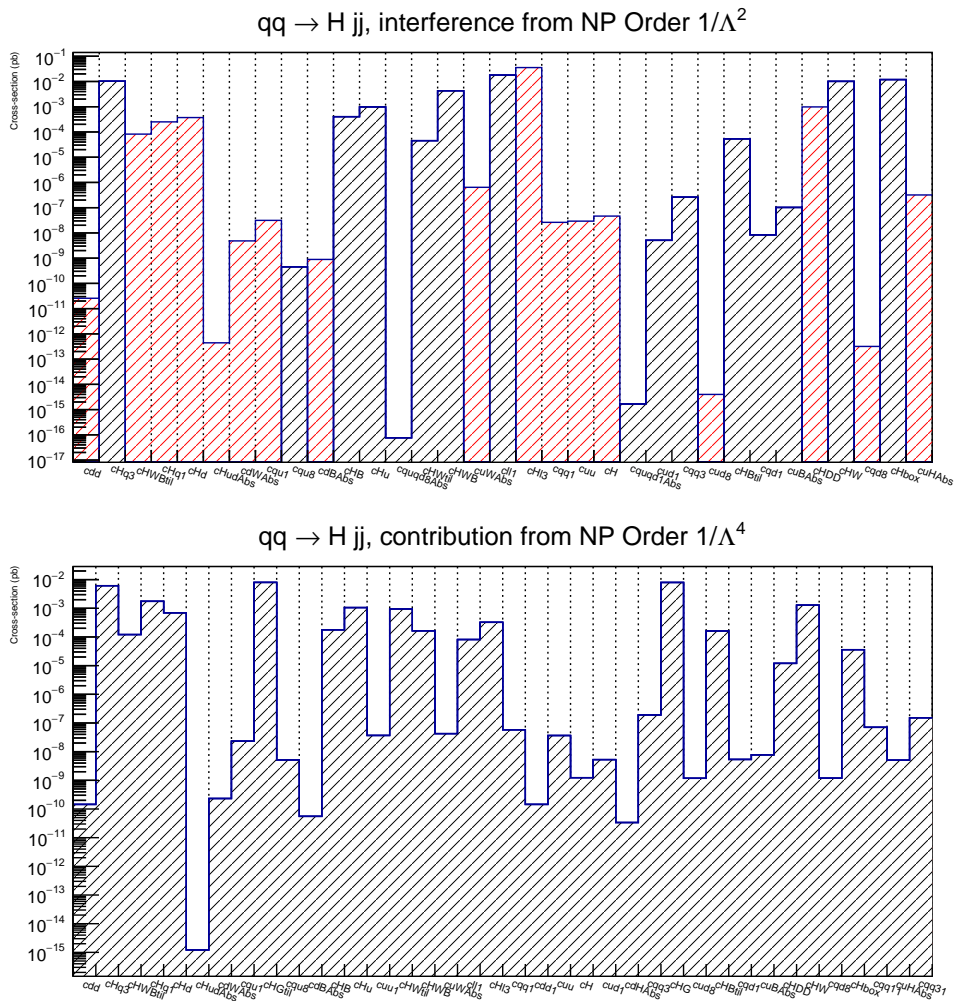


FIGURE 10.3: The interference with the standard model shown per operator for the VBF single Higgs production mode

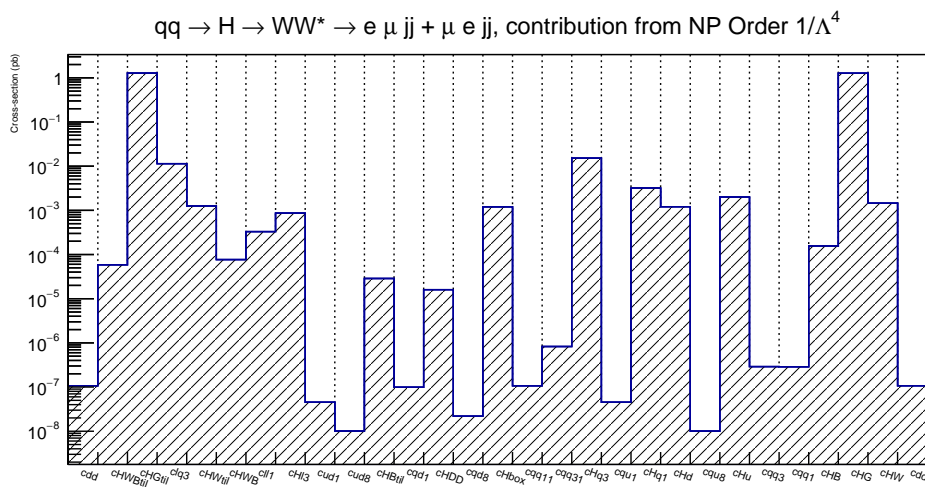
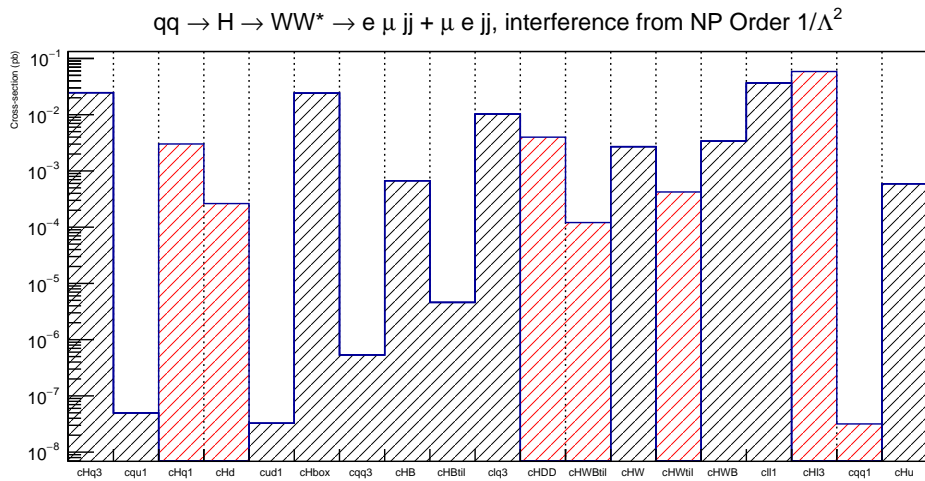


FIGURE 10.4: The interference with the standard model shown per operator for the VBF single Higgs production mode, subsequently decaying into vector bosons

While doing this, many operators which cause minor interference do not enter the process anymore, keeping all the operators that effect the massive vector bosons, such as H, Z, W^\pm . These are also the operators which cause the most interference with the SM. In Tab. 10.1 we formulate the operators that are going to be measured. For now we will only consider CP-even operators. However, we can include the CP-odd ones at any point in the future should more measurements become sensitive to them.

$Q_{Hl}^{(3)}$	$(H^\dagger i \overleftrightarrow{D}_\mu^I H)(\bar{l} \tau^I \gamma^\mu l)$	
$Q_{Hl}^{(1)}$	$(H^\dagger i \overleftrightarrow{D}^\mu H)(\bar{l} \gamma^\mu l)$	
$Q_{ll}^{(1)}$	$(\bar{l}_p \gamma_\mu l_r)(\bar{l}_s \gamma^\mu l_t)$	
Q_{HDD}	$(H^\dagger D^\mu H)^*(H^\dagger D_\mu H)$	
Q_{HWB}	$(H^\dagger \tau^I H W_{\mu\nu}^I B^{\mu\nu})$	
Q_{Hu}	$(H^\dagger i \overleftrightarrow{D}_\mu^I H)(\bar{u} \gamma^\mu u)$	
Q_{Hd}	$(H^\dagger i \overleftrightarrow{D}_\mu^I H)(\bar{d} \gamma^\mu d)$	
$Q_{Hq}^{(3)}$	$(H^\dagger i \overleftrightarrow{D}_\mu^I H)(\bar{q} \tau^I \gamma^\mu q)$	
$Q_{Hq}^{(1)}$	$(H^\dagger i \overleftrightarrow{D}_\mu^I H)(\bar{q} \gamma^\mu q)$	
Q_W	$\epsilon^{ijk} W_\mu^{I\nu} W_\nu^{J\rho} W_\rho^{K\mu}$	
Q_{ld}	$(\bar{l}_p \gamma_\mu l_r)(\bar{d}_s \gamma^\mu d_t)$	
$Q_{lq}^{(3)}$	$(\bar{l}_p \gamma_\mu \tau^I l_r)(\bar{q}_s \gamma^\mu \tau^I q_t)$	
Q_{lu}	$(\bar{l}_p \gamma_\mu l_r)(\bar{u}_s \gamma^\mu u_t)$	
$Q_{H\Box}$	$(H^\dagger H)\Box(H^\dagger H)$	
Q_{HW}	$H^\dagger H W_{\mu\nu}^I W^{I\mu\nu}$	
Q_{HB}	$H^\dagger H B_{\mu\nu} B^{\mu\nu}$	
Q_{HG}	$H^\dagger H G_{\mu\nu}^A G^{A\mu\nu}$	

TABLE 10.1: All operators that enter in the interpretation. Left, operators important for the WW production decaying into $e\mu$ of any kind. Right, operators directly affecting the SM Higgs operators.

When treating the SM as a low-energy Effective Field Theory the SMEFT is the SM Lagrangian extended to include a series of dimension-6 operators. There are also dimension 8 operators which might contribute to deviations from the standard model. Only including them proves to be quite difficult. Which is why in this analysis the dimension-8 operators will not be taken into account. See Appendix G for a more extensive study on the effect of the dimension-8 operators.

Focusing on the effects of the leading lepton-number-conserving operators \mathcal{O}_i of dimension 6 we find the Lagrangian of the new model to be

$$\mathcal{L} = \mathcal{L}_{SM} + \mathcal{L}^{(6)} + \dots \quad (10.1)$$

Where $\mathcal{L}^{(6)}$ represents the dimension-6 effects and the rest is neglected. When moving to the SMEFT representation this transforms in,

$$\mathcal{L}_{SMEFT} = \mathcal{L}_{SM} + \sum_i \frac{c_i}{\Lambda_i^2} \mathcal{O}_i + \dots \quad (10.2)$$

Here the ... denote the operators of dimension greater than six suppressed by additional powers of Λ . c_i are the Wilson coefficients introduced by integrating out the heavy degrees of freedom of new physics at a scale of Λ . In our model, the SMEFT Lagrangian is now build up by adding the operators chosen and write this as

$$\begin{aligned}
\mathcal{L}_{SMEFT} \supset & \frac{c_{HI}^{(3)}}{\Lambda^2} (H^\dagger i \overleftrightarrow{D}_\mu H) (\bar{l} \tau^I \gamma^\mu l) + \frac{c_{HI}^{(1)}}{\Lambda^2} (H^\dagger i \overleftrightarrow{D}^\mu H) (\bar{l} \gamma^\mu l) + \frac{c_{ll}^{(1)}}{\Lambda^2} (\bar{l}_p \gamma_\mu l_r) (\bar{l}_s \gamma^\mu l_t) \\
& + \frac{c_{HDD}}{\Lambda^2} (H^\dagger D^\mu H)^* (H^\dagger D_\mu H) + \frac{c_{HWB}}{\Lambda^2} (H^\dagger \tau^I H W_{\mu\nu}^I B^{\mu\nu}) + \frac{c_{Hu}}{\Lambda^2} (H^\dagger i \overleftrightarrow{D}_\mu H) (\bar{u} \gamma^\mu u) \\
& + \frac{c_{Hd}}{\Lambda^2} (H^\dagger i \overleftrightarrow{D}_\mu H) (\bar{d} \gamma^\mu d) + \frac{c_{Hq}^{(3)}}{\Lambda^2} (H^\dagger i \overleftrightarrow{D}_\mu H) (\bar{q} \tau^I \gamma^\mu q) + \frac{c_{Hq}^{(1)}}{\Lambda^2} (H^\dagger i \overleftrightarrow{D}_\mu H) (\bar{q} \gamma^\mu q) \\
& + \frac{c_W}{\Lambda^2} \epsilon^{ijk} W_\mu^{I\nu} W_\nu^{J\rho} W_\rho^{K\mu} + \frac{c_{ld}}{\Lambda^2} (\bar{l}_p \gamma_\mu l_r) (\bar{d}_s \gamma^\mu d_t) + \frac{c_{lq}^{(3)}}{\Lambda^2} (\bar{l}_p \gamma_\mu \tau^I l_r) (\bar{q}_s \gamma^\mu \tau^I q_t) \\
& + \frac{c_{lu}}{\Lambda^2} (\bar{l}_p \gamma_\mu l_r) (\bar{u}_s \gamma^\mu u_t) + \frac{c_{H\Box}}{\Lambda^2} (H^\dagger H) \Box (H^\dagger H) + \frac{c_{HW}}{\Lambda^2} H^\dagger H W_{\mu\nu}^I W^{I\mu\nu} \\
& + \frac{c_{HB}}{\Lambda^2} H^\dagger H B_{\mu\nu} B^{\mu\nu} + \frac{c_{HG}}{\Lambda^2} H^\dagger H G_{\mu\nu}^A G^{A\mu\nu}
\end{aligned} \tag{10.3}$$

The Warsaw Basis and the SMEFT model is used to obtain this Lagrangian [30].

10.2 Phenomenology

In this part we will only focus on the operators which are most present in the Higgs observables. The phenomenological interpretation of these operators needs to be done with care, since the way the SMEFT package is build up. A single operator does not just introduce a new coupling but can also cause a shift in the mass, introduce a X amount of couplings or a single operator to interfere less or more with other SM operators. We will go over some of the main changes the operators introduce to the Standard model.

10.2.1 Effective operators

For ggF the only operator of significance in the production mode is the Q_{HG} operator and contributes to the Higgs production rate via this production mode only. This $\mathcal{L}^{(6)}$ is important because the normal SM amplitude starts at one loop order, with no tree-level contribution. The reason for the large value of c_{HG} relative to the other operator corrections is that it competes with a loop effect in the SM, this means that the interference ends up being loop enhanced [61]. The leading contribution comes from a top quark loop where the interaction $h G_{\mu\nu}^A G^{A\mu\nu}$ is present. This coupling receives a contribution [62] from the operator c_{HG} according to

$$\frac{\sigma(gg \rightarrow h)}{\sigma^{SM}(gg \rightarrow h)} \approx \left| 1 + \frac{16\pi^2 \bar{v}_T^2}{\bar{g}_3^2 I^g} c_{HG} \right| \tag{10.4}$$

Where I^g is a Feynman integral that accounts for the top quark loop contribution. Now for each parameter scheme the physical observables depend on the shifts introduced by all of Wilson coefficients.

The SMEFT also introduces $h Z^\mu \bar{\psi} \gamma^\mu \psi$ couplings, which are normally forbidden in the SM due to it being limited to $d \leq 3$ interactions. These operators are mostly depended on $C_{HI}^{(1,3)}$, $C_{Hq}^{(1,3)}$, C_{Hu} and C_{Hd} . Effective $h W^\mu \bar{\psi}_L \gamma^\mu \psi_L$ couplings, Fig. 10.6, are introduced which are influenced by the same operators. The operators also introduce shifts in the propagators of the massive bosons which alter the interactions relative to the SM and

are thus effecting the partial and total decay widths of the Higgs boson. The VBF production is influenced [62] by the extra neutral current contributions which receives additional contributions from diagrams with $Z\gamma$ and $\gamma\gamma$ fusion and are influenced by the $C_{Hbox}, C_{HDD}, C_{HI}^{(3)}, C_{II1}, C_{HW}, C_{HWB}, C_{HB}$. For the charged current case, there are no additional contributions from diagrams. It is rather altered by the overall shift in amplitude due to $C_{HW}, C_{HDD}, C_{HI}^{(3)}, C_{II1}, C_{Hbox}$ and C_{HWB} .

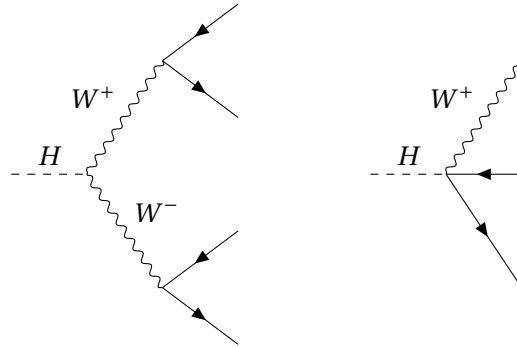


FIGURE 10.6: The charged current contributions to $H \rightarrow 4\psi$ in the SMEFT

10.2.2 The $1/\Lambda^4$ contribution

In order to visualise the impact of the SMEFT operators by the additional couplings or normalising effects, full process samples are generated setting single Wilson coefficients to 1. The same preselection cuts are applied as in the ggF and VBF analyses on truth level. To justify only taking into account the interference contribution, the separate contributions are shown in a stacked plot. The observables used in the STXS interpretation are plotted, such as p_T^H and p_T^{j0} , using the ggF and VBF Higgs production decaying via $H \rightarrow W^+W^-e\nu\mu\nu$. But also m_{ll} , m_T and. Shown in Fig. 10.7 the operator Q_{HW} has a significant interference effect, but a negligible pure dimension-6 contribution. Only on the operator Q_{HG} has a significant pure dimension-6 contribution because of the enhanced loop effect. Therefore, at this stage of the analysis, the $\frac{1}{\Lambda^4}$ contribution is safely neglected. Fig. 10.8 illustrates the impact of the $\frac{1}{\Lambda^2}$ order on VBF observables for Q_{HW} , $Q_{HI}^{(3)}$ and $Q_{H\Box}$.

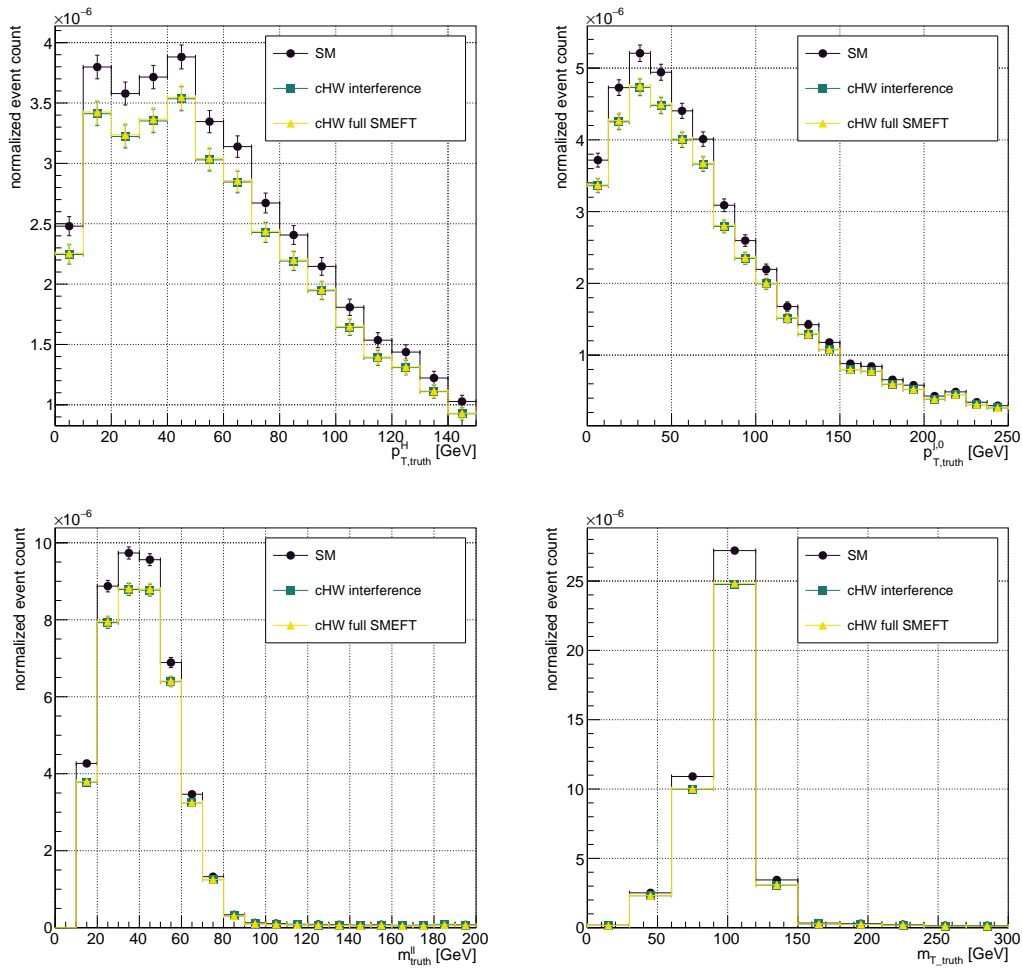


FIGURE 10.7: Kinematic distributions of observables showing the dependence of ggF production on the C_{HW} operator for $c_{HW} = 1$. The Standard Model contribution, the interference corrected SMEFT distribution and the full SMEFT distribution including all dim-6 correction are plotted respectively. Top-left, the Higgs p_T distribution. Top-right, the leading Jet p_T distribution. Bottom left, invariant mass of the opposite sign leptons. Bottom-right, the recombined transverse mass m_T

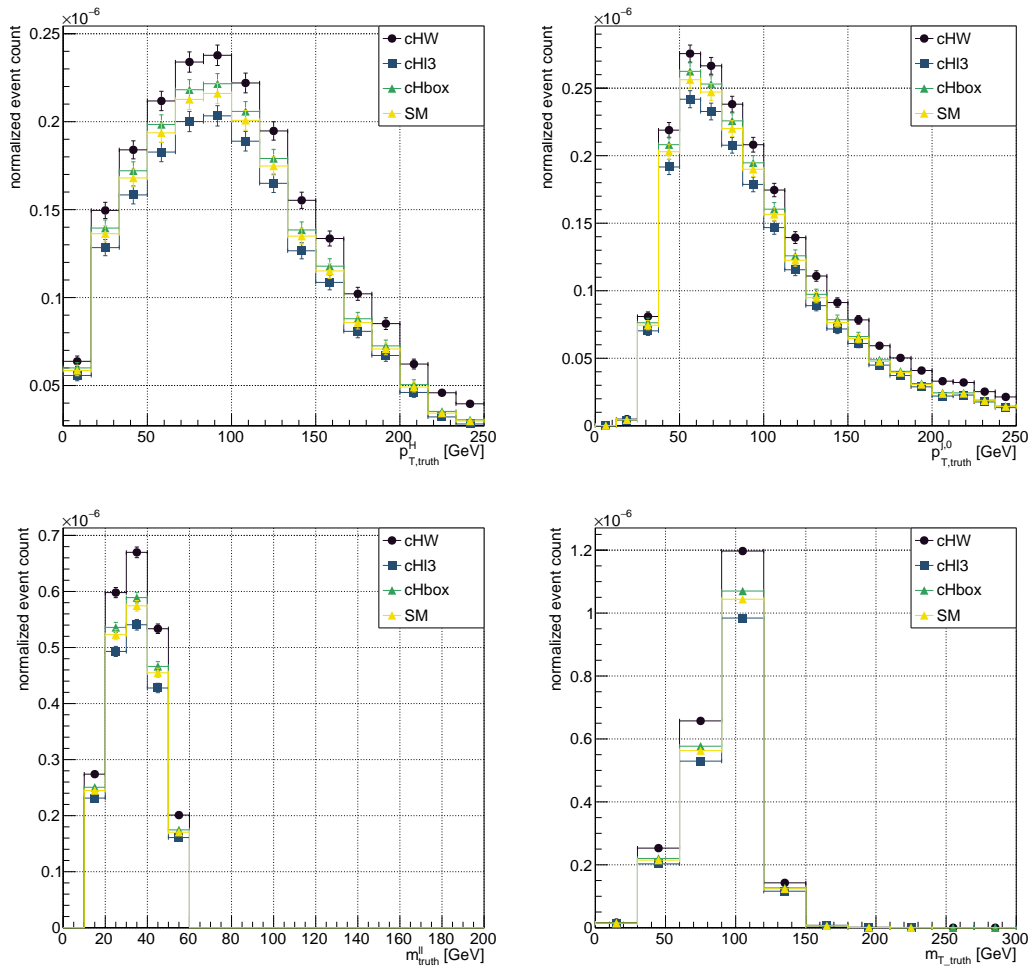


FIGURE 10.8: Kinematic distributions of observables showing the dependence of VBF and VH hadronic decay production on the C_{HW} , $C_{Hl}^{(3)}$ and C_{Hbox} operator for $c_i = 1$. The Standard Model contribution, the interference corrected SMEFT distribution and the full SMEFT distribution including all dim-6 correction are plotted respectively. Top-left, the Higgs p_T distribution. Top-right, the leading Jet p_T distribution. Bottom left, invariant mass M_{ll} of the opposite sign leptons. Bottom-right, the recombinant transverse mass m_T

10.3 Impact of EFT operators on the STXS analysis

In order to couple the SMEFT theory to possible deviations of the Standard Model in the STXS framework we need to simulate these deviations and compare them to the analyses results. The way to realise this is to parametrize the cross section in each STXS bin in terms of the Wilson coefficients that enter in the process sensitive to that particular phase space. Using the framework provided in we treat each STXS fiducial region as a separate signal region. First a Standard Model sample is generated at LO using Madgraph5. This provides us with the Standard model cross section in that particular bin. Next we can generate the first order interference of each Wilson coefficient in that bin and interpolate between them using the analytical Lagrangian morphing method. The cross section in each STXS bin is defined as follows, assuming the narrow width approximation.

$$\sigma_{STXSregion_i} = \sigma_{SM} + \sigma_{int} + \sigma_{BSM} \quad (10.5)$$

Normalising this region to the total luminosity of 36.1 fb^{-1} we find the number of events expected in that bin according to the standard model when only taking the SM sample. Now using Madgraph5 we also generate the interference contribution of each individual Wilson coefficient at value c_i . This cross section is then added to the STXS bin to get the expected value of events in the bin should this operator be present in the data. Finally the full dimension-6 contribution to the STXS cross section may also be simulated using Madgraph5. With this final part of the STXS cross-sections and interpolating for each value of c_i using analytical Lagrangian morphing we have a prediction for the cross section of the bin in terms of the theory. Extending this process to all of the STXS bins measured gives us a set of predictions for each bin in terms of the Wilson coefficients. Since the STXS bins only quote normalised cross sections, we also normalise our STXS predictions to the Standard Model. This results in a function for each bin linking the signal strength directly to the Wilson coefficients. The interference component (σ_{int}) and the full dimension-6 contribution (σ_{BSM}) to the standard model cross-section are then expressed according to

$$\mu_{STXSregion_i} = \frac{\sigma_{observed}}{\sigma_{SM}} = \frac{\sigma_{SM}}{\sigma_{SM}} + \frac{\sigma_{int}}{\sigma_{SM}} + \frac{\sigma_{BSM}}{\sigma_{SM}}. \quad (10.6)$$

This can be written as,

$$\mu_{STXSregion_i} = 1 + \sum_i A_i c_i + \sum_{ij} B_{ij} c_i c_j. \quad (10.7)$$

Here $c_{i,j}$ are the Wilson coefficients and A_i, B_{ij} are constants that are evaluated via simulation and illustrate the impact of that particular Wilson coefficients to the normalised cross section in the bin. In most cases the pure dimension-6 contribution is of very low impact and probably also beyond our sensitivity to probe. Since we are not taking this contribution into account we also will not probe the interference between different dimension-6 operators.

Now we have provided a parameterization of dimension-6 effects relative to the SM prediction. Because the reparameterization is normalised to the SM. The integrity of the sample structure used by the analyses is kept intact. These MC samples are state of the art (N)NLO simulated samples. When plugging this expression into the workspace of the analyses, the SMEFT interpretation only provides the LO corrections to the SM, this is now used to correct to NNLO samples to possible deviations in the data. The assumption that

is taken here is that the relative correction to the cross section is the same at LO as higher orders. Finally we now evaluate the inclusive cross section in a STXS bin as

$$\sigma_i = \sigma_{SM,i}^{(N)NLO} \times \left(1 + \frac{\sigma_{int,i}^{LO}}{\sigma_{SM,i}^{LO}} + \frac{\sigma_{int,i}^{BSM}}{\sigma_{SM,i}^{BSM}} \right), \quad (10.8)$$

when plugged into the workspace for each STXS bin i .

Because the HWW analyses targets the resonant Higgs production decaying into two vector bosons we need to take into account the Higgs branching ratio's. The on shell Higgs targeting the production cross section and the branching ratio can be evaluated separately. Therefore, the branching ratio is separately effected by the dimension-6 effects and can also be parameterised in terms of Wilson coefficients. In the analysis the cross section in the STXS bin is seen as

$$\sigma_{STXSregion_i}^{H \rightarrow W^+ W^- \rightarrow e\mu\nu_e\nu_\mu} = \sigma_i \times B^{H \rightarrow W^+ W^- \rightarrow e\mu\nu_e\nu_\mu}. \quad (10.9)$$

After the reparameterization of the branching ratio this becomes

$$\sigma_{STXSregion_i}^{H \rightarrow W^+ W^- \rightarrow e\mu\nu_e\nu_\mu} = \sigma_i \times \left(B_{SM}^{H \rightarrow W^+ W^- \rightarrow e\mu\nu_e\nu_\mu} + B_{int}^{H \rightarrow W^+ W^- \rightarrow e\mu\nu_e\nu_\mu} + B_{BSM}^{H \rightarrow W^+ W^- \rightarrow e\mu\nu_e\nu_\mu} \right). \quad (10.10)$$

A further challenge is also to take into account the acceptance of each STXS region to each of dimension-6 operators, one can imagine that if an effect is represented by an operators with a Wilson coefficient value of say 5, the dependence of this STXS cross section may shift towards other regions. Currently we are expecting only small deviations of the SM and is not taken into account. This dependence will hopefully be included in future work including the higher order terms e.g. $\frac{1}{\Lambda^4}$. When applying the assumptions explained above we arrive at the new cross section interpretation of the $H \rightarrow W^+ W^- \rightarrow e\mu\nu_e\nu_\mu$ STXS measurement used in this interpretation.

$$\sigma_{STXSregion_i}^{H \rightarrow W^+ W^- \rightarrow e\mu\nu_e\nu_\mu} = \left(\sigma_{SM,i}^{(N)NLO} \times \left(1 + \frac{\sigma_{int,i}^{LO}}{\sigma_{SM,i}^{LO}} \right) \right) \times \left(B_{SM}^{H \rightarrow W^+ W^- \rightarrow e\mu\nu_e\nu_\mu} + B_{int}^{H \rightarrow W^+ W^- \rightarrow e\mu\nu_e\nu_\mu} \right) \quad (10.11)$$

10.3.1 Parameterization of the STXS regions

The Monte Carlo generator used to model the hard process is Madgraph v2.6.2. and the parton showering is performed with Pythia8 v8.210. We will quickly recap the most important MC generation settings.

The modelling of the background is not necessary since we are working with the signal minus background signal region only. The parton distribution function LHAPDF-NPDF23LO(247000) [63] is used. For all of the samples the A14 Pythia8 tune is used [64]. All of the samples are generated with a Higgs boson mass of 125 GeV to be consistent with the $H \rightarrow WW$ analysis. In order to compute the event yields in each STXS region a SM LO sample is generated for the ggF and VBF Higgs production accompanied with a interference only sample for each Wilson coefficient setting the value to $c_i = 0.1$. This value is chosen instead of one to prevent Madgraph5 from generating extremely big corrections.

gluon gluon fusion	cross section [pb]
SM	45.25 ± 0.05
$c_i = 0.1$	correction to the prod. cross section [pb]
c_{HG}	125.96 ± 0.12
vector boson fusion	cross section [pb]
SM	3.343 ± 0.0043 pb
$c_i = 0.1$	correction to the prod. cross section [pb]
c_{HB}	$-0.6 \times 10^{-3} \pm 2.1 \times 10^{-5}$
c_{Hbox}	$0.03151 \pm 4.3 \times 10^{-5}$
c_{HDD}	$-0.029 \times 10^{-1} \pm 1.7 \times 10^{-5}$
c_{Hd}	$0.026 \times 10^{-1} \pm 8.2 \times 10^{-5}$
c_{Hl3}	$-0.095 \pm 1.2 \times 10^{-4}$
c_{Hq1}	$0.028 \times 10^{-1} \pm 3.9 \times 10^{-5}$
c_{Hq3}	$-0.12 \pm 1.6 \times 10^{-4}$
c_{Hu}	$-0.07 \times 10^{-1} \pm 1.16 \times 10^{-5}$
c_{HWB}	$-0.06 \times 10^{-1} \pm 3.29 \times 10^{-5}$
c_{HW}	$-0.02 \pm 2 \times 10^{-3}$
c_{ll1}	$-0.047 \pm 6.3 \times 10^{-5}$

TABLE 10.2: SM Higgs production cross sections for ggF and VBF accompanied with the corrections of SMEFT model for each operator

A total of 100.000 events have been generated per interference sample which are then passed through the STXS decoration cuts. This assigns every event in their respective stage 1 STXS fiducial region based on the requirements explained in the STXS framework chapter. The cutflow can be found in the Appendix C. Changes the EFT operators have propagated onto the STXS observables have now been translated into the STXS bins. All of the bins are normalised respectively to their cross section and passed to the analytical Lagrangian morphing package. This package provides an analytical function that links the truth event yield for each of the STXS bin to the Wilson coefficients that influence that particular bin. This can be seen in Fig. 10.9 or in Tab. 10.3.

Fiducial region	SM	c_{HB}	c_{HDD}	c_{HWB}	c_{HW}	c_{Hbox}	c_{Hd}	$c_{Hl}^{(3)}$	$c_{Hq}^{(1)}$	$c_{Hq}^{(3)}$	$c_{ll}^{(1)}$	c_{Hu}	c_{HG}
Vector Boson Fusion													
VBF topology cuts \approx 2-jet	1	-0.00185	-0.0110	0.0214	-0.07	0.121	0.00715	-0.365	0.00722	-0.344	0.182	-0.0201	
VBF p_T jet ¹ \geq 200	1	-0.0038	-0.0119	0.0499	-0.3063	0.12	0.0509	-0.3674	0.0666	-2.3095	0.1739	-0.1566	
VBF topology cuts \geq 3-jet	1	-0.0019	-0.0115	0.0227	-0.0869	0.1217	0.0092	-0.3656	0.0096	-0.4313	0.1847	-0.0275	
VBF VH cuts \geq 2-jet	1	-0.0023	-0.0108	0.0254	-0.0929	0.1175	0.0097	-0.3501	0.0106	-0.4306	0.1765	-0.025	
VBF rest	1	-0.0023	-0.0108	0.0236	-0.0716	0.1208	0.007	-0.3631	0.0072	-0.3209	0.1818	-0.0179	
VBF $Y_H > 2.5$	1	-0.0025	-0.0111	0.0269	-0.0862	0.1227	0.0064	-0.3593	0.0079	-0.3494	0.1808	-0.0225	
Gluon-Gluon Fusion													
gg2H 0-jet	1												97.6
gg2H 1-jet p_T^H [0,60]	1												87.4
gg2H 1-jet p_T^H [120,200]	1												85.0
gg2H 1-jet p_T^H [60,120]	1												82.3
gg2H 1-jet p_T^H [200, ∞]	1												73.9
gg2H VBF topology cuts \geq 3-jet	1												51.6
gg2H VBF topology cuts \approx 2-jet	1												66.17
gg2H $Y_H > 2.5$	1												87.3
gg2H 2-jet p_T^H [0,60]	1												63.9
gg2H 2-jet p_T^H [120,200]	1												82.3
gg2H 2-jet p_T^H [60,120]	1												64.3
gg2H 2-jet p_T^H [200, ∞]	1												50.0

TABLE 10.3: Reparameterization of the $H \rightarrow WW$ ggF + VBF STXS measurement, neglecting the mass of the light quarks and fermions. The acceptance dependence on the Wilson Coefficients is neglected in the parameterization

Following is the parameterization of the $H \rightarrow e\mu\nu e\nu\mu$ branching ratio. The impact of the EFT operators on this branching ratio is evaluated by simulating the decay widths $\Gamma^{H \rightarrow e\mu\nu e\nu\mu}$. Using the same method as for the production only samples. The Higgs Boson is assumed to be at rest and in the initial state. The definition of the decay we are looking for is defined by the analyses cuts as in Table 10.4.

Now the SM width of $\Gamma^{H \rightarrow e\mu\nu e\nu\mu}$ is calculated, then for each Wilson coefficient in the SMEFT framework the correction to SM the width is evaluated taking order up to $\frac{1}{\Lambda^2}$. Only the operators which have a significant effect on the decay width are used for the reparameterization. According to the PDG reviews [10] we expect a total Higgs SM width of $\Gamma_H = 4.07 \times 10^{-3} \text{ GeV}^{+4.0\%}_{-3.9\%}$. Which leads to a branching ratio of $H \rightarrow WW$ of about 21.4% and knowing that the branching ratio of a Vector boson decaying leptonically is about 30% of which 10% percent consists of tau decays. Since we are searching for to opposite flavour isolated leptons, the branching ratio for this happening is $B^{H \rightarrow WW \rightarrow e\mu\nu\nu} = 2.5 \times 10^{-3}$ [10]. Now multiplying this by because by two of the conjugate states yields about 0.05%. Which is consistent with the Madgraph5 calculations.

$\Gamma^{H \rightarrow e\mu\nu e\nu\mu}$	Width [GeV]	Normalised
SM	$2.027 \times 10^{-5} \pm 7.8 \times 10^{-8}$	1
$\Gamma^{H \rightarrow e\mu\nu e\nu\mu} c_i = 0.1$	correction to the SM Width [GeV]	Normalized with $c_i = 1.0$
c_{HDD}	$-6.1 \times 10^{-8} \pm 8.1 \times 10^{-10}$	-0.0303
c_{HW}	$-1.8 \times 10^{-7} \pm 2.4 \times 10^{-10}$	-0.0901
$c_{H\Box}$	$2.5 \times 10^{-7} \pm 9.5 \times 10^{-10}$	0.1213
$c_{Hl}^{(3)}$	$-4.6 \times 10^{-7} \pm 1.7 \times 10^{-9}$	-0.2287
$c_{ll}^{(1)}$	$3.7 \times 10^{-7} \pm 1.4 \times 10^{-9}$	0.1818

TABLE 10.4: Partial SM Higgs decay width and the relative SMEFT correction to the $\Gamma^{H \rightarrow e\mu\nu e\nu\mu}$ decay width using the \hat{M}_W input scheme. Taking a Higgs mass of $m_H = 125$ GeV and taking into account fermion masses.

We end up with a equation that parameterizes the branching ratio of the searched after signal and is inserted in each of the STXS regions. This is all taking into account the narrow width approximation of both H and W^\pm , since then one just has

$$\frac{B_{H \rightarrow e\mu\nu\nu}^{SMEFT}}{B_{H \rightarrow e\mu\nu\nu}^{SM}} = \frac{\Gamma_{H \rightarrow e\mu\nu\nu}^{SMEFT}}{\Gamma_{H \rightarrow e\mu\nu\nu}^{SM}} = 1 + \sum_i \frac{\delta\Gamma_{c_i}}{\Gamma_{H \rightarrow e\mu\nu\nu}^{SM}}, \quad (10.12)$$

Taking into account off-shell effects and beyond LO precision this description changes and needs to be revised, however for the purpose of this thesis we will leave it like this and arrive at

$$\frac{B_{H \rightarrow e\mu\nu\nu}^{SMEFT}}{B_{H \rightarrow e\mu\nu\nu}^{SM}} = 1 - 0.0303 \cdot c_{HDD} - 0.0901 \cdot c_{HW} + 0.121 \cdot c_{H\Box} - 0.229 \cdot c_{Hl}^{(3)} + 0.182 \cdot c_{ll}^{(1)}. \quad (10.13)$$

The final reparameterization for the $\Gamma^{H \rightarrow e\mu\nu e\nu\mu}$ STXS measurement is graphically shown in Fig 10.9.

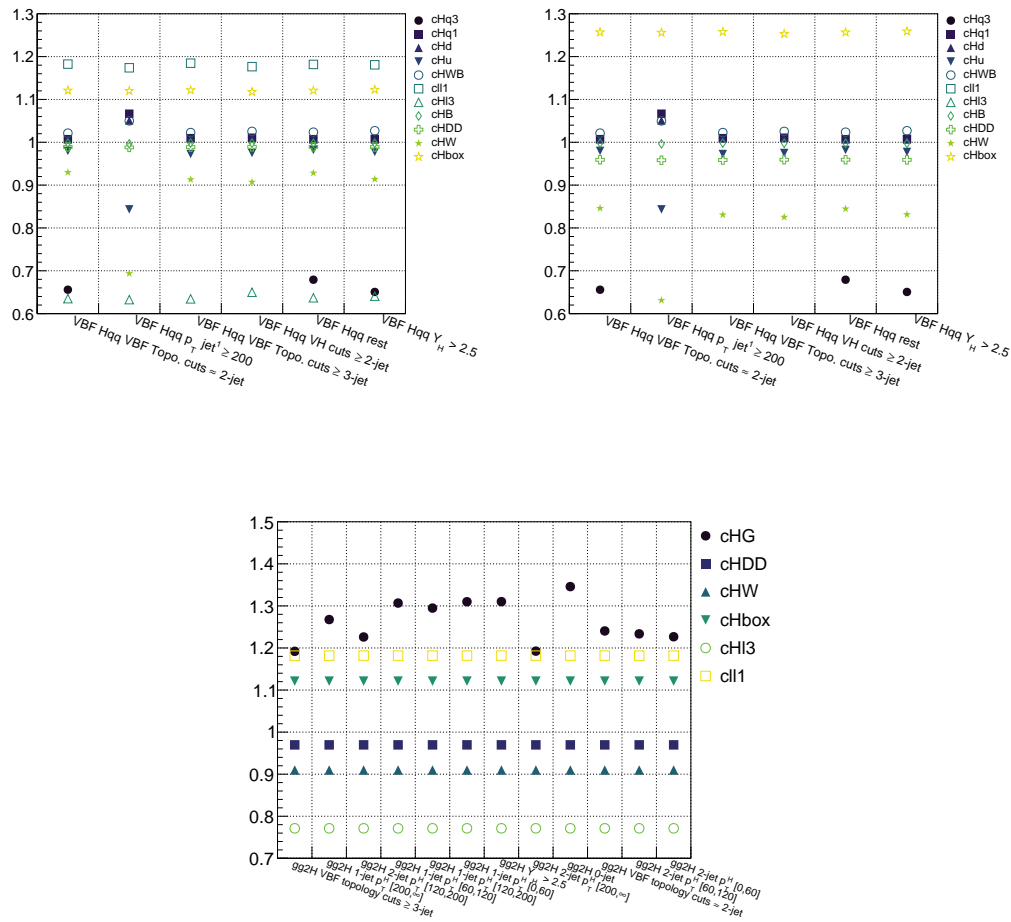


FIGURE 10.9: The nominal change that each Wilson coefficient c_i introduces to the signal strength. Top left, impact of c_i on the VBF STXS signal strength taking into account production only. Top right, impact of c_i on the VBF STXS signal strength taking into account production and decay. Bottom, impact of c_i on the ggF STXS signal strength taking into account production and decay. c_i is set to 1 for the deviations, for c_{HG} the value is 0.01

Chapter 11

Individual and simultaneous Wilson Coefficient fitting

In this Chapter the fits will be performed and the data set is gradually build up section by section to include up to 17 operators.

In order to constrain the Wilson coefficients using the data, a likelihood fit of the combined STXS bins is used. Signal strength modifiers for each fiducial region are reparameterised as a function of the Wilson coefficients according to chapter 10. We perform fits on each of the single measurements and combine them as we continue to monitor the impact of the combinations. The best-fit values and the 68% C.L. ranges in the Warsaw basis are reported. All individual fits are performed by setting the fitted operator floating while fixing the others at zero. Simultaneous fits are performed letting every parameter of interest c_i float. The errors reported include both the systematic and statistical uncertainties. Generally, the uncertainties in each operator coefficients become smaller when incorporating additional data. The constraints that are obtained from each data set is shown in Tab. 11.1.

11.1 $ggF \rightarrow H \rightarrow WW$ analysis

The first measurement we are evaluating is the $ggF \rightarrow H \rightarrow WW$ measurement. This measurement is able to constrain the c_{HG} operator as it directly probes the top loop. It also offers the highest precision signal strength for the ggF 0-jet bin and is thus well equipped to constrain the operators entering the the Higgs branching ratio. The c_{HG} operator is the only contribution that introduces shape effects in the STXS bins. While the other operators all enter in the branching ratio as a normalisation. In Figure 11.1 the correlation matrix of the Wilson coefficients is shown. The matrices shown in this chapter are calculated using the hessian approximation of the likelihood.

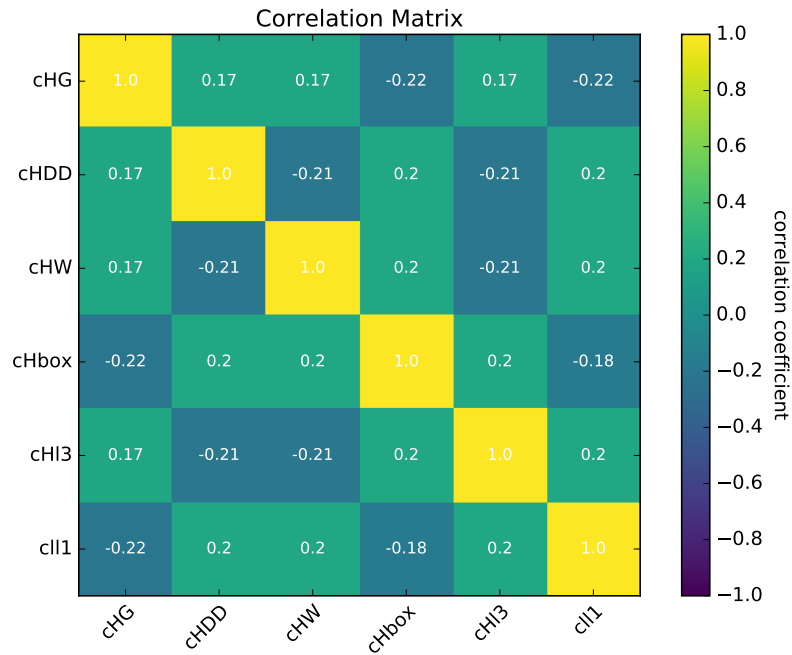


FIGURE 11.1: Matrix of correlation among the operators that enter in the ggF measurement.

In the correlation matrix we see negative correlation between the operators c_{HG} and c_{HW} as expected as they change the normalisation the distribution in different directions. The correlations between the other operators are also of expected sign.

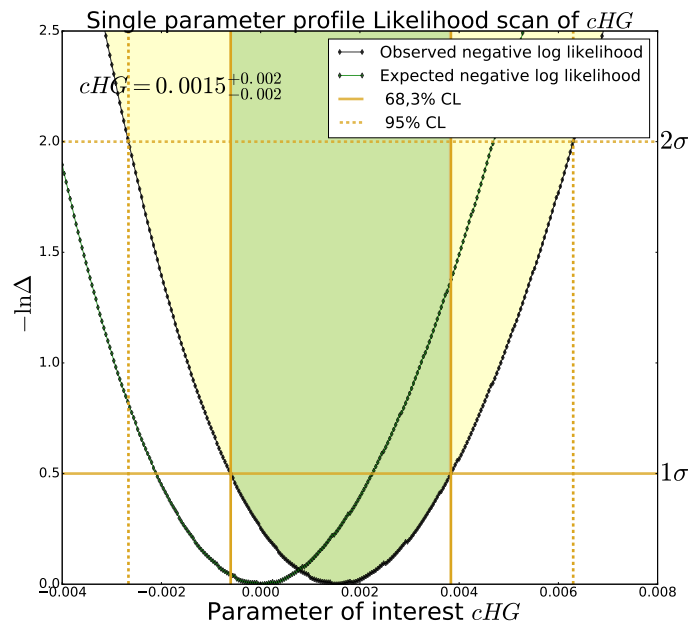


FIGURE 11.2: Profile Likelihood scan of the c_{HG} operator. Shown are likelihood scans corresponding to the observed data and the expected Asimov data representing the Standard Model prediction $c_{HG} = 0$. The horizontal lines represent the respective confidence levels.

In order to check if the fit behaves as expected the likelihood of the parameter of interest is scanned. This is done by first fitting all of the parameters of interest to their best fit value, then varying the parameter of interest over a range and calculating the Negative Log likelihood (NNL). Which is half of the test statistic and corresponds to the significance exclusion levels. For a succeeded fit, the scan should have a minimum at the best-fitted value. For the c_{HG} fit using the ggF data we find the likelihood scan in Fig. 11.2. Additionally a measurement on Asimov data using the Standard Model hypothesis is conducted, showing the expected Standard Model case. A profile likelihood scan has been made for every fit and can be found in Appendix D.

11.2 $VBF \rightarrow H \rightarrow WW$ analysis

The second measurement is the $VBF \rightarrow H \rightarrow WW$ analyses. This measurement introduces the coupling of Higgs to light quarks via the vector boson fusion. There are also operators which enter in both the decay and production vertices, which makes it so that these are better constrained using this measurement. Some of the operators are barely constrained using this measurement only but are kept because of the future combination of data with other measurements. In Fig. 11.3 the correlation matrix is shown. This matrix does not include c_{HB} since these operator show low sensitivity and will not be fitted simultaneously.

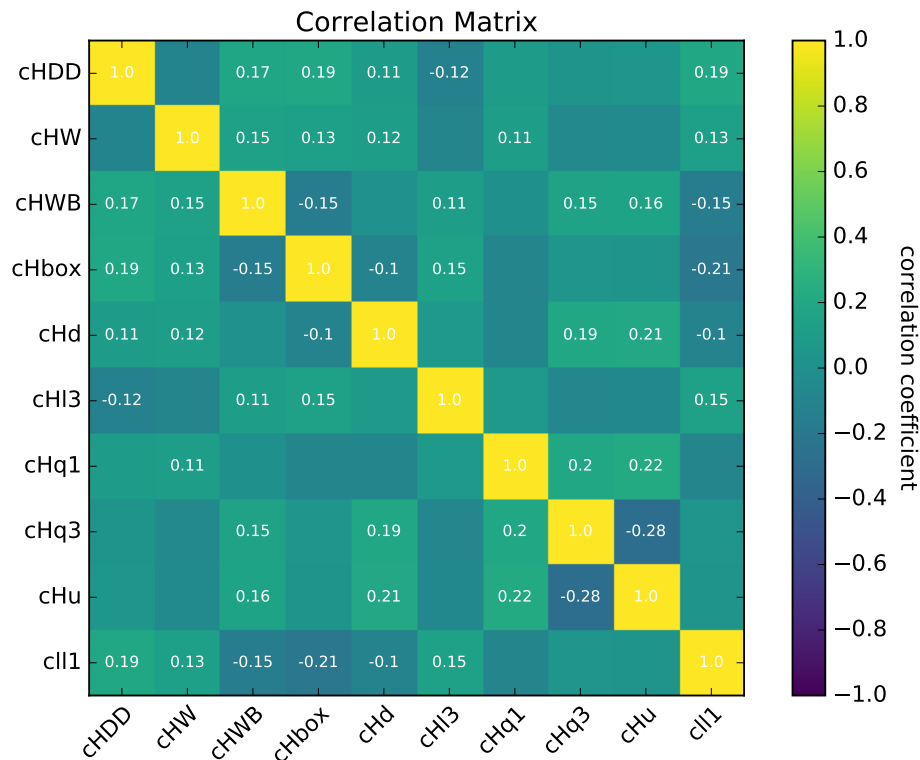


FIGURE 11.3: Matrix of correlation among the operators that enter in the VBF measurement.

11.3 $qq/gg \rightarrow W^+W^-$ analysis

The inclusion of the $qq/gg \rightarrow W^+W^-$ (SMWW) measurement allows the possibility to explore a new set of operators involving the direct WW couplings in addition to the Higgs operators and also directly probes the light quark and fermion couplings. In addition providing extra data on the couplings that are also influencing the Higgs observables. The knowledge of the extra operators can introduce more or remove correlations. This workspace fits all of the possible EFT effects to the distribution of the leading lepton transverse momentum $p_T^{lead,l}$ shown in Fig. 9.5, which is the background subtracted data. The uncertainties of the measurement are taken into account in the nuisance parameters accompanied with the workspace. This measurement introduces the sensitivity to the operators involving light fermions in the Warsaw basis. As well as the operator c_W which introduces a triple gauge coupling. In Fig. 11.4 the correlation matrix is shown. The correlations look to be higher compared to the Higgs operators, this is because the operators are fitted on a single distribution.

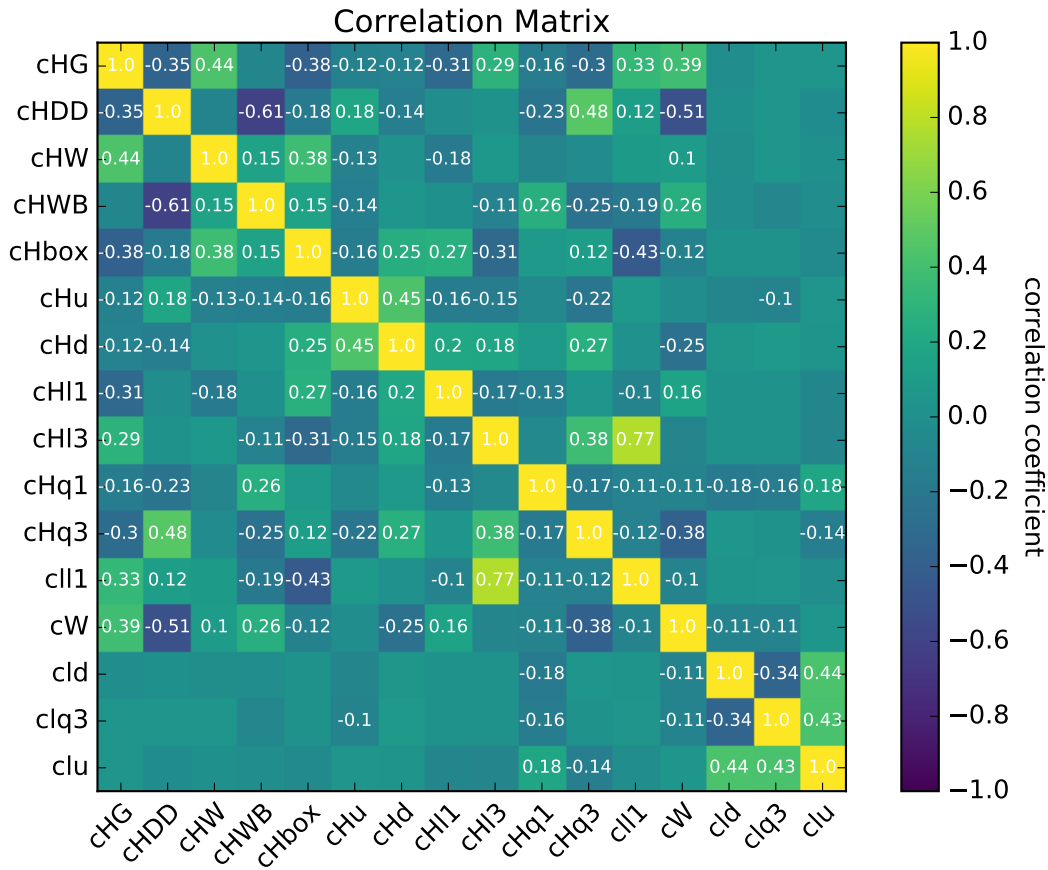


FIGURE 11.4: Matrix of correlation among the operators that enter in the SMWW measurement.

11.4 Combined $ggF + VBF \rightarrow H \rightarrow W^+W^-$ analysis

In the combined ggF and VBF (HWW) measurement the overlapping control regions in both measurements get correlated. Also all of the parameters that carry the same name and thus introduce the same effects get correlated. This results in a bigger data set for the all of the parameters introduced. In Fig. 11.5 the correlation matrix is shown.

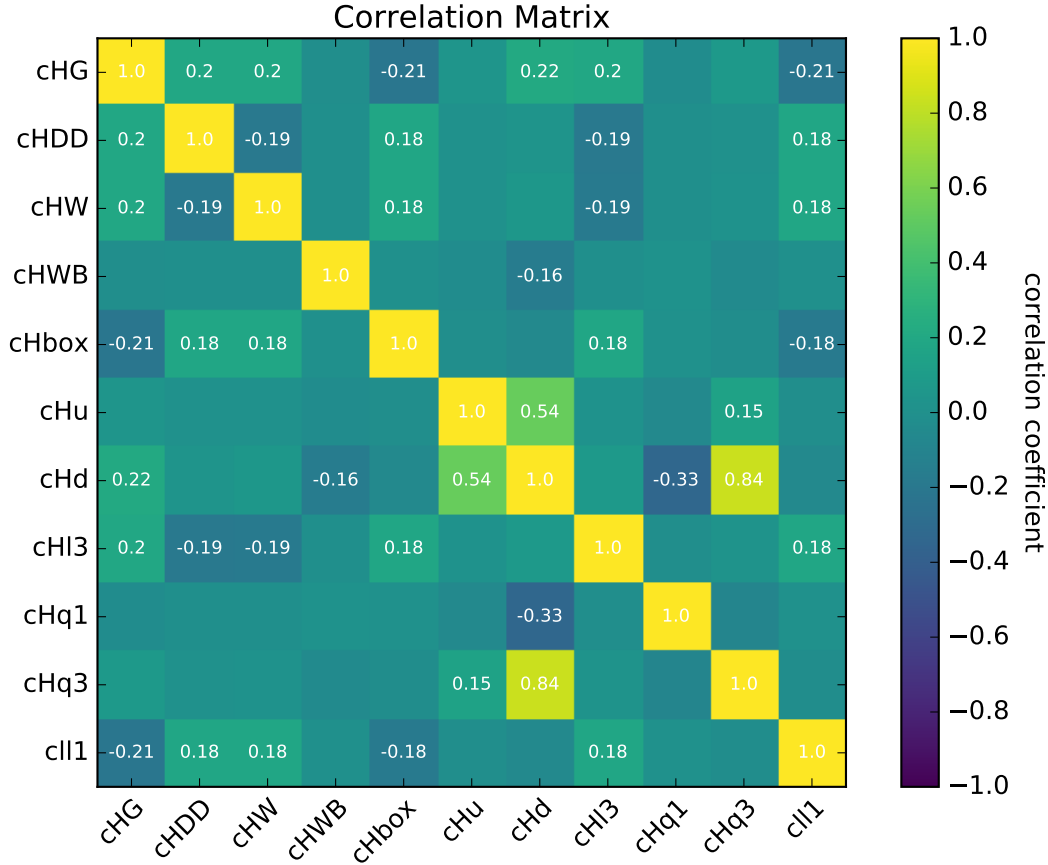


FIGURE 11.5: Matrix of correlation among the operators that enter in the HWW measurement.

11.5 Combined $ggF + VBF \rightarrow H \rightarrow W^+W^- + qq/gg \rightarrow W^+W^-$ analysis

The combination of the SMWW and HWW measurements made by taking out the $WW0-jet$ control region of the HWW measurement and replacing it with the SMWW measurement. Essentially introducing another signal region. The normalisation of the $WW0-jet$ background for the VBF and ggF processes is correlated with the normalisation used in the SMWW measurement. Also the uncertainty on the PDF and the scale uncertainties are replaced with the SMWW uncertainties. The correlation scheme is located in Appendix E. In Fig. 11.6 the correlation matrix is shown. The operator c_{HB} from the HWW VBF measurement is not taken into account. The nuisance parameter pull of the c_{HG} and $c_{HI}^{(3)}$ can be found in Appendix D.

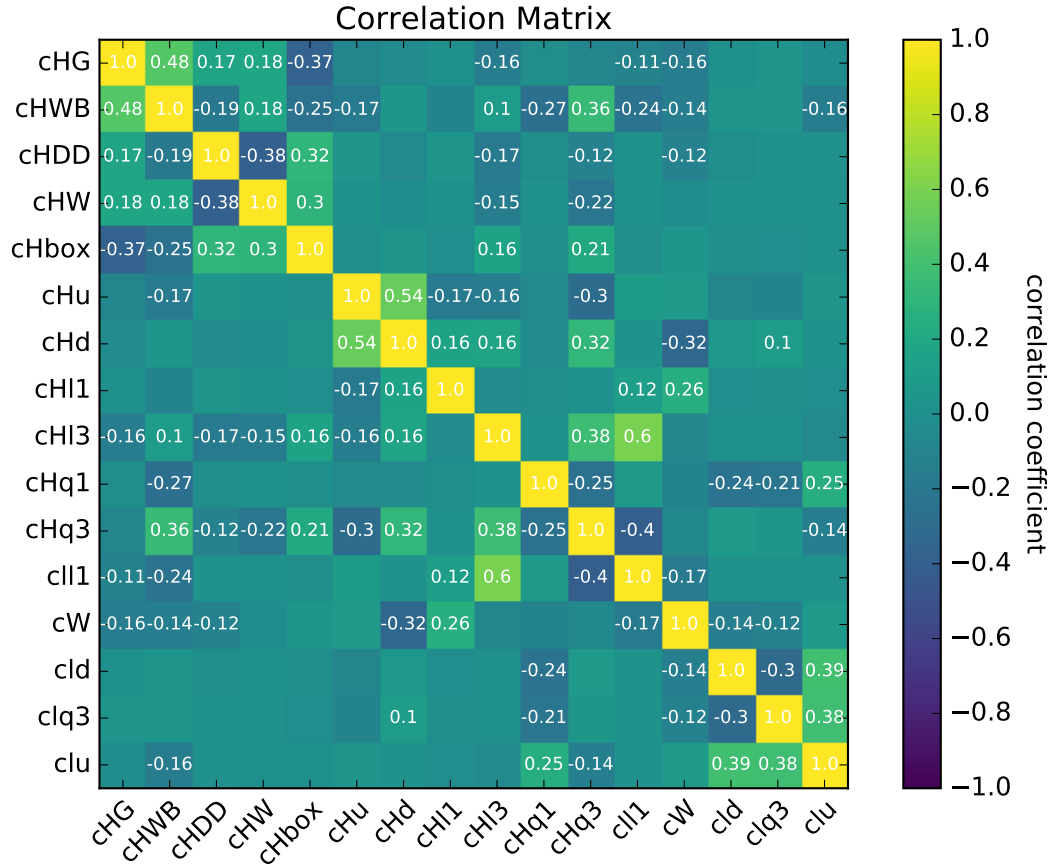


FIGURE 11.6: Matrix of correlation among the operators that enter in the HWW + SMWW combined measurement.

11.6 Individual fit results

In this section the results of each combination are presented. Comparisons of the Wilson coefficients limits are made after each iteration of combinations of the EFT interpretations. In Table 11.1 the results of the individual measurements and the combined measurements are shown.

Wilson Coefficients c_i	Gluon-Gluon fusion	Vector Boson fusion	HWW combined (ggF + VBF)	SM WW 0-jet	HWW + SMWW combination
c_{HG}	$0.0015^{+0.002}_{-0.002}$	-	$0.0013^{+0.002}_{-0.002}$	$0.048^{+0.14}_{-0.13}$	$0.0013^{+0.002}_{-0.002}$
c_{HB}	-	0.005^{+299}_{-82}	184^{+160}_{-170}	-	178^{+162}_{-166}
c_{Hbox}	$1.0^{+1.8}_{-1.7}$	$-1.6^{+1.7}_{-2.2}$	$-0.45^{+1.0}_{-1.1}$	20^{+43}_{-41}	$-0.76^{+1.0}_{-1.1}$
c_{HDD}	$-4.2^{+6.8}_{-7.0}$	$-8.9^{+11}_{-9.8}$	$-1.05^{+5.1}_{-4.9}$	$11^{+25.9}_{-28}$	$3.0^{+5.2}_{-4.9}$
$c_{HI}^{(1)}$	-	-	-	-163^{+102}_{-93}	-199^{+96}_{-96}
$c_{HI}^{(3)}$	$-0.51^{+0.86}_{-0.97}$	$-0.62^{+0.87}_{-0.69}$	$-0.25^{+0.51}_{-0.46}$	$-0.636^{+0.32}_{-0.32}$	$-0.48^{+0.25}_{-0.23}$
$c_{HI}^{(1)}$	-	0.02^{+58}_{-59}	-26^{+26}_{-24}	$0.12^{+1.4}_{-1.1}$	$-0.28^{+1.1}_{-1.4}$
$c_{HIq}^{(3)}$	-	$0.59^{+0.65}_{-0.67}$	$0.63^{+0.61}_{-0.63}$	$0.41^{+0.36}_{-0.33}$	$0.62^{+0.31}_{-0.29}$
c_{Hu}	-	9.5^{+10}_{-11}	$10^{+9.6}_{-10}$	$-1.1^{+1.4}_{-1.1}$	$-1.2^{+1.4}_{-1.2}$
c_{Hd}	-	-28^{+32}_{-30}	-29^{+29}_{-29}	$4.1^{+3.7}_{-4.5}$	$-4.4^{+3.7}_{-4.5}$
c_{HWB}	-	10.4^{+27}_{-26}	-15^{+14}_{-13}	10^{+26}_{-26}	-7.9^{+13}_{-13}
c_{HW}	$-1.45^{+2.3}_{-2.3}$	$2.0^{+2.8}_{-2.2}$	$0.58^{+1.4}_{-1.3}$	-82.0^{+77}_{-79}	$-0.95^{+1.4}_{-1.3}$
c_W	-	-	-	$4.70^{+2.6}_{-2.6}$	$6.04^{+2.7}_{-2.6}$
$c_{II}^{(1)}$	$0.73^{+1.1}_{-1.2}$	$-1.0^{+1.1}_{-1.5}$	$-0.29^{+0.68}_{-0.71}$	$-0.58^{+0.32}_{-0.30}$	$-0.58^{+0.26}_{-0.26}$
c_{ld}	-	-	-	$-0.512^{+4.318}_{-3.6}$	$-1.35^{+4.2}_{-3.5}$
$c_{lq}^{(3)}$	-	-	-	$-0.024^{+0.14}_{-0.16}$	$-0.053^{+0.16}_{-0.14}$
c_{lu}	-	-	-	$-0.048^{+1.3}_{-1.1}$	$-0.28^{+1.1}_{-1.3}$

TABLE 11.1: Numerical results of the different stages of data combinations and the combined HWW + SMWW individual fits to data, evaluated in the Warsaw basis.

This table shows the results for the best-fit values and their 68%CL ranges in the Warsaw basis where every operator is set to float individually. The error bars are the fit error including the systematic and statistical errors of all of the combined measurements. For the different Wilson coefficients in the basis, a stripe means no sensitivity to the operator in question. A graphical depiction is shown in Fig. 11.7. In Fig. 11.8 and 11.9 a comparison relative comparison of the best fit values is made between the *HWW* only constraints and the combined *SMWW* + *HWW* showing the importance of the combination for the operators involving the Higgs particle which the Higgs only measurement is having a hard time to constrain.

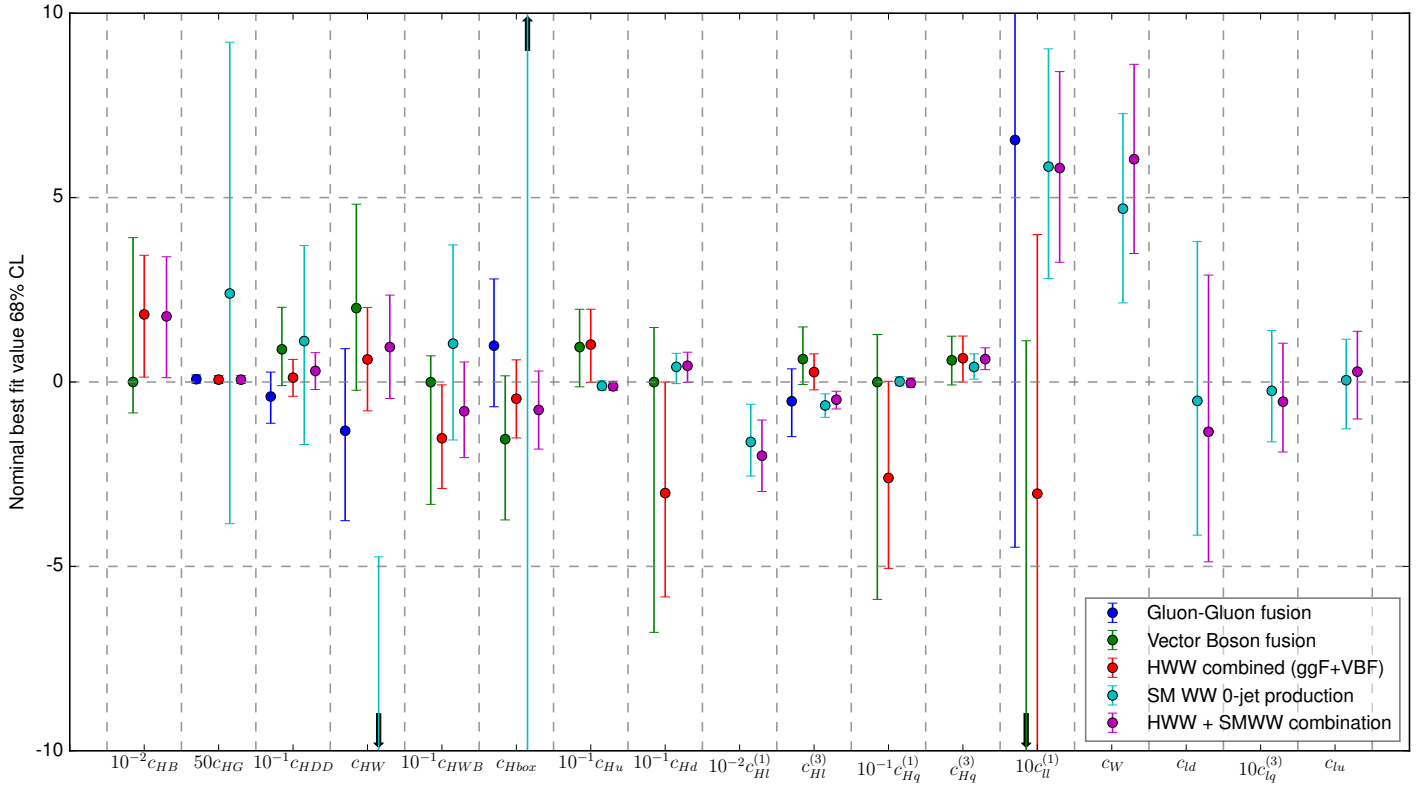


FIGURE 11.7: Results of the individual fits in the Warsaw basis. Showing the best fit values including the 68%CL of each of the measurement and combination made

Taking the smallest constraints out of both the measurements and comparing them to the combined measurements show that both analyses have gained from the combination in the region where the Higgs and the light fermions interact. Notice that the *HWW* measurement is not very sensitive to the operators involving light fermions, this is compensated by the addition of the *SMWW* measurement. Minor improvement is seen in the c_{HB} , c_{HWB} when combining with the *SMWW* measurement. The biggest improvements are found on the operator constraints of c_{Hu} , c_{Hd} , $c_{Hl}^{(3)}$, $c_{Hq}^{(1)}$, $c_{Hl}^{(3)}$ and $c_{ll}^{(1)}$. The overall sensitivity is increased for to the operators c_{HWB} , c_{Hu} , c_{Hd} , $c_{Hl}^{(1)}$, $c_{Hl}^{(3)}$, $c_{Hq}^{(3)}$, $c_{ll}^{(1)}$, c_{ld} , $c_{lq}^{(3)}$ and c_{lu} . Shown in Fig. 11.8 and 11.9.

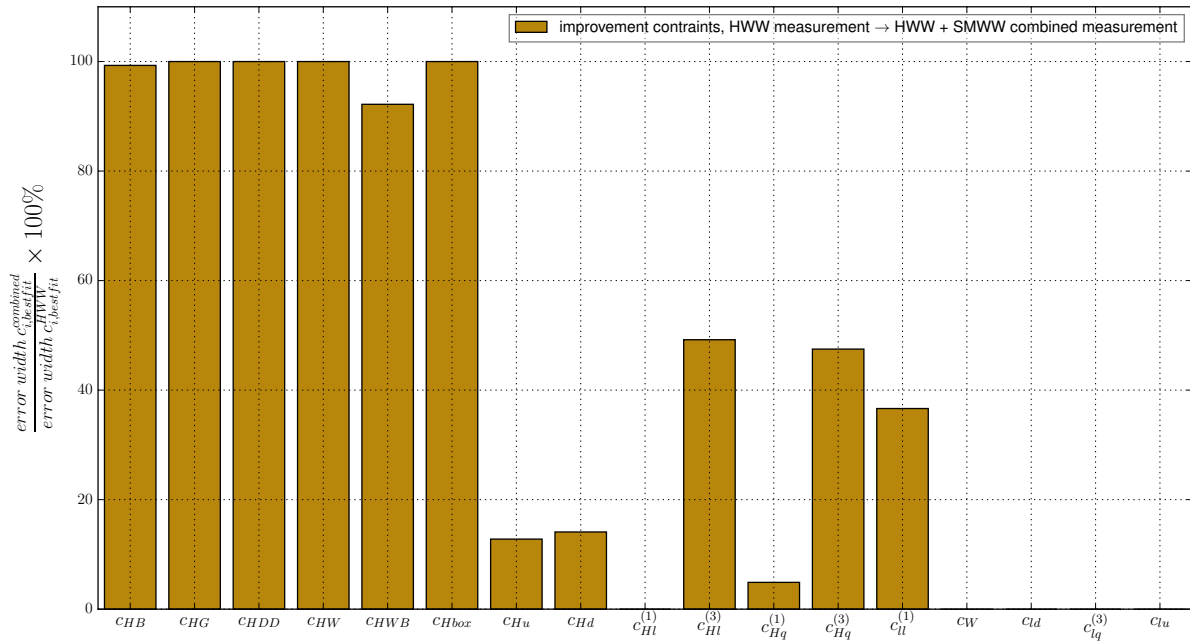


FIGURE 11.8: The improvement of the standard deviations of the Individually fitted Wilson coefficients in the Warsaw basis when adding the SMWW data to the HWW measurement

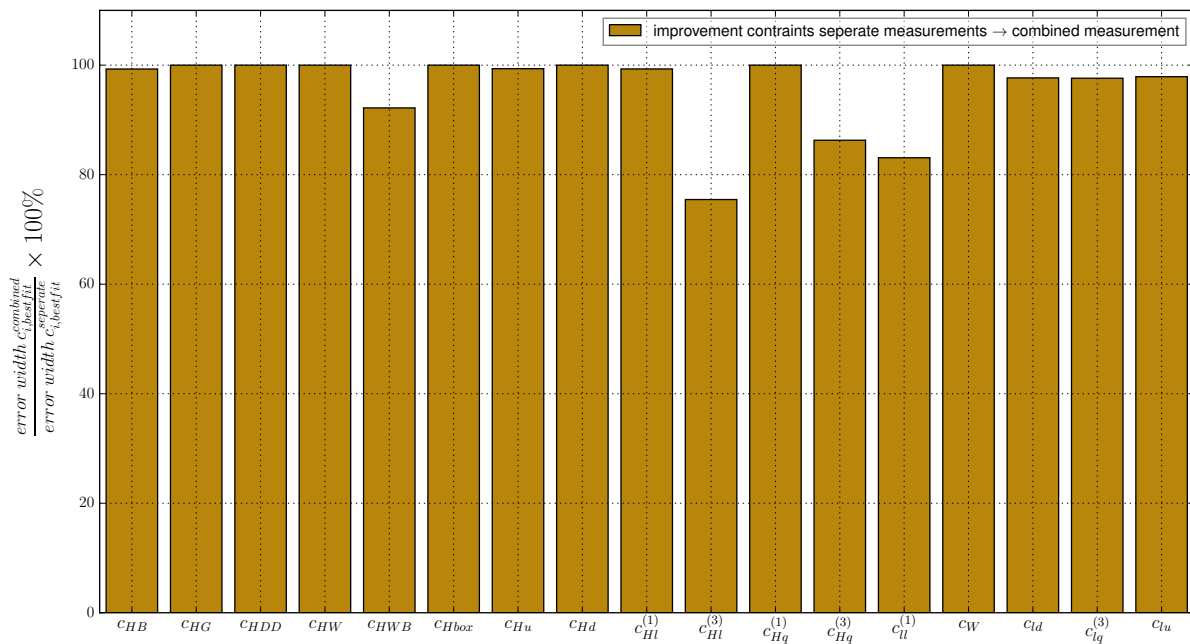


FIGURE 11.9: The improvement of the standard deviations of the Individually fitted Wilson coefficients in the Warsaw basis when comparing the best constrained value of each of the measurements and comparing it to the combined measurement results

11.7 Simultaneous fits

When fitting multiple parameters at the same time one needs to be considerate which effects they have on the distributions. In this part some parameter combinations considered to be well constrained by the model are shown. Other parameters are problematic

to fit together since they introduce the same changes in the distribution. An example of this is the parameters that introduce a simple normalisation effect. These operators are best fitted one at a time since different normalisation effects cannot be separated from each other if the effect is of relatively same magnitude. Also operators that cause the same shape effect result in large errors in the simultaneous fits.

11.7.1 Individual measurements versus combined measurements

In this section we will fit the operators $c_{Hl}^{(3)}$, $c_{Hq}^{(3)}$ and $c_{Hq}^{(1)}$ simultaneously by selecting 2 operators at a time and cycling between them. These operators were chosen because they received the most improvement after the combination. To illustrate the improvement of the combination measurement with respect to the individual HWW measurement in terms of these constraints. First, we focus on the HWW EFT interpretation alone. The constraints we obtained after HWW fitting are visible in the table below. Table 11.2. Also provided is the 2D likelihood scan, this scan computes the likelihood for each point in the 2D operator space. These are shown for the HWW data set in Fig. 11.10 and for the combined dataset in Fig. 11.11.

#fit	$c_{Hl}^{(3)}$	$c_{Hq}^{(3)}$	$c_{Hq}^{(1)}$	#fit	$c_{Hl}^{(3)}$	$c_{Hq}^{(3)}$	$c_{Hq}^{(1)}$
1	$-0.347^{+0.82}_{-0.86}$	$0.970^{+0.90}_{-1.04}$	-	1	$-0.33^{+0.28}_{-0.27}$	$0.44^{+0.33}_{-0.32}$	-
2	$-0.335^{+0.82}_{-0.85}$	-	$-38.8^{+42.0}_{-36.5}$	2	$-0.49^{+0.24}_{-0.25}$	-	$-0.30^{+1.51}_{-1.45}$
3	-	$0.723^{+5.46}_{-5.61}$	3.22^{+197}_{-203}	3	-	$0.67^{+0.30}_{-0.29}$	$-1.40^{+1.77}_{-1.52}$

TABLE 11.2: Results from the simultaneous fits to the c_{Hq} and c_{Hl} operators. Left, the results from the HWW data only. Right, the results from the total combined dataset.

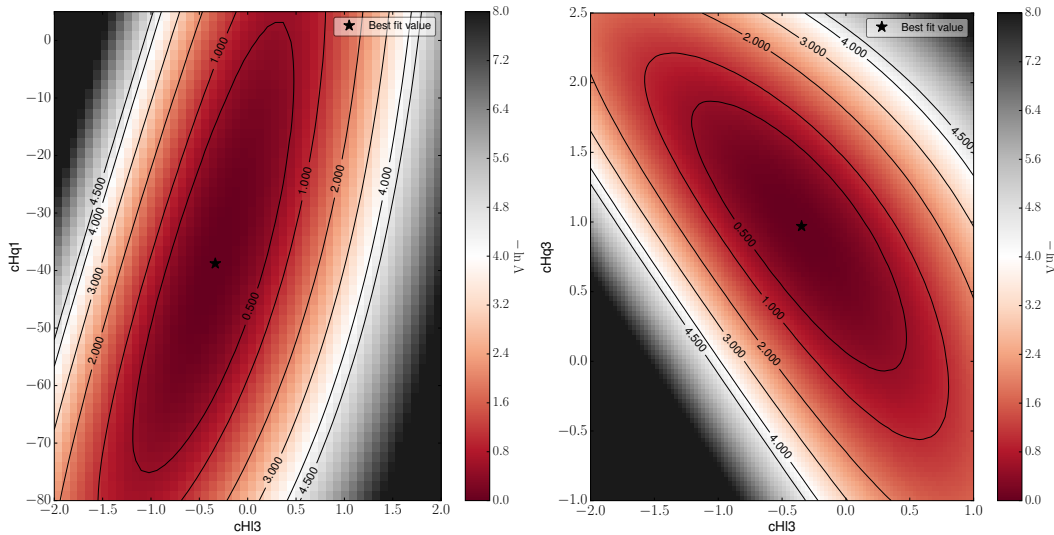


FIGURE 11.10: 2D likelihood scans after the fit is performed on the 2-operator model using only the HWW data. left, the likelihood for the operator model of $c_{Hl}^{(3)}$ and $c_{Hq}^{(3)}$. Right, the likelihood for the operator model of $c_{Hl}^{(3)}$ and $c_{Hq}^{(1)}$. The z-axis corresponds to the likelihood and is indicated by colour. Also the best fit value is shown.

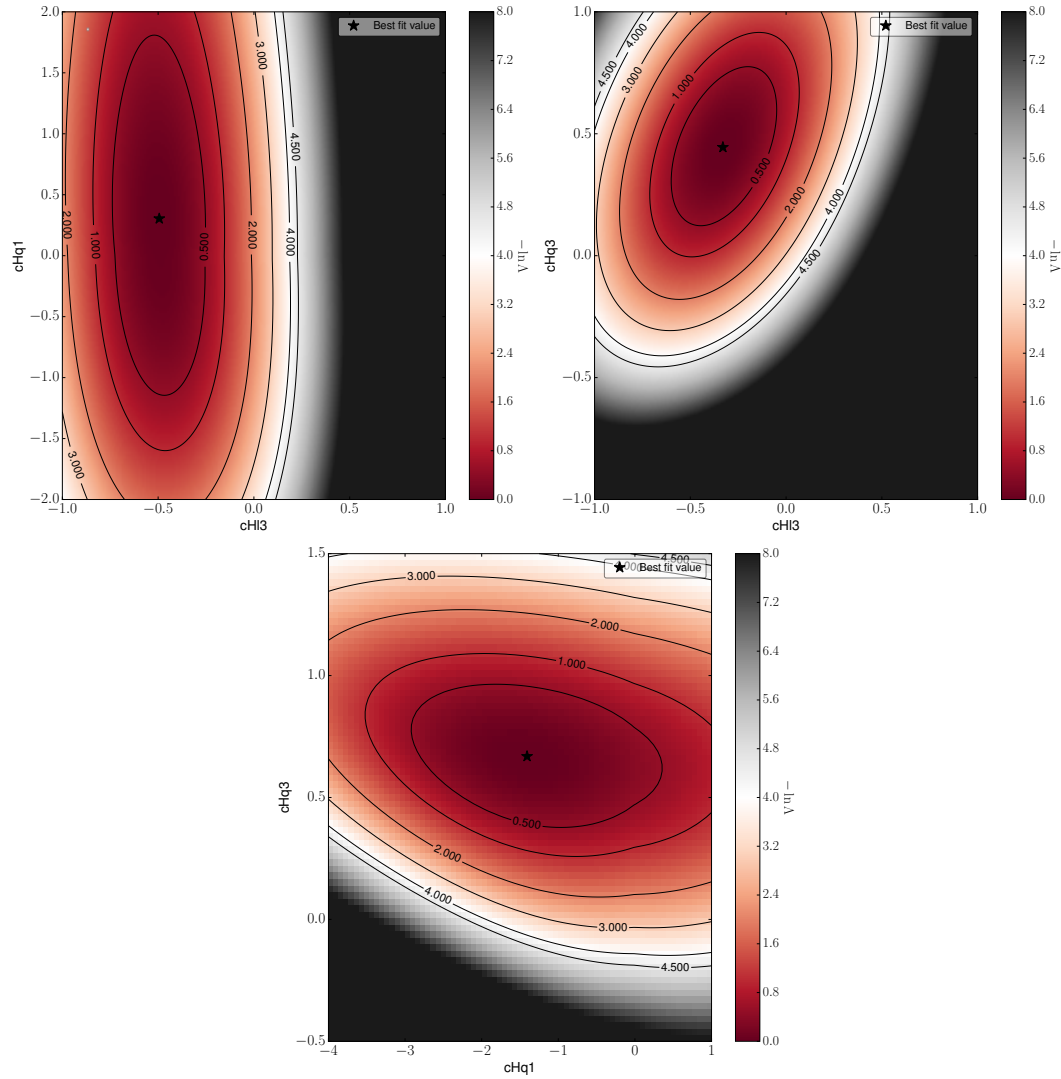


FIGURE 11.11: 2D likelihood scans after the fit is performed on the 2-operator model using the full combined HWW+SMWW dataset. left, the likelihood for the operator model of $c_{Hl}^{(3)}$ and $c_{Hq}^{(1)}$. Right, the likelihood for the operator model of $c_{Hl}^{(3)}$ and $c_{Hq}^{(1)}$. Below, the likelihood for the operator model of $c_{Hq}^{(3)}$ and $c_{Hq}^{(1)}$. The z-axis corresponds to the likelihood and is indicated by colour. Also the best fit value is shown.

The correlation matrix, Fig. 11.12, of the three parameters also shows that the parameters are not able to be constrained using only HWW data.

In this study we find that by that addition of the SMWW dataset, the $c_{Hq}^{(3)}$ operator can be constrained within the limits of ± 2 together with the $c_{Hq}^{(1)}$ operator. Using only the HWW dataset this operator combination caused such high limits that it could not be constrained. Therefore, the added value of the extra dataset is high and paves the way for more data combinations in the future.

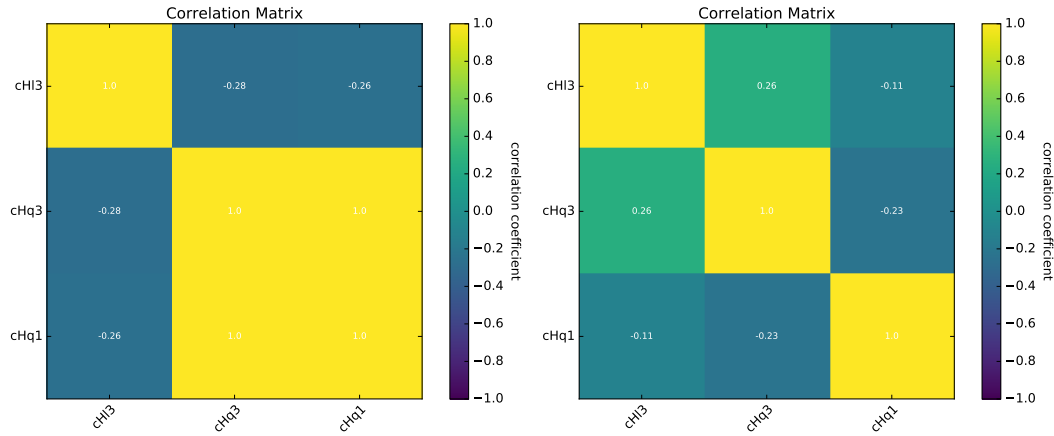


FIGURE 11.12: Correlation matrices of $c_{HI}^{(3)}$, $c_{Hq}^{(3)}$ and $c_{Hq}^{(1)}$ operator fits. Left, the correlation matrix using HWW data. Right, the correlation matrix using SMWW+HWW data.

11.8 Sanity check

In order to make sure that the fits succeeded we normally look at the likelihood plots and the pull of the nuisance parameters. However, a added value is to check whether the new constraints on the individual Wilson coefficients fall in between the limits of the signal strengths that we used as an input for the HWW analysis. In addition, that the extra sensitivity to some of the operators that we obtain does not violate the HWW predictions for the signal strength of the STXS regions that particular operator also influences. So we compare the unaltered signal strength measurement of the HWW STXS measurement to the signal strength predictions limits of the newly constrained operators. First we check for the c_{HG} operator since we obtain the best constraints on this operator. For this operator the VBF signal strengths are left freely floating, while the ggF signal strength are linked to the value of c_{HG} , see Fig 11.13. Interesting is to check if the also holds for the operators that had a hard time being constrained, such as c_{HB} . Which we actually could not constrain at all. For this fit the ggF signal strength are left floating, see Fig. 11.14. It is also viable to check whether the operators that enter in both channels also obey this requirement. In Fig. 11.15. After seeing that for these three cases the signal strength predictions are within the errors of the initial measurement, we conclude that the fit has provided reliable results in accordance with the intended method.

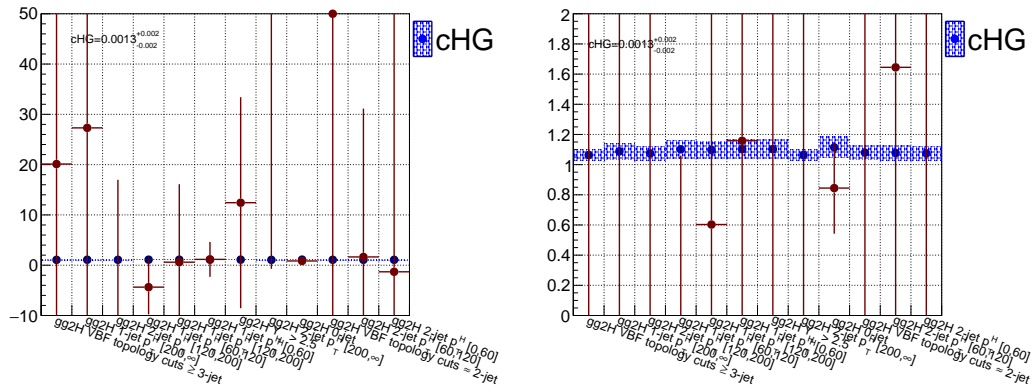


FIGURE 11.13: Post fit plot of the operator c_{HG} comparing it to the input signal strengths of ggF

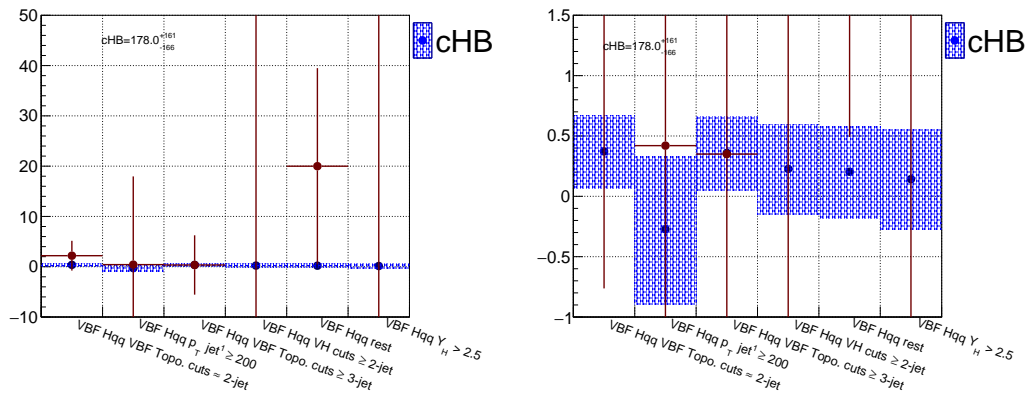


FIGURE 11.14: Post fit plot of the operator c_{HB} comparing it to the input signal strengths of VBF

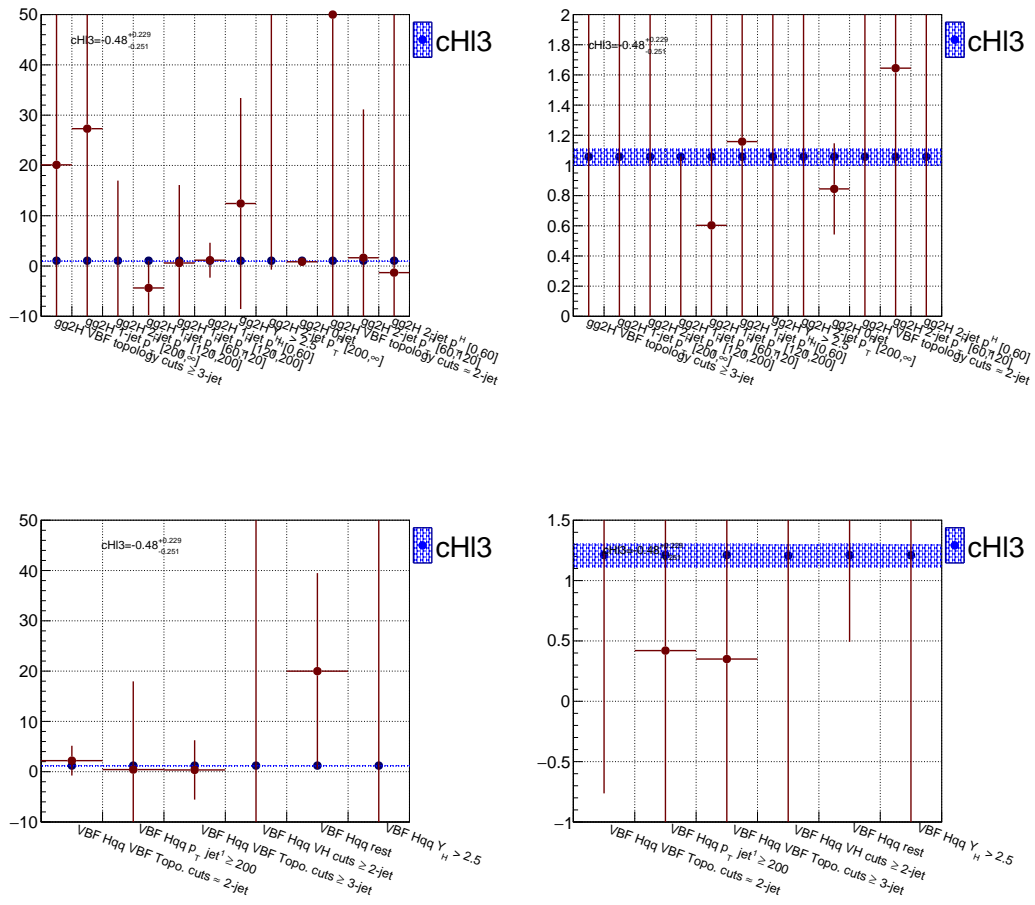


FIGURE 11.15: Post fit plot of the operator $c_{HI}^{(3)}$ comparing it to the input signal strengths of ggF and VBF

Chapter 12

Results

Constraints on operators of the Standard Model effective field theory affecting Higgs and charged vector boson interactions are determined using simplified template cross sections and an unfolded differential cross section. The interpretation takes into account 17 dimension-6 operators. The uncertainties enter the fit as nuisance parameters in the likelihood function. Constraints on the Wilson coefficients corresponding to EFT operators, up to $1/\Lambda^2$, are summarised in Fig. 11.7 and Tab. 11.1. Fig. 11.8 shows the improvement of the sensitivity to the operators after adding the $qq/gg \rightarrow W^+W^- \rightarrow e\nu\mu\nu$ data. Fig. 11.9 shows the overall improvement in sensitivity. Correlations between the Wilson coefficients are shown in Fig. 11.6. The combination of different analyses has proven to better constrain Wilson coefficients when doing simultaneous fits, shown in Fig. 11.11.

Chapter 13

Discussion and conclusion

The added value of the combination is the increased sensitivity to the operators involving light fermions. As a result of this combination, the data is analysed jointly, revealing and lifting correlations between the EFT operators. The lifting of correlations allows for the simultaneous fitting of the Wilson coefficients. This is preferable since it provides a more accurate description of the data. We find a slight 1σ deviation from the SM for the Wilson coefficients $c_{Hl}^{(3)}$, $c_{Hq}^{(3)}$, c_W and $c_{ll}^{(1)}$. However, this deviation is not sufficient to be observed as deviations from the SM predictions. The results indicate a promising sensitivity should we move towards the full run-2 dataset of 80 fb^{-1} or even 300 fb^{-1} envisioned for run-3. We expect a substantial increase in the amount of information from diboson and Higgs production, resulting in better constraints for our operators. The constraints presented in this analysis do not improve on the constraints already set by the Global SMEFT fit [60].

When performing the fits to multiple parameters at the same time, high correlations between operators were observed. This complicated the fit and resulted into a maximum of two operators fitted simultaneously during this study. Additional studies are needed to improve and completely analyse the 17-dimensional operator-space of the model build during this research.

In order to improve the constraints of the Wilson coefficients presented in this study, we do not only ask for more pp -collisions. We also need to extract more information out of existing data to gain more sensitivity. Therefore, we strongly suggest to provide as much information as possible on the kinematics of the Higgs production. Next, spending more time on the analyses incorporated in the EFT interpretation allows to reshape the input of the EFT interpretation into a form that has most sensitivity. An example would be to merge any STXS regions that have a hard time being constrained, slightly altering the Stage 1 STXS binning. This is not implemented, because altering of the measurements included is beyond the scope of this study.

To improve on the EFT interpretation part, including the higher order EFT contributions either in the reparameterization or systematic uncertainty improves the reliability of the analysis. Uncertainties on the generation of the EFT reparameterization samples, and of the reparameterization itself, have not been taken into account. These uncertainties and higher order contributions are to be included in future studies. Ultimately, we would also like to combine our EFT interpretation with other Higgs decay channels. Such as $H \rightarrow \gamma\gamma$ and $H \rightarrow ZZ$. This would result in including new operators in the analysis while adding data for the already existing operators. Doing this would also encourage us to include the $qq/gg \rightarrow \gamma\gamma$ and $qq/gg \rightarrow ZZ$ processes to complement the $qq/gg \rightarrow W^+W^- \rightarrow e\nu\mu\nu$ measurement. Another way of improving the EFT measurement is taking into account the effects of the EFT operators in the backgrounds as well. Right now, the backgrounds are assumed to be SM. However, when fitting to any operator that influences interactions.

These interactions should also be taken into account when doing the background subtraction, which is currently not the case.

This study concludes with constraints found on 17 dimension-6 operators of the Standard Model effective field theory, taking into account dimension-6 cross section contributions up to order $1/\Lambda^2$. The constraints are based on 36.1 fb^{-1} of $\sqrt{s} = 13 \text{ TeV}$ proton-proton collisions recorded by the ATLAS detector at the LHC in 2015 and 2016 and the $qq/gg \rightarrow W^+W^- \rightarrow e\nu\mu\nu$ [3] and $H \rightarrow W^+W^- \rightarrow e\nu\mu\nu$ [2] analyses of this data. The best fit values as well as the 68% *C.L.* are shown in Fig. 11.7 and Tab. 11.1. The results imply Higgs coupling properties in agreement with the SM predictions.

Bibliography

- [1] I. Brivio, T. Corbett, and M. Trott, “The Higgs width in the SMEFT”, Tech. Rep., 2019.
- [2] M. Aaboud, G. Aad, B. Abbott, *et al.*, “Measurements of gluon-gluon fusion and vector-boson fusion Higgs boson production cross-sections in the $HW\bar{W}\nu\mu\nu$ decay channel in pp collisions at $\sqrt{s}=13\text{TeV}$ with the ATLAS detector”, *Physics Letters, Section B: Nuclear, Elementary Particle and High-Energy Physics*, vol. 789, pp. 508–529, 2019, ISSN: 03702693. DOI: [10.1016/j.physletb.2018.11.064](https://doi.org/10.1016/j.physletb.2018.11.064).
- [3] “Measurement of fiducial and differential W + W production cross-sections at $\sqrt{s}=13\text{TeV}$ with the ATLAS detector The ATLAS Collaboration”, Tech. Rep., 2019. [Online]. Available: <https://arxiv.org/pdf/1905.04242.pdf>.
- [4] N. Belyaev, V. Bortolotto, L. Brenner, *et al.*, “A morphing technique for signal modelling in a multidimensional space of non-SM coupling parameters”, no. October, 2015.
- [5] K. Tackmann, T. Guillemin, C. Hays, G. Isidori, S. Kraml, J. Lacey, C. Pandini, E. Pianori, and M. Rauch, “LHC Higgs Cross Section Working Group: Simplified template cross sections”, 2016.
- [6] A. Lazzaro and L. Moneta, “MINUIT package parallelization and applications using the RooFit package”, DOI: [10.1088/1742-6596/219/4/042044](https://doi.org/10.1088/1742-6596/219/4/042044).
- [7] The ATLAS Collaboration, “Observation of a new particle in the search for the Standard Model Higgs boson with the ATLAS detector at the LHC”, Jul. 2012. DOI: [10.1016/j.physletb.2012.08.020](https://doi.org/10.1016/j.physletb.2012.08.020). [Online]. Available: <http://arxiv.org/abs/1207.7214><http://dx.doi.org/10.1016/j.physletb.2012.08.020>.
- [8] M. Aaboud, G. Aad, B. Abbott, *et al.*, “Measurement of the Higgs boson mass in the $HZZ4$ and $H\gamma\gamma$ channels with $\sqrt{s}=13\text{TeV}$ pp collisions using the ATLAS detector”, *Physics Letters, Section B: Nuclear, Elementary Particle and High-Energy Physics*, vol. 784, no. October, pp. 345–366, 2018, ISSN: 03702693. DOI: [10.1016/j.physletb.2018.07.050](https://doi.org/10.1016/j.physletb.2018.07.050).
- [9] *File:Standard Model of Elementary Particles modified version.svg - Wikimedia Commons*. [Online]. Available: https://commons.wikimedia.org/wiki/File:Standard_Model_of_Elementary_Particles_modified_version.svg.
- [10] M. Tanabashi, K. Hagiwara, K. Hikasa, *et al.*, “Review of Particle Physics”, *Physical Review D*, vol. 98, no. 3, p. 030001, Aug. 2018, ISSN: 2470-0010. DOI: [10.1103/PhysRevD.98.030001](https://doi.org/10.1103/PhysRevD.98.030001). [Online]. Available: <https://link.aps.org/doi/10.1103/PhysRevD.98.030001>.
- [11] D. de Florian, C. Grojean, F. Maltoni, *et al.*, “Handbook of LHC Higgs Cross Sections: 4. Deciphering the Nature of the Higgs Sector”, Oct. 2016. DOI: [10.23731/CYRM-2017-002](https://doi.org/10.23731/CYRM-2017-002). [Online]. Available: <http://arxiv.org/abs/1610.07922><http://dx.doi.org/10.23731/CYRM-2017-002>.
- [12] The CMS Collaboration, “Evidence for the direct decay of the 125 GeV Higgs boson to fermions”, *Nature Physics*, vol. 10, no. 8, pp. 557–560, 2014, ISSN: 17452481. DOI: [10.1038/nphys3005](https://doi.org/10.1038/nphys3005).

- [13] LHC Higgs Cross Section Working Group, C. Mariotti, G. Passarino, *et al.*, “Handbook of LHC Higgs Cross Sections: 3. Higgs Properties”, *Handbook of LHC Higgs Cross Sections*, p. 404, 2013, ISSN: 05503213. DOI: [10.5170/CERN-2013-004](https://doi.org/10.5170/CERN-2013-004). [Online]. Available: <http://inspirehep.net/record/1241571%5Cnhttp://arxiv.org/abs/1307.1347>.
- [14] V. Khachatryan, A. Sirunyan, A. Tumasyan, *et al.*, “Constraints on the spin-parity and anomalous H V V couplings of the Higgs boson in proton collisions at 7 and 8 TeV”, *Physical Review D*, vol. 92, no. 1, p. 012004, Jul. 2015, ISSN: 1550-7998. DOI: [10.1103/PhysRevD.92.012004](https://doi.org/10.1103/PhysRevD.92.012004). [Online]. Available: <https://link.aps.org/doi/10.1103/PhysRevD.92.012004>.
- [15] ATLAS Collaboration, “Combination of searches for Higgs boson pairs in pp collisions at $\sqrt{s} = 13$ TeV with the ATLAS detector”, no. June, 2019. [Online]. Available: <http://arxiv.org/abs/1906.02025>.
- [16] D. Griffiths, *Introduction to Elementary Particles*. 2004, ISBN: 9780874216561. DOI: [10.3769/radioisotopes.60.527](https://doi.org/10.3769/radioisotopes.60.527). [Online]. Available: [http://zamalik.weebly.com/uploads/5/6/1/9/56198443/\[griffiths_d.\]_introduction_to_elementary_particle.pdf](http://zamalik.weebly.com/uploads/5/6/1/9/56198443/[griffiths_d.]_introduction_to_elementary_particle.pdf).
- [17] F. F. Halzen and A. D. A. D. Martin, *Quarks and leptons : an introductory course in modern particle physics*, p. 396, ISBN: 0471887412.
- [18] C. D. Anderson, “The Positive Electron”, Tech. Rep., p. 491. [Online]. Available: <http://web.ihep.su/dbserv/compas/src/anderson33/eng.pdf>.
- [19] G. Costa and F. Gianluigi, *Symmetries and Group Theory in Particle Physics*, ISBN: 9783642154812.
- [20] S. L. Glashow, “TOWARDS A UNIFIED THEORY-THREADS IN A TAPESTRY”, Tech. Rep., 1979. [Online]. Available: <https://www.nobelprize.org/uploads/2018/06/glashow-lecture.pdf>.
- [21] M. Merk, W. Hulsbergen, and I. V. Vulpen, “Particle Physics 1”, 2016.
- [22] M. Botje, “Lecture notes Particle Physics II Quantum Chromo Dynamics Michiel Botje Nikhef, Science Park, Amsterdam QCD in Eight Lectures”, 2013.
- [23] A. Deur, S. J. Brodsky, and G. E. De Téramond, “The QCD Running Coupling”, Tech. Rep., 2016. [Online]. Available: <https://arxiv.org/pdf/1604.08082.pdf>.
- [24] A. Höcker and Z. Ligeti, “CP violation and the CKM matrix”, Tech. Rep., 2006. [Online]. Available: <https://arxiv.org/pdf/hep-ph/0605217.pdf>.
- [25] P. Kooijman and N. Tuning, “Lectures on CP violation”, no. January, p. 112, 2015. [Online]. Available: <https://www.nikhef.nl/~h71/Lectures/2015/ppII-cpviolation-29012015.pdf> <http://www.nikhef.nl/~h71/Lectures/2015/ppII-cpviolation-29012015.pdf>.
- [26] J. Smit, “Introduction to relativistic quantum fields”, 2005. [Online]. Available: <http://arxiv.org/abs/quant-ph/0508049>.
- [27] L. Roszkowski, E. M. Sessolo, and S. Trojanowski, “WIMP dark matter candidates and searches-current status and future prospects”, Tech. Rep., 2018. [Online]. Available: <https://arxiv.org/pdf/1707.06277.pdf>.
- [28] G. Bhattacharyya, “Hierarchy problem and BSM physics”, *Pramana-J. Phys*, vol. 89, p. 53, 2043. DOI: [10.1007/s12043-017-1448-2](https://doi.org/10.1007/s12043-017-1448-2). [Online]. Available: <https://www.ias.ac.in/article/fulltext/pram/089/04/0053>.

- [29] D. B. Kaplan, “Five lectures on effective field theory”, 2005. [Online]. Available: <http://arxiv.org/abs/nucl-th/0510023>.
- [30] I. Brivio, Y. Jiang, and M. Trott, “The SMEFTsim package, theory and tools”, Sep. 2017. DOI: [10.1007/JHEP12\(2017\)070](https://doi.org/10.1007/JHEP12(2017)070). [Online]. Available: <http://arxiv.org/abs/1709.06492>[http://dx.doi.org/10.1007/JHEP12\(2017\)070](http://dx.doi.org/10.1007/JHEP12(2017)070).
- [31] B. Grzadkowski, M. Iskrzynski, M. Misiak, and J. Rosiek, “Dimension-Six Terms in the Standard Model Lagrangian”, Aug. 2010. DOI: [10.1007/JHEP10\(2010\)085](https://doi.org/10.1007/JHEP10(2010)085). [Online]. Available: <http://arxiv.org/abs/1008.4884>[http://dx.doi.org/10.1007/JHEP10\(2010\)085](http://dx.doi.org/10.1007/JHEP10(2010)085).
- [32] A. Dedes, W. Materkowska, M. Paraskevas, J. Rosiek, and K. Suxho, “Feynman Rules for the Standard Model Effective Field Theory in $U(1)$ -gauges”, Apr. 2017. DOI: [10.1007/JHEP06\(2017\)143](https://doi.org/10.1007/JHEP06(2017)143). [Online]. Available: <http://arxiv.org/abs/1704.03888>[http://dx.doi.org/10.1007/JHEP06\(2017\)143](http://dx.doi.org/10.1007/JHEP06(2017)143).
- [33] R. Alonso, E. E. Jenkins, A. V. Manohar, and M. Trott, “Renormalization Group Evolution of the Standard Model Dimension Six Operators III: Gauge Coupling Dependence and Phenomenology”, Dec. 2013. DOI: [10.1007/JHEP04\(2014\)159](https://doi.org/10.1007/JHEP04(2014)159). [Online]. Available: <http://arxiv.org/abs/1312.2014>[http://dx.doi.org/10.1007/JHEP04\(2014\)159](http://dx.doi.org/10.1007/JHEP04(2014)159).
- [34] L Rossi, “THE LHC SUPERCONDUCTING MAGNETS”, Tech. Rep. [Online]. Available: <http://accelconf.web.cern.ch/accelconf/p03/papers/toab001.pdf>.
- [35] E. Mobs, *The CERN accelerator complex*, Jul. 2016. [Online]. Available: <https://cds.cern.ch/record/2197559>.
- [36] M. Thomson, *Modern Particle Physics*. Cambridge University Press, Sep. 2013. DOI: [10.1017/cbo9781139525367](https://doi.org/10.1017/cbo9781139525367).
- [37] M. Aaboud, G. Aad, B. Abbott, *et al.*, “The ATLAS Experiment at the CERN Large Hadron Collider”, *Nuclear Physics A*, vol. 982, pp. 985–1009, 2019, ISSN: 03759474. DOI: [10.1016/S0375-9474\(18\)30499-8](https://doi.org/10.1016/S0375-9474(18)30499-8).
- [38] *Detector & Technology*. [Online]. Available: <https://atlas.cern/discover/detector>.
- [39] M. Aaboud, G. Aad, B. Abbott, *et al.*, “Performance of the ATLAS trigger system in 2015”, *European Physical Journal C*, vol. 77, no. 5, pp. 1–77, 2017, ISSN: 14346052. DOI: [10.1140/epjc/s10052-017-4852-3](https://doi.org/10.1140/epjc/s10052-017-4852-3).
- [40] M. Dobbs, S Frixione, E Laenen, and K Tollefson, “Les Houches Guidebook to Monte Carlo Generators for Hadron Collider Physics”, Tech. Rep., 2004.
- [41] G. Altarelli, “QCD evolution equations for parton densities”, *Scholarpedia*, vol. 4, no. 1, p. 7124, 2009, ISSN: 1941-6016. DOI: [10.4249/scholarpedia.7124](https://doi.org/10.4249/scholarpedia.7124).
- [42] A. D. Martin, W. J. Stirling, R. S. Thorne, and G. Watt, “Parton distributions for the LHC”, Jan. 2009. DOI: [10.1140/epjc/s10052-009-1072-5](https://doi.org/10.1140/epjc/s10052-009-1072-5). [Online]. Available: <http://arxiv.org/abs/0901.0002><http://dx.doi.org/10.1140/epjc/s10052-009-1072-5>.
- [43] A. Buckley, J. Butterworth, S. Gieseke, *et al.*, “General-purpose event generators for LHC physics”, Tech. Rep., 2011.
- [44] M. H. Seymour and M. Marx, “Monte Carlo Event Generators”, Tech. Rep.

- [45] M. L. Mangano, F. Piccinini, A. D. Polosa, M. Moretti, and R. Pittau, “ALPGEN, a generator for hard multiparton processes in hadronic collisions”, *Journal of High Energy Physics*, vol. 2003, no. 07, pp. 001–001, Jul. 2003, ISSN: 1029-8479. DOI: [10.1088/1126-6708/2003/07/001](https://doi.org/10.1088/1126-6708/2003/07/001). [Online]. Available: <http://stacks.iop.org/1126-6708/2003/i=07/a=001?key=crossref.8d9456967c3fd10e94e494eb55c2e4d2>.
- [46] *Sherpa Hepforge*. [Online]. Available: <https://sherpa.hepforge.org/trac/wiki>.
- [47] J. Alwall, R. Frederix, S. Frixione, V. Hirschi, F. Maltoni, O. Mattelaer, H. S. Shao, T. Stelzer, P. Torrielli, and M. Zaro, “The automated computation of tree-level and next-to-leading order differential cross sections, and their matching to parton shower simulations”, May 2014. DOI: [10.1007/JHEP07\(2014\)079](https://doi.org/10.1007/JHEP07(2014)079). [Online]. Available: [http://arxiv.org/abs/1405.0301http://dx.doi.org/10.1007/JHEP07\(2014\)079](http://arxiv.org/abs/1405.0301http://dx.doi.org/10.1007/JHEP07(2014)079).
- [48] T. Sjöstrand, S. Ask, J. R. Christiansen, R. Corke, N. Desai, P. Ilten, S. Mrenna, S. Prestel, C. O. Rasmussen, and P. Z. Skands, “An introduction to PYTHIA 8.2”, *Computer Physics Communications*, vol. 191, no. 1, pp. 159–177, 2015, ISSN: 00104655. DOI: [10.1016/j.cpc.2015.01.024](https://doi.org/10.1016/j.cpc.2015.01.024).
- [49] M. Cacciari, G. P. Salam, and G. Soyez, “The anti-kt jet clustering algorithm”, *Journal of High Energy Physics*, vol. 2008, no. 4, pp. 1–12, 2008, ISSN: 11266708. DOI: [10.1088/1126-6708/2008/04/063](https://doi.org/10.1088/1126-6708/2008/04/063).
- [50] J. Alwall, M. Herquet, F. Maltoni, O. Mattelaer, and T. Stelzer, “MadGraph 5: Going beyond”, *Journal of High Energy Physics*, vol. 2011, no. 6, 2011, ISSN: 11266708. DOI: [10.1007/JHEP06\(2011\)128](https://doi.org/10.1007/JHEP06(2011)128).
- [51] M. Dobbs, J. B. Hansen, L. Garren, and L. Sonnenschein, “HepMC 2 a C++ Event Record for Monte Carlo Generators”, 2012. [Online]. Available: http://lcgapp.cern.ch/project/simu/HepMC/206/HepMC2_user_manual.pdf.
- [52] *Index of validationpdfs Hepforge*. [Online]. Available: <https://lhapdf.hepforge.org/validationpdfs/>.
- [53] A. Buckley, J. Butterworth, D. Grellscheid, H. Hoeth, L. Lönnblad, J. Monk, H. Schulz, and F. Siegert, “Rivet user manual”, *Computer Physics Communications*, vol. 184, no. 12, pp. 2803–2819, 2013, ISSN: 00104655. DOI: [10.1016/j.cpc.2013.05.021](https://doi.org/10.1016/j.cpc.2013.05.021).
- [54] H. Yang, *Implementation of STXS framework in coupling analysis*, 2018. [Online]. Available: <https://twiki.cern.ch/twiki/bin/viewauth/AtlasProtected/STXSImplementation>.
- [55] N. Berger, *Classification Tool for the Template Higgs Cross-section Framework*, 2018. [Online]. Available: <https://twiki.cern.ch/twiki/bin/viewauth/AtlasProtected/SXSClassificationTool>.
- [56] O. Mattelaer, “On the maximal use of Monte Carlo samples: re-weighting events at NLO accuracy”, *European Physical Journal C*, vol. 76, no. 12, 2016, ISSN: 14346052. DOI: [10.1140/epjc/s10052-016-4533-7](https://doi.org/10.1140/epjc/s10052-016-4533-7).
- [57] H. B. Prosper, “Practical statistics for particle physicists”, *2012 European School of High-Energy Physics, ESHEP 2012 - Proceedings*, pp. 195–216, 2018. DOI: [10.5170/CERN-2014-008.195](https://doi.org/10.5170/CERN-2014-008.195).
- [58] E. Gross, “Practical statistics for high energy physics”, *2017 European School of High-Energy Physics, ESHEP 2017*, vol. 2017-Sept, no. September 2015, pp. 2–15, 2017.

- [59] G. Cowan, K. Cranmer, E. Gross, and O. Vitells, “Asymptotic formulae for likelihood-based tests of new physics”, *European Physical Journal C*, vol. 71, no. 2, Feb. 2011, ISSN: 14346052. DOI: [10.1140/epjc/s10052-011-1554-0](https://doi.org/10.1140/epjc/s10052-011-1554-0).
- [60] J. Ellis, C. W. Murphy, V. Sanz, and T. You, “Updated global SMEFT fit to Higgs, di-boson and electroweak data”, *Journal of High Energy Physics*, vol. 2018, no. 6, 2018, ISSN: 10298479. DOI: [10.1007/JHEP06\(2018\)146](https://doi.org/10.1007/JHEP06(2018)146).
- [61] A. V. Manohar and M. B. Wise, “Modifications to the Properties of the Higgs Boson”, Tech. Rep., 2006. [Online]. Available: <https://arxiv.org/pdf/hep-ph/0601212.pdf>.
- [62] I. Brivio and M. Trott, “The Standard Model as an Effective Field Theory”, Tech. Rep., 2018.
- [63] *LHAPDF: PDF sets Hepforge*. [Online]. Available: <https://lhapdf.hepforge.org/pdfsets>.
- [64] ATLAS Collaboration, “ATLAS Run1 Pythia⁸ tunes”, *Atlas-Phys-Pub-2014-021*, no. November, pp. 0–16, 2014. [Online]. Available: <http://cds.cern.ch/record/1966419>.
- [65] D. Berdine, N. Kauer, and D. Rainwater, “Breakdown of the Narrow Width Approximation for New Physics”, *Physical Review Letters*, vol. 99, no. 11, p. 111 601, Sep. 2007, ISSN: 0031-9007. DOI: [10.1103/PhysRevLett.99.111601](https://doi.org/10.1103/PhysRevLett.99.111601). [Online]. Available: <http://arxiv.org/abs/hep-ph/0703058><http://dx.doi.org/10.1103/PhysRevLett.99.111601><https://link.aps.org/doi/10.1103/PhysRevLett.99.111601>.
- [66] A Djouadi, J Kalinowski, and M Spira, “HDECAY: a Program for Higgs Boson Decays in the Standard Model and its Supersymmetric Extension”, Tech. Rep., 1997. [Online]. Available: <http://wwcn.cern.ch/mspira/or><http://www.lpm.univ-montp2.fr/djouadi/program.html>, or via.
- [67] C. Hays, A. Martin, V. Sanz, and J. Setford, “On the impact of dimension-eight SMEFT operators on Higgs measurements”, *Journal of High Energy Physics*, vol. 2019, no. 2, 2019, ISSN: 10298479. DOI: [10.1007/JHEP02\(2019\)123](https://doi.org/10.1007/JHEP02(2019)123).

Appendix A

Fit results and Nuisance parameter pulls of the STXS signal strength fits

In this Appendix the fit results and nuisance parameter pulls of the non-reparameterized $H \rightarrow W^+ W^- \rightarrow e\nu\mu\nu$ measurements are shown.

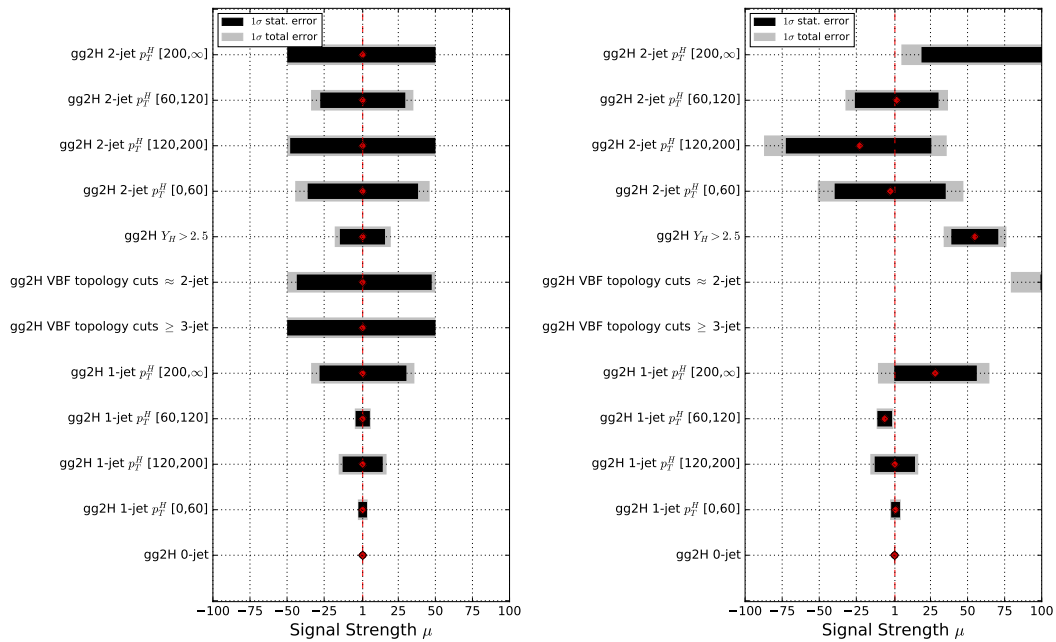


FIGURE A.1: ggF STXS fiducial region signal strength constraints. Left fitted on Asimov data right fitted to observed data.

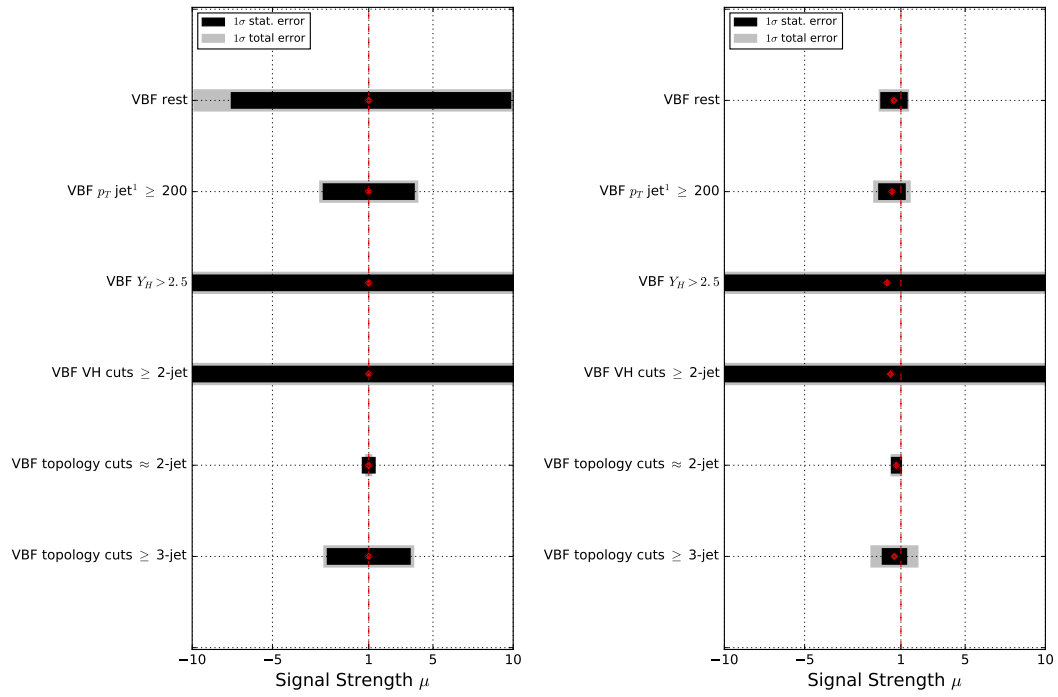


FIGURE A.2: The VBF STXS fiducial region signal strength constraints. Left fitted on Asimov data right fitted to observed data.

STXS region	signal strength μ
VBF qq2Hqq VBFtopo jet3	$0.60^{+1.50}_{-1.50}$
VBF qq2Hqq VBFtopo jet3 veto	$0.72^{+0.37}_{-0.36}$
VBF qq2Hqq VH \geq 2-jet	0.35^{+24}_{-24}
VBF qq2Hqq fwdH	0.14^{+24}_{-24}
VBF qq2Hqq p_T jet-1 $>$ 200	$0.44^{+1.17}_{-1.17}$
VBF qq2Hqq p_T jet-1 $>$ 200	$0.56^{+0.95}_{-0.94}$

TABLE A.1: Observed signal strengths in VBF STXS regions.

STXS region	signal strength μ	fiducial region	signal strength μ	fiducial region	signal strength μ
gg2H 0-jet	$0.84^{+0.31}_{-0.29}$	gg2H 1-jet p_T H 0-60	$1.5^{+3.5}_{-3.7}$	gg2H 2-jet p_T H 0-60	-2.0^{+49}_{-49}
gg2H VBF topo jet3	258^{+155}_{-130}	gg2H 1-jet p_T H 60-120	$-5.9^{+5.8}_{-5.4}$	gg2H 2-jet p_T H 60-120	-2.2^{+35}_{-35}
gg2H VBF topo jet3 veto	145^{+78}_{-66}	gg2H 1-jet p_T H 120-200	1.0^{+16}_{-17}	gg2H 2-jet p_T H 120-200	-22^{+58}_{-64}
gg2H fwdH	54^{+21}_{-21}	gg2H 1-jet p_T H \geq 200	28^{+37}_{-39}	gg2H 2-jet p_T H \geq 200	-112^{+116}_{-106}

TABLE A.2: Observed signal strengths in GGF STXS regions.



FIGURE A.3: Fitted nuisance parameters to the Asimov data set with the signal plus background hypothesis of $gg^F H \rightarrow W^+ W^- \rightarrow e\nu\mu\nu$ measurement.



FIGURE A.4: Fitted nuisance parameters to the observed data set of the ggF $H \rightarrow W^+W^- \rightarrow e\nu\mu\nu$ measurement.

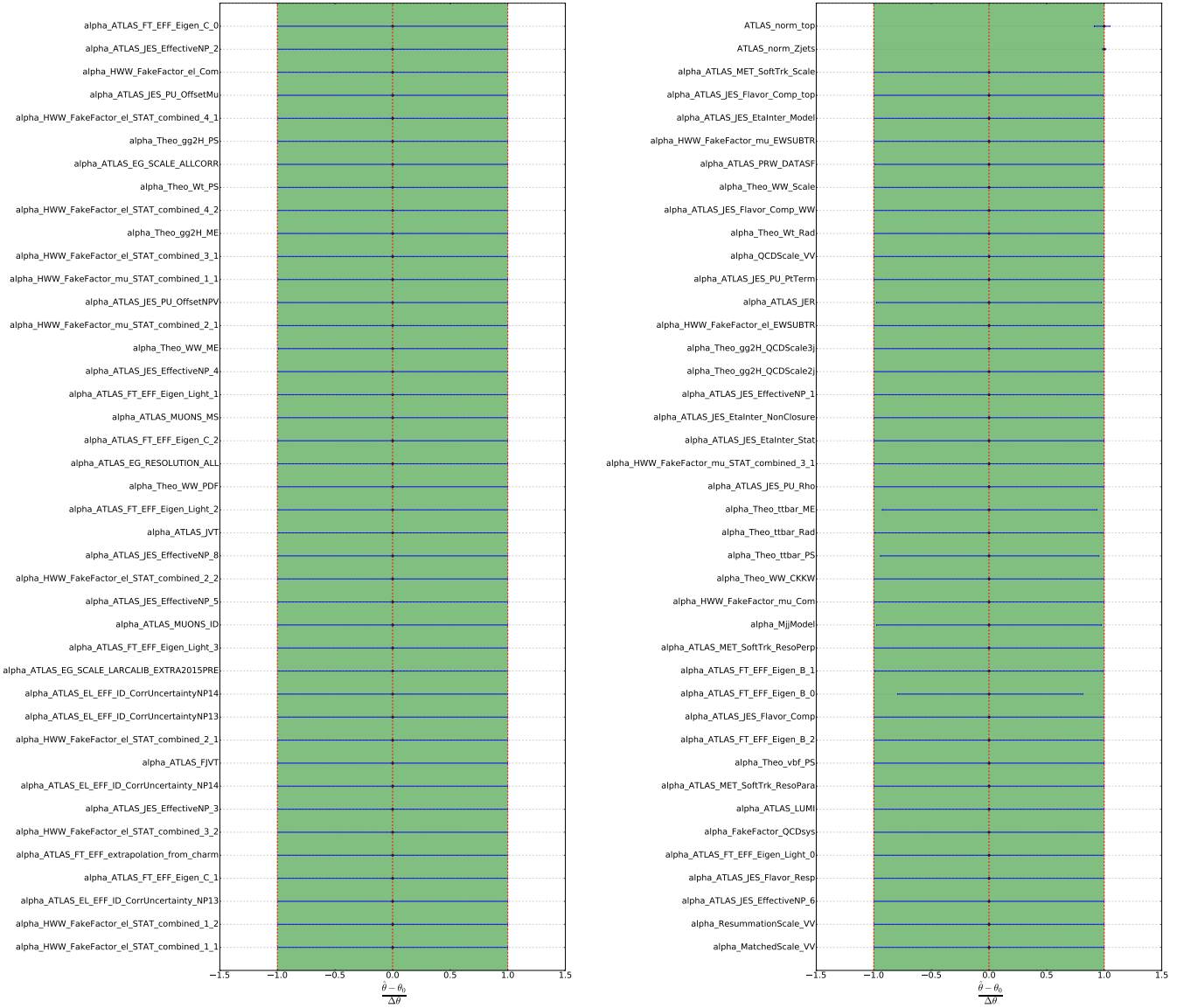


FIGURE A.5: Fitted nuisance parameters to the Asimov data set with the signal plus background hypothesis of VBF $H \rightarrow W^+ W^- \rightarrow e\nu\mu\nu$ measurement.

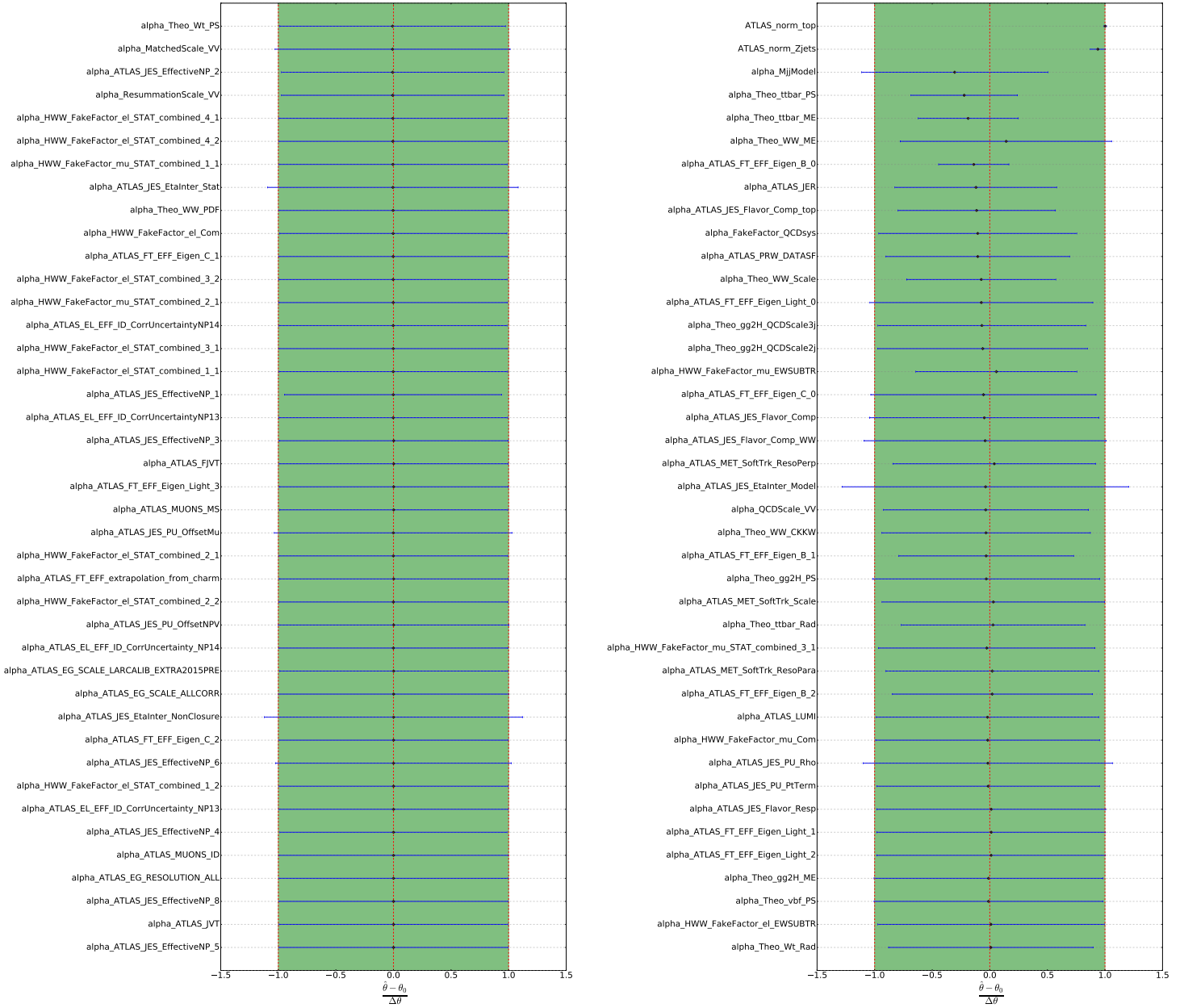


FIGURE A.6: Fitted nuisance parameters to the observed data set of the VBF $H \rightarrow W^+ W^- \rightarrow e \nu \mu \nu$ measurement.



FIGURE A.8: Fitted nuisance parameters to the observed data set of the combined ggF and VBF $H \rightarrow W^+ W^- \rightarrow e \nu \mu \nu$ measurements.

Appendix B

Operator Analysis Cutflow

In this appendix the cutflows from the morphing validation and operator analysis are shown. The tables can be found on the next pages.

TABLE B.1: ggF full decay Wilson Coefficient cutflow. The ggF Higgs sample comprises the Standard Model sample. The other columns represent the Standard Model interference samples and the event count after every phase space cut. The CutBase represents the initial number of events. The errors on the event count represent the statistical error. In the most left column the phase space cuts are described.

	ggF Higgs	cHG interference	cHG squared order	cHW interference	cHW squared order
CutBase	100000 ± 316.23	100000 ± 316.23	100000 ± 316.23	100000 ± 316.23	100000 ± 316.23
Overlap removal	89786 ± 299.64	91056 ± 301.75	91268 ± 302.11	88383 ± 297.29	88963 ± 298.27
Opposite sign lepton req. electron $p_T > 17\text{GeV}$	45569 ± 213.47	46669 ± 216.03	46733 ± 216.18	45190 ± 212.58	45607 ± 213.56
Electron pseudorapidity $ \eta _e < 2.47$	42046 ± 205.05	42926 ± 207.19	42974 ± 207.30	41531 ± 203.79	42526 ± 206.22
Muon $p_T > 14\text{GeV}$	38661 ± 196.62	39314 ± 198.28	39224 ± 198.05	38232 ± 195.53	39534 ± 198.83
Muon pseudorapidity $ \eta _\mu < 2.5$	23389 ± 152.93	23787 ± 154.23	23710 ± 153.98	23798 ± 154.27	25993 ± 161.22
Leading lepton $p_T > 22\text{GeV}$	22710 ± 150.70	23048 ± 151.82	22948 ± 151.49	23177 ± 152.24	25319 ± 159.12
Subleading lepton $p_T > 15\text{GeV}$	21674 ± 147.22	21953 ± 148.17	21774 ± 147.56	22117 ± 148.72	24377 ± 156.13
Invariant lepton mass $m_{ll} > 10\text{GeV}$	20457 ± 143.03	20681 ± 143.81	20494 ± 143.16	20974 ± 144.82	23296 ± 152.63
Missing Energy $> 20\text{GeV}$	20423 ± 142.91	20638 ± 143.66	20443 ± 142.98	20912 ± 144.61	23261 ± 152.52
	18452 ± 135.84	18529 ± 136.12	18419 ± 135.72	19068 ± 138.09	21697 ± 147.30
0 jet cut	257 ± 16.03	311 ± 17.64	332 ± 18.22	265 ± 16.28	248 ± 15.75
Delta Phi leptons $\Delta\phi_{ll} > \pi/2$	257 ± 16.03	311 ± 17.64	332 ± 18.22	265 ± 16.28	248 ± 15.75
$p_T^{ll} > 30\text{GeV}$	227 ± 15.07	275 ± 16.58	295 ± 17.18	242 ± 15.56	222 ± 14.90
Invariant lepton mass, $m_{ll} < 55\text{GeV}$	195 ± 13.96	227 ± 15.07	248 ± 15.75	217 ± 14.73	186 ± 13.64
0-jet b-veto	176 ± 13.27	210 ± 14.49	225 ± 15	206 ± 14.35	177 ± 13.30
1 jet cut	666 ± 25.81	874 ± 29.56	881 ± 29.68	668 ± 25.85	683 ± 26.13
$\max(M_T^l) > 50\text{GeV}$	614 ± 24.78	826 ± 28.74	823 ± 28.69	639 ± 25.28	650 ± 25.50
$M_{ll} < 55\text{GeV}$	502 ± 22.41	659 ± 25.67	664 ± 25.77	554 ± 23.54	489 ± 22.11
$\Delta\phi_{ll} < 1.8$	438 ± 20.93	562 ± 23.71	586 ± 24.21	498 ± 22.32	455 ± 21.33
2-jet cut	1031 ± 32.11	1293 ± 35.96	1406 ± 37.50	1067 ± 32.66	1082 ± 32.89

TABLE B.2: VBF full decay Wilson Coefficient cutflow. The VBF Higgs sample comprises the Standard Model sample. The other columns represent the Standard Model interference samples and the event count after every phase space cut. The CutBase represents the initial number of events. The errors on the event count represent the statistical error. In the most left column the phase space cuts are described.

	VBF Higgs	cHI3 interference	cHI3 squared order	cHW interference	cHW squared order	cHbox interference	cHbox squared order	cHbox squared order
CutBase	100000 ± 316.23	100000 ± 316.23	100000 ± 316.23	100000 ± 316.23	100000 ± 316.23	100000 ± 316.23	100000 ± 316.23	100000 ± 316.23
Overlap removal	89082 ± 298.47	89061 ± 298.43	88942 ± 298.23	86456 ± 294.03	80023 ± 282.88	88763 ± 297.93	89439 ± 299.06	89439 ± 299.06
Opposite sign lepton req.	45462 ± 213.22	45423 ± 213.13	45202 ± 212.61	43873 ± 209.46	40457 ± 201.14	45513 ± 213.34	45612 ± 213.57	45612 ± 213.57
Electron $p_T > 17\text{GeV}$	41940 ± 204.79	41957 ± 204.83	41657 ± 204.10	40633 ± 201.58	38061 ± 195.09	42115 ± 205.22	45151 ± 212.49	45151 ± 212.49
Electron pseudorapidity $ \eta _e < 2.47$	38836 ± 197.07	38752 ± 196.86	38557 ± 196.36	37513 ± 193.68	35421 ± 188.20	39012 ± 197.51	44041 ± 209.86	44041 ± 209.86
Muon $p_T > 14\text{GeV}$	24409 ± 156.23	24346 ± 156.03	24027 ± 155.01	23797 ± 154.26	23907 ± 154.62	24668 ± 157.06	39795 ± 199.49	39795 ± 199.49
Muon pseudorapidity $ \eta _\mu < 2.5$	23672 ± 153.86	23645 ± 153.77	23367 ± 152.86	23062 ± 151.86	23206 ± 152.34	23956 ± 154.78	39367 ± 198.41	39367 ± 198.41
Leading lepton $p_T > 22\text{GeV}$	22754 ± 150.84	22659 ± 150.53	22419 ± 149.73	22273 ± 149.24	22667 ± 150.56	23018 ± 151.72	39263 ± 198.15	39263 ± 198.15
Subleading lepton $p_T > 15\text{GeV}$	21643 ± 147.12	21553 ± 146.81	21260 ± 145.81	21303 ± 145.96	21856 ± 147.84	21884 ± 147.93	39047 ± 197.60	39047 ± 197.60
Invariant lepton mass $m_{ll} > 10\text{GeV}$	21610 ± 147	21528 ± 146.72	21231 ± 145.71	21280 ± 145.88	21839 ± 147.78	21848 ± 147.81	39040 ± 197.59	39040 ± 197.59
Missing Energy $> 20\text{GeV}$	19327 ± 139.02	19210 ± 138.60	19038 ± 137.98	19359 ± 139.14	20377 ± 142.75	19658 ± 140.21	38559 ± 196.36	38559 ± 196.36

Appendix C

STXS Truth Decoration Cutflow

In this Appendix the cutflows/decorations by the STXS decoration tool are shown. In the tables the number of events assigned to each STXS region is visible.

STXS region	Standard Model	c_{HG} interference
gg2H 0-jet	22651.00 ± 150.50	28137.00 ± 167.74
gg2H 1-jet p_T^H [0,60]	11556.00 ± 107.50	12862.00 ± 113.41
gg2H 1-jet p_T^H [120,200]	2867.00 ± 53.54	3036.00 ± 55.10
gg2H 1-jet p_T^H [60,120]	11183.00 ± 105.75	12321.00 ± 111.00
gg2H 1-jet p_T^H [200, ∞]	1072.00 ± 32.74	1030.00 ± 32.09
gg2H VBF topology cuts \geq 3-jet	4267.00 ± 65.32	2943.00 ± 54.25
gg2H VBF topology cuts \approx 2-jet	1753.00 ± 41.87	1514.00 ± 38.91
gg2H $Y_H > 2.5$	7960.00 ± 89.22	8867.00 ± 94.16
gg2H 2-jet p_T^H [0,60]	7893.00 ± 88.84	6427.00 ± 80.17
gg2H 2-jet p_T^H [120,200]	8328.00 ± 91.26	6764.00 ± 82.24
gg2H 2-jet p_T^H [60,120]	13202.00 ± 114.90	11074.00 ± 105.23
gg2H 2-jet p_T^H [200, ∞]	7266.00 ± 85.24	5024.00 ± 70.88

TABLE C.1: ggF STXS decoration decoration of 100.000 events per MC sample. First column describes the ggF STXS regions, next column the Standard Model events separated over the STXS regions. The last column separates the interference events over the STXS regions. The errors on the event count represent the statistical error.

STXS region	Standard Model	c_{110} interference	c_{1100} interference	c_{1101} interference	c_{1102} interference	c_{1103} interference	c_{1104} interference	c_{1105} interference	c_{1106} interference	c_{1107} interference	c_{1108} interference	c_{1109} interference	c_{1110} interference
VBFF-qq2Hqq	17475.00 ± 132.19	14695.00 ± 121.22	18153.00 ± 134.73	16931.00 ± 126.61	17047.00 ± 130.56	17389.00 ± 132.62	16079.00 ± 126.80	17570.00 ± 132.55	14935.00 ± 122.21	16195.00 ± 127.26	16798.00 ± 129.61	16798.00 ± 129.61	17754.00 ± 133.24
VBFF-qq2Hqq	22629.00 ± 150.43	18653.00 ± 136.58	22589.00 ± 150.23	19578.00 ± 139.92	17846.00 ± 133.59	22815.00 ± 150.38	16169.00 ± 127.16	22721.00 ± 150.73	14553.00 ± 120.64	16738.00 ± 129.38	15916.00 ± 126.16	15916.00 ± 126.16	22717.00 ± 150.72
VBFF-qq2Hqq	2940.00 ± 54.22	2982.00 ± 54.61	2867.00 ± 53.54	3024.00 ± 54.99	3065.00 ± 55.36	2857.00 ± 53.45	2855.00 ± 53.43	2831.00 ± 53.21	2769.00 ± 52.62	2720.00 ± 52.15	2571.00 ± 50.71	2571.00 ± 50.71	2855.00 ± 53.43
VBFF-qq2Hqq	6446.00 ± 80.29	7255.00 ± 85.18	6488.00 ± 80.55	7021.00 ± 83.79	6237.00 ± 78.97	6541.00 ± 80.88	4146.00 ± 64.39	6370.00 ± 79.81	4564.00 ± 67.56	4840.00 ± 68.57	5083.00 ± 71.30	5083.00 ± 71.30	6413.00 ± 80.08
VBFF-qq2Hqq	5776.00 ± 76.00	9650.00 ± 98.23	6251.00 ± 79.06	11668.00 ± 108.02	19854.00 ± 140.90	5731.00 ± 75.70	29373.00 ± 171.39	5836.00 ± 76.39	34292.00 ± 185.18	28664.00 ± 169.30	31636.00 ± 177.87	31636.00 ± 177.87	5525.00 ± 74.33
VBFF-qq2Hqq	44734.00 ± 211.50	46764.00 ± 216.25	43671.00 ± 208.98	42677.00 ± 206.58	35951.00 ± 189.61	44667.00 ± 211.35	31378.00 ± 177.14	44669.00 ± 211.35	28886.00 ± 169.96	30843.00 ± 175.62	27993.00 ± 167.31	27993.00 ± 167.31	44734.00 ± 211.50

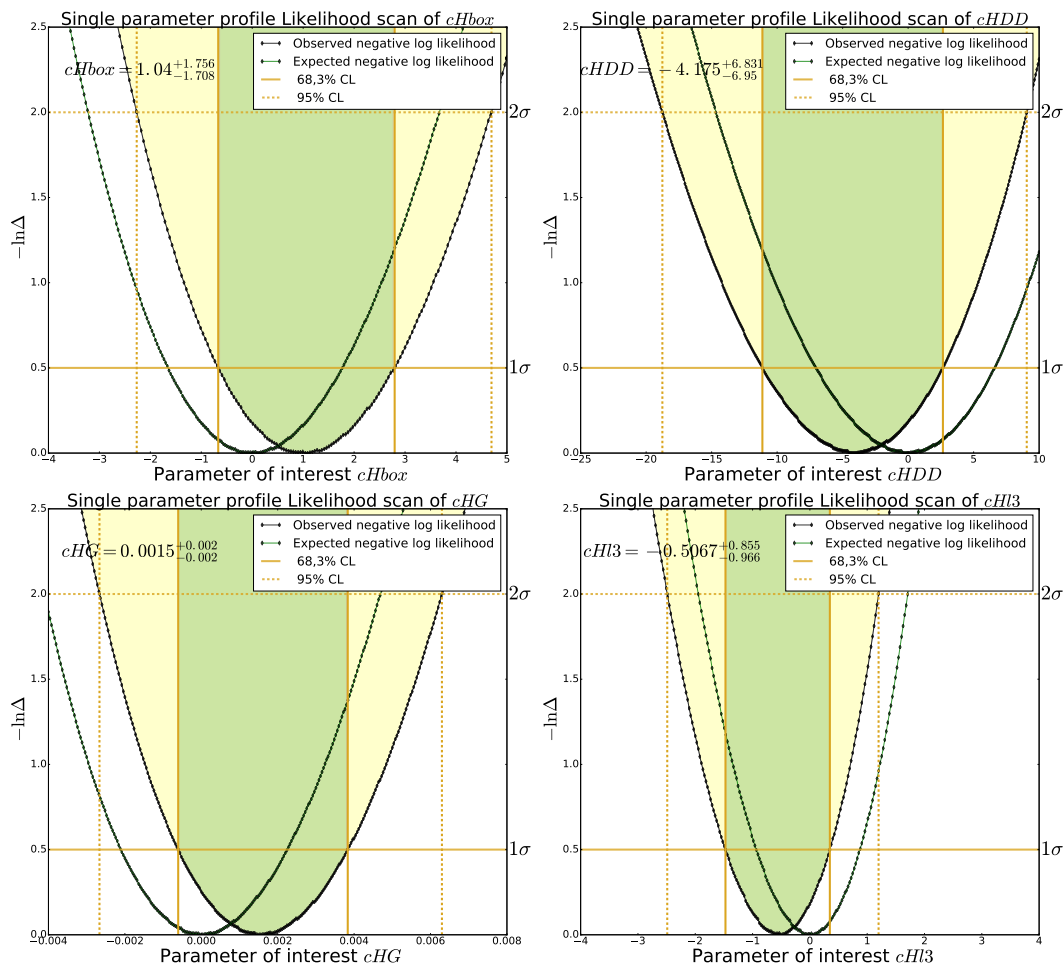
TABLE C.2: VBFF STXS decoration of 100,000 events per MC sample. First column describes the ggF STXS regions, next column the Standard Model events separated over the STXS regions. The next columns separate the interference events over the STXS regions. The errors on the event count represent the statistical error.

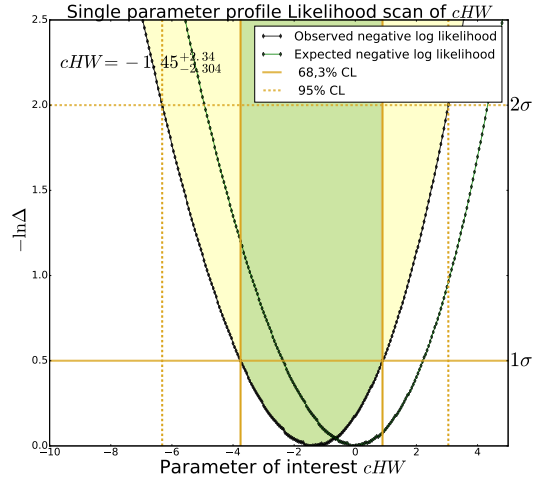
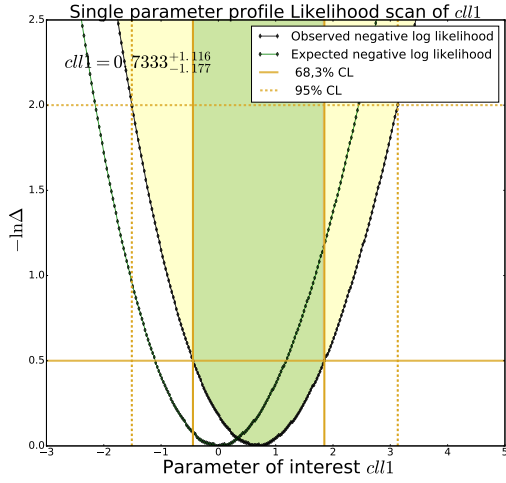
Appendix D

Profile Likelihood scans

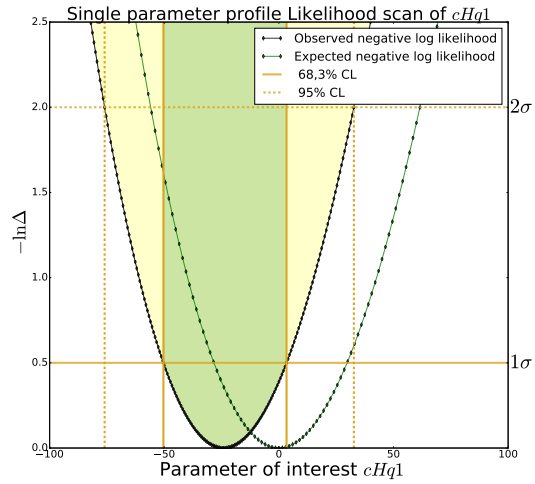
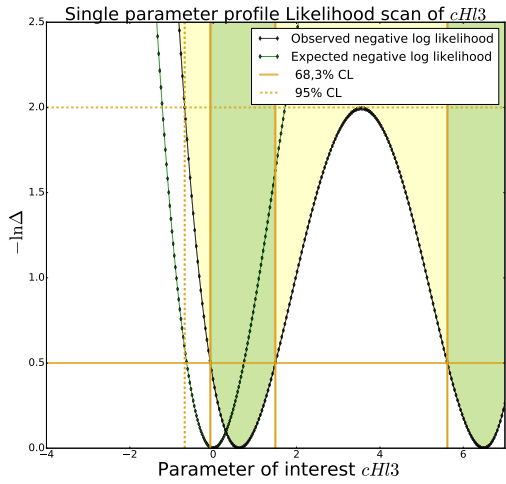
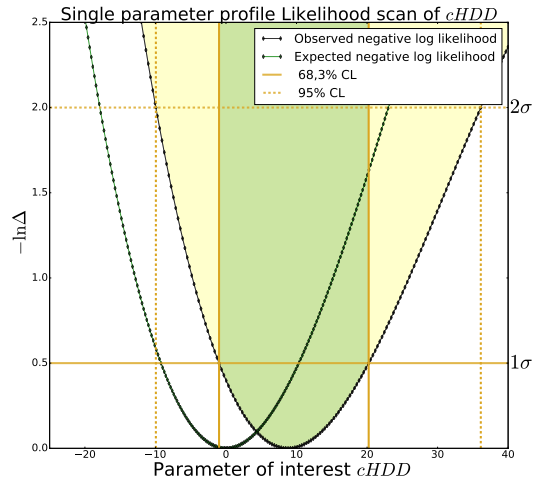
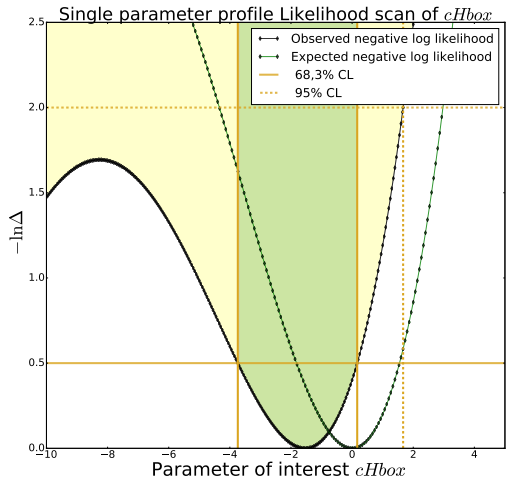
This appendix contains all of the likelihood scans performed in the individual fits. Each section represents a data set. In the last section the nuisance parameter pulls from the c_{HG} and $c_{HI}^{(3)}$ are shown for the total combined data set fit.

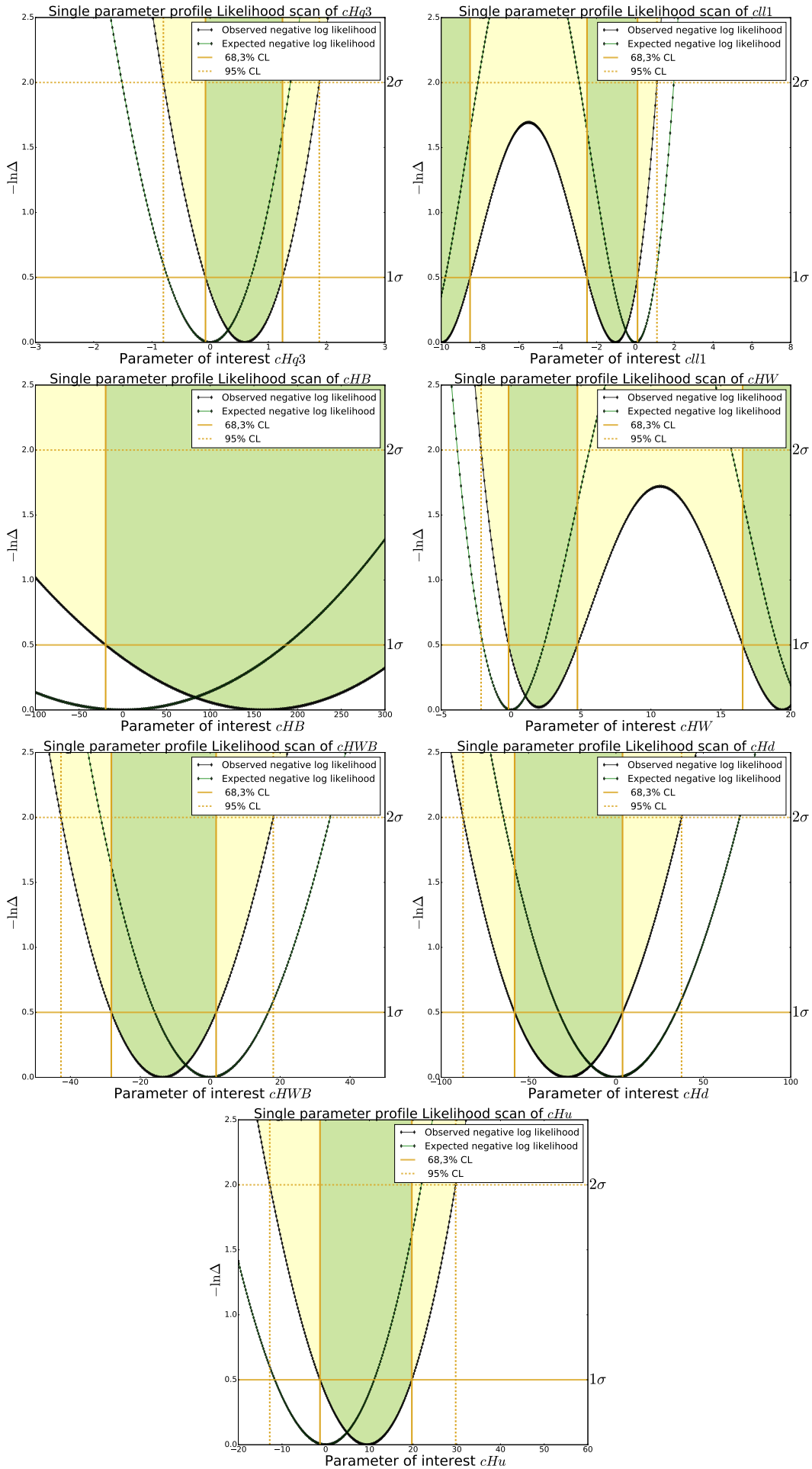
D.1 $ggF \rightarrow H \rightarrow WW$ analysis



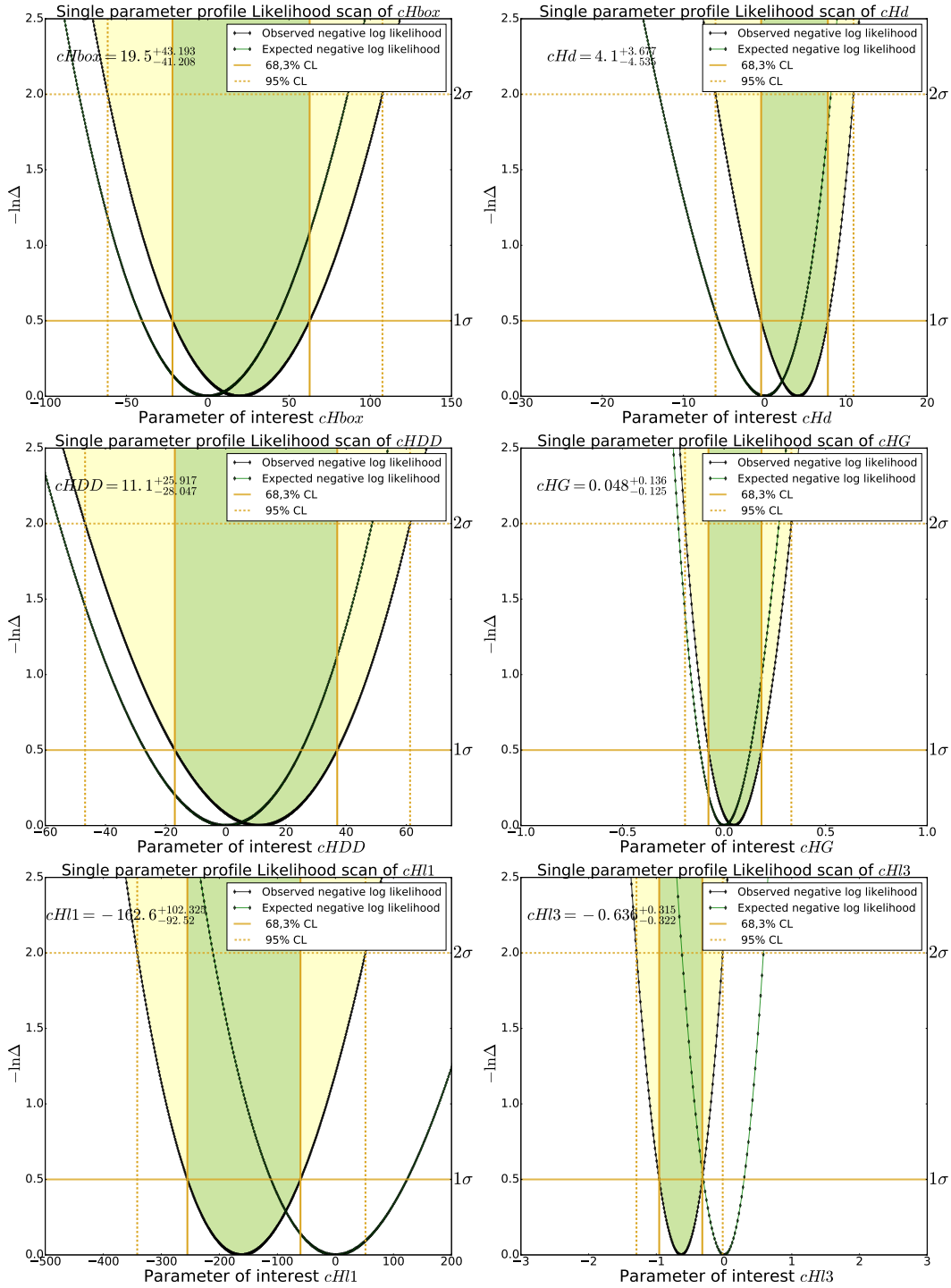


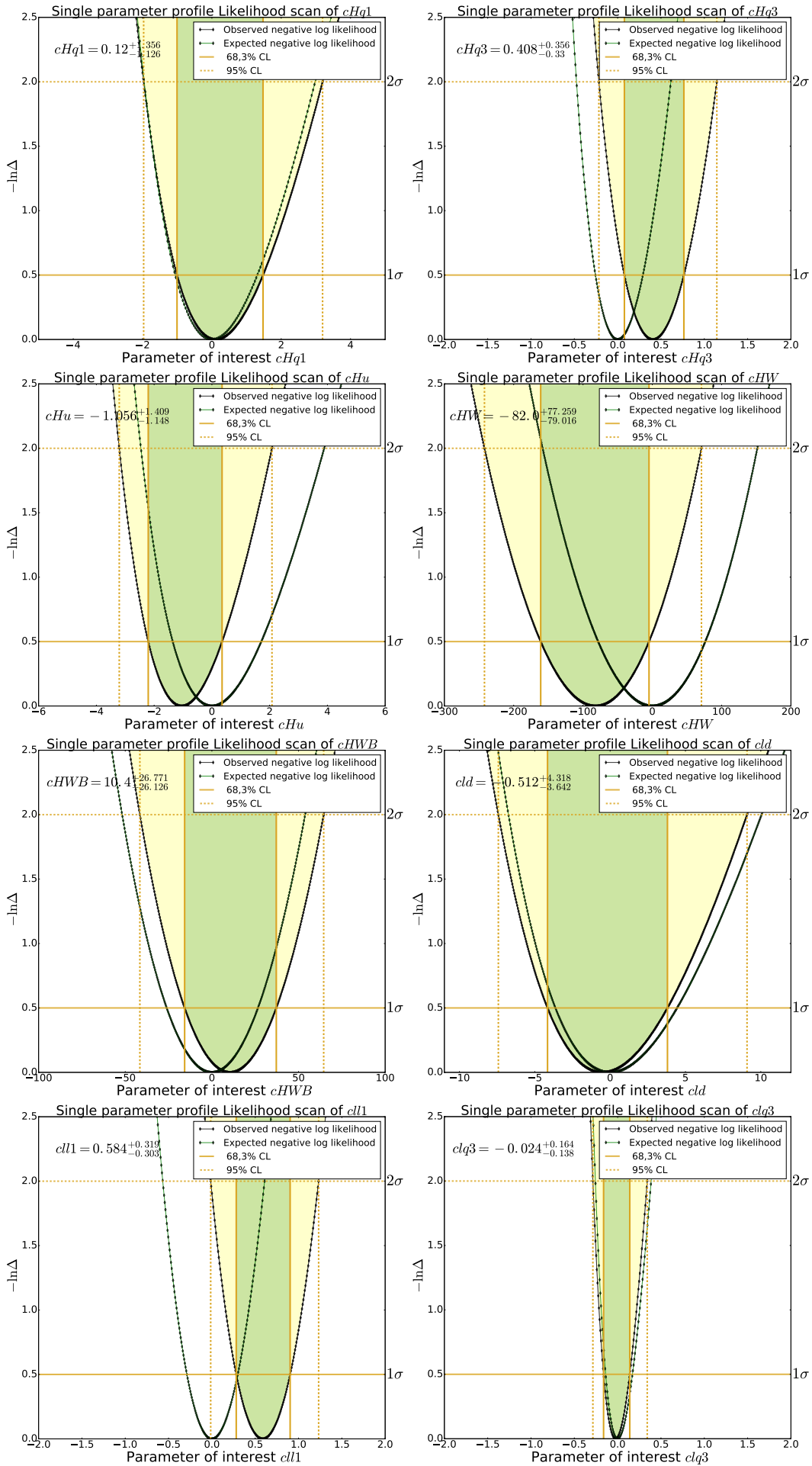
D.2 $VBF \rightarrow H \rightarrow WW$ analysis

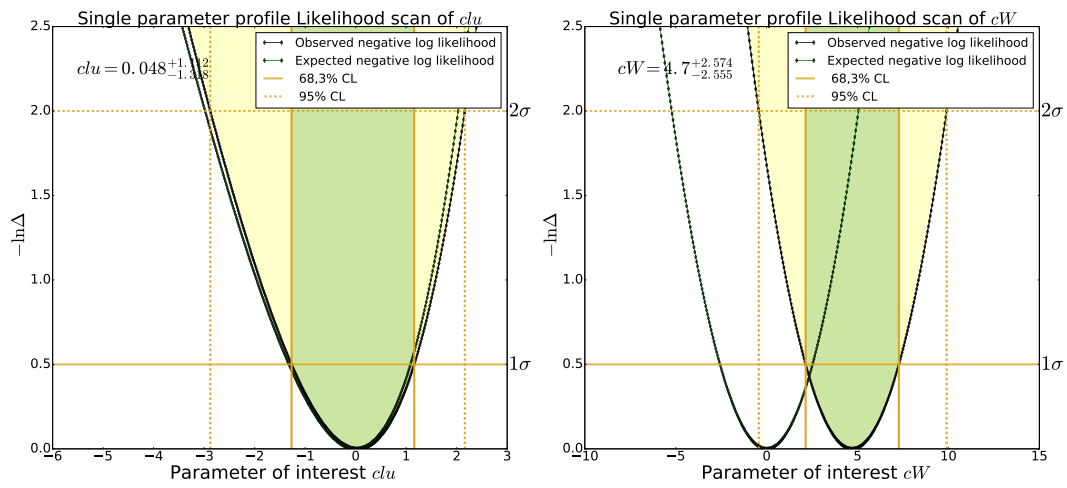




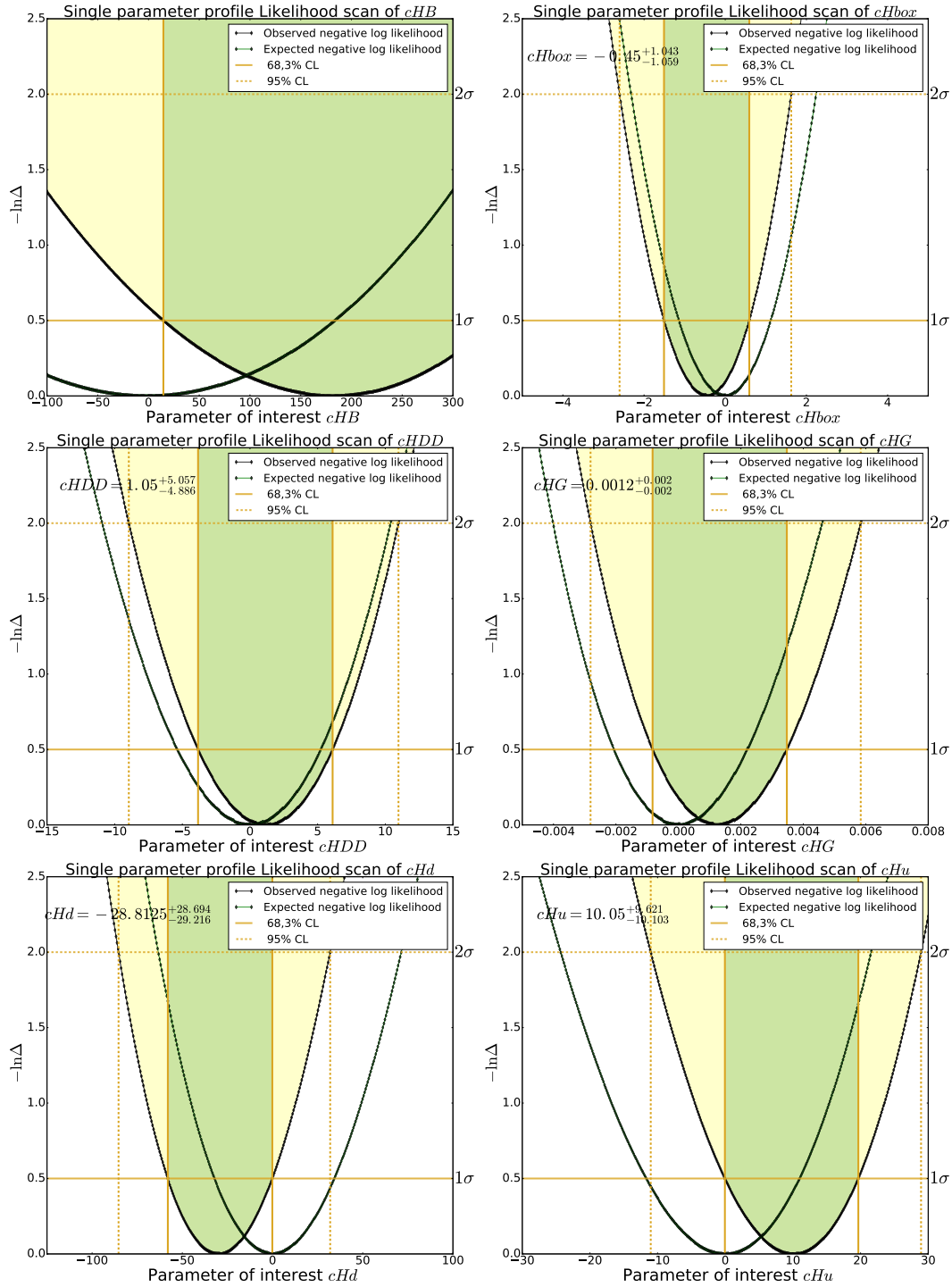
D.3 $qq/gg \rightarrow W^+W^-$ analysis

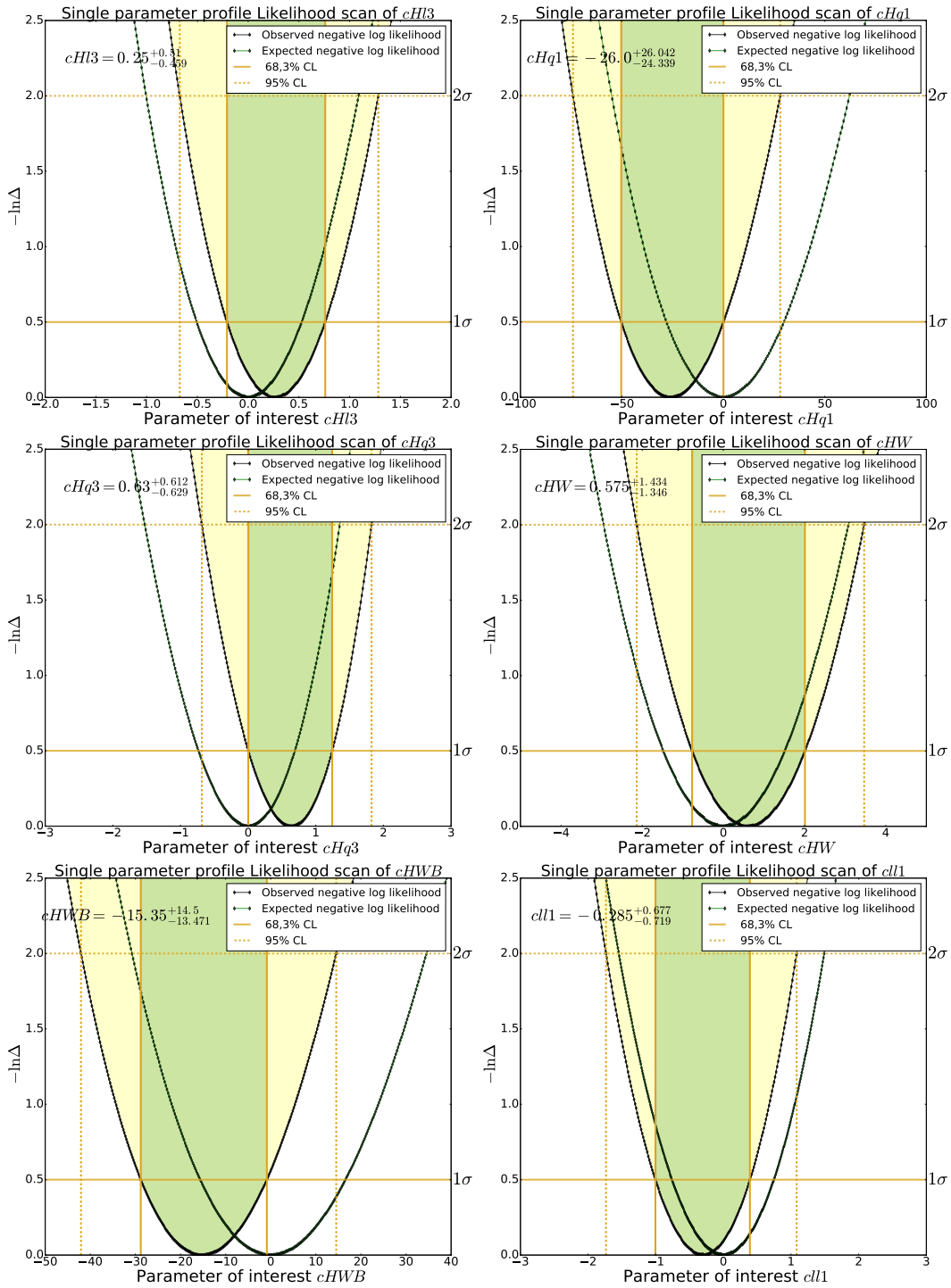




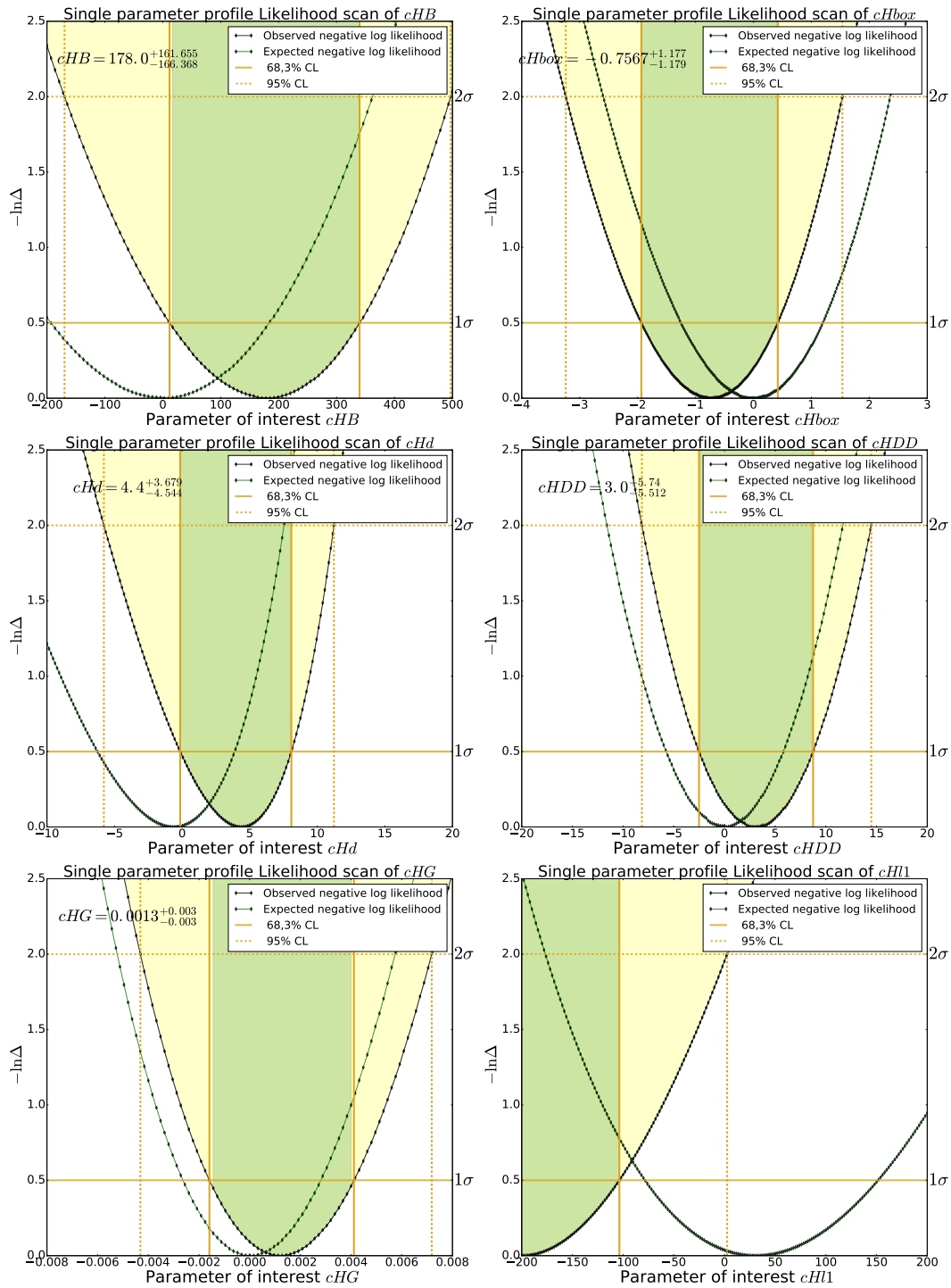


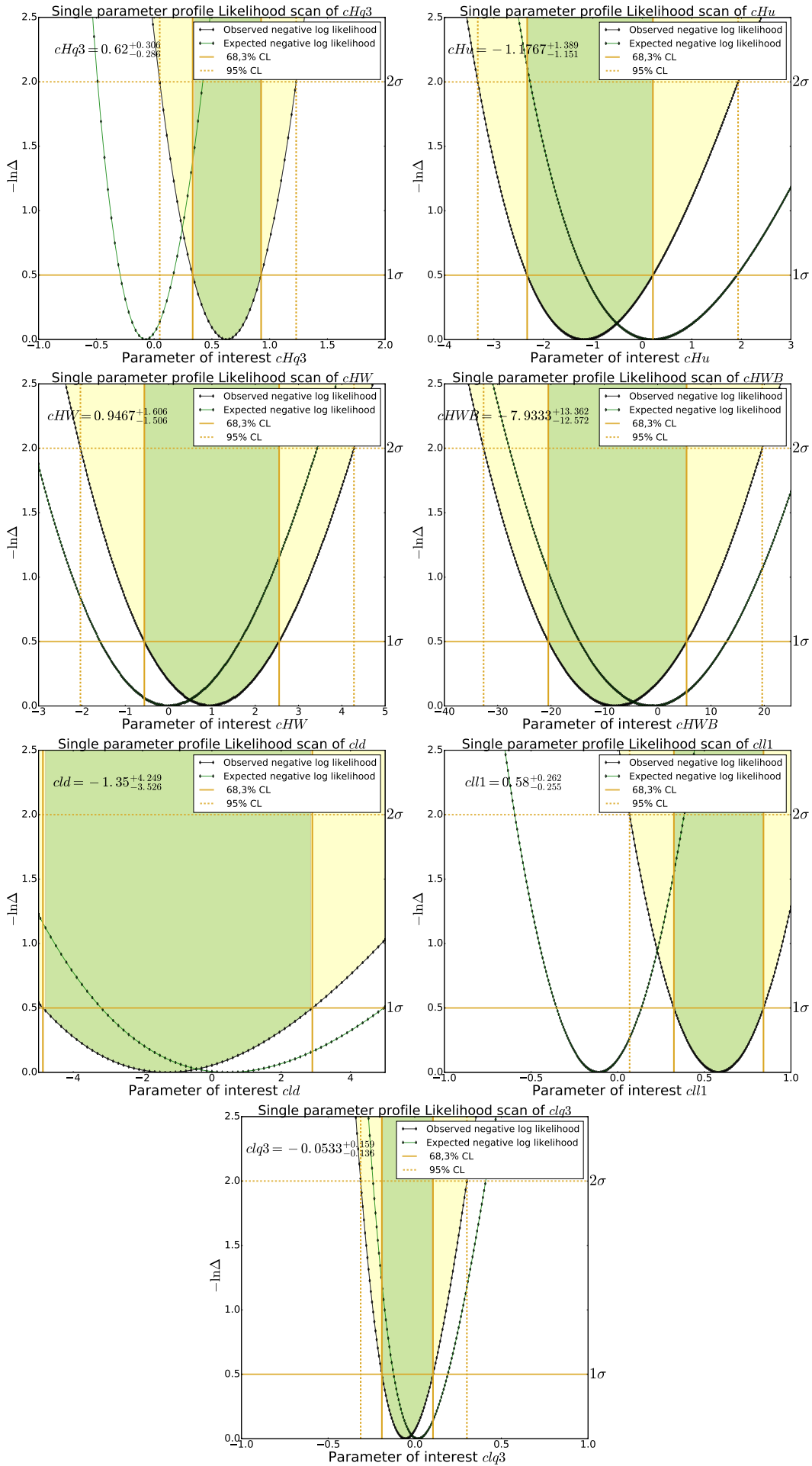
D.4 Combined $ggF + VBF \rightarrow H \rightarrow W^+W^-$ analysis

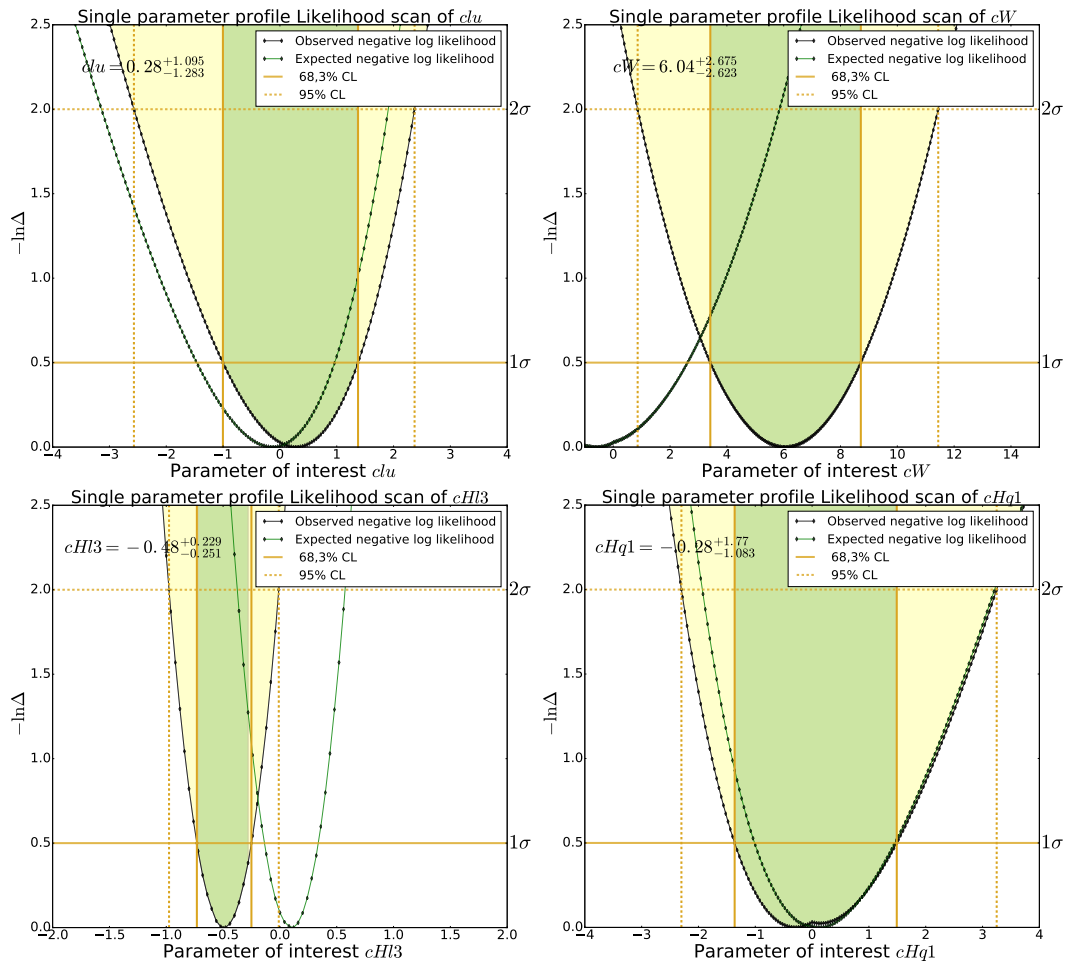




D.5 Combined $ggF+VBF \rightarrow H \rightarrow W^+W^- + qq/gg \rightarrow W^+W^-$ analysis







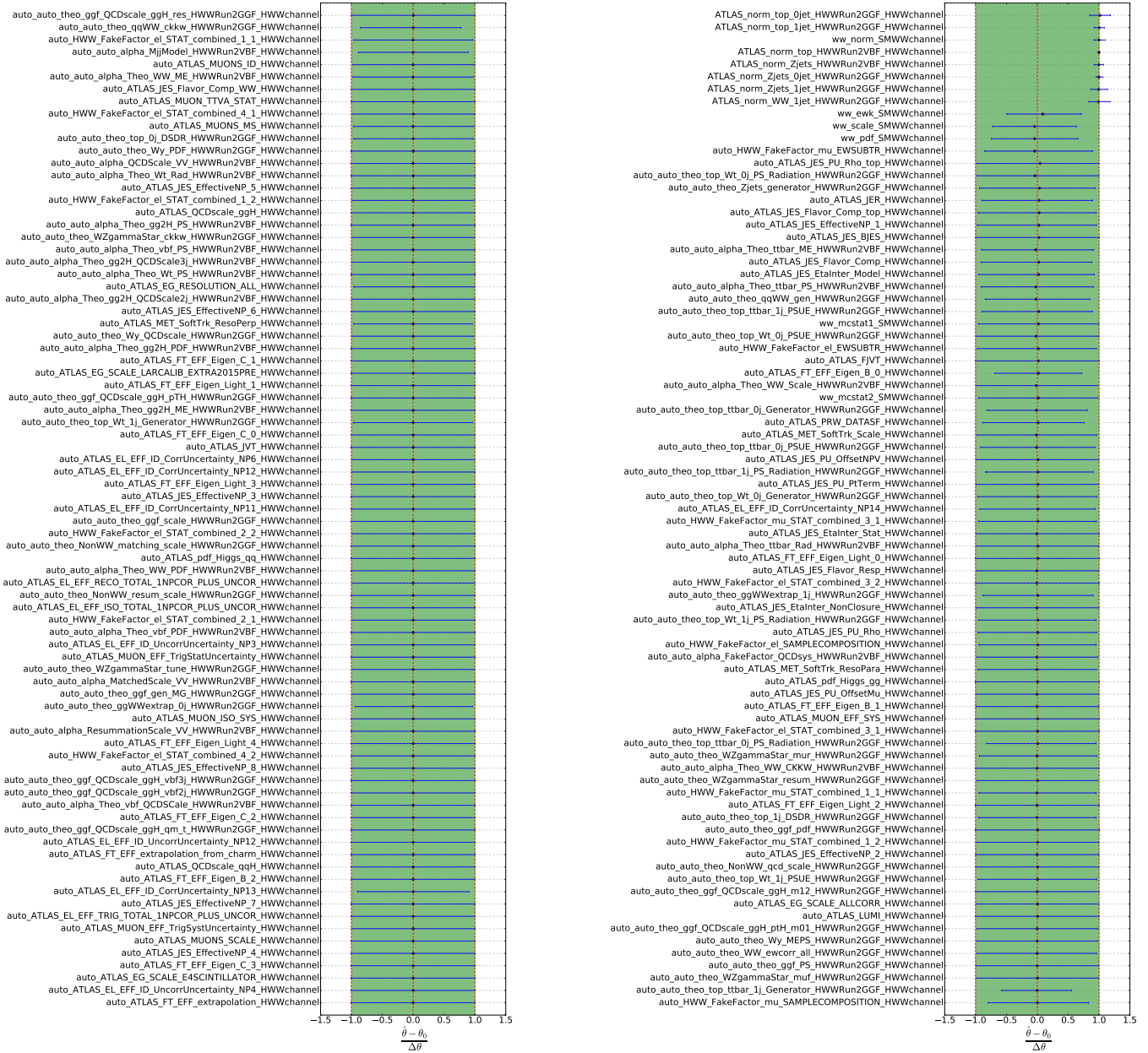


FIGURE D.1: Fitted nuisance parameters to the Asimov data set with the signal plus background hypothesis of parameter of interest c_{HG} .

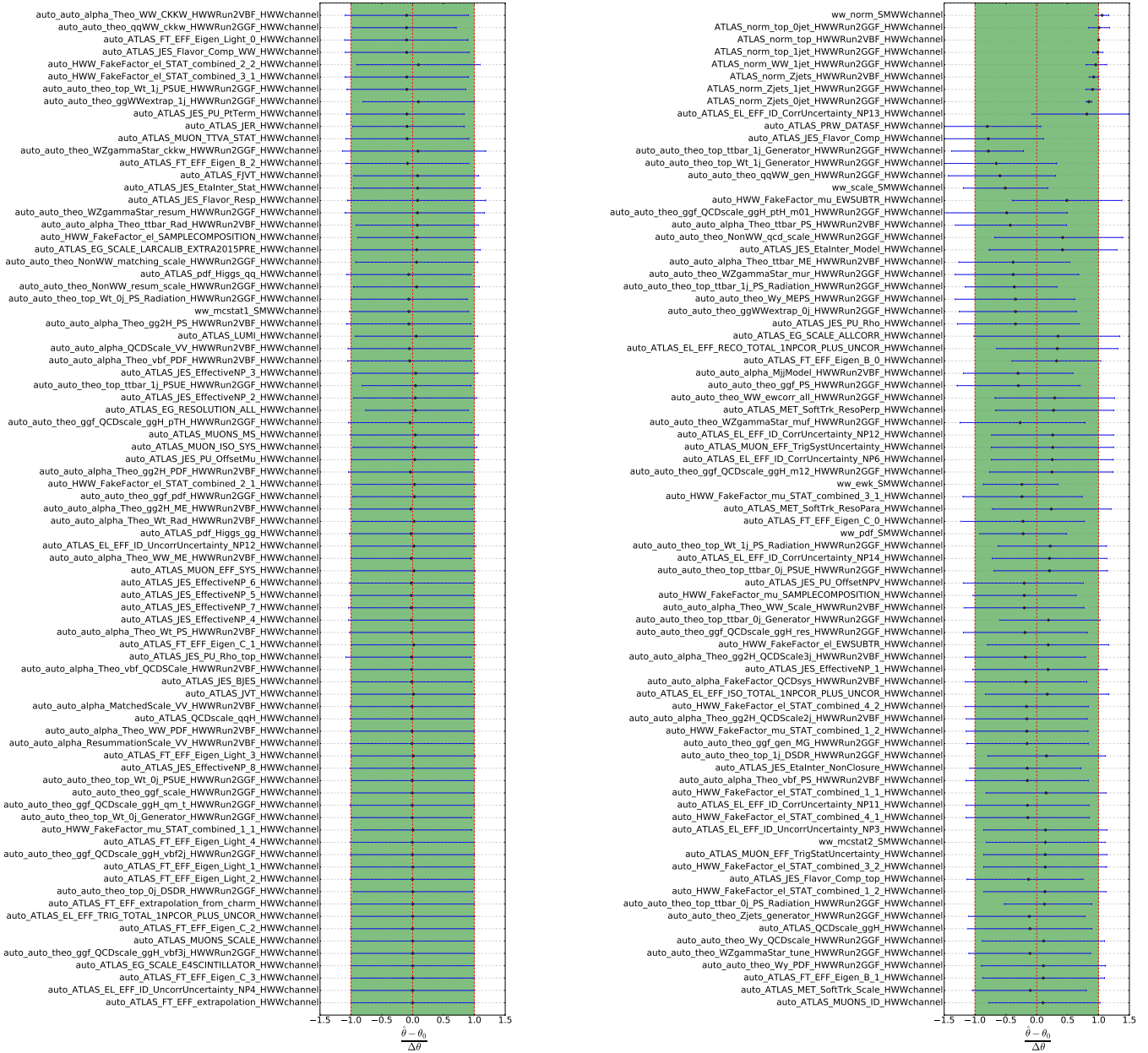


FIGURE D.2: Fitted nuisance parameters to the observed data set of parameter of interest c_{HG} .

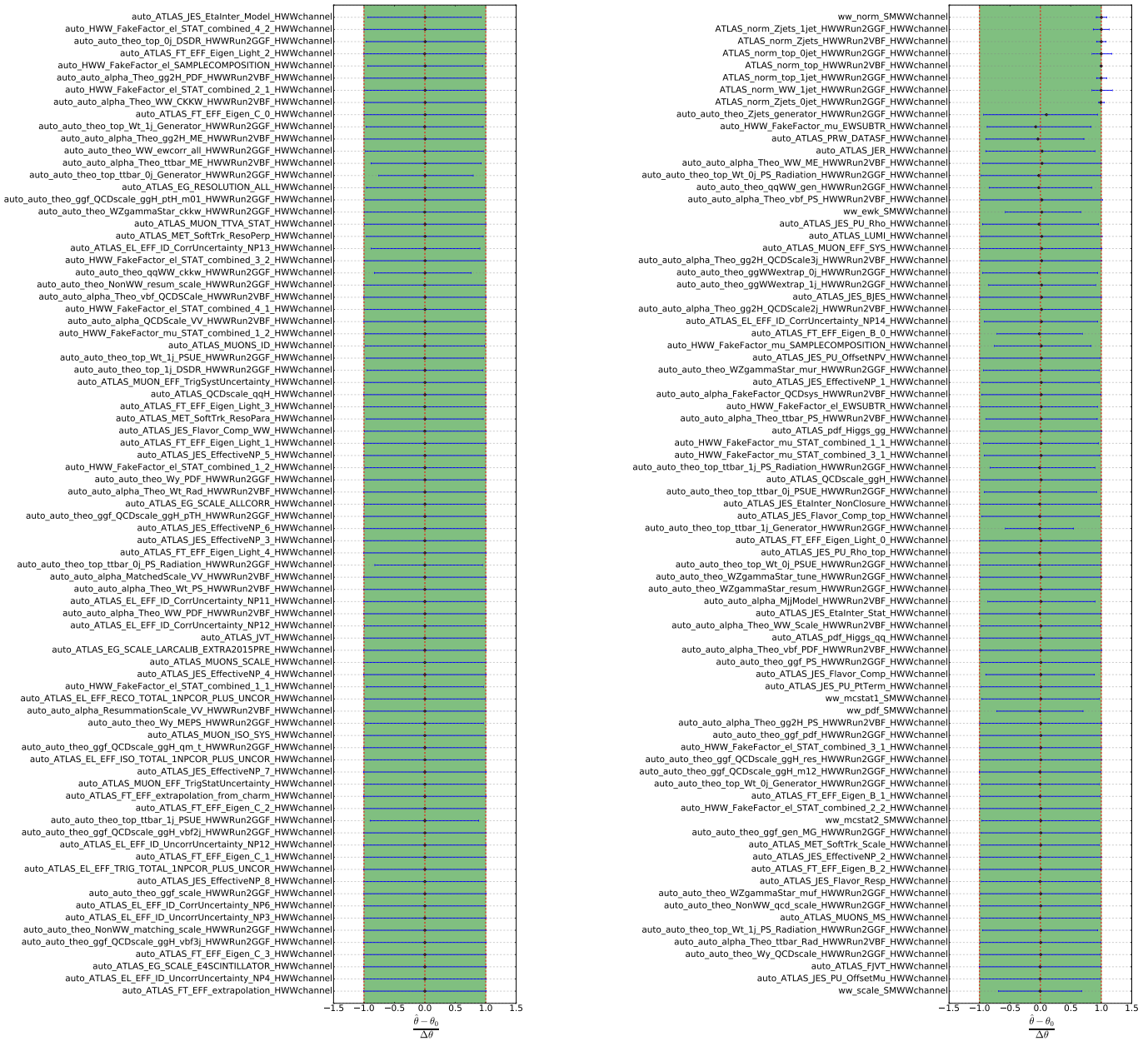


FIGURE D.3: Fitted nuisance parameters to the Asimov data set with the signal plus background hypothesis of parameter of interest $c_{HI}^{(3)}$.

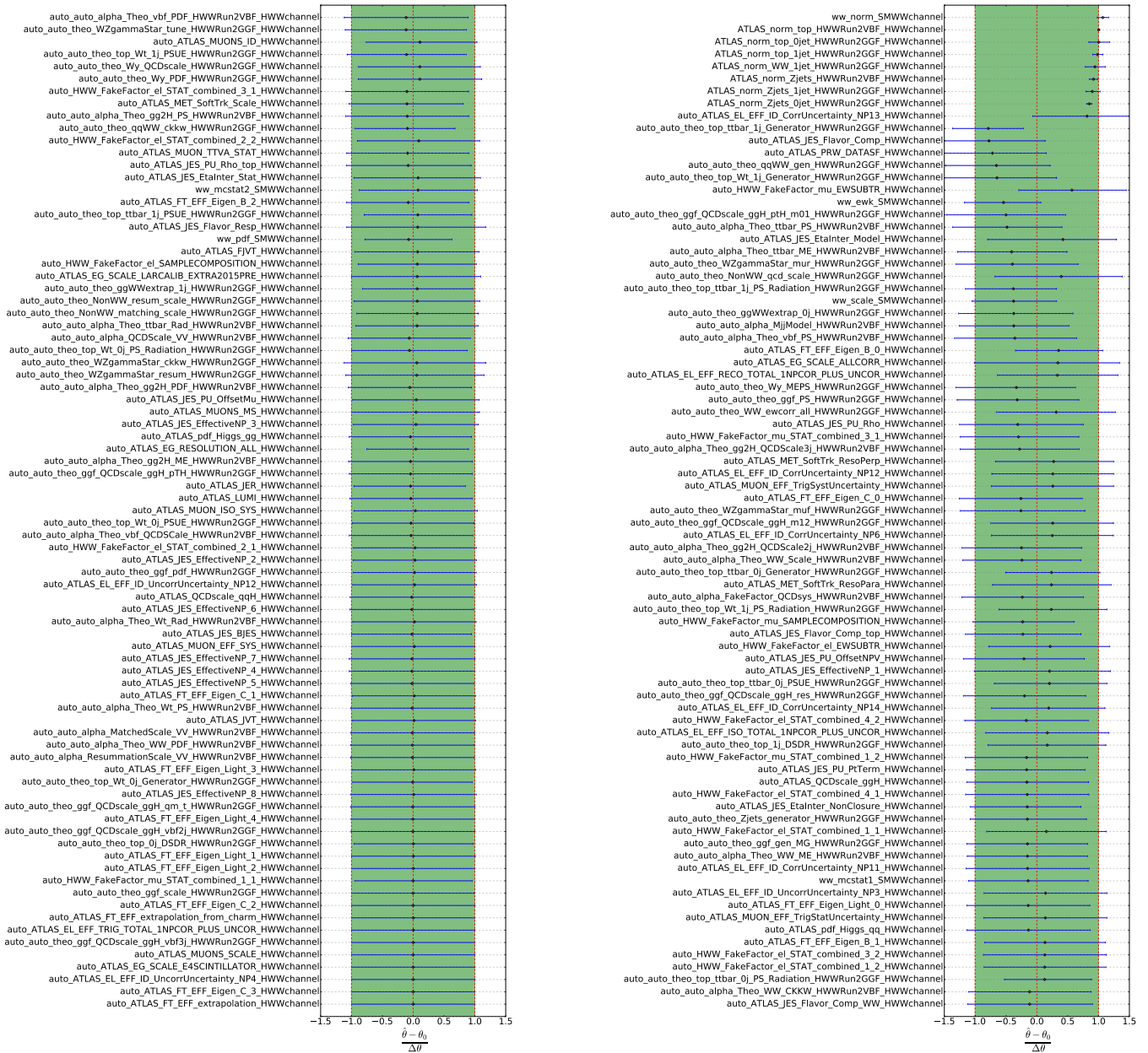


FIGURE D.4: Fitted nuisance parameters to the observed data set of parameter of interest $c_{HI}^{(3)}$.

Appendix E

Analytical Lagrangian Morphing validation plots

Appendix E presents all of the plots made for the Effective Lagrangian Morphing validation. The distribution used are M_T , p_T^e , M_{ll} , $\Delta\eta_{ll}$ and p_H^T .

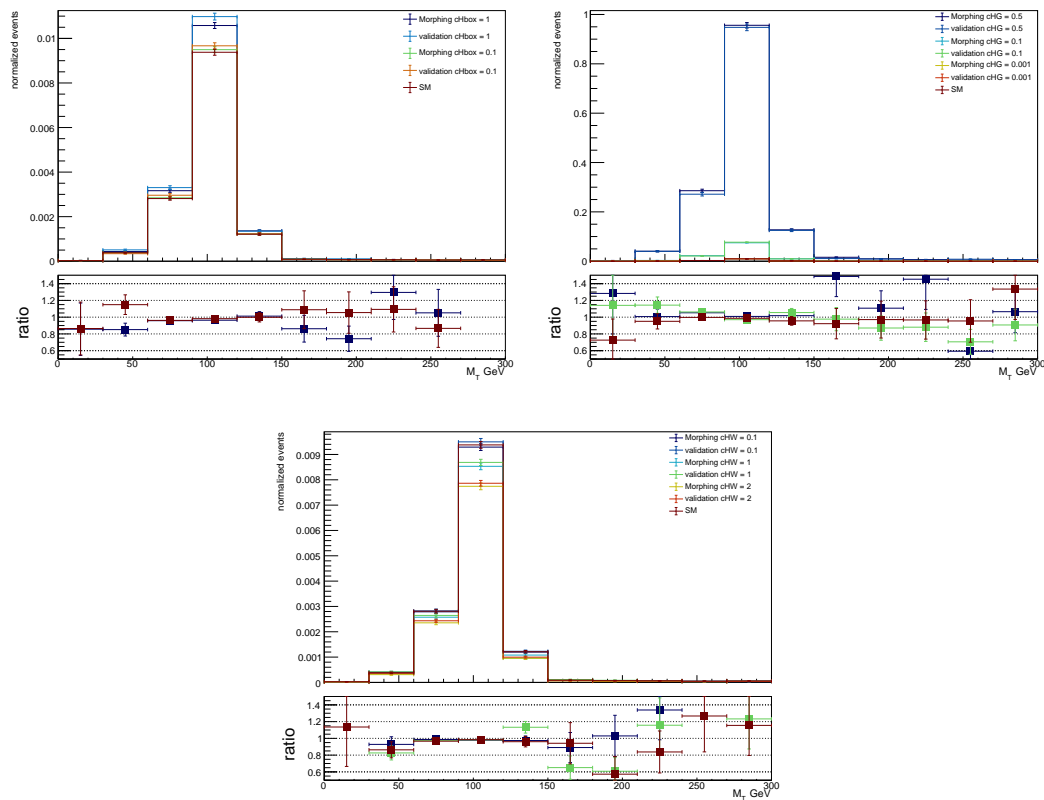


FIGURE E.1: Morphed and validation distribution of M_T plotted together to show the validity of the morphing approach. Top-left: c_{Hbox} . Top-right: c_{HG} . Bottom: c_{HW}

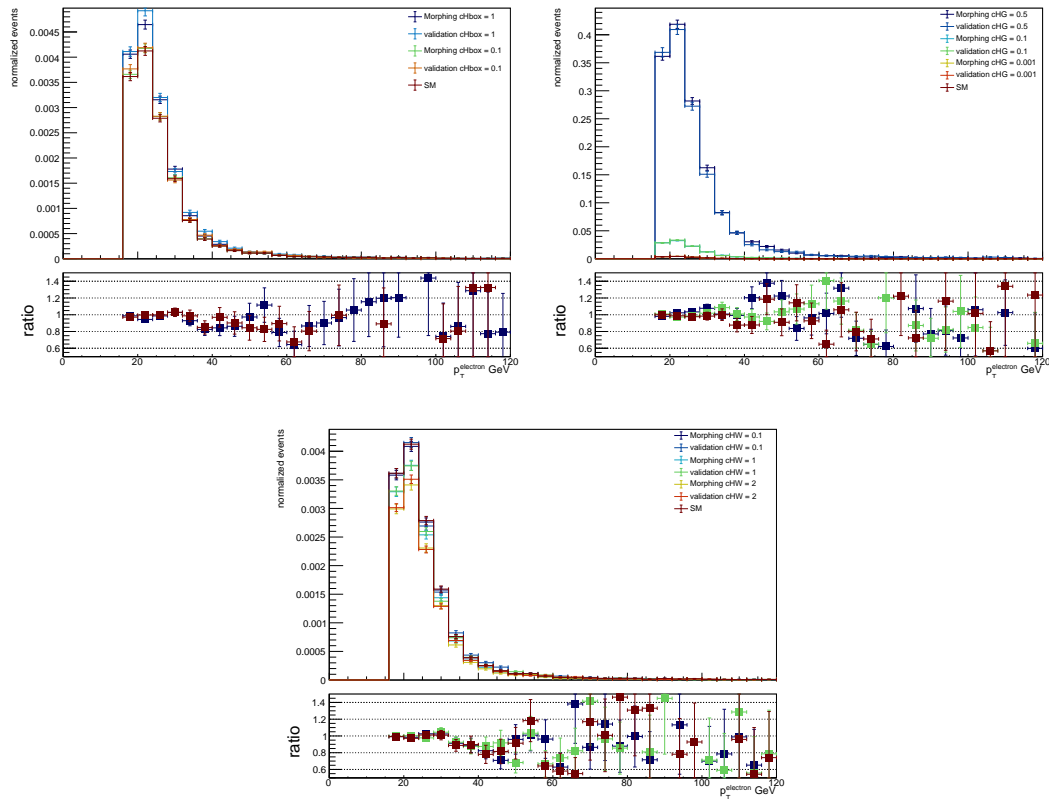


FIGURE E.2: Morphed and validation distribution of p_T^e plotted together to show the validity of the morphing approach. Top-left: c_{Hbox} . Top-right: c_{HG} . Bottom: c_{HW}

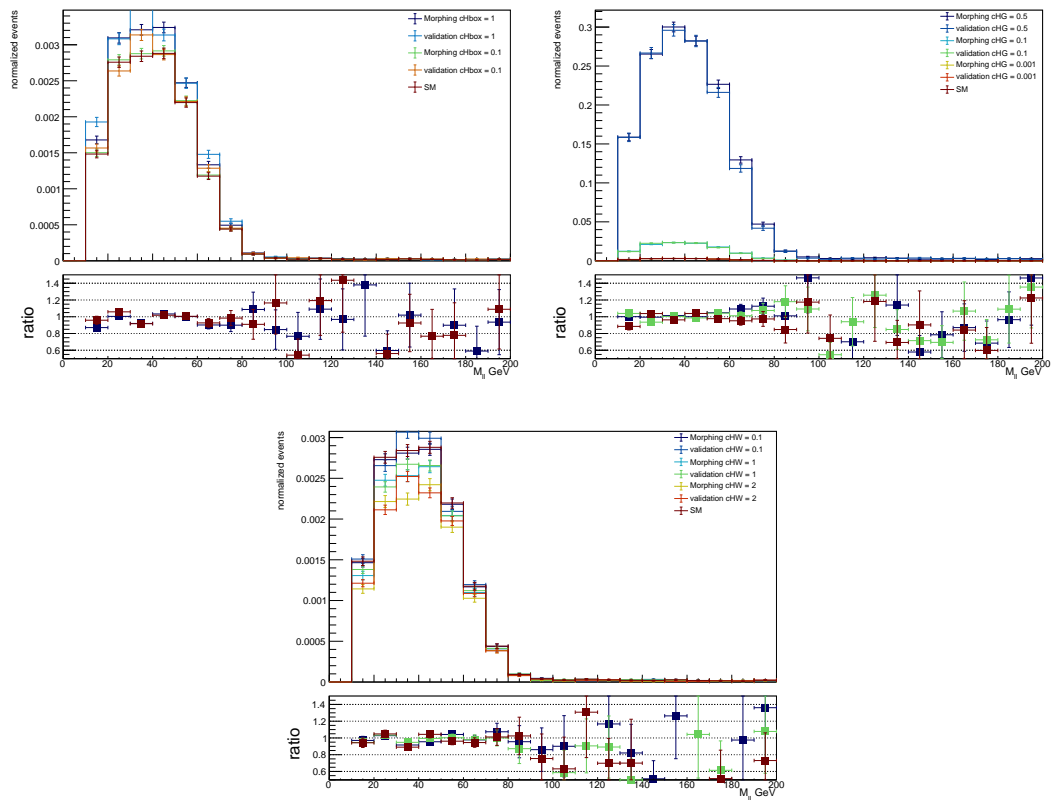


FIGURE E.3: Morphed and validation distribution of M_{ll} plotted together to show the validity of the morphing approach. Top-left: c_{Hbox} . Top-right: c_{HG} . Bottom: c_{HW}

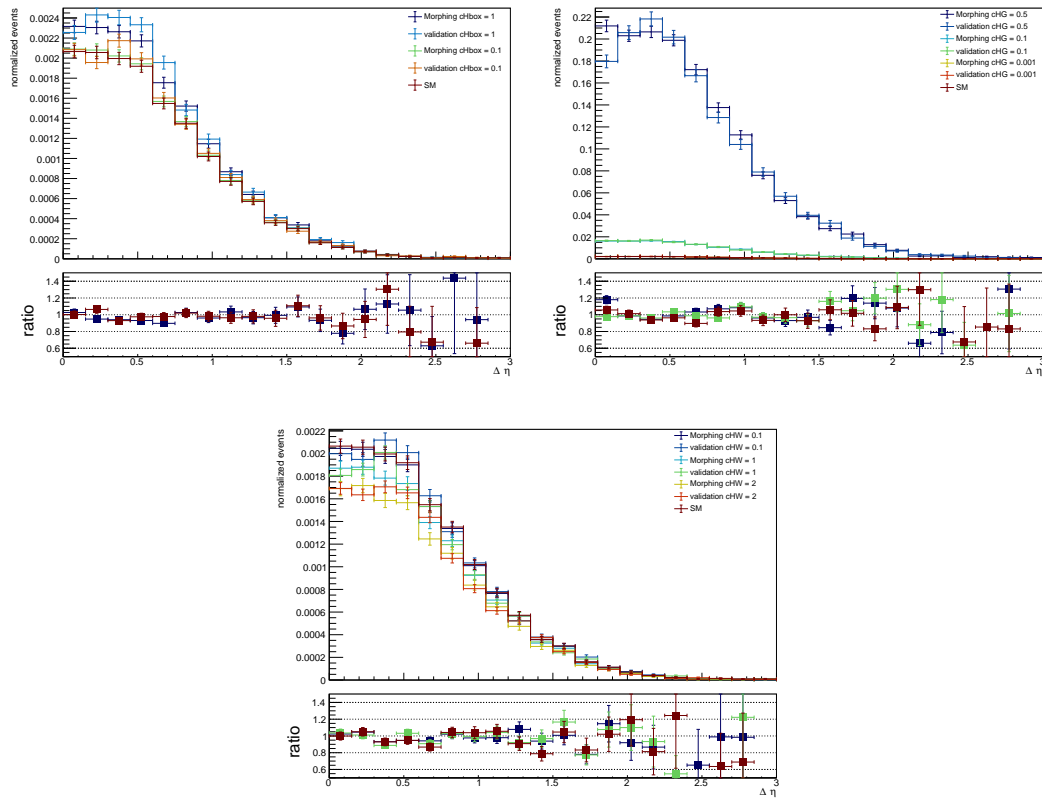


FIGURE E.4: Morphed and validation distribution of $\Delta\eta_{ll}$ plotted together to show the validity of the morphing approach. Top-left: c_{Hbox} . Top-right: c_{HG} . Bottom: c_{HW}

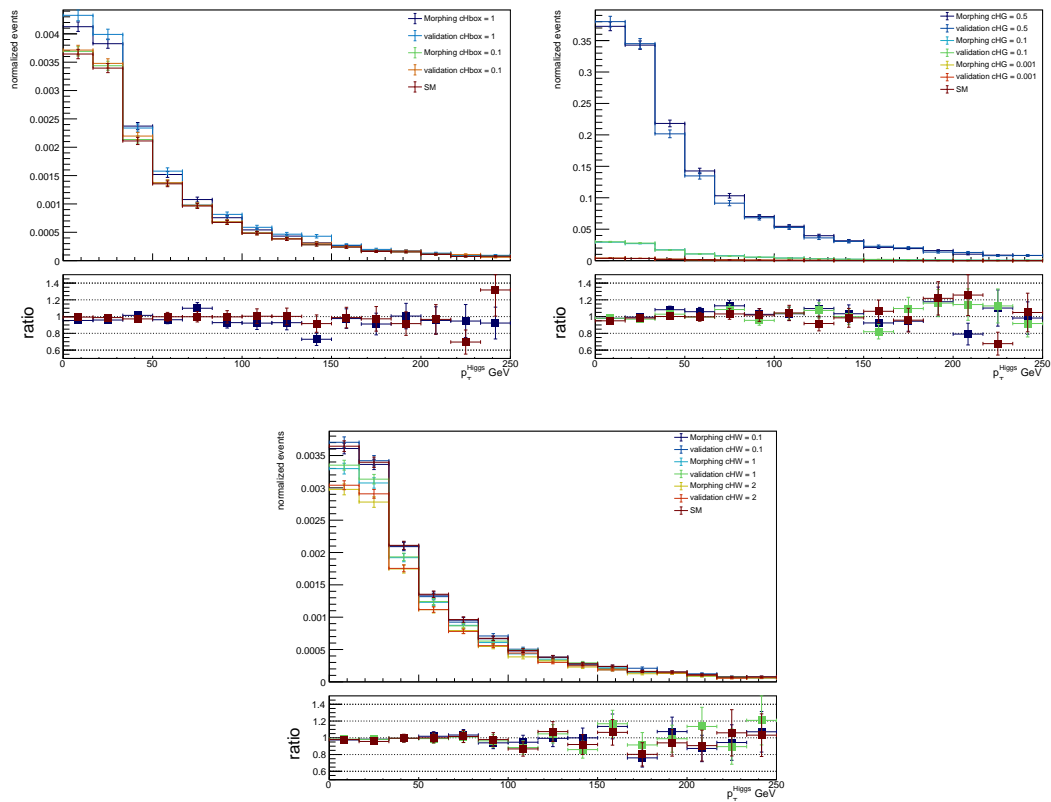


FIGURE E.5: Morphed and validation distribution of p_T^H plotted together to show the validity of the morphing approach. Top-left: c_{Hbox} . Top-right: c_{HG} . Bottom: c_{HW}

Appendix F

Narrow Width Approximation

The narrow-width approximation (NWA) is used extensively to calculate cross sections for production of quickly decaying particles having a relatively small decay width. The Higgs particle is a good example, which has a peaked mass distribution and decays in about 10^{-22} seconds [65]. The use of this approximation is justified if some critical conditions are met

- the total width of a resonance is much smaller than its mass
- daughter particles are much less massive than the parent, $m \ll M$
- the centre-of-mass energy is much larger than the parent mass, $\sqrt{s} \gg M$
- there must be no significant interference with non-resonant processes
- The resonant propagator is separable from the matrix element

Assuming the stated requisites are satisfied in the considered scenario, the propagator can be integrated independently over all q^2 to obtain a constant

$$\int_{-\infty}^{+\infty} \left| \frac{1}{q^2 - M^2 + iM\Gamma} \right|^2 dq^2 = \frac{\pi}{M\Gamma} \quad (\text{E.1})$$

This approximation assumes that massive states are always produced exactly at their mass pole as an asymptotic final state, such that its decay is an independent process, expressed by the branching ratio.

The NWA is used often for heavy particle production such as W, Z or top quarks, excluding hadronic and flavour physics because of the composite nature of the particles involved. This is mostly because their decay products are so much lighter than its parents. It is used in calculating the branching fraction of Higgs boson decay to weak bosons [66]. In the context of new physics extensions to the SM, it is generally the case that massive particles widths are much smaller than their masses, $\Gamma \ll M$, leading to a conclusion that the NWA is valid in this regime. Typically, the collision energy is far above production threshold, $E_{CM} - M \equiv \sqrt{s} - M \gg \Gamma$, and thus avoiding a cut Breit-Wigner lineshape. There are some drawbacks to this. Rarely does scattering of a given initial and final states result from only one resonant process. Interference with other processes can occur, rendering the NWA inapplicable. However, this is reduced when looking at Higgs production. This production has relatively few resonant configurations compared to SM production modes. Assuming this approximation may result in the neglecting significant off-shell corrections in the BSM scenarios, when the listed requirements do not hold. A critical ingredient in this is massive daughters. These differences from the SM may yield unexpected behaviour and must be taken into account when interpreting the results.

Appendix G

Impact of dimension-8 operators

When taking into account that the SMEFT is an effective theory, we need to say something about the higher order operators. The dimension 8 SM interference and the dimension 6 squared terms appear at the same order in an expansion in $1/\Lambda$.

Thus the dimension 8 effects and in this case also the dimension 6 squared terms may be treated as a systematic uncertainty on the new physics observed from the analyses. This can be realised at later state to see the contribution of the higher order operators by turning them on one by one and setting the coefficients of the same Wilson coefficient to the same value.

This was studied in Ref. [67] and found to be of a very small scale, of the order of a few percent. A comparison was made with the inclusive cross section of the $\sigma(pp \rightarrow hW^\pm)$. Here the dimension 8 and dimension 6 effects have been compared and the dimension 8 effects have showed to be significantly smaller and are typically at the percent level. But, can be quite significant when reaching higher energies.

For example the dimension-8 effects on the operators $Q_{Hq}^{(3)}$ and $Q_{H\Box}$. In this study[67] the shift in $\sigma(pp \rightarrow hW^\pm)$ rate relative to the SM is calculated as $|\Delta\mu(pp \rightarrow hW^\pm)| = |(\sigma(pp \rightarrow hW^\pm)_{\Lambda_6, \Lambda_8} - \sigma(pp \rightarrow hW^\pm)_{SM}) / \sigma(pp \rightarrow hW^\pm)_{SM}|$. It has been calculated for a different process than VBF or ggF. However, we believe the effects on the other production processes involving W^\pm to be of the same order and can thus used as an estimate. In Fig. G.1 the blue line represents the relative deviation of the SM taking into account only dim-6 effects, thus $\Lambda_8 \rightarrow \infty$. The dashed black line is the case where both dimension 6 and 8 effects carry equal value Wilson coefficient. The red line denotes where Λ_8 has been reduced so much to where the EFT approximation breaks down and thus denotes the maximum possible difference in rate. This criteria is $A_{SM} \cdot A_{dim_6} > A_{SM} \cdot A_{dim_8}$.

Two regions are used, the total fiducial phase space and the high mass phase space requiring $m_{hW^\pm} > 500 GeV$. From Fig. G.1 we can conclude that the dimension-6 operators cause most significant altering of the SM cross section and will therefore be a first start in this analysis. When the sensitivity is achieved to probe the higher order operators we can include them, before, they can be taken into account as a source of systematic uncertainty.

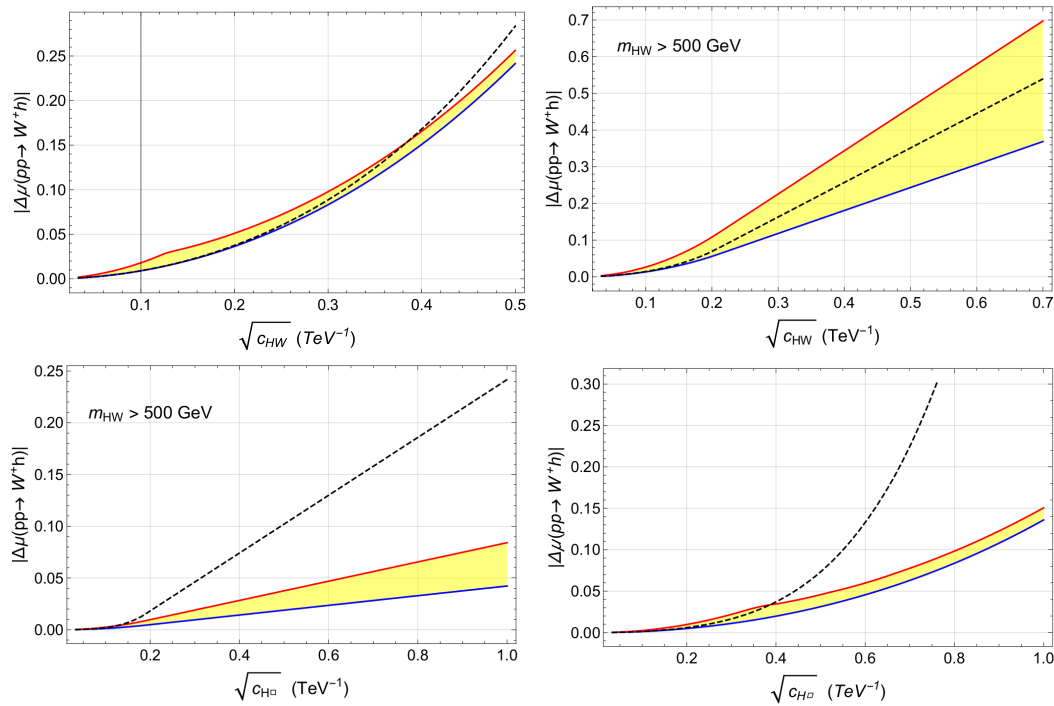


FIGURE G.1: Relative deviation of the SM cross section of the total fiducial phase space(left) and the high mass region(right) for the c_{HW} operator(upper) and the c_{HBox} operator(lower). The blue line showing the result of the operator as the only dimension-6 operator and without including the dimension-8 effects. The red line indicates the derivation as function of the operator c_i including the maximum number of possible dimension-8 effects consistent with the EFT expansion. The black dashed line is the change in rate if the dimension-6 and dimension-8 Wilson coefficients are all equal, $c_{i,6} = c_{j,8}$ [67]